

**INNOVATIVE SYSTEM FOR DEPLOYING NOVEL
BIOSENSORS FOR WATER CONTAMINANT MONITORING**

Douglas James Pike

Submitted in accordance with the requirements for the degree of
Doctor of Philosophy

The University of Leeds
School of Civil Engineering

September, 2014

Jointly authored publications

The candidate confirms that the work submitted is his own, except where work which has formed part of jointly-authored publications has been included. The contribution of the candidate and the other authors to this work has been explicitly indicated below. The candidate confirms that appropriate credit has been given within the thesis where reference has been made to the work of others.

1) Chapter 3 of the thesis includes work which has appeared in the following publication:

Flow cell design for effective Biosensing, 2013, **Pike, D.**, Kapur N, Millner PA and Stewart DI.; *Sensors (Switzerland)*, 13(1), pp.58-70.

All of the work carried out in relation to this publication was conducted by the author of this thesis. This consisted of development and manipulation of mathematical computer models, and development and conductance of laboratory based experiments. The role of each of the co-authors for this publication was to provide guidance with respect to the development of the study investigation work, along with guidance on publication content and structure. This included some suggested re-wording of written passages and suggestions on the development of figures.

Publications involving works that do not appear in this thesis

The candidate was a co-author on the following publications, for which works from the publications were not included in this thesis:

1) Comparative electrochemical analysis of two flow cell systems, 2014, Goode JA., Ahmed A, **Pike D**, Millner PA, Kapur N, and Stewart D.; *Systems. Journal of the Electrochemical Society*, 161(6), pp.B143-B146.

2) Impedimetric Biosensors for Medical Applications: Current Progress and Challenges, 2013, Rushworth JV, Hirst NA, Goode JA, **Pike D**, Ahmed A and Millner PA. 2013.; Momentum Press.

This copy has been supplied on the understanding that it is copyright material and that no quotation from the thesis may be published without proper acknowledgement.

The right of Douglas James Pike to be identified as Author of this work has been asserted by him in accordance with the Copyright, Designs and Patents Act 1988.

© 2014 The University of Leeds and Douglas James Pike.

Acknowledgements

Thank you first of all to the Nuclear Decommissioning Authority (NDA) for providing the funding for this project, and to Divyesh Trivedi of National Nuclear Laboratory (NNL) for his support in the role of industry project supervisor on behalf of the NDA.

Thank you to my University of Leeds supervision team, Dr Doug Stewart, Professor Nik Kapur, and Professor Paul Millner. I feel very fortunate to have had a team of such knowledgeable and professional academics to support me. Specifically, Doug has been a trusted source of forthright and useful feedback and advice throughout the project. Nik has provided both pertinent technical guidance and personal encouragement, particularly at times when the project became most difficult. Paul has offered valuable technical input on issues relating to the biosensor investigations along with his own unique brand of enthusiasm.

Thank you to my study room colleagues in the School of Civil Engineering, both past and present, namely Oldouz Payan, Abdulrahman Bashawri, Manal Elgallal, Olusola Idowu, Nor Zalina Kasim, Matthew Oke, and Tejumola Akojede. They have provided essential encouragement and conversation during the duration of the project. Thank you also to Joseph Ghaffari Motlagh for his kind and patient technical advice.

I would also like to thank the members, past and present, of the Millner lab group for their friendly support. In particular, I feel it is important that I direct personal thanks to David Conroy for his technical guidance both during and after completion of his own PhD. Special thanks also go to Asif Ahmed and Jack Goode who provided invaluable technical guidance relating to the electrochemistry lab, all whilst conducting their own PhD studies.

Thank you to Brian Leslie of Lindum Precision Components whose diligent, timely and professional work on the construction of bespoke flow cells and other components was absolutely essential to the successful completion of this project.

Finally, I would like to thank my family and friends for their unwavering encouragement and belief in me. This applies not only to this PhD project but to my entire study journey, which commenced long ago in 2004. Specifically, they are Bill Pike (father); Christine Turner and Clare Fowler (sisters); Janelle Thomas, Tony Vickers, Graham Young, and Jon Brooks (friends). Special thanks also to my mother Betty Pike who, although sadly no longer with us by the time I started this project, was the most encouraging of all with respect to my studies and remained an inspiration throughout.

Abstract

The ability to remotely sense contaminants in surface and sub-surface waters can offer a deeper understanding of environmental conditions and an early warning system that will improve the efficiency of response to contaminant transport. The aim of this thesis was to develop an innovative system for field deployment of biosensors to facilitate environmental water quality monitoring. Two strands of work were addressed in developing the monitoring system (i) a flow cell in which to deploy the biosensor and (ii) integration of a uranyl ion (UO_2^{2+}) biosensor.

Three different flow cell designs were investigated using both a finite element computational model and a flow-fluorescence experimental technique. These comprised a flow channel featuring an expanded central region to accommodate the sensor, but the rates of channel expansion were varied between each design. A reduction in flow cell efficiency with increasing flow rate for all three cell designs was linked to the development of regions of flow recirculation (eddies). However, the most gradually expanding flow channel restricted eddy development to higher flow rates in comparison to the other designs. This more efficient design, and an optimised operational protocol, was thus identified as a recommended method of biosensor deployment.

A biosensor for the detection of aqueous uranyl ions (UO_2^{2+}) was developed from a sensor element created by Conroy (2012). Two different integration methods, screen-printed electrodes and solid gold electrodes for biosensor construction, were investigated. The biosensor response was linked to electrode nano-surface topography and electrode chemical composition, and was observed to be higher for the solid gold electrodes. The operational dynamic range of the integrated biosensor was improved by four orders of magnitude in comparison to the original laboratory proof of concept investigations for the sensor. Furthermore, recommendations for operational protocols were developed with respect to optimisation of integrated biosensor operation within a remotely controlled and automated water monitoring system.

CONROY, D. 2012. *Nanostructured surfaces for sensing heavy metals and radionuclides in aqueous systems*. PhD thesis, The University of Leeds.

Table of Contents

Acknowledgements.....	iii
Abstract.....	v
Chapter 1 Introduction	2
1.1 Research background	2
1.2 Research aim and objectives	4
1.2.1 Research aim.....	4
1.2.2 Research objectives.....	5
1.3 Research methodology	5
1.4 Research scope and limitations	6
1.5 Organisation of the thesis	8
Chapter 2 Literature review and background.....	11
2.1 Chapter introduction.....	11
2.2 Radioactive and uranium land and water contamination.....	13
2.2.1 Contamination characterisation	13
2.2.1.1 Causes of contamination	13
2.2.1.2 Land contaminated with uranium	13
2.2.1.3 Environmental mobility and biogeochemistry	14
2.2.2 Remediation methods and risk	15
2.2.2.1 Remediation methods overview.....	15
2.2.2.2 Brief case study – Pécs, Hungary	17
2.2.2.3 The risks of uranyl contamination	18
2.3 Environmental water contamination monitoring.....	20
2.3.1 Monitoring approaches.....	20
2.3.2 Real-time water monitoring.....	20
2.3.2.1 Wireless sensor networks	21
2.3.2.2 Automated water sampling systems	23
2.4 Biosensors	27
2.4.1 Biosensors introduction	27
2.4.1.1 What are biosensors?.....	27
2.4.1.2 Biosensor components	27
2.4.1.3 Biorecognition element response.....	29
2.4.2 Electrochemical biosensors and range of applications	32

2.4.2.1	Electrochemical biosensors	32
2.4.2.2	Impedimetric biosensor applications	38
2.4.3	Uranyl ion biosensor.....	38
2.4.3.1	Biosensor development background	39
2.4.3.2	Biosensor construction	39
2.4.3.3	Biosensor performance and stability	40
2.4.3.4	Biosensor deployment investigations.....	43
2.4.4	Electrode preparation methods	44
2.4.4.1	Initial electrode preparation – uranyl biosensor.....	45
2.4.4.2	Gold chip electrode preparation and electrode regeneration methods.....	45
2.4.5	Impedimetric biosensor and electrode analysis methods.....	48
2.4.5.1	Impedance basic theory.....	48
2.4.5.2	Electrochemical Impedance Spectroscopy (EIS)	51
2.4.5.3	Cyclic voltammetry.....	53
2.4.6	Biosensor deployment.....	55
2.4.6.1	General considerations.....	56
2.4.6.2	Successful biosensor commercialisation.....	57
2.4.6.3	Barriers to commercialisation.....	58
2.5	Fluid delivery systems.....	60
2.5.1	Flow cell design.....	60
2.5.1.1	Scaling of fluidic systems.....	60
2.5.1.2	Minifluidic flow cell types.....	65
2.5.1.3	Flow cell design investigations.....	69
2.5.2	Fluid mechanics principles	70
2.5.2.1	Flow conditions.....	70
2.5.2.2	Channel flow geometry and eddy development	72
2.6	Flow analysis techniques	76
2.6.1	Investigative methods - numerical modelling	76
2.6.2	Investigative methods - laboratory techniques.....	82
2.6.2.1	Summary of laboratory flow visualisation analysis techniques	82
2.6.2.2	Flow fluorescence.....	83
2.7	Chapter summary.....	88
2.7.1	Project background	88
2.7.2	Implications for current research investigations.....	89

	2.7.2.1	Cross-disciplinary research.....	89
	2.7.2.2	Identifying the knowledge gap	89
Chapter 3		Flow cell design for effective biosensing – investigation design	92
3.1		Chapter introduction.....	92
3.2		Fluid delivery system optimisation process	93
	3.2.1	Optimisation process design	93
	3.2.1.1	Rationale for study.....	93
	3.2.1.2	Optimisation process design strategy	94
	3.2.2	Fluid delivery system design principles.....	96
	3.2.3	Fluid delivery system design	97
	3.2.3.1	Design approach	97
	3.2.3.2	Experimental design tool.....	97
	3.2.3.3	Flow channel geometry design	100
	3.2.3.4	Computational design tool	104
	3.2.4	Guiding investigative strategy.....	110
3.3		Chapter summary.....	112
Chapter 4		Flow cell design for effective biosensing - investigation process, results and discussion.....	114
4.1		Chapter introduction.....	114
4.2		Experimental investigation procedure	115
	4.2.1	Experimental setup	115
	4.2.2	Validation of the experimental tool.....	120
	4.2.3	Flow-fluorescence experiments.....	123
4.3		Computational investigation procedure	126
	4.3.1	Investigation setup	126
	4.3.2	Computational tool validation	131
	4.3.3	Computational flow simulations	136
4.4		Comparative validation.....	138
4.5		Investigation results	139
	4.5.1	Comparative validation results	139
	4.5.2	Flow field.....	140
	4.5.2.1	Flow field development	140
	4.5.2.2	Eddy and 3D flow development	146
	4.5.2.3	Dilute species response to flow field	150

4.5.3	Flow cell efficiency	152
4.5.3.1	Time study analysis	153
4.5.3.2	Flow throughput analysis	154
4.5.3.3	Time to reach a given concentration	155
4.6	Discussion.....	157
4.6.1	Validity of investigative approach	157
4.6.2	Advection and diffusion processes	158
4.6.2.1	Advection and diffusion relationship.....	158
4.6.2.2	Flow domain geometry	158
4.6.3	Practical operational considerations	160
4.6.3.1	Flow cell operations	160
4.6.3.2	Implications for sensor operation	160
4.6.4	Contribution to field of study	161
4.6.4.1	Expansion of subject knowledge.....	161
4.6.4.2	Scope of investigations.....	162
4.7	Chapter summary.....	164
4.7.1	General summary.....	164
4.7.2	Operational protocol recommendations.....	164
Chapter 5	Biosensor-flow cell integration.....	167
5.1	Chapter introduction.....	167
5.2	Biosensor-flow cell integration process design.....	168
5.2.1	Rationale for integration, and investigative scope.....	168
5.2.2	Integration process design strategy.....	170
5.3	Integration investigation methods.....	172
5.3.1	Biosensor integration process	172
5.3.1.1	Physical transducer options and flow cell evolution.....	172
5.3.1.2	Electrode preparation method.....	176
5.3.1.3	Biosensor construction method.....	177
5.3.1.4	Physical transducer selection method.....	178
5.3.2	Integrated biosensor performance.....	179
5.3.2.1	Experimental setup.....	179
5.3.2.2	General biosensor performance investigative approach.....	181
5.3.2.3	Biosensor frequency sensitivity.....	182
5.3.2.4	Biosensor regeneration (reusability)	182
5.3.2.5	Biosensor storage stability	183

5.3.3	Analysis methods	183
5.3.3.1	Electrochemical analysis methods	183
5.3.3.2	Non-electrochemical analysis methods	184
5.4	Investigation results	187
5.4.1	Physical transducer selection	187
5.4.2	Integrated biosensor performance	191
5.4.2.1	System frequency sensitivity	191
5.4.2.2	Integrated biosensor single chip regeneration	193
5.4.2.3	Integrated biosensor chip-to-chip repeatability	198
5.4.2.4	Integrated biosensor storage stability	200
5.5	Discussion - transition to field deployment	202
5.5.1	Physical transducer selection	202
5.5.2	Integrated biosensor regeneration	204
5.5.3	Integrated system storage stability	205
5.5.4	Integrated biosensor practical operation	206
5.5.4.1	Optimised flow cell	206
5.5.4.2	Integrated biosensor performance overview	207
5.5.4.3	Adsorption models	209
5.6	Chapter summary	214
Chapter 6	Further discussion	217
6.1	Chapter introduction	217
6.2	Robust measurements from uranyl biosensors deployed on real contaminated sites	218
6.2.1	Early warning sensor system	218
6.2.2	Integrated biosensor measurement optimisation	220
6.3	Biosensor/electrode batch variability	224
6.4	Associated work	226
6.4.1	Production flow cell	226
6.4.2	Automated pump and flow control system	227
Chapter 7	Conclusions	232
7.1	Project outcomes with respect to research aim and objectives	232
7.2	Contribution to knowledge and practice	234
7.3	Recommended further research	237

REFERENCES..... 239
APPENDIX A Matlab code for experimental investigations..... 252

List of Tables

Table 2-1	Summary of selected wireless sensor network (WSN) system projects for environmental water monitoring	22
Table 2-2	Summary review of different environmental water contaminant monitoring methods	26
Table 2-3	Commonly used materials for the electrodes that comprise a typical three-electrode electrochemical system.....	33
Table 2-4	Summary review of different types of electrochemical biosensor	37
Table 2-5	Selection of published studies on preparation methods for pure gold electrodes.....	47
Table 2-6	Selection of prominent micro-fluidic platform types	63
Table 2-7	Selection of published biosensors integrated into microfluidic platforms	64
Table 2-8	Minifluidic flow cell type descriptions, and examples of their application for integrated sensor/biosensor systems.....	67
Table 3-1	Volumetric flow chamber capacity for three flow channel geometries.....	103
Table 3-2	Estimated maximum and minimum Reynolds numbers (Re) for flow cell flow channel, at three selected inlet flow rates.....	103
Table 3-3	Element size parameters and approximate number of elements for predefined size settings for the entire circular flow channel geometry.....	108
Table 4-1	Image capture software (LabVIEW 8.0) key parameter settings and selections	120
Table 4-2	Selected material (water) property values used for computational models	128
Table 4-3	Mesh settings for computational tool validation process.	132
Table 4-4	Custom mesh configuration parameter settings.....	132
Table 4-5	Study duration for flow simulations	137
Table 5-1	Grinding and polishing process for bespoke gold chip electrode	177
Table 5-2	Analysis methods for the different aspects of biosensor-flow cell integration investigation.	186

List of Figures

Figure 1-1	Conceptual model visualisation for an automated and remotely controlled water monitoring system.	7
Figure 2-1	Uranium speciation in chalk groundwater (in the presence of dissolved carbonates).	15
Figure 2-2	Uranyl (UO_2^{2+}) ion	15
Figure 2-3	Schematic diagram of biosensor composition.....	28
Figure 2-4	Schematic of a three-electrode circuit system as applied to an electrochemical biosensor unit	34
Figure 2-5	Uranyl biosensor construction.....	40
Figure 2-6	Self assembled monolayer (SAM) ordering on a gold substrate	41
Figure 2-7	Proposed mechanisms for binding uranyl ion to the surface layer protein of <i>Bacillus sphaericus</i> JG-A12.....	42
Figure 2-8	Response of uranyl biosensor to uranyl analyte, compared to the response to potential interfering ions....	42
Figure 2-9	Dropsens C223AT screen-printed electrode	45
Figure 2-10	Randles equivalent circuit	51
Figure 2-11	Nyquist plot schematic for electrochemical impedance spectroscopy analysis.	53
Figure 2-12	Cyclic voltammogram schematic diagram for an electroactive redox couple	54
Figure 2-13	Commercially available wall-jet style flow cell	65
Figure 2-14	Schematic diagrams of common flow cell design types used with biosensors and other sensor types	66
Figure 2-15	Schematic diagrams of a flow cell designed by Coldrick <i>et al.</i> (2009).....	68
Figure 2-16	Velocity distribution curve for laminar channel flow.....	72
Figure 2-17	Schematic diagram of eddy development within a 60° corner formed by solid wall boundaries.....	73
Figure 2-18	Schematic plan view of laminar flow in an open channel with a sudden expansion in width.....	74
Figure 2-19	Fluorescent intensity of fluorescein as a function of pH ..	87
Figure 3-1	Fluid delivery system optimisation process outline	95
Figure 3-2	3D representation of fundamental flow domain dimensions for experimental flow cell	98
Figure 3-3	Bespoke flow cell construction schematic diagram	99
Figure 3-4	Images of bespoke flow cell	99

Figure 3-5	Flow channel geometries	102
Figure 3-6	Computational design tool developmental process	105
Figure 3-7	Numerical model building, part 1. Flow channel model construction.....	107
Figure 3-8	Flow channel model 3D tetrahedral mesh, for iCell geometry	108
Figure 3-9	Model of commercial flow cell flow domain	110
Figure 4-1	Experimental design tool investigation process	116
Figure 4-2	Schematic diagram of experimental flow analysis setup	117
Figure 4-3	Light transmission spectra for 490 nm bandpass filter ..	118
Figure 4-4	Light transmission spectra for Dolan Jenner mercury lamp MHR-100.....	118
Figure 4-5	Light transmission spectra for 520 nm bandpass filter ..	119
Figure 4-6	Mask applied to image of an iCell flow channel containing 100 μM fluorescein sodium solution.....	121
Figure 4-7	Normalised luminescence response to fluorescein sodium salt solution concentration	122
Figure 4-8	Mean luminescent intensity against time for a flow channel containing 100 μM fluorescein sodium solution.....	123
Figure 4-9	Luminescent intensity response to inflow of fluorescein sodium solution for circular geometry channel @ 1 mL min^{-1} inflow rate.....	125
Figure 4-10	Computational design tool investigation process	127
Figure 4-11	Numerical model building, part 2; and boundary conditions.....	130
Figure 4-12	Mesh sensitivity analysis 1	135
Figure 4-13	Mesh sensitivity analysis 2.....	136
Figure 4-14	Comparative validation 1.....	139
Figure 4-15	Comparative validation 2.....	140
Figure 4-16	Arrow velocity plots at two selected 'low' flow rates	142
Figure 4-17	Flow velocity plots at an inlet flow rate of 1 mL min^{-1} at mid-depth of the 3D channel.....	144
Figure 4-18	Flow velocity plots at an inlet flow rate of 1 mL min^{-1} at three selected channel depths.	145
Figure 4-19	Arrow velocity plots at three selected 'medium' to 'high' flow rates	146
Figure 4-20	Flow velocity plots at an inlet flow rate of A) 1 mL min^{-1} and B) 5 mL min^{-1} for the square channel geometry.....	148

Figure 4-21	Flow velocity plots at an inlet flow rate of 7.5 mL min^{-1} at three selected channel depths.	149
Figure 4-22	Normalised arrow velocity plots for the commercial flow cell at two selected flow rates	150
Figure 4-23	Computational results showing concentration maps (top) and streamlines (bottom), after 5 flow cell volume changes.....	151
Figure 4-24	Temporal response of flow cell to injection of analyte for the four flow cell geometries at flow rates	154
Figure 4-25	Fluid volume response of flow cell to injection of analyte at four selected inflow rates.....	155
Figure 4-26	(A) Time taken and (B) required influent volume for cell concentration ratios of (1) 75% and (2) 99% of that of injected fluid	156
Figure 5-1	Flow cell-biosensor integration investigation process outline	171
Figure 5-2	Dropsens C223AT screen-printed electrode on bespoke 30 mm x 30 mm ceramic substrate.....	173
Figure 5-3	Flow cell evolution 1. Integration of bespoke screen-printed electrode	174
Figure 5-4	Bespoke electrode unit featuring a gold chip embedded into a polycarbonate block.....	174
Figure 5-5	Flow cell evolution 2. Electrochemical flow cell - integration of bespoke gold chip electrode.....	175
Figure 5-6	Schematic diagram showing the setup for biosensor performance investigations, using bespoke gold chip electrode and modified flow cell.	180
Figure 5-7	Transducer selection investigation results	189
Figure 5-8	Coherence scanning interferometry (CSI) analysis of the gold working electrode of a Dropsens screen-printed electrode	190
Figure 5-9	Scanning electron microscope (SEM) images of the gold working electrode of a Dropsens screen-printed electrode	190
Figure 5-10	Coherence scanning interferometry (CSI) analysis of the working electrode of a bespoke gold chip electrode	191
Figure 5-11	Frequency sensitivity of full uranyl biosensor constructed upon a bespoke gold chip electrode	193
Figure 5-12	Impedance response to biosensor-analyte interaction for three selected frequencies for the regeneration of a single biosensor chip.....	196

Figure 5-13	Triplicate regenerated uranyl biosensor chip impedance response to uranyl nitrate ($\text{UO}_2(\text{NO}_3)_2$) analyte	197
Figure 5-14	Impedance response to biosensor-analyte interaction for two selected frequencies for biosensors constructed upon three different (previously unused) electrode chips.....	198
Figure 5-15	Integrated uranyl biosensor stability analysis.....	200
Figure 5-16	Idealised Langmuir isotherm with a logarithmic concentration scale (x-axis), fitted to uranyl-biosensor binding for an analyte concentration range of 10^{-12} M to 10^{-6} M.....	210
Figure 5-17	Idealised Freundlich adsorption isotherm with a logarithmic concentration scale (x-axis), fitted to uranyl-biosensor binding for an analyte concentration range of 10^{-12} M to 10^{-6} M.	212
Figure 6-1	Production iCell flow cell design.....	227
Figure 6-2	Early prototype automated pump and flow control system with data transmission capabilities.....	229

List of Abbreviations

4-ATP	4-Aminothiophenol
AVI	Audio Video Interleaved
AWACSS	Automated Water Analyser Computer Supported System
CCD	Charge Coupled Device
CCR	Cell Concentration Ratio
C_{dl}	Double Layer Capacitance
CER	Channel Expansion Ratio
CFD	Computational Fluid Dynamics
CPE	Constant Phase Element
CSI	Coherence Scanning Interferometry
CV	Cyclic Voltammetry
CW	Centre Wavelength
DIAMOND	Decommissioning, Immobilisation And Management Of Nuclear wastes for Disposal (<i>university consortium</i>)
DMSO	Dimethyl Sulfoxide
EIS	Electrochemical Impedance Spectroscopy
EU	European Union
FDM	Finite Difference Method
FEM	Finite Element Method
FVM	Finite Volume Method
FWHM	Full Width Half Maximum
GPRS	General Packet Radio Service
GSM	Global System for Mobile communications

HDPE	High Density Polyethylene
HLW	High Level Radioactive Waste
HPC	High Performance Computing
ID	Internal Diameter
ISE	Ion Selective Electrode
LOC	Lab On a Chip
MEMS	Microelectromechanical Systems
mLSI	Microfluidic Large Scale Integration
μPAD	Microfluidic Paper-based Analytical Device
μTAS	Micro Total Analysis System
NDA	Nuclear Decommissioning Authority
OD	Outer Diameter
PBS	Phosphate Buffered Saline
PCA	Portable Clinical Analyzer
PDMS	Polydimethylsiloxane
PMMA	Polymethylmethacrylate
POC	Point Of Care
POM	Polyoxymethylene
POU	Point Of Use
PRB	Permeable Reactive Barrier(s)
PTFE	Polytetrafluoroethylene
R_{ct}	Charge Transfer Resistance
Re	Reynolds Number(s)
R_s	Solution Resistance
ROI	Region Of Interest
RTD	Residence Time Distribution
SAM	Self Assembled Monolayer

SEM	Scanning Electron Microscope
SLP	Surface Layer Protein
SPE	Screen-Printed Electrode
Sulfo-SMCC	4-(<i>N</i> -Maleimidomethyl)cyclohexane-1-carboxylic acid 3- Sulfo- <i>N</i> -hydroxysuccinimide ester sodium
TCE	Trichloroethylene
UNF	UNified Fine thread
WFD	Water Framework Directive
WHO	World Health Organisation
WSN	Wireless Sensor Network(s)

CHAPTER 1

Introduction

Chapter 1 Introduction

1.1 Research background

Production of solid radioactive waste materials in the United Kingdom date from the 1920's onwards. Sources include nuclear power generation, nuclear weapons development, hospitals, pharmaceutical production and educational establishments (e.g. DEFRA 2007). An estimate for the Sellafield nuclear reprocessing site alone, the site of previous nuclear power generation, suggests the presence of approximately 20 million cubic metres of land contaminated by radioactive materials from historical leaks (NDA 2006).

The presence of both natural (e.g. fractured rock formations) and man-made (e.g. drainage systems) migration pathways can lead to subsequent contamination of natural water bodies such as aquifers (permeable rock containing usable volumes of water) (El Ghonemy 2004). However, the full extent of legacy contamination and the subsequent level of environmental hazard in the United Kingdom are not well understood. This is because much of the potentially contaminated land and water in the United Kingdom "has yet to be well characterised" (NDA 2011).

The traditional approach to environmental water sampling and monitoring has involved time consuming regular and routine collection of samples at the potentially contaminated site, and subsequent transfer to a laboratory for relatively costly analysis. Additionally, there is a desire within the nuclear industry in the United Kingdom to streamline the process of contamination characterisation. The development of an automated and remotely controlled monitoring system for potentially contaminated water bodies would provide a near real-time continuous 'early warning system', eliminating the need for costly and time consuming routine sample collection.

A biosensor utilises a biological sensing component linked to a signal transducer to produce an electrochemical signal response in the presence of a target contaminant (or contaminants). Biosensors have been developed for

the purposes of monitoring both the nature and extent of environmental contamination, and allowing the success of the remediation of contaminated sites to be evaluated. Biosensors are often identified as a high-sensitivity, low cost, and portable option for real-time or near real-time monitoring of targeted environmental contaminants (Van Dorst *et al.* 2010). Specifically, Conroy *et al.* (2010) developed a novel biosensor for the detection of uranyl ions (UO_2^{2+}) in contaminated water sources. The starting point for this study therefore was to investigate a method of achieving the transition of the laboratory proof-of-concept biosensor developed by Conroy to an integrated biosensor-sample delivery unit suitable for incorporation into a real-time automated monitoring system. However, ultimately a study with a more targeted aim was identified.

Two main elements form the rationale for the focus on the detection of the uranyl ion in water samples. First, a real legacy of land and water contaminated with uranium was identified (an example from Pécs, Hungary is described in Section 2.2.2). This demonstrates potential practical deployment opportunity for a real-time monitoring system incorporating a uranyl sensor unit. Secondly, elevated concentrations of uranium in water resources have been identified as a potential risk to human and environmental health (briefly described in Section 2.2.2). This demonstrates a practical purpose for monitoring, and potentially attempting remediation of, land and water contaminated with uranium (for which the aqueous uranyl ion is an indicator).

Flow cells have commonly been used for sample delivery to biosensor surfaces for a range of applications such as the detection of food analysis (Prodromidis and Karayannis 2002) pathogenic bacteria (Ivnitski *et al.* 1999), and clinical diagnostics (Luppa *et al.* 2001). Yet there is no wide consensus on flow cell design for such purposes, with the examples considered above each utilising slightly different flow cell designs. One of the more common flow cell design types however is a channel flow cell where an impinging jet delivers the analyte solution to the flow chamber, and subsequent flow is parallel to a surface containing an embedded sensor (e.g. Komaitis *et al.* (2010)). The flow channel for such flow cells is typically rectangular in shape and features an expansion of channel width from the inlet channel to a

region containing the embedded sensor, followed by a symmetrical channel contraction to the outlet.

A number of publications within the field of fluid mechanics have considered the flow response to an expanding flow channel, including Acrivos and Schrader (1982) and Biswas *et al.* (2004). These studies show that even under laminar flow conditions, regions of reversed fluid motion (eddies) can develop in a flow channel with an expanding channel width. For a flow cell already containing fluid, such as an integrated biosensor stored in buffer solution, such features can develop under the application of flow. Furthermore, flow patterns that develop within a flow cell, such as eddies, will determine how quickly the concentration of the analyte within the flow cell equilibrates with that of the fluid entering the inlet (termed the influent). This is because the transport of analyte within fluid flow without eddies will be dominated by the process of advection (movement in the direction of flow), whilst analyte within eddies can only be transported by the slower mechanism of diffusion (transport due to concentration gradients within the fluid).

A limited number of previous studies, such as Cooper and Compton (1998) and Lammertyn *et al.* (2006), have considered the impact of the design and operation of flow cells on the accuracy of biosensor measurement. However, these focused primarily on kinetics of a particular sensor, and did not explicitly consider the impact of variations in flow cell channel geometry. Specifically, no previous studies had been conducted that explicitly examined the relationship between the design geometry of flow cell units for the deployment of biosensors, and the equilibration or control of a target analyte concentration between the flow cell and the influent.

1.2 Research aim and objectives

1.2.1 Research aim

Develop a fluid delivery system for sensor units, and biosensors specifically, for which the geometrical design and operational protocol are optimised to enable control over the equilibration of the sample analyte concentration within the flow cell with that within the influent. Such a fluid delivery system

would be designed to ultimately form a modular component of an automated water monitoring system.

1.2.2 Research objectives

Four specific project objectives were developed to support the project aim:

- 1)** Investigate and quantify an optimal design for a fluid delivery system (flow cell) that will contribute to the transition of laboratory proof-of-concept biosensors to point-of-use deployment.
- 2)** Develop specific recommendations for an operational protocol for the optimally-designed flow cell unit.
- 3)** Investigate and quantify the successful integration of a specific biosensor unit, a biosensor for the detection of aqueous uranyl ions, into the optimally-designed flow cell unit.
- 4)** Develop specific recommendations for a successful biosensor integration approach, and for an operational protocol for the integrated biosensor-flow cell unit.

1.3 Research methodology

The investigation into an optimally-designed flow cell and associated operational protocol (objectives (1) and (2), Section 1.2.2) was conducted through a parallel investigative approach. This consisted of a computational investigation using computational fluid dynamics software, and a laboratory-based experimental flow visualisation method. The rationale behind this approach was that the use of two different investigative tools to examine the same aspects of flow cell design would provide a more robust study than would the application of just one approach. The two investigative approaches were developed and operated in parallel, with each influencing the development of the other. Additionally, a common investigative methodology was applied to the two investigative approaches as much as possible, which meant that results from both could be directly compared as part of a validation method for the investigation as a whole. Thus, the validation of the computational investigative method indicated that the

numerical models were a correct representation of the physics of fluid flow within the cell. This in turn allowed for robust exploration of parameter space to seek explanations of fluid flow phenomena e.g. through investigation of the flow field response to varying flow conditions.

For the investigation relating to the integration of a biosensor into the optimised flow cell (objectives (3) and (4), Section 1.2.2), laboratory-based electrochemical analysis methods were primarily used to assess the degree of success of the integration process. These methods were supported by non-electrochemical analysis methods. Specifically these were around the assessment of the surface topography of electrodes which would form the base upon which the biosensors were constructed.

1.4 Research scope and limitations

From the previous two sections it was determined that there are two main elements to this research project:

- 1) Design of an optimised flow cell for biosensor point-of-use deployment
- 2) Integration of a selected biosensor, for the detection of aqueous uranyl ions, into the optimally-designed flow cell

This study forms part of a research strand which ultimately could lead to the incorporation of the uranyl biosensor into a remotely controlled automated water monitoring system. From the two main elements of this study as outlined above it is clear that this study is a crucial element towards achieving the aim of this research strand. A conceptual model was developed that identified the main attributes and components of such an automated water monitoring system, within which an optimised uranyl biosensor deployment system could be incorporated. Figure 1-1 shows a visualisation of the conceptual model for the specific case of groundwater monitoring. The area of the model applicable to this study, incorporation of a flow cell integrated biosensor unit and optimised flow control, is indicated on the figure.

In a research study such as this it was also necessary to define the scope and set limitations for the two individual elements of the research project as defined above. These factors will be discussed fully in the investigative/experimental chapters of the thesis, Chapters 3, 4 and 5, but are summarised here to provide the reader with an outline of the nature of the research study presented in the following chapters:

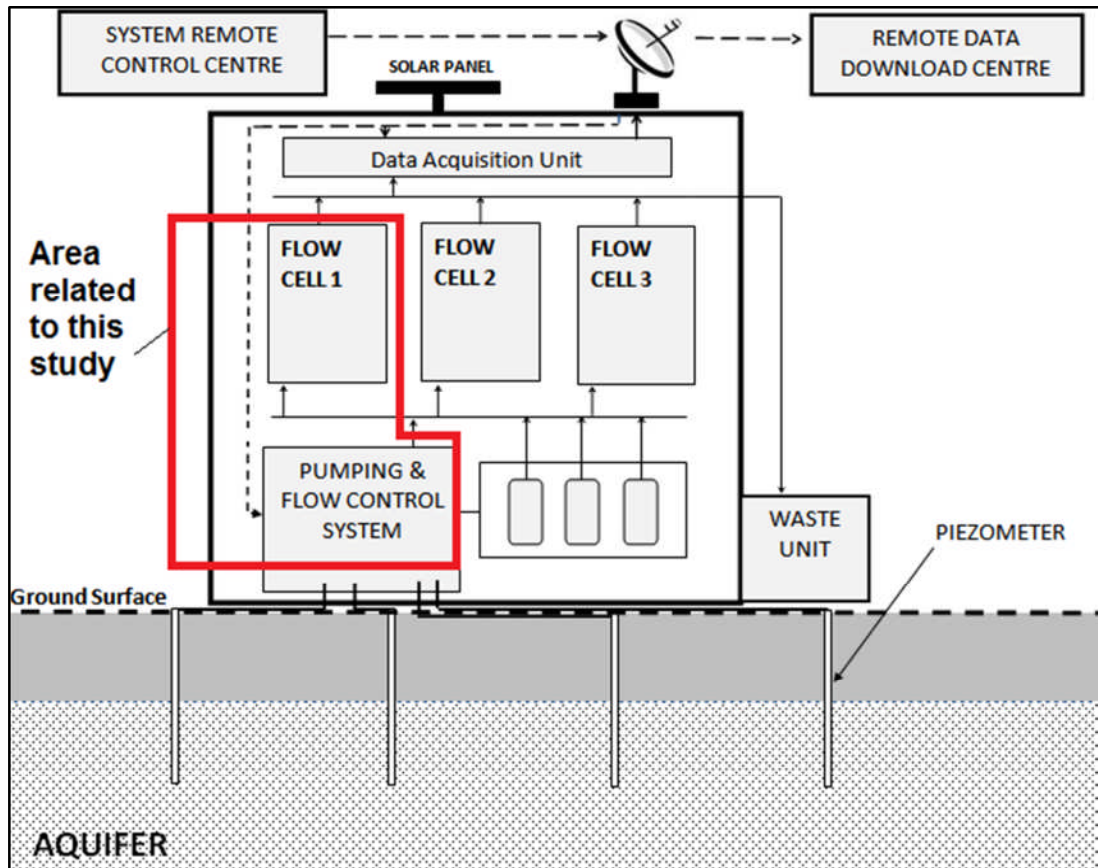


Figure 1-1 Conceptual model visualisation for an automated and remotely controlled water monitoring system. The integrated uranyl biosensor-flow cell unit would form one of the 'flow cell' modules shown in the model. The area of the model applicable to this study is highlighted.

Optimal flow cell design investigation scope and limitations

- Investigate the design of flow cell domains with dimensions at the mm scale (minifluidic cell) only, as opposed to flow cell domains with dimensions at the μm scale (microfluidic cell).
- A broad range of fluid delivery system (flow cell) types have been previously utilised for sensor integration (and this will be considered in detail in Chapter 2). This study investigates the design of a specific flow

cell type, featuring a contained flow 'channel'. However, the effectiveness of a commercially available flow cell of a different design was also considered as part of this study for comparative purposes.

Biosensor-flow cell integration investigation limitations

- The focus of the investigation was the integration of a specific biosensor, for the detection of aqueous uranyl ions.
- The investigation was conducted from the perspective of an engineer end-user. That is, the investigation outcome would be used to estimate the level of success of the integration process for the existing biosensor with respect to its practical operation in a point-of-use deployment setting. Additionally, it would be used to identify the future challenges in improving the biosensor with respect to enabling repeatable, reliable and robust operation in a point-of-use deployment setting.
- The investigative scope did not extend to redesigning the existing uranyl biosensor or to seek alternative methods of aqueous uranyl detection. Additionally, the investigation was not intended to be a full-scale investigation that would seek to tackle the existing big challenges associated with the point-of-use deployment of biosensors, and impedimetric biosensors in particular. These 'big challenges' are primarily repeatable electrode surfaces for biosensor construction, chip-to-chip performance repeatability, sensor stability issues, and non-specific binding. These issues will be discussed further within Chapters 5 and 6.

1.5 Organisation of the thesis

This thesis consists of a total of seven chapters. This first chapter has introduced the background to the development of the study project, specified the project aim and objectives, provided an outline of the research methodology, and the scope of the research study.

Chapter 2 provides an extended background and review of literature appropriate to the project background and the investigative approaches employed. Because of the cross-disciplinary nature of the study,

incorporating the fields of engineering design, principles of fluid mechanics and principles of biosensor design and operation; no pre-existing knowledge is assumed on the part of the reader.

The following three chapters (Chapters 3, 4 and 5) outline the experimental investigations of the study. These chapters are presented according to subject focus. That is, the investigative rationale, experimental methodology, investigative results, and investigative discussion are presented separately for a) the fluid delivery system design and optimisation investigation (**Chapters 3 and 4**), and b) the flow cell-biosensor integration investigation (**Chapter 5**).

In **Chapter 6** (further discussion), progress towards incorporation of the integrated uranyl biosensor into an automated water monitoring system is considered, with a focus on developing operational protocols for providing robust and repeatable biosensor measurements. Additionally, the issue of batch variability with respect to biosensor/electrode units is briefly discussed. Also, two pieces of work associated with this study, but not conducted by the thesis author, are summarised. These provide an indication of the impact of the research study beyond the primary work described in these pages.

Finally, **Chapter 7** draws together the study conclusions with respect to the project aim and objectives outlined in this chapter, and specifies the contribution made to subject knowledge and practice through the study. Furthermore, the chapter makes recommendations for the direction and nature of future research studies.

CHAPTER 2

Literature review and
background

Chapter 2 Literature review and background

2.1 Chapter introduction

This chapter provides a comprehensive and critical review of current and historical literature relevant to the development of a biosensing system for uranyl ions. Additionally, because the thesis presents research that is multi-disciplinary some background material is also presented. Background material has been selected for presentation based upon providing any reader with the relevant technical and contextual knowledge with respect to the original research work presented in Chapters 3, 4 and 5. The subject areas included in this combined literature review and background chapter are:

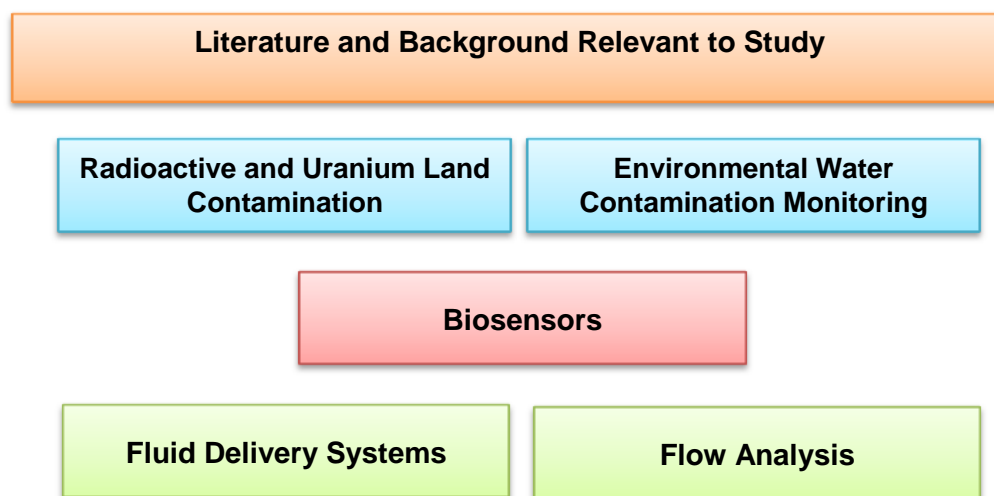
- I. Characterisation of radioactive land contamination and an overview of remediation methods; a brief study of a real site contaminated with uranium, and the risks of uranium contamination (Section 2.2).
- II. Environmental contamination monitoring, including the automation and remote control of monitoring technology (Section 2.3).
- III. The design and application of biosensors, electrochemical analysis methods, and other methods used to analyse biosensor units and electrode surfaces, and the key considerations in the deployment of biosensors (Section 2.4).

(I) & (II) provide the context to how the research project seeks to address a real need in the management of radioactive contaminated land, whilst (III) addresses the more technical aspects of the research since the aim of the research project is to develop a deployment system and protocol for a pre-existing uranyl biosensor which would provide near real-time monitoring of contaminated land.

- IV. Fluid delivery systems, including flow cell design, including relevant flow dynamics principles (Section 2.5)
- V. Flow analysis techniques (Section 2.6)

(IV) provides an understanding of how fluid delivery systems for sensor units have been considered within the literature. Specifically, flow cell devices are explored along with the fundamental principles of fluid flow that underpin the design and operation of such fluid delivery systems. Finally, (V) explores the techniques and approaches that can be utilised to investigate the response of fluid flow to variation in flow cell geometry and flow conditions.

Chapter Outline Map



- Chapter Theme ■ Sub-chapters supporting project rationale and context
- Sub-chapters supporting experimental chapters : biosensors and electrochemical methods
- Sub-chapters supporting experimental chapters : flow cell design and flow analysis methods

2.2 Radioactive and uranium land and water contamination

2.2.1 Contamination characterisation

2.2.1.1 Causes of contamination

Globally, there have been a number of routes by which land has become contaminated by radioactive materials and associated species. The most influential of these are testing of nuclear weapons (Oliver *et al.* 2007), accidental releases of radioactive materials from nuclear sites e.g. Chernobyl, 1986 (Saenko *et al.* 2011) ; Fukushima Daiichi, 2011 (Yoshida and Takahashi 2012), and the activities associated with mining and processing of uranium (Vandenhove 2002). Additionally, leakage from the storage of radioactive waste materials has also contributed to the radioactively contaminated land problem. This has occurred where the tanks or containers used for storage did not prove resilient enough to prevent leakages (Fredrickson *et al.* 2004). Indeed, the search for safe storage materials and methods for radioactive waste disposal, and high-level radioactive waste (HLW) in particular, remains a strong focus for both governmental bodies (e.g. Powell *et al.* 2010) and the scientific research community (Kademani *et al.* 2013).

2.2.1.2 Land contaminated with uranium

Naturally occurring uranium present in soil and rocks is distributed in greater quantities by natural earth processes (e.g. wind, rivers, and groundwater) than uranium released through the activities of the global nuclear fuels and weapons industries. However, a considerably larger hazard is posed by the latter in relation to the large volumes of contamination within specific limited localities. The activities of industries associated with the nuclear fuel cycle historically provide the most significant contaminant legacy; namely uranium mining, milling and processing, fuel enrichment and fabrication, and through the conversion of uranium oxide (U_3O_8) to Uranium hexafluoride (UF_6) for fuel enrichment purposes (Gavrilescu *et al.* 2009). Land contamination can occur either indirectly via atmospheric release or direct discharge of fluid or leached waste products.

Within Europe the most significant cases of contamination, associated primarily with uranium extraction and processing, occur in Eastern Germany largely through the historical development of a total 311 Mm³ of ore dumps and 161 Mm³ of tailing ponds. Additionally, both the Czech Republic and Hungary also have a notable uranium land contamination legacy through their own historical mining operations (Vandenhove 2002). The specific case of land contaminated through a uranium mining legacy near the city of Pécs in Hungary is considered further in Section 2.2.2.2.

2.2.1.3 Environmental mobility and biogeochemistry

The hazard present as a result of uranium land contamination is determined to a large extent by environmental factors and uranium biogeochemistry. Environmental factors are dominated by contaminant migration pathways as with any land contaminant. Migration to groundwater resources (aquifers) through both man-made and natural sub-strata permeability is one common significant contaminant pathway (Cruickshank 2012).

Uranium exists in several oxidation states in nature. However, the most common states present in the environment are uranium(IV) and uranium(VI) (Grenthe *et al.* 2006). The species formed in solution with uranium are dependent on aqueous chemistry, the redox conditions present, and the pH of the aqueous solution. Figure 2-1 shows uranium speciation with respect to pH and Eh for the specific example of a chalk groundwater (i.e. with the presence of dissolved carbonates) (Crançon *et al.* 2012). Compounds that contain U (IV), such as those found in the mineral uraninite, predominate in reducing conditions and are insoluble and typically immobile. The presence of the linear uranyl moiety (UO_2^{2+} , Figure 2-2) however in oxidising conditions, formed of uranium in the (VI) state, produces compounds that are much more mobile as a result of their high solubility (Grenthe *et al.* 2006).

Microbial activity can impact upon the speciation and mobility of uranium in natural environments, typically by reducing mobility. This influence has led to the use of such biogeochemical processes being harnessed in the remediation of land contaminated with uranium and other radionuclides

(Newsome *et al.* 2014). Remediation methods, including bioremediation, will be discussed in further detail in Section 2.2.2.

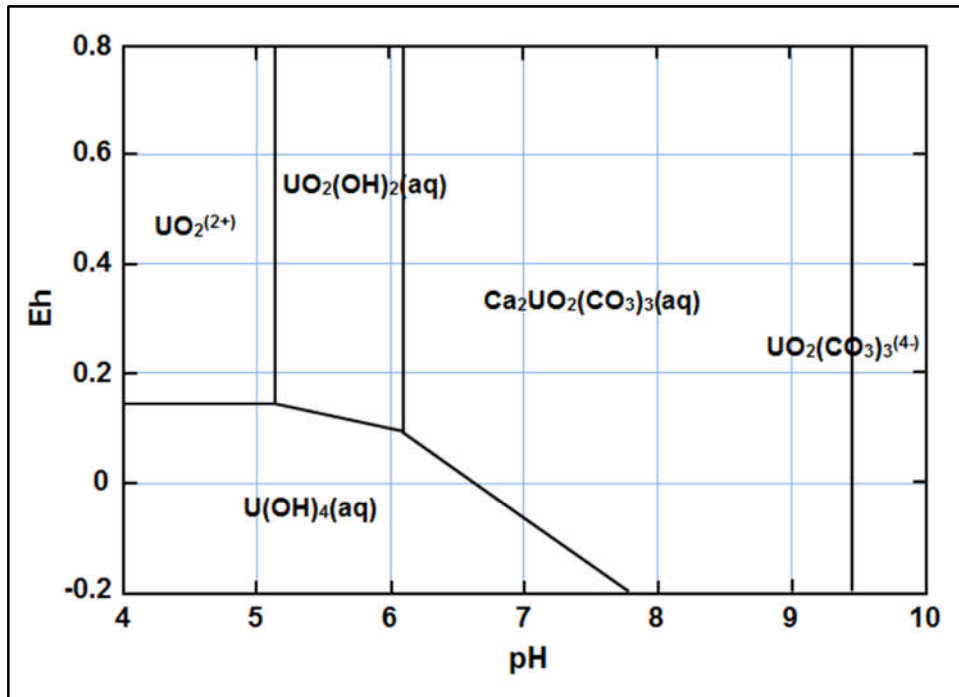


Figure 2-1 Uranium speciation in chalk groundwater (in the presence of dissolved carbonates) (redrawn from Crançon *et al.* (2012)).

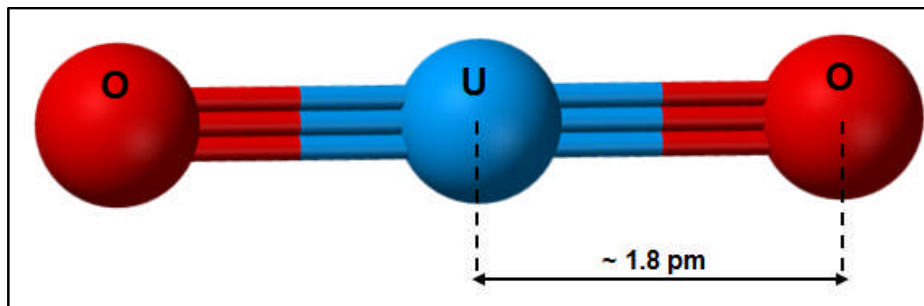


Figure 2-2 Uranyl (UO_2^{2+}) ion

2.2.2 Remediation methods and risk

2.2.2.1 Remediation methods overview

The decision on whether to deploy remediation methods for radioactive contaminated land, and the type of method(s) to be used, is determined (as with non-radioactive contaminated land) by consideration of a number of factors:

- *The type and nature of the contaminant(s) within the contaminated environment* - e.g. species mobility, suitability for bioremediation methods (see paragraph below for brief description of these methods).
- *Assessment of the degree of risks to human and environmental health* – consideration of the pathways for contaminant mobilisation, and potential contamination receptors, together with the potential identified impacts on human and environmental health at a range of concentrations of the target contaminant(s).
- *Local legislation and guidelines* – e.g. for the UK, the contaminated land guidelines associated with the Environmental Protection Act 1990 provide guidance on the requirement for contaminated land remediation, methods of remediation and consideration of the environmental impact of remediation methods themselves (DEFRA 2012).
- *Timescales and cost* – timescales for remediation work may be stipulated by local authorities as part of the guidelines/legislation mentioned above. These in turn may influence the choice of remediation method. Additionally, the cost of remediation work may be a key driver for the remediation method selection process.
- *Remediation project objectives* – once the above factors have been considered, a set of objectives for the remediation project will be devised. These may range from ongoing site monitoring only (i.e. no active remediation activity in the short term), remediation activity focussed on blocking or restricting contaminant pathways to potential receptors, to deployment of active remediation methods. Examples of the latter are considered in the following paragraph.

The physical removal of contaminated soil and sediments is a common remediation method, including for land contaminated with radionuclides and other species associated with radioactive materials. However, it is recognised as a potentially high cost option (Zhu and Shaw 2000). In the past 15-20 years therefore, the application of alternative methods has become more prevalent. These include bioaccumulation methods such as

phytoextraction (Jadia and Fulekar 2009; Saleh 2012), biotransformation through the application of microorganisms (Tabak *et al.* 2005), and biosorption approaches. Biosorption differs from bioaccumulation in that it is a passive process removed from the biological processes of the utilised organism (i.e. respiration), and in recent years has been recognised as a cost effective remediation technique for contaminated groundwater in particular (Das 2012).

The relevance of this for this study is that the apparent shift of focus onto cost-effective remediation methods that are typically in-situ techniques increases the relevance and importance of developing accurate and time efficient contamination characterisation and monitoring methods.

2.2.2.2 Brief case study – Pécs, Hungary

Because this project is focussed upon characterisation and monitoring of water contaminated with uranium, it is useful to briefly consider a site specific example.

The mining and milling of uranium ore was a prevalent industry near the Hungarian city of Pécs until 1997. The source of legacy groundwater contamination in the area is associated primarily with two tailing ponds, ultimately consisting of ~20 Mt of solid milling waste. Traditional groundwater sampling via a series of boreholes indicated groundwater uranium levels in the area surrounding the tailing ponds of between $50 \mu\text{g L}^{-1}$ and 0.5 mg L^{-1} (this equates to 10^{-7} to 10^{-6} M for uranyl nitrate for example), in comparison to a typical background level of $10 \mu\text{g L}^{-1}$ (10^{-8} M uranyl nitrate ($\text{UO}_2(\text{NO}_3)_2$)) (Csővári *et al.* 2005a).

One method of groundwater remediation applied to the Pécs site is the deployment of permeable reactive barriers (PRB). These are a passive method of groundwater remediation, for which specific identified contaminants are immobilised or chemically transformed through contact with reactive treated membranes inserted into the path of groundwater flow. They are regarded as a potentially cost effective method of groundwater contamination treatment, and are particularly useful when physical removal

or bioaccumulation and biotransformation methods are too expensive or not practical (Roehl *et al.* 2005).

For the Pécs uranium contamination site Csóvári *et al.* (2005b) developed an experimental iron-based barrier. The PRB was deployed into a shallow sandstone aquifer at a part of the site for which a continuous increase in uranium concentration had been observed prior to the PRB deployment. The PRB was constructed of two distinct zones, characterised by the content of coarse elemental iron (the reactive element of the PRB) by volume. The barrier was placed in position by a standard method of shallow trench digging, filling out the PRB volume with sand, and sealing on the top and at the two ends with a high density polyethylene (HDPE) geomembrane. A clay barrier was positioned on top of the PRB before closing the trench. Csóvári *et al.* (2005b) reported a decrease in average aqueous uranium (U) concentration in groundwater at a selected monitoring well of ~650 µg/L (a change from 718 to 70 µg L⁻¹) following deployment of the experimental PRB.

One of the main points of note from this brief case study with respect to this project is that the Pécs example provides a benchmark range of aqueous uranium concentrations for a real contaminated site. This will help to focus the analysis of the integrated uranyl biosensor performance. Additionally, the method used to monitor the performance of the remediation method at Pécs was one involving manual collection of samples via a series of monitoring wells, and included laboratory analysis away from the site. Therefore, it is clear that an automated and remotely controlled aqueous uranium monitoring system would have provided significant benefits in terms of ease of evaluation for the experimental technology, and for the monitoring of real-world deployed remediation approaches of this type.

2.2.2.3 *The risks of uranyl contamination*

The current World Health Organisation (WHO) guideline for drinking water quality for uranium is 30 µg L⁻¹ (Frisbie *et al.* 2013). Many of the published concerns about the hazard posed by environmental uranium relate to its chemical toxicity rather than radiological effects (WHO 2004). Specifically, studies have proposed that the human and animal health impacts of

exposure to uranyl ions include impairment of kidney function (Zamora *et al.* 1998), potential for impacts upon reproductive fertility (Lin *et al.* 1993; Domingo 2001), and potential developmental impacts related to accumulation in bone (Kurttio *et al.* 2005).

2.3 Environmental water contamination monitoring

2.3.1 Monitoring approaches

The conventional method of monitoring contaminated and potentially contaminated water bodies involves manually collecting water samples and transporting the samples for laboratory-based analysis. For surface water, sample collection is typically straight forward using standard sample collection vessels filled manually from a water-borne vessel or from land. Conventional groundwater sampling will typically involve the strategic drilling and screening of sampling boreholes appropriate to the prevailing geology, and the pumped extraction of water to be sampled. Groundwater sampling also typically involves 'purging' of the borehole to be sampled prior to sample collection (Martin *et al.* 2003).

To minimise the potential for disturbing the bulk solution of the water body being sampled, and to reduce costs, passive sampling techniques have become more common in recent years. These are sample collection systems that are placed within the water body in a manner that enables collection of samples that accurately reflect the natural composition of the bulk solution for that location. Passive samplers also have the advantage over conventional sampling of allowing for some time-integrated element to contaminant measurements for the duration of sampling, rather than a simple 'snapshot' of contaminant conditions. Passive samplers operate by retaining the target analyte through use of a solvent, chemical reagent or porous membrane. The method used to retain the analyte can be selected to allow for sampling of a narrow or wide range of contaminants (Vrana *et al.* 2005).

2.3.2 Real-time water monitoring

Whilst passive sampling devices can provide some indication of mean contaminant concentration over time, they still require removal and analysis ex-situ. For agencies and organisations tasked with monitoring contaminated land and water, the possibility of the application of systems which can provide continuous or selectively controlled real-time in-situ monitoring are

attractive. This is partly because they offer the potential of long term cost savings due to reduced routine site sample collection and subsequent laboratory analysis. Additionally, deployment of a network of such systems provide an opportunity to respond more rapidly to temporal and/or spatial changes in contaminant concentration. This is a particular benefit where pathways and receptors have been identified for contaminants that, beyond established threshold concentration ranges, offer potential environmental risk.

2.3.2.1 *Wireless sensor networks*

In the past 10-15 years the deployment of wireless sensor networks (WSN's) for water quality monitoring has become more prevalent. In part, the driver behind development of such monitoring systems (along with automated sampling systems, to be discussed below), has been linked to the implementation of water quality legislation and regulation, such as the European Union's (EU) Water Framework Directive (WFD) (O'Flyrm *et al.* 2007). This should be considered in parallel with previous developments in Microelectromechanical systems (MEMS) and wireless communication technologies (Akyildiz *et al.* 2002). Wireless sensor networks for water monitoring typically consist of a dense network of monitoring sensor nodes that communicate automatically with a central data control system.

Table 2-1 gives a very brief summary of selected published water quality wireless sensor network projects, indicating the parameters that were measured in each case. These studies were selected to represent the range of measured parameters for WSN projects published within the past 10 years. The data presented in Table 2-1 provides an indication of some of the limitations of wireless sensor networks for real-time monitoring of contaminated water bodies. Presently, the sensors deployed are largely limited to quite a narrow range of measurement parameters, typically including pH, water temperature, water turbidity and electrical conductance. These are all useful indicators for the monitoring of contamination plumes but do not provide any information on specific potentially hazardous contaminants, such as those encountered in association with radioactive contamination. A small number of WSN's have been developed using ion

selective probes, including for the measurement of aqueous nitrate (Table 2-1). Generally however, the advancements in WSN infrastructure have outpaced the advancement of sensors suitable for deployment within the networks.

Table 2-1 Summary of selected published wireless sensor network (WSN) system projects for environmental water monitoring

WSN study	Primary water quality parameters	Sensors Used	WSN Network Deployment
Niederbacher and Nahold (2005)	<ol style="list-style-type: none"> 1. Water level 2. Electrical conductance 3. Water temperature 	Not specified	Groundwater – PRB remediation monitoring
Kotsilieris and Karetsos (2008)	<ol style="list-style-type: none"> 1. Water pH 2. Water turbidity 3. Electrical conductance 4. Water temperature 	Not Specified	Rivers
Kotamäki <i>et al.</i> (2009)	<ol style="list-style-type: none"> 1. Water turbidity 2. Nitrate concentration 	<ol style="list-style-type: none"> 1. OBS-3⁺ Turbidity Probe 2. scan Spectrometry Probe 	Rivers, Ditches, Wetlands
Porta <i>et al.</i> (2009)	Electrical conductivity	ECH2O-TE Conductivity Probe	Groundwater (Lab tested only)
Gartia <i>et al.</i> (2012)	Nitrate concentration	Bespoke electrochemical Nitrate sensor	Lab tested only
Capella <i>et al.</i> (2013)	Nitrate concentration	Not Specified	Rivers

Furthermore, there are few studies demonstrating WSN development for groundwater monitoring. For example, the study by Porta *et al.* (2009) was a laboratory based groundwater WSN system (i.e. field deployment was not attempted), and was limited to electrical conductivity measurement only. An exception is the study by Niederbacher and Nahold (2005) which utilised a wireless sensor network for the monitoring of the permeable reactive barrier (PRB) remediation scheme, described in Section 2.2.2.2, for the contaminated site at Pécs in Hungary. However, this study was limited to the monitoring of general environmental indicators (Table 2-1).

A further drawback to wireless sensor networks, one that partially explains the limited range of deployable sensors, is the lack of scope for any sample pre-treatment, application of necessary reagents and any built-in method for dealing with bio-fouling of sensor surfaces, access to calibration processes, and other routine maintenance tasks. These factors perhaps help to explain why the development of automated water sampling systems exists as an independent research strand (Section 2.3.2.2).

2.3.2.2 Automated water sampling systems

Automated water sampling systems are self-contained units typically capable of sample acquisition, fluid control, sample pre-treatment (where applicable), analytical measurement, and system re-preparation (i.e. they include a post analytical 'cleaning stage'). Such systems may also incorporate remote control capabilities for the off-site operation and monitoring of field-deployed units.

A number of examples of automated water sampling systems, with or without remote control capabilities, are presented in the literature. Zhou and Zhu (1997) reported an automated process for monitoring iron and dissolved manganese in groundwater. The automated system consisted of a 12cm Teflon spiral tube flow cell connected to a rotary injection micro-valve and peristaltic pump controlled by a microprocessor. The automated system was inserted into a pre-existing water treatment process, and the analytical method was based upon a chemiluminescence process. Burge and May (2005) developed a 'universal' automated sampling system for groundwater

monitoring wells. They used the system specifically for the monitoring of trichloroethene (TCE) with the deployment of a commercially available TCE optrode (an optical/chemical electrode). The sampling system consisted of two main elements, a water sample collection module placed directly into the monitoring well, and a connected analytical module inserted into a separate adjacent dry sub-surface vault. The analytical chamber housed the analytical electrode within a 750 mL analytical chamber.

Tschmelak *et al.* (2005) described the collaborative Automated Water Analyser Computer Supported System (AWACSS). This system was designed to provide automated and remotely controlled monitoring of a range of organic pollutants for the monitoring of rivers, streams, estuaries, coastlines, and industrial outflow pipes. The analytical methods were typically optical, based upon fluorescence techniques. Part of the design was a network system that would enable “unattended and centrally controlled monitoring and surveillance”. McGraw *et al.* (2007) encapsulated a smaller scale fluidic delivery system (i.e. flow cell, these will be covered in greater detail in Section 2.5) into a deployable waterproof box containing pumping capability, reagent supplies and a data control board to analyse and process acquired data. The pump contained its own battery power source. The data control board was attached via cabling to a separate ‘base station’ box, and contained a rechargeable battery, a microprocessor and memory board, and a Global System for Mobile Communications (GSM) modem enabling wireless communication with a remote laptop computer. The analytical method deployed was a commercially available photodiode for the detection of phosphates in water samples.

Crew *et al.* (2011) developed a biosensor array of 12 *amperometric* biosensors for the detection of a range of organophosphate pesticides in water samples (*amperometric biosensors are one of a number of different biosensor types, and these are summarised in Section 2.4*). The biosensor was portably deployed within a prototype analytical system consisting of a 12 channel potentiostat, powered via a car battery. However, this system was limited in its automation, as it required water samples to firstly be collected separately, and then delivered to the analytical system. Beaton *et al.* (2011) demonstrated actual deployment of a sensor for the measurement

of nitrate concentration in seawater. The sensor was integrated into a microfluidic platform (see Section 2.5 for further consideration), and fluid was microchip controlled through use of a custom-made syringe pump and series of microvalves. The power source was a battery powered custom-made electronics package. Successful nitrate measurements were taken automatically over a period of 57 hours, and data stored on a memory card from which analytical data was later retrieved. Specifically for the purposes of radioactive contaminant monitoring, O'Hara *et al.* (2009) reported the development of an automated system for the detection of strontium-90 (^{90}Sr) in environmental water samples. This system was not tested for field deployment, remaining as a laboratory proof-of-concept only. A commercially available automated fluid sampler was used to control pre-collected groundwater samples, which were passed to a radiation counter.

These examples demonstrate the application of automation techniques for the monitoring of environmental water samples, including contaminants related to radioactive contamination sources. The degree of portability and automation is variable, but it is clear that the technology is already available for the automated collection of water samples, sample and reagent fluid handling and sensor delivery, data acquisition and storage, and real-time data transmission. However, it is clear that no standard process exists for the integration of sensors into automated water sampling systems. Each sensor unit has a unique set of operational requirements, detection mechanisms, and analytical protocols which need to be considered within the integration process. This particularly holds true for biosensors, for which the semi-portable deployment demonstrated by O'Hara *et al.* (2009) was a truly rare example of biosensor integration into an analytical system with automation potential. The construction, operation and barriers to deployment of biosensors will therefore be considered in the next sub-section (Section 2.4).

To complete this sub-section Table 2-2 summarises the key characteristics and advantages/disadvantages of the different environmental water contaminant monitoring approaches reviewed.

Table 2-2 Summary review of different environmental water contaminant monitoring methods

Monitoring method	Characteristics	Advantages Of method	Disadvantages of method
Basic manual sample collection	1) manual filling of sample collection vessels (surface water), 2) pumped water extraction (groundwater), 3) laboratory-based analysis	1) typically utilises 'gold standard' laboratory analysis methods	routine manual sampling and analysis costly, 2) no real-time measurements
Passive Sampling	1) sampling device placed within water body, 2) chemical agent(s) or porous membrane retains target analyte(s), 3) laboratory-based analysis	1) minimises disturbance of sampled water body, 2) allows for time integrated measurement	still requires sample removal and laboratory-based analysis
Wireless sensor networks	1) network of sensor nodes communicate wirelessly with a computerised central control system, 2) in-situ measurements taken	1) in-situ real-time measurement, 2) rapid spatial contaminant behaviour information	1) limited range of suitable sensor types, 2) no sample pre-treatment
Automated water sampling systems	1) automated sample acquisition from water body, 2) fluid control and sample pre-treatment, 3) automated measurement, 4) System re-preparation, 5) option for wireless operation and transmission of data	1) as per wireless sensor networks, 2) allows for sample pre-treatment, use of reagents and automated calibration, 3) potential for portability	Requires detailed system integration investigation for each deployed sensor

2.4 Biosensors

The research objectives for this project include investigating the integration into a fluid delivery system of a specific biosensor; an impedimetric biosensor for the detection of uranyl (UO_2^{2+}) ions (Section 1.2.2). This section therefore firstly summarises what biosensors are, describes different biosensor types, and explains how biosensors are developed. Additionally, electrochemical biosensors, and specifically impedimetric biosensors, are considered in more detail. Next, a full presentation and review of the uranyl biosensor upon which this project is focused is conducted. This is followed by an outline of methods used to prepare electrodes for biosensor construction, an introduction to the impedance-based method of biosensor analysis, and issues associated with the deployment of biosensors for point-of-use (POU) applications.

2.4.1 Biosensors introduction

2.4.1.1 *What are biosensors?*

A biosensor is an analytical tool, typically miniaturised, that is used to detect and measure the presence and/or concentration level of a target analyte or analytes within a fluid. Specifically, the 'active' element of the sensor which is used to identify the target analyte is biological in nature. Biosensor development research has increased dramatically in the past 15-20 years, because they offer a potentially mobile and low cost alternative to more traditional analytical processes.

2.4.1.2 *Biosensor components*

A biosensor typically consists of three main components. Each component is described below, and presented schematically in Figure 2-3:

- Biorecognition Element (Figure 2-3A)
A biological component (bioreceptor) that interacts with the target analyte to produce an effect change that is measured through a transducer. For a biosensor to be practically usable, the chemical

and/or biological interaction between analyte and receptor needs to be highly selective (within acceptable margins of error) with respect to the target analyte. Common biorecognition element types include antibodies, non-antibody binding proteins, enzymes and bacteria.

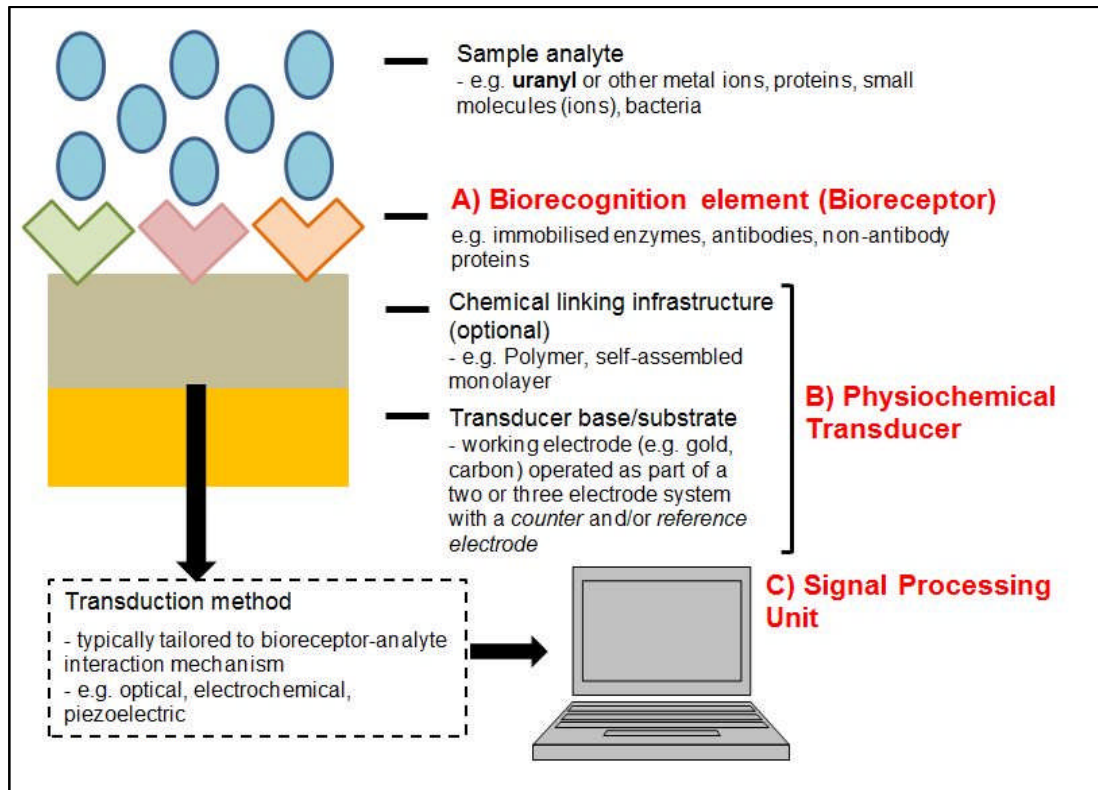


Figure 2-3 Schematic diagram of biosensor composition. The three main biosensor components i.e. the biorecognition element, physiochemical transducer, and signal processing unit are labelled A, B and C respectively. Figure developed by author with reference to Rushworth *et al.* (2013).

- Physiochemical Transducer (Figure 2-3B)

The physiochemical transducer converts the biorecognition event into a measurable signal, and may have purely physical components (e.g. electrodes) or include a chemical infrastructure linking the biorecognition element to the physical base. The biosensor is most commonly constructed upon the working electrode (common materials used are gold and carbon) of a three electrode system, completed by a counter and/or reference electrode.

The term *transducer*, with respect to biosensor literature, therefore usually refers to the combination of the complete three electrode setup and the chemical infrastructure linking the biorecognition

element to the working electrode (if present). However, within this thesis the terms *physical transducer and transducer base/substrate* are also used. The former refers to just the complete three electrode system used to convert the biochemical event to a measurable signal (i.e. excluding any chemical linking infrastructure), whilst the latter refers specifically to the electrode upon which the biosensor is constructed (i.e. the working electrode). The nature and operation of the three electrode system for biosensor analysis is explored further in Section 2.4.2.1.

A range of different methods of transduction are used for research biosensors, with the selected method typically being the most appropriate to the analyte-bioreceptor binding mechanism (this point is considered further in Section 2.4.1.3 below). The method of transduction is one common approach to categorising biosensor type:

- Electrochemical (e.g. Ronkainen *et al.* (2010))
- Optical (e.g. Goral *et al.* (2011))
- Piezoelectric (e.g. Sankaran *et al.* (2011))
- Acoustic (e.g. Matatagui *et al.* (2013))

This project is concerned with deployment of a specific type of *electrochemical* biosensor; this will therefore be the main focus within this thesis. However, a specific type of optical biosensor (whole cell toxicity biosensor) is briefly discussed in section 2.4.1.3.

- Signal Processing Unit (Figure 2-3C)

The signal processing unit converts the transducer signal to data suitable for analysis and manipulation. The unit can be either integral to, such as in handheld point-of-care (POC) medical biosensor units (e.g. glucose biosensor, Newman and Turner (2005)), or separate from the biosensor system.

2.4.1.3 Biorecognition element response

The preceding sub-section described how biosensors can be categorised by the method of transduction used to convert the biorecognition event of a

biosensor into a measurable signal. However, before turning the focus onto one specific type of transduction method (electrochemical biosensors, Section 2.4.2) it is useful to briefly consider, in general terms, the nature of the biorecognition event itself. That is, consideration of how the biological element of the sensor responds to/interacts with the stimulus provided by the presence of a target analyte or the prevailing environmental conditions.

First, two different general responses can be identified to the presence in an analytical sample of a target analyte or class of analytes:

1) *Physical binding or adsorption between the biorecognition element and the target analyte molecule(s) only* – the uranyl biosensor utilised as part of this study is an excellent example of this (Conroy 2012). The analyte molecule is adsorbed to the biorecognition element of the sensor either with or without chemical bonding (this issue will be considered further in the discussion section of Chapter 5, Section 5.5.4.3). The adsorption/binding event itself produces a change in a specified property, a change in electrochemical impedance in the case of the uranyl biosensor (Conroy 2012, Sections 2.4.2 and 2.4.3), which the transducer converts to a measurable signal. That is, a chemical or biochemical reaction is not required to produce a measurable signal.

2) *A chemical/biochemical response or reaction by the biorecognition element to the presence of the target analyte (or vice versa)* – most biosensors which utilise an enzyme as the biorecognition element are of this type. The immobilised enzyme catalyses a reaction in response to interaction with the analyte, which is suitable for transduction to a measurable signal (the transduction method will depend on the nature and/or products of the reaction). The most well known enzymatic biosensor is for glucose monitoring, for which the enzyme glucose oxidase is the biorecognition element. The enzyme catalyses the oxidation of glucose to hydrogen peroxide, from which a measurable electrochemical signal is detected and measured (electrochemical biosensors will be considered further in Section 2.4.2).

However, the biosensor model described above and presented in Figure 2-3, with respect specifically to analyte interaction, is not universal. Instead

research has included development of biosensors which respond to, and provide an indication of, the degree of toxicity within an analytical sample rather than recognising specific analyte species (Belkin 2006). Such biosensors have potential applications in environmental monitoring, such as for waste water (Olaniran *et al.* 2011).

One method of sample toxicity analysis is the use of *whole cell bioassays and biosensors*. These are assays/biosensors for which the biorecognition element is an intact whole live cell, rather than a molecular component of a cell such as an enzyme, protein or antibody. The reaction of the whole live cell to an analytical sample provides a measure of toxicity, genotoxicity or even nutrient bioavailability (Belkin 2006). Here, the distinction between *toxicity* and *genotoxicity* relates to the potential to cause harm to biological organisms (and humans in particular) for the former, and specific harm to genetic information (e.g. DNA) for the latter (Kocsis and Molnar 2009).

An example of the use of whole cells for toxicity analysis is the marine bacterium *Vibrio fischeri*. The transduction method employed to provide a measure of toxicity is bioluminescence (an *optical* sensor method). The presence of toxins leads to depression of metabolism and results in a reduction in natural bacterial bioluminescence (Tencaliec *et al.* 2006). Therefore, the decrease in light emission of the bacterium is related to the overall concentration of (non-specified) toxins within a sample. *Vibrio fischeri* has most commonly been utilised as a commercially available bioassay kit for the measurement of toxicity in environmental water samples (e.g. the Microtox Assay (Bitton and Koopman 1992)).

Biological assays for the detection and measurement of the genotoxicity of a sample typically consist of a bacterial promoter-reporter gene system. A promoter that responds to the genotoxicity of a sample effectively acts as the biorecognition element of the sensor. The binding of the inducer molecule (e.g. a toxin) activates or represses a reporter gene. The reporter gene produces a measureable signal, often optical in nature (fluorescence or bioluminescence). Common gene types utilised in these sensors are those involved with repair of DNA. The genes are utilised within a host whole cell (Biran *et al.* 2009).

Whilst laboratory-based assays for the above methods are currently in practical operation, the development of miniaturised and potentially mobile biosensors of the type described in Sections 2.4.1.1 and 2.4.1.2 for whole cell toxicity biosensors and biosensors for genotoxicity analysis has been limited by issues including long-term storage difficulties and performance repeatability problems (e.g. Michelini *et al.* 2013 for bioluminescence whole cell toxicity biosensors specifically).

2.4.2 Electrochemical biosensors and range of applications

2.4.2.1 Electrochemical biosensors

Electrochemical biosensors utilise an electrical circuit response to the interaction between the biorecognition element of the sensor and the target analyte. Different aspects of this electrical circuit response can be investigated, and the method of electrochemical investigation employed is commonly used as one method of electrochemical biosensor classification. The most common electrochemical research biosensors (as classified by type of electrochemical measurement) are (Thévenot *et al.* 2001):

- Voltammetric
- Amperometric
- Impedimetric
- Potentiometric

Before outlining the differences between these types of electrochemical biosensor however, it is useful to firstly describe the electrode configurations that allow for biosensor interrogation.

With the exception of potentiometric biosensors (the nature of this exception will be described below), a three electrode system is typically used for the electrochemical biosensor types listed above. This system is an electrical circuit comprised of a working electrode, counter electrode, and a reference electrode (Figure 2-4) (Bard and Faulkner 1980; Li and Miao 2013; Rushworth *et al.* 2013). The most commonly used materials for each electrode type is presented in Table 2-3.

The biosensor is constructed upon the working electrode of the three electrode system, and therefore the measurable biosensor-analyte reaction or interaction takes place at the surface of this electrode. The main purpose of the counter electrode in a three electrode electrochemical system is to complete the circuit between itself and the working electrode, for which the flow of current can be measured. The reference electrode utilises materials which provide an established stable electrode potential (Table 2-3), and operates as a half-cell with the working electrode. The fixed stable potential of the reference electrode therefore allows for the control of a fixed potential, or range of potentials, as applied at the working electrode (Figure 2-4)(Bard and Faulkner 1980; Zoski 2007; Banica 2012).

Table 2-3 Commonly used materials for the electrodes that comprise a typical three-electrode electrochemical system

Electrode	Commonly used materials	Key material requirements
Working	Gold, silver, platinum, carbon (a range of different types including graphene, glassy carbon)	Chemically inert, chemical structural properties specific to biosensor chemical and/or biological binding
Counter	Gold, platinum, carbon	Chemically inert
Reference	Silver/Silver Chloride, saturated calomel electrode (SCE)	Provide a stable electrode potential

The analysis of an *amperometric*, *voltammetric* or *impedimetric* biosensor is typically conducted by using a potentiostat to control an applied potential (V, Figure 2-4) between the working electrode (upon which a biosensor has been constructed) and reference electrode of a three electrode system. The resultant current (A, Figure 2-4) that subsequently flows between the working and counter electrodes is measured, and a relationship between the electrical circuit response and biosensor-analyte interaction is investigated using the output data. The differences between biosensors employing

amperometric, *voltammetric* and *impedimetric* methodology relate to how the application of potential is controlled with respect to the electrical circuit of the three electrode system, and how the output data obtained from the current-flow response is manipulated.

For **voltammetric** biosensors a ramped voltage range is applied and the current resultant from the biosensor-analyte interaction is expressed as a function of the changing potential. Common methods of voltammetry include *linear sweep voltammetry* where the potential is simply ramped linearly from a minimum to a maximum value (e.g. -0.4V to 0.4 V), and *cyclic voltammetry*

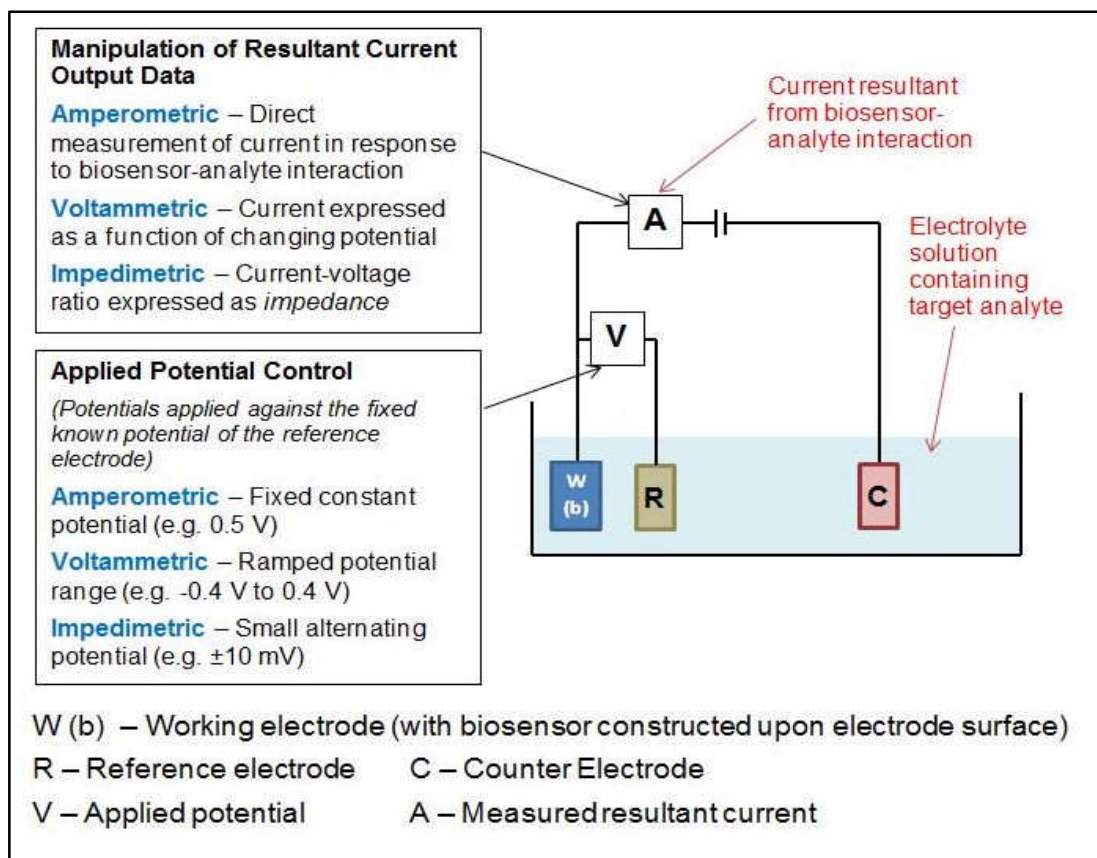


Figure 2-4 Schematic of a three-electrode circuit system as applied to an electrochemical biosensor unit. The variations in applied potential control and current output data handling for three different electrochemical biosensor types are also highlighted. Figure developed by author with reference to Bard and Faulkner (1980); Li and Miao (2013); Rushworth *et al.* (2013).

where an initial sweep between a minimum and maximum potential is made but then a reverse sweep is also conducted from the maximum potential to the minimum potential. For **Amperometric** biosensors there is no ramping of

the potential, a fixed potential only is applied, and the resultant change in current is typically expressed as a function of time.

Impedimetric biosensors utilise the change in impedance resultant from the interaction between the biosensor's biorecognition element and the target analyte. In this case, a small alternating potential is applied between the working and reference electrodes (e.g. ± 10 mV). Impedance is a complex property that describes the opposition that an electrical circuit provides when a potential is applied. The basis of impedance measurements is the ratio between the current resultant from the biosensor-analyte interaction and the applied voltage. Analysis is typically conducted through electrochemical impedance spectroscopy (EIS). These, along with the mathematical foundation of impedance will be discussed in further detail in Section 2.4.5.

Potentiometric biosensors typically employ a two electrode system only, comprised of an ion-selective electrode (ISE, the working electrode) and a reference electrode. Most usually the ISE operates by sensing either H^+ or NH_4^+ ions. The sensor specificity is conferred by an immobilised enzyme where action on the analyte generates one of these two ions. The current flow through the working electrode is very low, and often zero. The other difference, when compared to the other three electrochemical biosensor types described above, is that the measured output is the potential (V).

Ultimately, whether a biosensor is operated using amperometric, voltammetric, impedimetric, or potentiometric methods will be determined by the biochemical interaction between the biorecognition element of the biosensor and the target analyte. Amperometric and voltammetric methods are typically used where the bioreceptor of the biosensor (e.g. an enzyme) produces an electroactive species in response to a target analyte. The measured current is generated by the oxidation or reduction of an electroactive species as an appropriate potential is applied to the system. Because impedimetric biosensors measure the change in impedance caused by a binding event at the biosensor surface, an electrochemical reaction is not required. For all of the electrochemical biosensor types considered above, the practical operation of the biosensor relies upon the identification of a demonstrable and calibrated relationship between the

analyte concentration and the appropriate signal output (e.g. impedance in the case of impedimetric biosensors).

To conclude this sub-section, Table 2-4 summarises the attributes and considers the operational advantages/disadvantages of each type of electrochemical biosensor.

Cont'd.....

Table 2-4 Summary review of different types of electrochemical biosensor

Electrochemical biosensor type	Operational defining characteristics	Operational advantages	Operational disadvantages	Supporting references
Voltammetric	1) Analysis with three electrode system, 2) Application of ramped potential, 3) Electroactive species produced from analyte –sensor interaction 4) Resultant change in current measured	1) Rapid response signal measurement, 2) High sensitivity to changing analyte concentrations	1) Species detection selectivity dependent on operating potential, 2) Limited range of measurable analytes	Bard and Faulkner (1980); Korotcenkov (2010)
Amperometric	As for voltammetric biosensors except: 1) Application of fixed potential	As for voltammetric biosensors	As for voltammetric biosensors	Bard and Faulkner (1980); Korotcenkov (2010)
Impedimetric	1) Analysis with three electrode system, 2) Application of alternating potential, 3) Change in impedance resulting from analyte-biosensor interaction measured	1) A greater range of measurable analytes than for amperometric or voltammetric biosensors (no need for electroactive species)	1) Reproducibility issues, 2) High detection limits, and, 3) non-specific binding <i>in some cases</i> (discussed in Chapters 5 and 6)	Bard and Faulkner (1980); Prodromidis (2010); Rushworth <i>et al.</i> (2013)
Potentiometric	1) Analysis with two electrode system, 2) Low current flow (usually zero), 3) Measured output is potential, 4) H ⁺ or NH ₄ ⁺ ions detected and measured	1) High portability, 2) High selectivity for target analytes, 3) Low cost, 4) Large dynamic range	1) Relatively longer response time (than other biosensor types), 2) low sensitivity to changing analyte concentrations	Koncki (2007); Grieshaber <i>et al.</i> (2008); Yunus <i>et al.</i> (2013)

2.4.2.2 Impedimetric biosensor applications

The development of impedimetric biosensors is a relatively new process. One of the earliest published applications of an impedance based biosensor was by Bataillard *et al.* (1988), who developed an antigen-antibody impedimetric biosensor for the detection of two immunospecies. Many of the impedimetric biosensors developed since this time have also been designed for medical applications. However, the advantage of impedimetric biosensors over the other types of electrochemical biosensors is that it is not necessary to produce an electroactive species through chemical interaction between the bioreceptor and the analyte (Section 2.4.1.3). In principle, any analyte through binding with an appropriate biorecognition element can produce a measurable impedimetric change. This actually provides opportunities for the application of impedimetric biosensors across a wide range of fields of study.

Examples of impedimetric biosensors developed for environmental water quality monitoring include the detection of a specific pesticide (Atrazine) (Helali 2013), hydrocarbons such as trichloroethylene (TCE) (Hnaïen *et al.* 2011), pathogenic microorganisms including *Staphylococcus aureus* (Choi *et al.* 2009) and a biosensor designed as an early warning system for the general presence of heavy metals in water samples (Guedri and Durrieu 2008).

2.4.3 Uranyl ion biosensor

An impedimetric biosensor for the detection of uranyl ions in aqueous solutions was developed by David Conroy at the University of Leeds, as part of his PhD studies. The development process and operation were presented in the journal publication Conroy *et al.* (2010), and in David Conroy's final thesis (Conroy 2012). Because one of the objectives of this project is to develop a deployment system specifically for this biosensor (Section 1.2.2) the key elements of the biosensor development work are presented in summary in this sub-section, and considered in context with current relevant

literature. This provides background to investigations conducted with respect to the uranyl biosensor as part of this study (as described in Chapter 5).

2.4.3.1 *Biosensor development background*

The uranyl biosensor was developed as a PhD project through the backing of a university consortium known as DIAMOND (Hyatt *et al.* 2009), and specifically under a strand of that consortium concerned with the legacy of UK nuclear sites.

The biorecognition element of the biosensor is a surface layer protein (S-layer protein, SLP) of the bacterium *Bacillus sphaericus* strain JG-A12, which had naturally developed tolerance for uranium through prolonged exposure in mine wastes. Pollmann *et al.* (2006) identified the uranyl binding capabilities of the S-layer protein, and its potential applications for contamination remediation (and therefore also for contamination monitoring).

2.4.3.2 *Biosensor construction*

The preferred biosensor construction method developed by Conroy *et al.* (2010) consisted of a gold electrode transducer base onto which a self-assembled monolayer (SAM) was formed through incubation of the gold electrode in 10 mM 4-Aminothiophenol (4-ATP) solution in ethanol. The physiochemical transducer was completed by incubating the sensor unit in 4-(N-Maleimidomethyl)cyclohexane-1-carboxylic acid 3-sulfo-N-hydroxysuccinimide ester sodium (Sulfo-SMCC) solution in phosphate buffered saline (PBS). The sulfo-SMCC bound to the 4-ATP self-assembled monolayer through amine groups. Finally, the biosensor was completed by coupling the S-layer protein via its thiol groups using the maleimide reactive moiety of the sulfo-SMCC (Figure 2-5).

The primary type of electrode used for biosensor construction was a bespoke-designed (~1mm diameter) electroplated gold electrode on a thin silicon wafer substrate (P3 electrode design (Conroy 2012)). An investigation (by Conroy (2012)) was conducted to establish the minimum incubation time for the self-assembled base layer, and 4 hours was identified as minimum

duration required for complete development and ordering of the self-assembled monolayer.

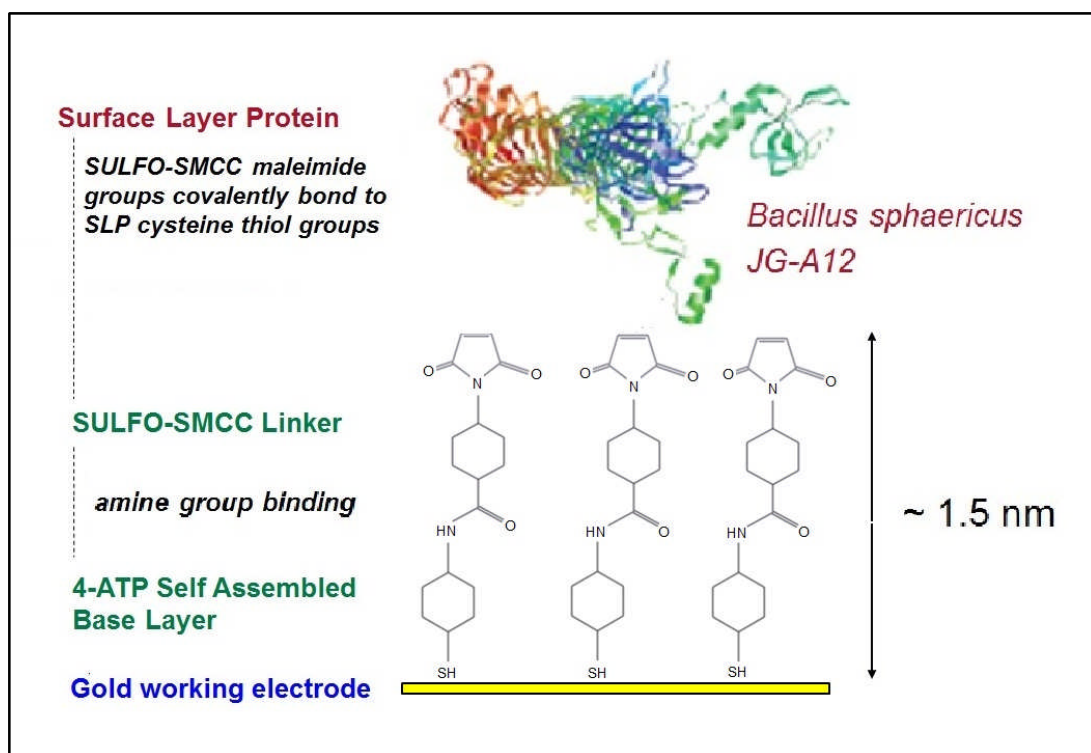


Figure 2-5 Uranyl biosensor construction (modified from Conroy *et al.* (2010))

As the base layer of the biosensor, the quality of the SAM is significant in determining the stability of the sensor as a whole. A high quality SAM features a high level of ordering and symmetry (Figure 2-6A). In an imperfectly ordered SAM, as observed through atomic force microscopy (AFM), gaps or 'pinholes' in the self-assembled layer are apparent (Figure 2-6B). However, the work of Schoenenberger *et al.* (1994) suggested that these apparent holes were actually depressions in the gold subsurface (Figure 2-6C) caused by chemical etching. The implication here is that chemical composition of the SAM solution, electrode surface topography, and perhaps solution concentration, may be more significant for this aspect of SAM quality than deposition methods and incubation time.

2.4.3.3 Biosensor performance and stability

A dual mechanism has been proposed for the binding of the uranyl ion analyte to the surface layer protein (SLP). The first is monodentate binding

to phosphate groups on the SLP, and the second is bidentate binding to carboxyl groups on the SLP (Merroun *et al.* 2005)(Figure 2-7). This is supported by work conducted by Conroy *et al.* (2010) as part of the original uranyl biosensor development process.

Conroy (2012) conducted investigations into the analyte response to the full uranyl biosensor. These investigations were conducted using a traditional electrochemical setup formed of a P3 gold working electrode, commercially sourced solid platinum counter electrode and a commercially sourced Ag/AgCl reference electrode. Electrochemical experiments were conducted within a glass vessel, containing at least 30 mL phosphate buffered saline electrolyte. The analyte concentration was increased sequentially by adding aliquots of uranyl solution prior to each electrochemical measurement. An average uranyl response from three different uranyl compounds was determined, and compared to the biosensor response to a selection of potentially interfering ions (Figure 2-8).

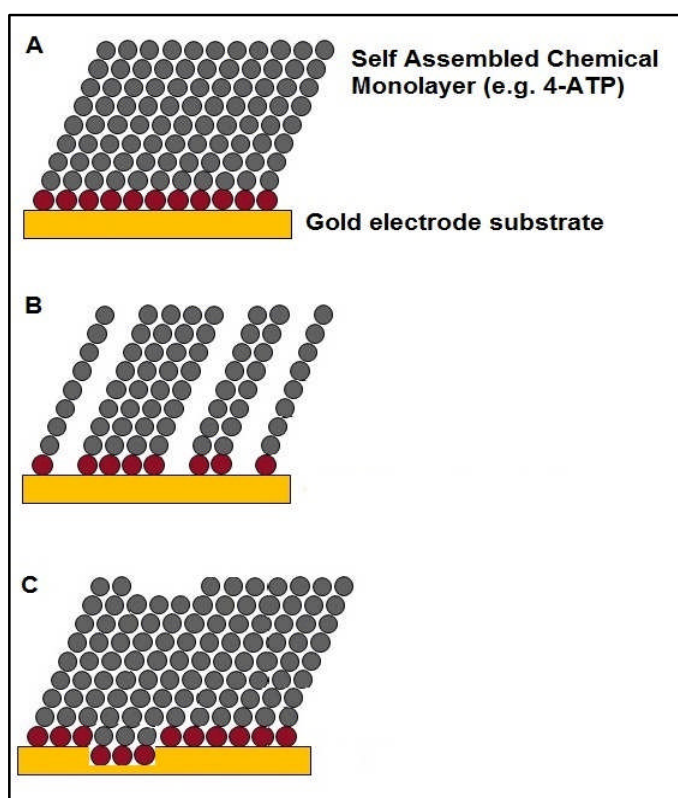


Figure 2-6 Self assembled monolayer (SAM) ordering on a gold substrate. A) complete and ordered SAM, B) incomplete SAM, 'pinhole' theory, C) incomplete SAM, 'depression' theory. Figure developed by author with reference to Sigma Aldrich (2014b) and Schoenenberger *et al.* (1994).

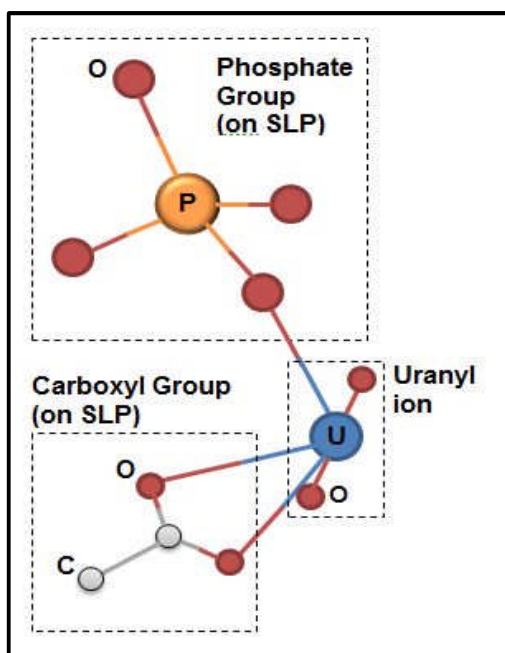


Figure 2-7 Proposed mechanisms for binding uranyl ion to the surface layer protein of *Bacillus sphaericus* JG-A12 (modified from Merroun *et al.* (2005)).

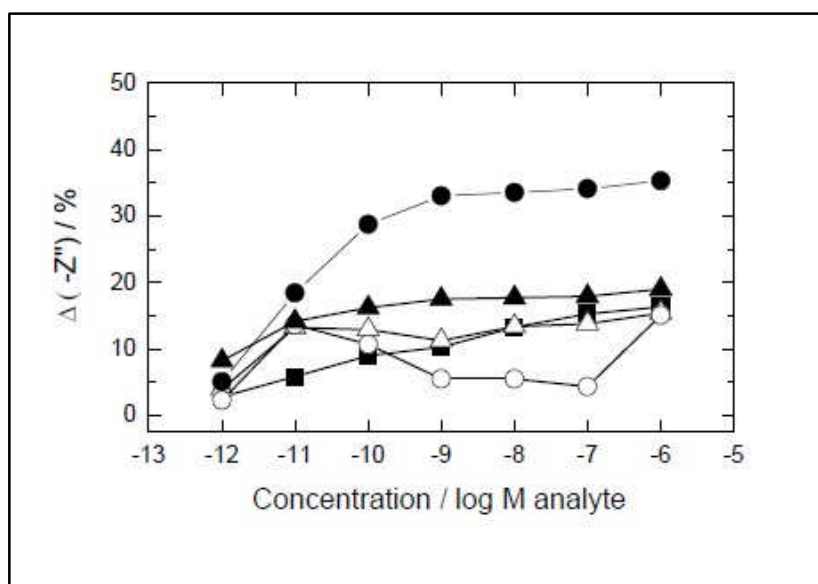


Figure 2-8 Response of uranyl biosensor to uranyl analyte, compared to the response to potential interfering ions. ● Average uranyl response, ▲ cobalt chloride, △ calcium sulphate, ■ nickel nitrate, ○ cadmium nitrate (Conroy 2012).

Note that the biosensor response presented in Figure 2-8 considers only the imaginary component (Z'') of impedance (for an explanation of impedance as applied to electrochemical impedance spectroscopy, see Section 2.4.5). At lower analyte concentrations it is clear that there is some overlap between the selected interfering ions and the average uranyl response (Figure 2-8). This suggests that a tentative lower working limit for the biosensor is 10^{-11} M

UO_2^{2+} . Also, at average uranyl concentrations higher than 10^{-10} M an apparent 'saturation' effect is observed. This suggests therefore that the biosensor has an operational dynamic range limited to between approximately 10^{-11} M and 10^{-9} M UO_2^{2+} .

Another aspect of biosensor performance worthy of consideration are the issues of regeneration and reusability. Conroy (through Conroy *et al.* (2010), and Conroy (2012)) did not present any investigative data relating to biosensor regeneration using the same working electrode substrate. A reference to biosensor reusability was made however, for which it was stated that a buffer wash following analyte binding returned the biosensor to its pre-binding state (i.e. successfully achieved complete analyte dissociation with the sensor's biorecognition element).

The stability and durability of the uranyl biosensors were tested by Conroy. The biosensors, constructed upon P3 electrodes were wet stored in PBS and 40% of the sensors stored remained functional after 1 month. After a storage period of four months only one single biosensor remained fully functional. However, in actual deployed biosensor operations dry storage for extended periods and wet storage deployment for one month or less would be most likely.

2.4.3.4 Biosensor deployment investigations

The traditional laboratory-based electrochemical setup utilised by Conroy (2012)(Section 2.4.3.3) is not suitable for making the transition to field deployment of the uranyl biosensor.

In light of this, Conroy (2012) presented the results of a short investigation into construction of the uranyl biosensor upon screen-printed electrodes. Screen-printed electrodes (SPE) offer a potential method for sensor deployment beyond the limitations of the traditional laboratory electrochemical setup. A commercially available SPE was used for the investigation (Dropsens C223AT), which consisted of a 1.6 mm diameter gold working electrode surrounded by a gold counter electrode and silver/silver chloride reference electrode screen-printed onto a ceramic

substrate. The three electrodes were encompassed within an 8 mm diameter circular 'active' region (Figure 2-9).

Conroy (2012) reported that the screen-printed electrode trials were not successful. Specifically, he stated that the electrodes responded poorly to electrode preparation methods in comparison to the P3 silicon wafer gold electrodes. Additionally, he observed instability issues relating to the silver/silver chloride reference electrode of the SPE's, exhibited through the development of a black residue on the reference electrodes after use.

2.4.4 Electrode preparation methods

As discussed in Section 2.4.3, the choice of electrode preparation method can influence the structure and stability of self-assembled monolayers, and therefore affects the quality of biosensors that utilise SAM's as a base layer (as in the case of Conroy's uranyl biosensor). This sub-section therefore reviews published electrode preparation techniques, specifically focussing upon electrodes for biosensor construction use. A distinction is made here between preparation methods employed for first-time use electrodes, and those utilised in regenerating electrodes upon which biosensors have been constructed (although some techniques are used for both). An additional focus for this sub-section is on preparation methods for working electrodes formed of 'pure' gold (i.e. at least 99.95% Au by weight). This is because this type of electrode would ultimately be used as an alternative to screen-printed electrodes for this study (Chapter 5).

Cont'd over....

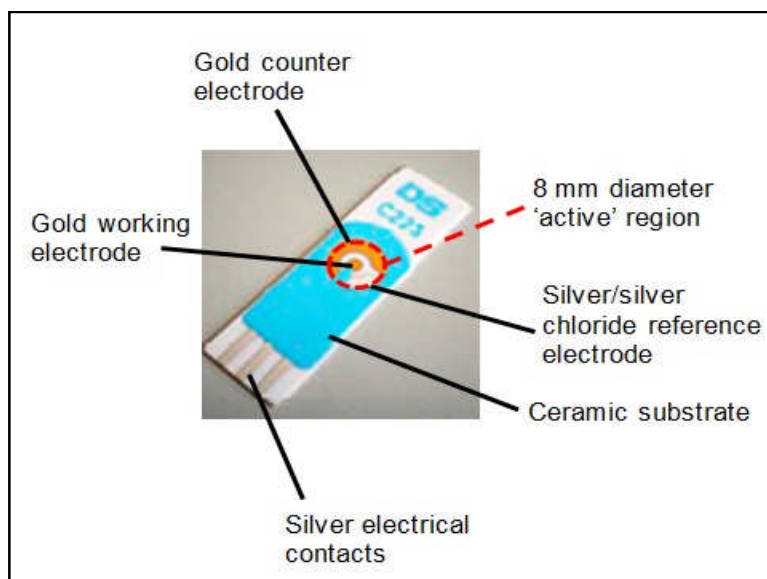


Figure 2-9 Dropsens C223AT screen-printed electrode (DropSens 2011b)

2.4.4.1 Initial electrode preparation – uranyl biosensor

For the uranyl biosensor construction on P3 silicon wafer gold electrodes Conroy (2012) employed a range of preparation methods. Through electrochemical analysis, specifically cyclic voltammetry (Section 2.4.5.3), and the optimal preparation was determined to be 2 minutes in a piranha solution (7:3 v/v 95-98% sulphuric acid : 30% hydrogen peroxide). For the uranyl biosensor trials using screen-printed electrodes (Section 2.4.3.4), Conroy (2012) employed a range of largely different preparation methods (with one exception). The optimal method for removing contaminants from the electrode surface was once again 2 minutes in piranha solution, but the solution was observed to dissolve the printing inks. This reduced the operational lifespan of the electrodes.

2.4.4.2 Gold chip electrode preparation and electrode regeneration methods

The electrode preparation methods utilised by Conroy *et al.* (2010), as considered in Section 2.4.4.1, are fairly typical of methods employed for initial electrode preparation. The use of piranha solution, in particular, is widely prevalent within the literature relating to novel biosensor development.

For electrodes formed of solid gold, a range of initial electrode preparation methods have been presented. Additionally, a number of studies considered the effectiveness of electrode preparation methods for the regeneration of used gold electrodes. Specifically, the focus of this research was the removal of self-assembled monolayers from the electrode surface, and consequent regeneration for repeated biosensor construction.

Table 2-5 presents six selected papers relating to preparation methods for gold electrodes with respect to biosensor construction/self-assembled monolayer deposition. These six were selected because of their relatively high number of citations, and as a representation of the range of methods presented in the literature as a whole. Studies such as that conducted by Hoogvliet *et al.* (2000) considered only one specific preparation method whilst others (Campiña *et al.* 2008; e.g. Bhalla *et al.* 2010) compared a range of different methods. Those authors which considered more than one preparation method would typically either recommend the use of either one of the considered methods only based on the study results (Bhalla *et al.* 2010), or a combination of more than one method used in succession (Ron *et al.* 1998; Carvalhal *et al.* 2005)(Table 2-5). Additionally, a distinction can be made between studies which considered the effectiveness of methods for a) pre-SAM deposition preparation, only, b) post-SAM deposition desorption, and c) both (a) and (b).






It was clear from these examples that a gold standard electrode preparation and/or SAM desorption method for gold chip electrodes was not agreed upon within the biosensor research community.

Cont'd over....

Table 2-5 Selection of published studies on preparation methods for pure gold electrodes (>99.95% Au by wt.)

Paper	Electrode Preparation Methods											
	A	B	C	D	E	F	G	H	I	J	K	L
Bhalla <i>et al.</i> (2010)	✓	✓	✓	✓								
Campiña <i>et al.</i> (2008)					✓	✓	✓	✓	✓			
Carvalho <i>et al.</i> (2005)	✓								✓	✓	✓	
Hoogvliet <i>et al.</i> (2000)											✓	
Ron <i>et al.</i> (1998)				✓								✓
Tkac and Davis (2008)	✓					✓			✓	✓		✓

A - Piranha Solution, **B** - Electro-chemical Oxidative Cleaning in PBS
C - Electro-chemical Reductive Cleaning in PBS, **D** – Plasma/UV Cleaning,
E - Flame annealing desorption,
F - Electro-chemical (CV) Reductive desorption in Alkaline media
G - Electro-chemical (CV) Oxidative desorption in Alkaline media
H - Electro-chemical (CV) Reductive desorption / cleaning in Acidic Solution
I - Electro-chemical (CV) Oxidative desorption / cleaning in Acidic Solution
J – Mechanical Cleaning, **K** - Electro-chemical (DPV) Reductive desorption in Alkaline media
L – Chemical Reduction of gold oxide by incubation with absolute EtOH

 Single method recommended by authors
 Combined methods recommended by authors
 Specified by author For pre and post SAM deposition cleaning / desorption
 Specified by author for post SAM deposition cleaning / desorption only
 Specified by author for pre SAM deposition cleaning / desorption only

2.4.5 Impedimetric biosensor and electrode analysis methods

This sub-section provides background information with respect to the electrochemical methods utilised in the analysis of electrode preparation, the biosensor construction process, and the operation of completed impedimetric sensors.

2.4.5.1 Impedance basic theory

An impedimetric biosensor, such as the uranyl biosensor developed by Conroy (2012), utilises the opposition to electrical current flow resultant from interaction between the biosensor's biorecognition element and the target analyte.

The concept of impedance can be understood by firstly considering Ohm's Law, which describes the relationship between the resistance to current flow (R), voltage amplitude (E), and current (I) (Eq. 2-1) (Bard and Faulkner 1980):

$$R = \frac{E}{I} \quad (2-1)$$

With respect to an electrical circuit however, only an ideal resistor is represented by this relationship. An ideal resistor does not fully represent the complexities inherent in real world circuit components due to the following simplifying limitations:

- The relationship stated in Ohm's law should apply at all currents and voltages
- The voltage and AC current signals that pass through the ideal resistor are in phase with each other
- The magnitude of resistance is not impacted by variations in frequency

The utilisation of the property of impedance instead of simple resistance in the analysis of electrochemical phenomena, avoids these limitations. Before examining the method of impedance analysis, electrochemical impedance

spectroscopy (EIS, Section 2.4.5.2), it is useful to introduce the most common equivalent electrical circuit elements in an impedimetric electrochemical system:

- **Solution resistance** (R_s) – Describes the electrical resistance present due to the ionic solution (electrolyte) under analysis in the electrochemical cell. Specifically, it is the solution resistance between the reference and working electrodes of the electrochemical cell that is relevant here. The parameters that determine the magnitude of solution resistance are cell surface area (A), cell length (l) and solution resistivity (ρ) (Eq.2-2)(Bard and Faulkner 1980):

$$R_s = \rho \frac{l}{A} \quad (2-2)$$

Because the solution resistance is determined by the fluid properties and fixed cell geometry dimensions, it will not usually change during electrochemical analytical investigations of biosensor-analyte systems.

- **Charge Transfer Resistance** (R_{ct}) – For a biosensor-analyte system the charge transfer resistance describes the resistance of electron flow from the analyte solution to the electrode. An equation can be derived from the Butler-Volmer equation for the determination of charge transfer resistance (Eq. 2-3)(Bard and Faulkner 1980).

$$R_{ct} = \frac{RT}{nFi_0} \quad (2-3)$$

where R is the universal gas constant, T is temperature, n represents the number electrons involved in the transfer reaction, F is the Faraday constant, and i_0 is exchange current density. In a biosensor-analyte system, the binding of target analyte ions to the biorecognition element of the biosensor will alter the exchange current density, and therefore lead to an increase or decrease in charge transfer resistance.

Double-layer Capacitance (C_{dl}) – A capacitance is associated with the formation of an electrical double layer due to the adsorption of ions onto the electrode (biosensor) surface. The double layer effectively insulates the electrode from the electrolyte (analyte containing fluid), and behaves like a capacitor.

- **Warburg Impedance (W)** - Warburg impedance is a constant phase element (CPE) which describes the finite rate of unhindered diffusion of electrons from an electrolyte solution to a planar electrode. The Warburg impedance is typically independent from the analyte-receptor binding activity (Rushworth *et al.* 2013).

In some electrical circuits describing electrochemical systems, a constant phase element (CPE) is used instead of double-layer capacitance. This is because C_{dl} describes a capacitor with ideal behaviour, whilst a constant phase element is sometimes considered more appropriate to real electrochemical systems (Orazem and Tribollet 2011).

The equivalent circuit developed through EIS analysis is commonly described by the Randles circuit model (Figure 2-10), for which the solution resistance (R_s) is in series with a parallel circuit consisting of double-layer capacitance (C_{dl}) in parallel to charge transfer resistance (R_{ct}) and Warburg impedance (W). The Randles equivalent circuit model applies to systems for which *faradaic currents* are generated. These are generated as a result of an electrochemical reaction at the electrode surface, setting up a charge transfer between the analyte solution and the electrode. Distinct from these are *non-faradaic currents*, for which electrochemical reactions and charge transfer are not involved. Instead, charge accumulates on or near the electrode as a result of the current (Lasia 2002).

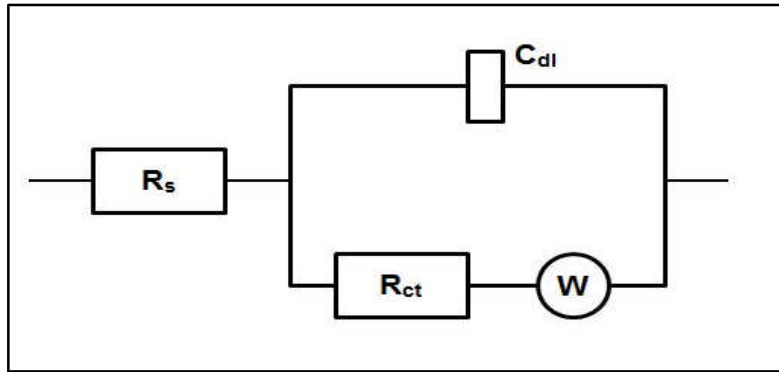


Figure 2-10 Randles equivalent circuit. Figure redrawn from Conroy (2012).

2.4.5.2 Electrochemical Impedance Spectroscopy (EIS)

Electrochemical impedance spectroscopy is the standard method used to measure and analyse biosensor-analyte interactions. An alternating (AC) potential (V), typically consisting of a small amplitude sine wave ($\pm 10\text{mV}$) set against a background voltage (of typically 0V , giving a potential range of $+10\text{mV}$ to -10mV) is applied through a potentiostat to the electrode unit containing the biosensor. The AC potential is applied across a range of selected frequencies. The biosensor unit is immersed in a solution containing the target analyte.

Fundamentally, the change in impedance due to analyte binding at the bioreceptor of the sensor is examined by calculating the ratio of the applied AC potential (V) to the change in current resultant from the biochemical binding. For any given frequency, the resultant current is typically also a sine wave, although it is shifted in phase with respect to the sinusoidal potential. When the amplitude of the sine wave is plotted against time, a phase angle can therefore be determined. Equation 2-4 describes the full relationship between impedance, phase angle and the voltage-current ratio (Macdonald 1992):

$$Z = \frac{V \sin(\omega t)}{I \sin(\omega t + \theta)} = Z_0 \frac{\sin(\omega t)}{\sin(\omega t + \theta)} \quad (2-4)$$

where Z is the total impedance of the system, V is the applied voltage, I is the resultant current, t is time, ω is radial frequency, θ is the phase angle of the sinusoidal current, and Z_0 is impedance magnitude. Overall therefore,

equation 2-4 describes impedance in terms of a magnitude and a phase shift. The radial frequency (ω) is determined from the frequency applied to the AC voltage (f), as described in equation 2-5 (Macdonald 1992):

$$\omega = 2\pi f \quad (2-5)$$

When presenting data obtained through electrochemical impedance spectroscopy methods, it is useful to convert the polar co-ordinates generated from the application of equation 2-4 to Cartesian values. Impedance in Cartesian co-ordinates form is presented in equation 2-6 (Macdonald 1992):

$$Z(\omega) = Z'(\omega) + jZ''(\omega) \quad (2-6)$$

where Z is total impedance, Z' is the real component of impedance, Z'' is the imaginary component of impedance, and j is equal to $\sqrt{-1}$.

From equation 2-6, it can be seen that impedance has been converted into real (Z') and imaginary (Z'') components. In general terms, the real component of impedance can be regarded as representing properties of the electrochemical system similar to resistance, whilst the imaginary component represents properties similar to capacitance.

When the real component of impedance (x -axis) is plotted against the imaginary component (y -axis) for a given EIS dataset, a Nyquist plot is created. A drawback of these Nyquist plots is that they do not explicitly display measurement frequency information. However, the impedance response appropriate to high frequencies is always displayed to the left of the plot, and those appropriate to low frequencies to the right (Figure 2-11). Based on this understanding information about the Randles equivalent circuit components associated with the analysed biosensor can be determined. Solution resistance (R_s) and charge transfer resistance (R_{ct}) are determined from x -axis intercepts at high and low measurement frequencies respectively, and double-layer capacitance (C_{dl}) from the y -axis intercept of a line tangential to the top of the resultant semi-circle. The Warburg

impedance element (W), if present, will always appear on such Nyquist plots as a 45° straight line at low frequencies (Figure 2-11).

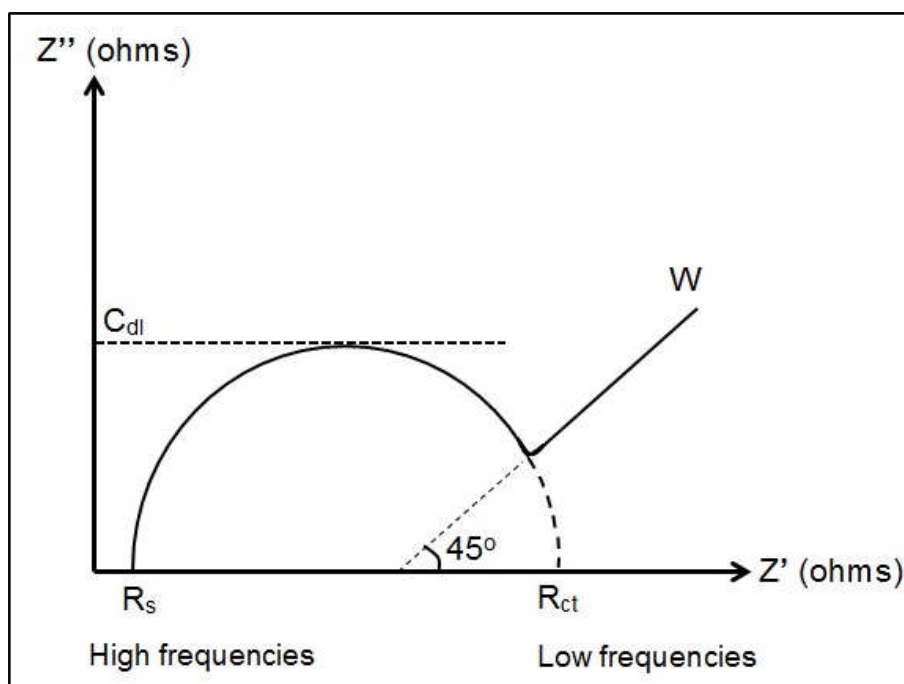


Figure 2-11 Nyquist plot schematic for electrochemical impedance spectroscopy analysis. Figure redrawn and modified from Rushworth *et al.* (2013).

2.4.5.3 Cyclic voltammetry

Cyclic voltammetry (CV) is a commonly used analytical tool in electrochemical experiments. For biosensor investigations it is regularly applied to the study of the effectiveness of electrode preparation (cleaning) methods, and to the process of biosensor layer deposition.

To conduct CV analysis an electrode/biosensor is immersed in an electroactive species; one commonly used species is the ferrocyanide/ferricyanide redox couple ($\text{Fe}(\text{CN})_6^{3-/4-}$). A potential (E) is applied between the reference and working electrodes of a three electrode system, and the resultant current (I) is measured between the working and counter electrodes. The applied potential is ramped linearly with time through a specified scan rate (mV s^{-1}) between 1st and 2nd potential limits, and the potential is applied between the limits in both forward and reverse directions. The potential limits are chosen specifically to allow for the oxidation and subsequent reduction of the electroactive species couple used

in the investigation. For a bare electrode immersed in an electroactive species, a plot similar to that presented in Figure 2-12 will be produced, where the potentials at which an oxidation peak (anodic peak potential, E_{pa}) and reduction peak (cathodic peak potential, E_{pc}) occur are identified on a voltammogram. Additionally, by utilising suitable baseline currents a peak anodic current (i_{pa}) and peak cathodic current (i_{pc}) can also be identified (Kissinger and Heineman 1983)(Figure 2-12).

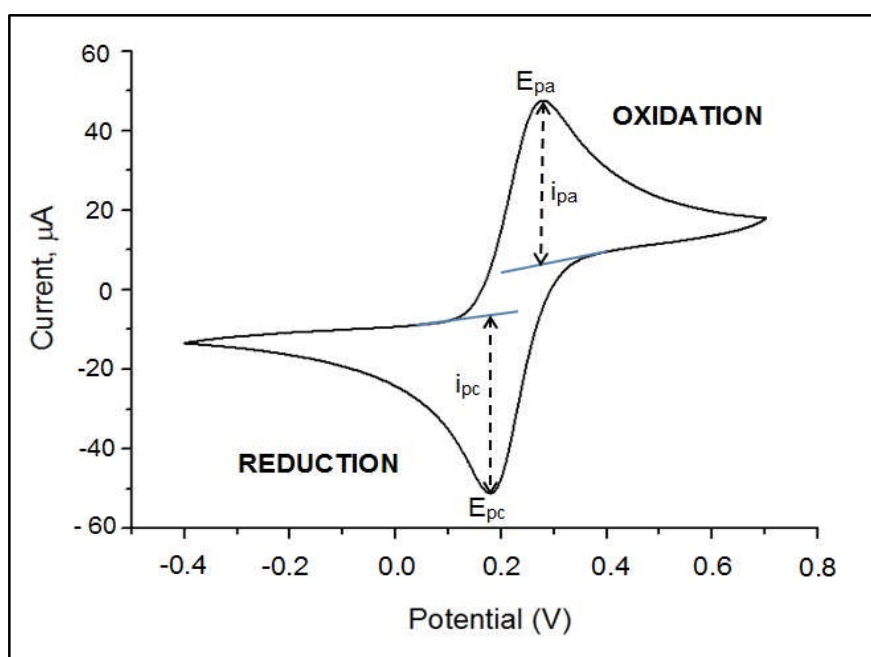


Figure 2-12 Cyclic voltammogram schematic diagram for an electroactive redox couple. E_{pa} – peak anodic (oxidation) potential, E_{pc} - peak cathodic (reduction) potential, i_{pa} – peak anodic current, i_{pc} – peak cathodic current. Figure developed by author from real experimental voltammogram example but with reference to Kissinger and Heineman (1983).

The mathematical determination of the peak currents, as represented on Figure 2-12, is given by the Randles–Sevcik equation (eq. 2-7) (Zanello 2003):

$$i_p = 2.69 \times 10^5 n^{3/2} A D^{1/2} C v^{1/2} \quad (2-7)$$

Where i_p is the peak current (anodic or cathodic, Amps), n is the number of electrons in the redox reaction, A is the electrode area (cm^2), D is the diffusion coefficient of the electroactive species ($cm^2 s^{-1}$), C is the

concentration of the electroactive species (mol cm^{-3}), and v is the scan rate (mV s^{-1}).

Comparative examination of cyclic voltammograms before and after the application of electrode cleaning methods, and following the deposition of biosensor layers on the electrode surface, can be used to assess the nature of electrode surface modification. This is typically done through relative analysis of parameters such as the peak currents and peak potentials, and the relative distance between peak potentials (i.e. $E_{\text{pa}} - E_{\text{pc}}$).

The impedance theory and electrochemical analytical methods described in Section 2.4.5 above was utilised in this work in the process of flow cell integration for the uranyl biosensor presented in Section 2.4.3 (Chapter 5). Specifically, electrochemical impedance spectroscopy methods were utilised in the analysis of biosensor construction and biosensor performance response to the target analyte (uranyl, UO_2^{2+}). Cyclic voltammetry techniques were utilised primarily in analysis of electrode preparation methods, for electrodes upon which the biosensors were constructed (full methodology described in Section 5.3).

2.4.6 Biosensor deployment

Although research into the design and development of biosensors across a range of applications has steadily increased over the past 10-15 years, the transition to successful deployable point-of-use (POU, usually referred to as point-of-care (POC) for medical applications) systems has been very limited. This in turn has limited the commercial exploitation of biosensors.

The main barriers to the commercialisation and otherwise successful deployment of biosensors, and impedimetric biosensors in particular, will be outlined in Section 2.4.6.3. Firstly, however, it is useful to briefly consider the main factors that will influence the measure of success for biosensor deployment (Section 2.4.6.1). Additionally, Section 2.4.6.2 will review the published research related to the transition of biosensors from laboratory to POU deployment.

2.4.6.1 General considerations

Four key components are identified to enable impedimetric biosensor transition from laboratory proof of concept to point-of-use deployment:

- **Impedimetric biosensor** – Incorporating a physio-chemical transducer and biosensor recognition element. The basic requirements for successful lab-to-field transition is reproducible and reliable performance, such that results are comparable to both laboratory-based biosensor operation and ‘gold standard’ non-biosensor laboratory methods for the analytical process concerned.
- **Fluid sample collection, delivery and processing capability** – Typically, a microfluidic platform will be utilised for fluid handling capabilities, incorporated with valves and pumping systems for fluid control. Pre-treatment may be required, and the deployment system will therefore be required to accommodate storage and handling of buffers and reagents. The uranyl biosensor for example would require delivery of buffer for storage of the biosensor within the deployment system, and for regenerating the biosensor surface after analysis (Conroy 2012).
- **Signal processing capability** – Incorporation of a compact potentiostat to enable electrochemical analysis. For automated, remotely controlled systems this would need to be battery operated or rechargeable (through renewable energy sources for example). Stand-alone commercial portable potentiostat products are available (e.g. *Uniscan Instruments, PG581 Potentiostat - Galvanostat* 2013), and the technology could be readily adapted to allow for built in incorporation into a fluid delivery system for example.
- **Sample disposal** – Disposal of sample fluids and buffers/reagents used in the biosensor preparation, analysis and regeneration processes. One approach to simplifying sample processing and disposal is to utilise single use self-contained cartridges that incorporate biosensor, and fluid storage (i.e. buffers/reagents). Such

systems have successfully been utilised in hand held portable devices for medical applications (Erickson and Wilding 1993).

2.4.6.2 *Successful biosensor commercialisation*

A significant proportion of biosensor development research has been focussed upon medical applications, driven by a desire to reduce diagnosis costs and times, particularly in the developing world. Therefore it is not particularly surprising that the main success in biosensor point-of-use (point-of-care) deployment and commercialisation have been in this area.

The most commercially successful, and most well-known, biosensor is the blood glucose biosensor (of which many variations are now available), utilised across the world by people with diabetes management. The commercial success of this sensor is at least in part related to the successful integration into a compact and mobile analytical device, making it suitable for home as well as professional clinical use. Additionally, the amperometrically analysed enzymic reaction of this biosensor is very stable and reproducible (Newman and Turner 2005).

The i-STAT Portable Clinical Analyzer (PCA) is one further example where biosensors have been integrated with a fluid control system, and signal processing capability to provide a portable medical diagnostic tool. This system has been used in healthcare applications for a number of years, specifically for the measurement of chemical diagnostic indicators (e.g. sodium, chloride, and urea nitrogen), haematological indicators (haematocrit and haemoglobin) and blood gases. A number of removable self-contained cartridges, each capable of analysing a different range of indicators, are available for incorporation into the PCA (Erickson and Wilding 1993; *Abbot Laboratories, Abbot Point Of Care* 2013). These successful transitions from laboratory proof-of-concept to point-of-use deployment are limited to amperometric and potentiometric biosensors. At the time of writing no details of a successfully commercialised deployed impedimetric biosensor has been reported in the literature.

These commercially successful examples demonstrate the potential for the integration of biosensors into portable hand-held devices, and for which the

fluid sample is applied manually. Such applications for environmental monitoring would be welcome, although no successfully commercialised examples were identified as part of this literature review. However, the work of Crew *et al.* (2011), first discussed in Section 2.3.2.2, was a rare example of where a biosensor array was operationally demonstrated as part of a 'portable' analysis system. But, in environmental monitoring terms this system had its limitations with respect to not being truly automated and not remotely controlled, and was not truly portable when compared to the medical application examples given above.

2.4.6.3 *Barriers to commercialisation*

The limited number of successful instances of biosensor integration into deployable analytical systems is in itself an indication of the presence of barriers limiting such transitions. Furthermore, the limited commercial opportunities provides an indication that challenges remain in the successful integration of biosensors with fluid control and signal processing systems.

Some of these barriers and challenges are not necessarily specifically expressed within the literature. However, the focus of published material can in itself highlight an ongoing problem or challenge that is not easy to resolve. The reproducibility of electrode biosensor substrates is one such area. A small section of published research related to gold electrode preparation for self-assembled monolayer construction, and for regeneration of electrode surfaces following biosensor construction, was considered in Section 2.4.4. From these sometimes contradictory publications alone, it is clear that a single definitive consensus approach to the preparation and regeneration of gold-based electrodes for SAM-based biosensor construction has yet to be reached. However, the assertion that reproducible quality standards for self-assembled base layers is essential for the development of reliable and reproducible biosensors is widely agreed upon.

Other methods of immobilising the biorecognition element of a biosensor are employed besides binding to SAM's. These include bio-affinity bonding, covalent coupling to polymeric supports, direct enzymic (or other biorecognition element) adsorption onto solid electrode surfaces, and

entrapment within a 3-D matrix such as a photopolymer. However, each of these methods have their disadvantages as well as advantages with respect to producing stable and reproducible biosensor construction (Sassolas *et al.* 2012). The matching of the biorecognition element to an ideally suitable immobilisation method to a degree that will enable reliable and reproducible biosensor performance is clearly therefore an important element of biosensor design.

Another challenge for integrated point-of-use biosensors, including for those deployed within environmental settings is the requirement to process or pre-treat the sample to be analysed prior to delivery to the sensor. This can afford additional complexity to the fabrication of the fluid delivery system in the process of miniaturisation of the integrated biosensor-fluidic system unit (Jokerst *et al.* 2012).

2.5 Fluid delivery systems

From the previous two sub-chapters (Sections 2.3 & 2.4), it is clear that the most practical approach to achieving the transition from laboratory proof of concept to point-of-use deployment for an impedimetric biosensor is to integrate the sensor with a fluid delivery system and signal processing unit. This sub-chapter therefore will examine the literature for examples of fluid delivery system design and application (Section 2.5.1), and consider the principles of fluid flow that require evaluation in the flow cell design process (Section 2.5.2).

2.5.1 Flow cell design

The published literature relating to fluid delivery systems is very broad, so it is necessary first of all to provide some scope limitations to this part of the literature review. Because the aim of this study is the deployment of a specific type of biosensor, the review of relevant literature will be confined to the following areas:

- a) An assessment of the different scales at which fluid delivery systems and platforms utilised for sensor/biosensor operation typically operate (Section 2.5.1.1)
- b) A brief overview of the most common types of fluid delivery system (at the 'minifluidic scale'), typically flow cells, utilised for sensor integration (Section 2.5.1.2)
- c) Studies that have purposefully examined the design of fluid delivery systems, for use with sensors and biosensors in particular (Section 2.5.1.3)

2.5.1.1 Scaling of fluidic systems

Fluid delivery systems for the deployment of point-of-use biosensors are typically developed at two different scales. Firstly, flow cell units with flow channels or flow domain regions (in the case of non-channel cells) at the millimetre (mm) scale may be utilised to integrate biosensor units, and these can be described as 'minifluidic' systems. An example of a commercially available flow cell of this type is shown in Figure 2-13 (Section 2.5.1.2).

Secondly, smaller scale platforms and systems may be utilised and these are termed 'microfluidic systems'. Minifluidic flow cell systems will be the primary focus of this study, and the different specific types of flow cell and their applications will be explored in Section 2.5.1.2. However, it is necessary initially to distinguish between the two different scales of fluid delivery system, and to explain why the larger scale system is appropriate to this study. Therefore, a broad overview of microfluidic systems will firstly be considered.

A good definition of the term 'microfluidics' is “..systems that process or manipulate small (10^{-9} to 10^{-18} litres) amounts of fluid, using channels with dimensions of tens to hundreds of micrometres” (Whitesides 2006). When microfluidic platforms are integrated with sensors, the entire unit is typically described as a lab-on-a-chip (LOC), also known as a Micro Total Analysis System (μ TAS) (Reyes *et al.* 2002). Materials commonly used for the fabrication of microfluidic platforms include silicon, polymer plastics (e.g. polydimethylsiloxane (PDMS), polymethyl methacrylate (PMMA)), and glass. These materials are attractive because of their low fabrication costs, and chemical resistance for a broad range of solutions (Marle and Greenway 2005).

Naturally, for the same reasons these materials, and in particular the plastic polymers, are also commonly used for the larger scale minifluidic flow cells. Recently however paper-based microfluidic platforms, known as microfluidic paper-based analytical devices (μ PADs), have become more prominent in the literature. The microchannels for these are typically constructed using porous hydrophilic cellulose fibres, providing an even lower relative cost and relatively simple fabrication processes (Glavan *et al.* 2013).

A number of different types of microfluidic platforms have been developed, each utilising alternative fluid control technologies (Mark *et al.* 2010). Four of the most prominent of these are summarised in Table 2-6. The small selection of examples is presented in Table 2-6 to provide some indication of the developments and advances that have been achieved in relation to microfluidic infrastructure and operational technologies. However, the incorporation of biosensor systems into these type of platforms remains

limited primarily to proof of concept laboratory systems. A representative selection of integrated biosensor-microfluidic systems presented in the literature is shown in Table 2-7, providing a sense of the type of biosensors that have been successfully incorporated into microfluidic platforms.

The main advantages offered by such microfluidic systems for biosensor integration are the maintenance and control of laminar flow conditions within the micro-scale channels across a wide range of flow rates, and utilisation of very small sample volumes and therefore minimised fluid wastes and elevated sensitivity for the analytical system (Rivet *et al.* 2011). Additionally, they can enable minimisation of reaction times, inherent portability possibilities due to compactness, and the analysis of multiple samples in parallel (Choi *et al.* 2011).

The reason for making the choice between microfluidic and minifluidic scaling for the integration of biosensors is rarely, if ever, explicitly expressed. However, it is reasonable to suggest that the relevant considerations include the reduced complexity of integrating larger biosensor transducer components, and the desire to limit the miniaturisation of biosensor chemical and biochemical components where the stability and robustness of the sensor is either questionable or not fully characterised. Also, from an end-user point of view there is an argument for developing larger scale biosensor deployment systems that are perhaps relatively easy to handle, and straightforward to maintain for repeated use.

For this study, which considers the integration of the uranyl biosensor with a fluid delivery system, the investigations will be conducted at the larger minifluidic scale. The primary reason for this choice is to avoid miniaturising the biosensor design developed by Conroy (2012), ensuring that investigative results from the two studies are broadly comparable. Additionally, from a flow-cell design perspective, the literature indicates that a knowledge gap exists with respect to the relationship between the geometry of minifluidic flow cell channels, and the understanding of sample control for sensor analysis. This latter point will be considered explicitly in Section 2.5.2.

Table 2-6 Selection of prominent micro-fluidic platform types

Microfluidic Platform Type	Operation outline	Reference Example
Lateral Flow Tests	Chemicals to enable analysis are all incorporated into a paper-based strip, to which the fluid to be analysed is applied. Fluid is controlled solely by capillary forces within the microfluidic strip. The test result is typically indicated by a colour change on the strip itself. The pregnancy test kit is a commercially successful example.	Fu <i>et al.</i> (2011)
Pressure driven laminar flow	Operates based upon pressure gradients applied to the inflowing fluid, and where pressure is controlled by external pumping systems and/or membranes. The narrow flow channels maintain laminar flow across a range of inflow rates.	Glavan <i>et al.</i> (2013)
Microfluidic large scale integration (mLSI)	These are microfluidic chips that utilise hundreds or thousands of micromechanical valves to compartmentalise fluid samples, and enable a vast range of different chemical and biochemical assays. Applications include protein crystallography, genetic analysis, and chemical synthesis.	Thorsen <i>et al.</i> (2002)
Segmented flow microfluidics	Liquid plugs and droplets are used to control and contain fluids with which they are immiscible, within a microchannel structure.	Gibb <i>et al.</i> (2014)

Table 2-7 Selection of published biosensors integrated into microfluidic platforms

Integrated Biosensor-microfluidics Reference	Analyte(s) Detected <i>(Application type)</i>	Microfluidic Platform Type <i>(Channel fabrication material)</i>	Biotransducer Type <i>(Type subcategory)</i>
Yu <i>et al.</i> (2011)	Uric acid <i>(Medical)</i>	Pressure driven laminar flow (μ PAD)	Optical (Chemiluminescence)
Safavieh <i>et al.</i> (2012)	Escherichia coli <i>(Food and Environment)</i>	Pressure driven laminar flow (PDMS)	Electrochemical (Voltammetric)
Boehm <i>et al.</i> (2007)	Various Bacteria <i>(Medical, Food and Environment)</i>	Pressure driven laminar flow (<i>Glass and silicon</i>)	Electrochemical (Impedimetric)
Kwakye <i>et al.</i> (2006)	Virus RNA <i>(Medical)</i>	Pressure driven laminar flow (PDMS)	Electrochemical (Amperometric)
Chikkaveeraiah <i>et al.</i> (2009)	Hydrogen Peroxide (H ₂ O ₂) <i>(Medical and Environmental)</i>	Pressure driven laminar flow (PDMS)	Electrochemical (Amperometric)
Islam <i>et al.</i> (2011)	Amyloid-beta (A β)(Medical)	Pressure driven laminar flow (PDMS)	Electrochemical (Voltammetric)

investigative results from the two studies are broadly comparable. Additionally, from a flow-cell design perspective, the literature indicates that a knowledge gap exists with respect to the relationship between the geometry of minifluidic flow cell channels, and the understanding of sample control for sensor analysis. This latter point will be considered explicitly in Section 2.5.2.

2.5.1.2 Minifluidic flow cell types

The minifluidic flow cells utilised in biosensor studies fall into two distinct categories, namely bespoke designed flow cells (e.g. Rippeth *et al.* (1997)) and those sourced commercially (e.g. Du *et al.* (2009)). The latter are commonly used when biosensors are constructed upon commercially sourced screen-printed electrodes (SPE's). The Dropsens flow cell 'FLWCL' for use with single working electrode SPE's is one of the most popular in current use (Figure 2-13).

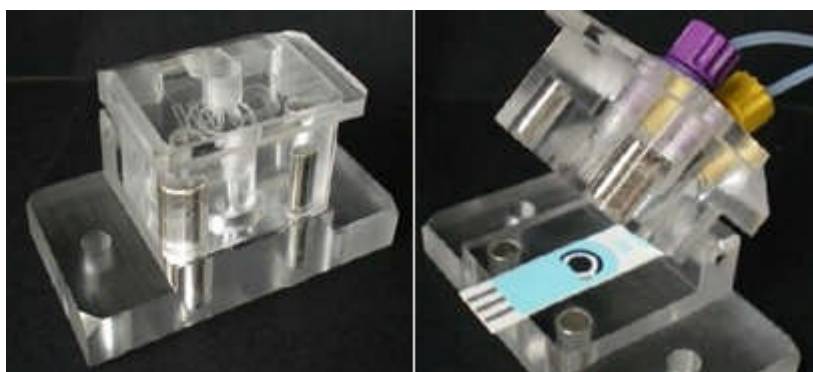


Figure 2-13 Commercially available wall-jet style flow cell for use with screen-printed electrodes (DropSens 2011a)

Although the bespoke nature of many of the flow cells featured in the literature provides a wide range of different designs, it is possible to categorise them into four common design types based upon the position of the fluid inlet and outlet with respect to the position of the incorporated electrode. The four main types are shown in Figure 2-14, for which the full descriptions and referenced examples of their application for integrated sensor systems is presented in Table 2-8.

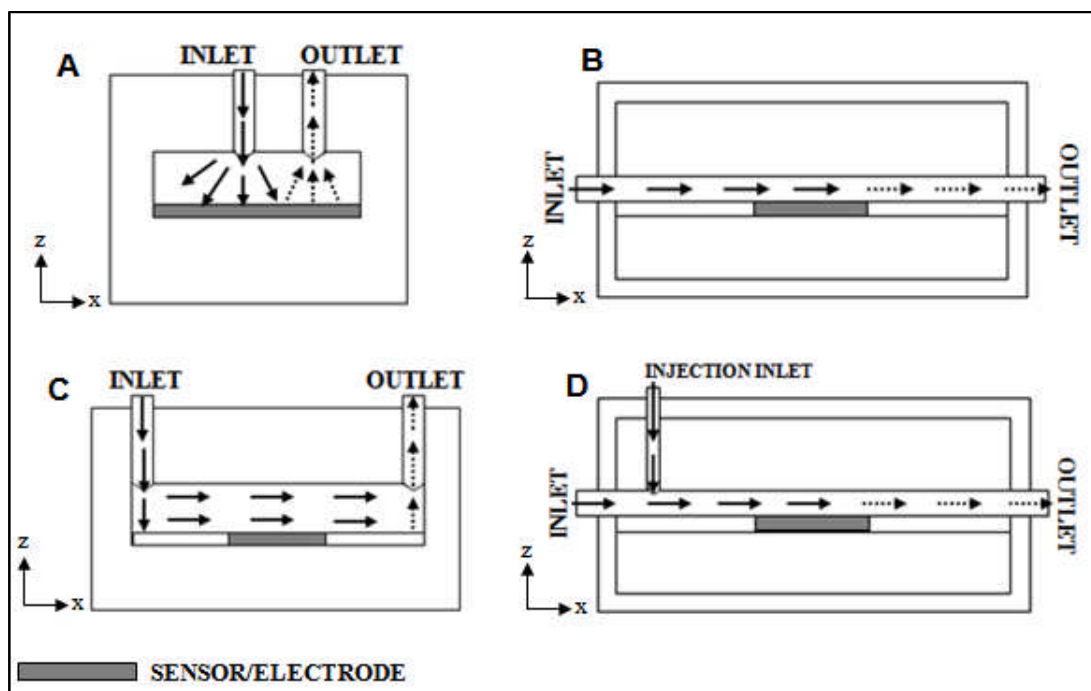


Figure 2-14 Schematic diagrams of common flow cell design types used with biosensors and other sensor types: (A) impinging jet direct onto sensor surface, (B) channel flow with embedded sensor, (C) impinging jet delivery with channel flow over embedded sensor, (D) injection into a flowing carrier channel flow. Figure designed and developed by author with reference to the published examples presented in Table 2-8.

Additionally, a distinction can be made between flow cells for which analyte-containing fluid is delivered to an initially dry flow cell (Koblizek *et al.* 2002) or to a flow cell already containing fluid (a wet cell). A wet cell will apply for some fluid injections systems, and also where the biosensor is to be stored in wet conditions prior to use (e.g. in buffer solution). This study will focus solely upon wet flow cells, because this reflects the requirement for wet storage of the uranyl biosensor under field deployment conditions (Section 2.4.3.3).

For all of the sensor-flow cell integration examples presented in Table 2-8, no rationale was provided for the selection of the flow cell type used, and certainly no investigations were conducted into the suitability of the flow cell for the purposes of integration of the specific type of sensor used. The main driver for flow cell design (or flow cell choice in the case of commercially sourced flow cells), appeared to be simply the practicalities of fitting the pre-designed sensor into a device to which an analyte-containing fluid could be applied to the sensor, whilst allowing connection to signal processing

Table 2-8 Minifluidic flow cell type descriptions, and examples of their application for integrated sensor/biosensor systems

Flow Cell Type	Description	Sensor Application Examples (Application)	Biotransducer type
Figure 2-13A	An impinging jet cell where the analyte-containing fluid is delivered directly into an (usually circular) area enclosing the active electrode elements	1. Neufeld <i>et al.</i> (2000) (Environment)	1. Electrochemical (Amperometric)
Figure 2-14B	Channel flow cell where analyte solution flow is entirely parallel to a surface containing an embedded/inserted sensor	1. Coldrick <i>et al.</i> (2009) (Medical/Environment) 2. Wu <i>et al.</i> (2006)(Medical)	1. Electrochemical (Amperometric) 2. Electrochemical (Voltammetric)
Figure 2-14C	A channel flow cell where an impinging jet delivers the analyte solution to the flow chamber, and subsequent flow is parallel to a surface containing an embedded sensor. Outlet flow perpendicular to the channel flow	1. Komaitis <i>et al.</i> (2010) (Environment)	1. Optical (Bioluminescence)
Figure 2-14D	Impinging jet injected pulses of analyte solution into a pre-existing channel flow (e.g. containing a reagent or buffer), flowing parallel to a surface containing an embedded sensor.	1. Okawa <i>et al.</i> (1995) (Medical)	1. Electrochemical (Amperometric)

capabilities. The impact of flow conditions or flow cell geometry upon the distribution of analyte concentrations within the flow cell were not explicitly considered either within the studies themselves, or through reference to separate focussed studies (the importance of this aspect of flow cell design will be considered further in Section 2.5.2).

A good example of this oversight is a bespoke flow cell design utilised by Coldrick *et al.* (2009)(Figure 2-15). The integrated electrode was a platinum wafer electrode onto which a mercury (Hg) film had been electrodeposited. The electrode was placed into a recess within the base of the flow cell. However, the cell was made watertight around the electrode by encircling it with a shallow rubber O-ring. This would naturally place an obstacle to the laminar flow (laminar flow at low flow rates is assumed) between the inlet and the outlet, the effects of which upon the distribution of analyte concentrations within the flow cell were not considered. Additionally, the rubber O-ring placed within the laminar flow path could arguably trap analyte particles, which could influence subsequent measurements through diffusion into the bulk solution with the flow domain, if not thoroughly cleaned between uses. Finally, the flow channel featured an expansion in channel width from the initial inlet channel and the main flow domain channel. Once again, no consideration was made with respect to the impact of this upon the concentration distribution within the cell.

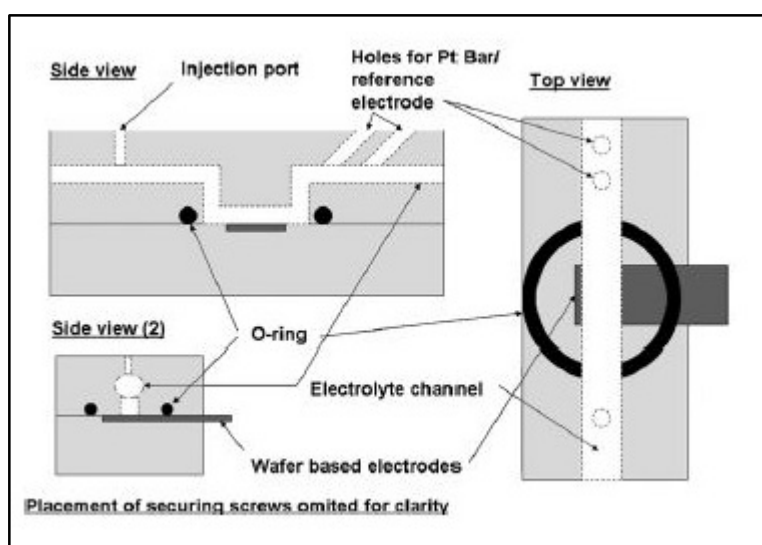


Figure 2-15 Schematic diagrams of a flow cell designed by Coldrick *et al.* (2009). The flow cell was used for the integration of bespoke Pt/Hg screen-printed electrodes.

For some integrated flow cell-sensor systems, the design of the flow cell unit is not even specifically described or mentioned within the published paper (Mishra *et al.* 2012).

2.5.1.3 Flow cell design investigations

Peer reviewed published detailed systematic investigations into the design of flow cells for the incorporation of analytical sensors, and biosensors in particular are very rare. This particularly includes studies that examine the relationship between flow cell design geometry and prevailing flow conditions, and the accuracy and reliability of biosensor measurements. Furthermore, commercially available flow cells such as the model presented in Figure 2-13 are typically not supported by published peer review publications, with respect to their design and operational protocol.

An exception is Cooper and Compton (1998), who considered the impact of analyte diffusion to the electrode surface on biosensor response. However, a big assumption was made in their study, namely that flow velocity in a channel flow-cell always varies parabolically with distance from the sensor surface. That is, the potential presence of flow features such as eddies in laminar flow, and therefore the influence of the cell geometry upon the structure of the flow regime (flow field) under varying flow rates was not considered. The only channel design considered was a rectangular flow channel that featured an expansion from a narrow inlet channel to the main flow domain (coupled with a symmetrical channel contraction to the outlet).

Meanwhile, Lammertyn *et al.* (2006) developed a model for the reaction kinetics of a specific biosensor system, using computational fluid dynamics software. The simulation results from the study provided a picture of flow development through time within a channel flow cell with an expanded central rectangular region, through the modelling of chemical reaction products associated with the biosensor-analyte interaction. Additionally, reference was made in discussion that varying the geometry of the flow channel could impact upon the efficiency of flushing of reaction products from the flow cell. However, no follow-up study was conducted to implicitly examine the influence of geometry variation upon the performance of the

biosensor. Furthermore, no attempt was made to understand the underlying flow field that produced the concentration distribution of reaction products through time within the flow channel.

Clearly, in the examples presented here the main focus of the studies was on biosensor kinetics, rather than the fundamental issue of establishing the relationship between the flow channel geometry, flow rates and equilibration of the biosensor.

However, there is a much deeper literature source related to the study of fluid mechanics principles of flow within a channel, and including flow within an expanding and contracting channel of the type commonly used for flow cell systems. This will be examined in the next sub-section, Section 2.5.2.

2.5.2 Fluid mechanics principles

From the previous sub-section it is clear that there is a knowledge gap with respect to understanding the influence of fluid dynamics principles upon the equilibration of integrated sensor-flow cell systems, and particularly the influence of flow cell geometry upon the characterisation of analyte concentration distribution within wet flow cell systems. In this sub-section therefore the main fluid dynamics principles relating to flow cell systems, and channel flow cells in particular, will be considered. In addition, the literature will be examined with respect to studies relating to flow development within channels that feature an expanded channel region.

2.5.2.1 Flow conditions

Firstly, it is important to establish the likely range of flow conditions within a flow cell at the minifluidic (mm) scale. Flow within a narrow channel (e.g. < 10 mm), or within an enclosed flow domain in impinging jet type flow cells (Figure 2-14A), is expected to be either laminar or turbulent. Laminar flow features the movement of particles of fluid in lines parallel to each other, such that each particle retains its relative position to all other particles along the entire length of the flow channel (or throughout the flow domain). Conversely, turbulent flow is characterised by small fluctuations in each fluid

particle's flow velocity magnitude and direction, along with small fluctuations in fluid pressure. Common features associated with turbulent flow include the development of areas of circulatory flow (eddies) of various scales (dependent on a number of factors) (Douglas *et al.* 2005).

In Section 2.5.1.1, the very small dimensions of microfluidic channels were identified as being an aid to the maintenance of laminar flow conditions across a range of inflow rates. For larger scale minifluidic flow cells however, the control of laminar flow conditions is less clear cut. This is ultimately because the development of either laminar or turbulent flow conditions within a flow cell system is dependent upon the relationship between viscous and inertial forces. The ratio between these two forces is neatly described by a dimensionless number known as the Reynolds Number (Re , Eq. 2-8)(Douglas *et al.* 2005):

$$Re = \frac{\rho U d}{\mu} \quad (\text{Eq. 2-8})$$

where U is the mean velocity within the flow cell, d is a characteristic length scale (e.g. the mean width of the cell), and ρ and μ are the fluid density and viscosity respectively. For flow within pipes, Re values of less than ~ 2000 are typically assumed to be laminar (Douglas *et al.* 2005). It is clear from equation 2-8 therefore that, for a given inflow rate, the size of the flow channel can have a significant bearing itself upon determining whether flow will be laminar or turbulent within a flow cell system.

At wall boundaries, such as the sides of a straight flow channel, the flow velocity will be equal to the velocity of the boundary (typically zero). The velocity distribution curve for laminar flow within a channel will be expected to resemble that presented in Figure 2-16. At very low Reynolds numbers (<1), typically at very low velocities and/or for very viscous fluids, inertial forces will be negligible and viscous forces will dominate. This type of flow is termed *creeping flow*, or *Stoke's flow*.

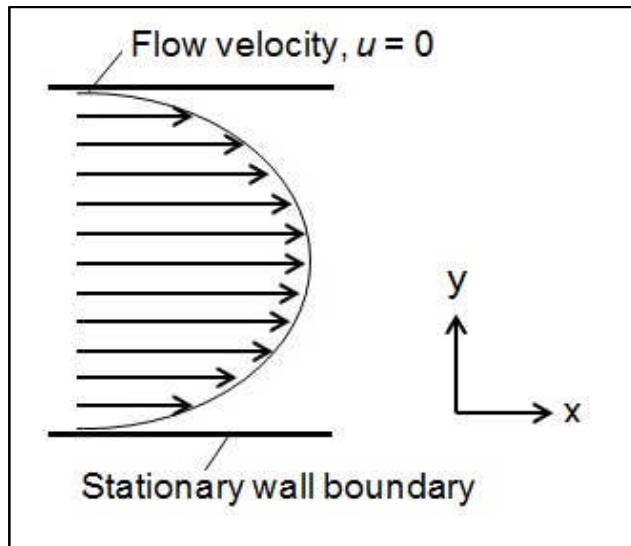


Figure 2-16 Velocity distribution curve for laminar channel flow. Relative flow velocity is represented by the length of each streamline (arrow). Figure developed by author with reference to Douglas *et al.* (2005).

2.5.2.2 Channel flow geometry and eddy development

As discussed in Section 2.5.2.1, areas of reversed fluid motion (eddies) are a typical factor associated with the development of turbulent flow conditions at sufficiently high Reynolds numbers. However, under certain circumstances eddies may also become a feature of laminar flow i.e. the presence of eddies is not necessarily in itself an indicator of a transition to turbulent flow conditions. Moffatt (1964) demonstrated that for viscous (laminar) flow contained by wall boundaries featuring a sharp corner, a series of eddies develop. The eddies increase in size (roughly proportionally) with distance from the corner (Figure 2-17). For the purposes of this study, this type of eddy development will be referred to as *corner eddies*. It should be noted however that corner eddy development was limited by corner angle, and no eddies were observed at corner angles $>146^\circ$.

Also relevant to flow cell design are a number of studies that considered the separation of flow within a flow channel featuring a channel expansion. In fluid dynamics literature, common studies are those which feature 'flow over a backward step', which essentially represents the same geometrical transition as the expanding flow channel. Hence, these studies are relevant here. Biswas *et al.* (2004) describe the evolution of the corner eddies described by Moffatt (1964) into regions of recirculation, associated with

separation of flow within the flow channel (Figure 2-18). The regions of recirculation develop once the series of eddies has reached the height of the channel expansion through an increase in Re . As well as continuing to increase in size with further increases in Re , these regions of recirculation also increase in size with an increase in channel expansion ratio (i.e. the ratio H/h , Figure 2-18).

Other studies have considered different aspects of this type of flow structure. Barkley *et al.* (2002) for example identified some three dimensional instability at high Reynolds numbers ($>Re$ 750) associated with the regions of recirculation for a sudden expansion channel of expansion ratio 2:1. Mizushima and Shiotani (2001) meanwhile implicitly considered a flow channel with both a sudden expansion, and a subsequent identical contraction through computational modelling. As with the other studies

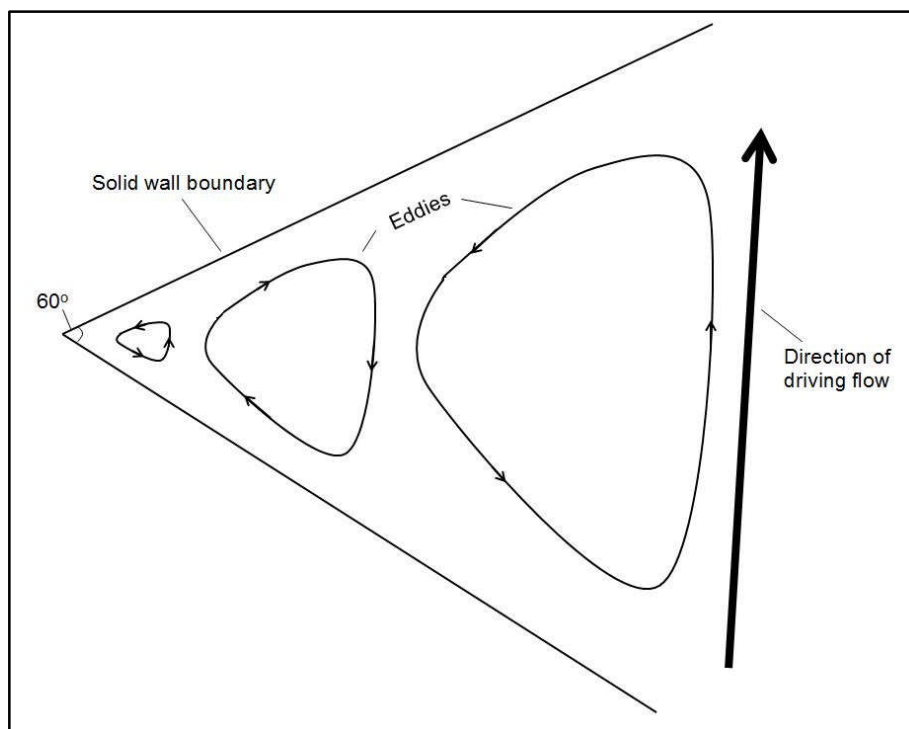


Figure 2-17 Schematic diagram of eddy development within a 60° corner formed by solid wall boundaries. The increase in eddy size is roughly proportional. Figure re-drawn and modified from Moffatt (1964).

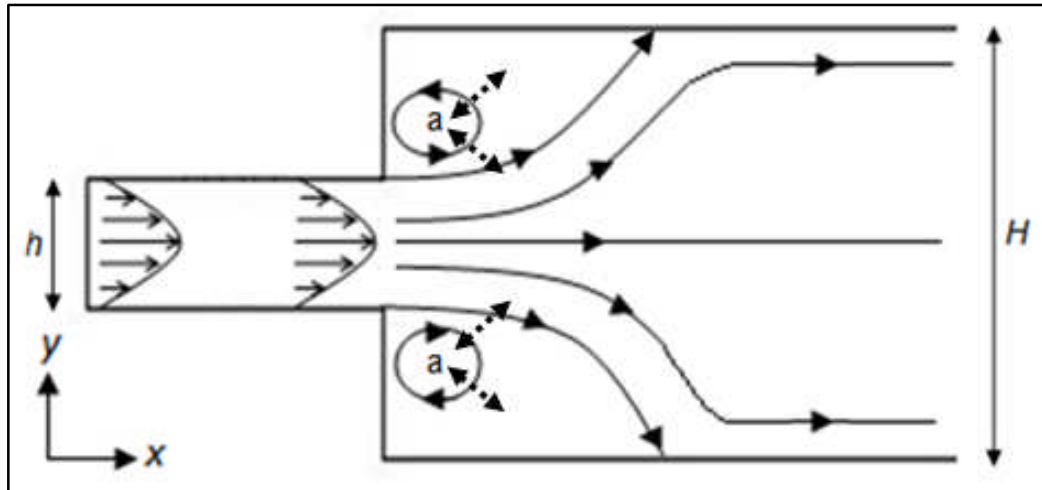


Figure 2-18 Schematic plan view of laminar flow in an open channel with a sudden expansion in width from h to H . Regions of recirculation (a) have developed in the region of channel expansion. Solid arrows indicate advective flow pattern from the inlet to the outlet. Analyte transport from within developed eddies occurs only through diffusion, as indicated by broken-line arrows. Figure re-drawn and modified from Acrivos and Schrader (1982).

mentioned, the development of regions of recirculation was observed. Once again, the size of these regions was related to the Reynolds number. Additionally, the determination of whether regions of recirculation either side of the central channel high-velocity flow (as shown in Figure 2-18) demonstrated geometrical symmetry was also related to the Reynolds number associated with the flow conditions.

All of the studies referenced above considered a flow channel that featured only a sudden expansion. That is, a narrow rectangular entrance channel expanding to a larger square or rectangular channel (and then a subsequent identical contraction in some studies). Perhaps surprisingly, the explicit consideration of variation in minifluidic flow channel geometry is absent within the published literature. A small number of studies were identified that focussed on the control of fluids using geometry variation for smaller scale microfluidic systems. These typically vary geometry by adding grooved structures to the microchannel base to promote and control fluid mixing (Stone *et al.* 2004; Cantu-Perez *et al.* 2010). These do not however provide any useful information with regards to the relationship between sensor/biosensor equilibration and flow cell geometry for minifluidic systems.

Finally, from examination of the literature as outlined above an observation/prediction can be made with respect to the development of eddies within laminar flow cell channels, and the influence of flow cell geometry. That is, where the geometry features a 'corner' of a sufficiently acute angle (estimated to be $<146^\circ$ by Moffatt (1964)) a series of eddies will always be present within the flow domain regardless of the flow rate, and this series will develop into larger 'regions of recirculation' at sufficiently high Reynolds numbers. However, for smoother geometries (i.e. those not including distinct 'corners' or those featuring corners of an angle $>146^\circ$) it can be expected that the development of eddies will not occur at lower Reynolds numbers. But, separation of flow will occur at a critical point determined by the flow rate (and therefore the Reynolds number) which will lead to the commencement of eddy development.

2.6 Flow analysis techniques

The previous sub-chapter (Section 2.5) established a knowledge gap within the published literature relating to the application of fluid mechanics principles to the design of flow cells for sensor/biosensor integration. In particular, no studies were identified that explicitly and systematically considered the relationship between flow cell geometry and biosensor performance.

Therefore, to enable such a study to be conducted as part of this project, it is first necessary to examine the literature for techniques relating to channel flow analysis. This sub-section examines literature and provides background information in relation to the two most common types of investigative techniques, computational modelling (Section 2.6.1) and laboratory-based methods (Section 2.6.2).

2.6.1 Investigative methods - numerical modelling

Numerical modelling is a term that describes the use of mathematical approaches for modelling the behaviour of a real world system. This can include the use of a computer, or network of computers, to run mathematical models. This approach may utilise visualisation of the simulations, although this is not necessarily a required outcome for a successful model. Numerical/computational models are utilised in a wide range of scientific fields of study such as medical applications (e.g. Korhonen *et al.* 2013), cognitive science (e.g. Roy and Pentland 2002), and sociological studies (e.g. Macy and Skvoretz 1998). This sub-section will focus solely upon computational models applied to the analysis of fluid flow phenomena.

The application of fluid mechanics mathematical principles for the analysis of fluid flows using computational hardware is termed Computational Fluid Dynamics (CFD). The use of CFD techniques is now the most common approach to analysing fluid flow problems, with rapid development of CFD methods and applications being associated with the parallel development of high-speed computing power (Douglas *et al.* 2005).

In broad terms, a number of key elements set within three primary components are identified for a CFD model developed for the analysis of flow cell fluid flow (Douglas *et al.* 2005; Zienkiewicz *et al.* 2005):

a) **Pre-Processor**

Main elements of a CFD pre-processor:

- *Geometric Model*

3D geometric representation of the flow cell dimensions, including inlet and outlet ports.

- *Physical Model(s)*

This aspect of the numerical model relates the real world flow phenomena to be modelled to one or more physical processes through a suite of parameter settings and governing equations. Although these physical processes can be constructed from scratch by the user, commercially available CFD program software is used in most cases (e.g. Comsol Multiphysics, Ansys Fluent).

A selection of physical models is typically available within commercial CFD codes, and the user should make a choice that best fits the phenomena they are modelling. For example, the Comsol Multiphysics CFD package (version 4.3a) provides both a 'laminar flow' physical model and a 'transport of diluted species' physical model. These could be utilised and tailored for the modelling of the flow channel laminar flow field and the analyte concentration distribution within the channel respectively (Comsol 2012).

Within the physical models, through the laminar flow model for Comsol Multiphysics for example, fluid will also be defined as compressible (typically gases) or incompressible. Although all fluids are compressible to some extent, steady liquid flows are typically assumed to be incompressible within CFD models, providing any fluid density changes are demonstrably small (Douglas *et al.* 2005).

- *Boundary and Initial Conditions*

Selection of appropriate and well defined boundary conditions is one of the most important elements of a CFD model. The major boundary conditions to be defined are (Versteeg and Malalasekera 2007):

- **Inlet** – Typically, inlet fluid velocity is specified although fluid pressure, mass inflow or normal stress may also be used.
- **Outlet** – The most commonly used outlet condition is a fluid pressure condition (e.g. zero pressure). However, velocity, mass inflow or normal stress may also be used.
- **Wall** – For a flow cell channel the wall boundary is used throughout the solid perimeter of the flow channel, and for the confining base and top solid surfaces. Most commonly, a ‘no slip’ condition is prescribed for all wall boundaries. This sets the fluid velocity normal to the velocity of the wall boundary as zero, and the tangential fluid velocity as equal to the wall boundary (which for a stationary flow cell solid boundary will also be zero). Other boundary conditions may be prescribed if applicable to the real world flow setup being modelled e.g. moving wall, leaking wall.

For the inlet and outlet boundary conditions, the selected condition variable (e.g. velocity) may be defined in different ways. Firstly, the variable may be implicitly prescribed through a set value. This is termed a ‘fixed’ or ‘Dirichlet’ boundary condition. Alternatively, the variable may be defined as a gradient normal to the boundary, specifying the rate of change of the variable value across the border. This is termed a ‘Neumann’ boundary condition.

- *Mesh/Grid Definition*

The mesh or grid* of a CFD model divides the model geometry into a framework of cells or elements. Typically, one of three types of mesh will be developed (Ferziger and Perić 2002):

1) Structured mesh

A uniform and regularly ordered mesh is developed through the discretisation process, such that all of the points (nodes) within the framework are connected in a regular manner. This means that any given point within the mesh can be easily identified and accessed with respect to the points directly neighbouring it. The resultant mesh is usually formed of quadrilateral cells for 2D models and hexahedra for 3D models.

2) Unstructured mesh

Conversely, the unstructured mesh type is not constrained by any specific structural rules; cell shapes are not limited to quadrilaterals or hexahedra for most unstructured solvers. This lack of defined structure however means that there is not necessarily any direct relationship, in computing memory terms, between a given point in the mesh and the points neighbouring it

3) Hybrid mesh

A hybrid mesh is a combination of structured and unstructured meshes. Those parts of the modelled geometry that are regular can be captured by structured meshes and those that are complex can have unstructured meshes.

The main advantages of using a structured instead of an unstructured mesh is that structured meshes are typically faster at solving governing equations. However, unstructured meshes typically provide greater flexibility because of the wider range of cell shapes that are usually permitted.

As part of the CFD model's pre-processor, the mesh element size distribution and quantity will usually be defined. Also, a mesh dependency exercise will typically be conducted to identify the optimum mesh element size and/or quantity with respect to computational accuracy and computational power efficiency.

**Note that the terms grid and mesh are commonly used interchangeably in the literature. In this thesis the term 'mesh' will be used from this point*

forward to describe the framework of cells/elements applied to the model geometry.

b) Solver

The solver of a CFD model discretizes governing partial differential equations. One of a number of different methods is employed to perform the discretization process, and to apply the discretization process to one of the mesh types described above. The three most commonly used methods are described in simple overview terms here:

- Finite Difference Method (FDM)

This is the oldest method for the numerical solution of partial differential equations. Finite difference methods (FDM) are numerical methods for approximating the solutions to differential equations using finite difference equations to approximate derivatives. Finite difference methods are typically applied only to structured meshes, upon which the FDM is very simple and effective, and can provide higher-order scheme solutions. A disadvantage of FDM is that it can be difficult to ensure that conservation (e.g. of mass, energy) is enforced. Also the use of structured meshes leads to a restriction of model geometry, which is a significant disadvantage in complex flows (Ferziger and Perić 2002; Douglas *et al.* 2005).

- Finite Volume Method (FVM)

The finite volume method (FVM) uses the integral form of governing equations as its starting point. The solution domain is subdivided into a finite number of contiguous control volumes (CV), and the governing equations are applied to each CV. The FVM can accommodate any type of mesh (i.e. structured, unstructured), so it is more suitable for complex geometries than the FDM. The main disadvantage of FVM compared to FDM is that methods of order higher than second are more difficult to develop, particularly for 3D models (Ferziger and Perić 2002; Douglas *et al.* 2005; Versteeg and Malalasekera 2007).

- *Finite element method (FEM)*

The FEM is similar to the FVM in many ways. The domain is divided into a set of discrete volume or finite elements that are generally unstructured. For 2D models the elements are usually triangles or quadrilaterals, whilst for 3D models tetrahedral or hexahedra are most often used. An important advantage of finite element methods is the ability to deal with arbitrary geometries. Also it is relatively easy to obtain a higher-order scheme on structured or unstructured meshes, than for the finite volume method (Ferziger and Perić 2002; Douglas *et al.* 2005; Mukhopadhyay 2005).

c) Post-processor

The post-processor of a CFD model provides a number of tools with which to analyse the computed solutions (e.g. velocity, concentration) for either the entire meshed geometry, or sections of it. Visualisation and other post-processing procedures are used, including (Douglas *et al.* 2005):

- Velocity streamline plots
- Velocity arrow plots (proportional or normalised)
- Particle tracking
- Concentration contours (e.g. for dilute species transport models)
- Volume, surface or line integration
- Flow simulation animations

The Comsol Multiphysics program, mentioned in (a) above, utilises the finite element method of mesh discretization, and this was the program chosen for the computational investigations conducted as part of this study (Chapter 3). This decision was based on the following factors:

- Clear user interface, particularly with respect to model geometry development
- Integrated pre-processor, solver and post-processor, therefore there is no requirement to utilise separate computer programs to develop and run models

- Unstructured mesh allows for variation of different model geometries, including complex shapes
- The potential for high computational power and memory needs of the FEM program was a potential drawback, but access to high performance computing was available should this prove to be a necessity.

2.6.2 Investigative methods - laboratory techniques

Although the computational fluid dynamics approach to fluid flow analysis provides a convenient investigative tool, laboratory-based investigative methods are also important. In particular, laboratory investigations provide a means of developing a validation feedback process for the numerical model(s).

2.6.2.1 Summary of laboratory flow visualisation analysis techniques

To enable the analysis of fluid flow patterns through laboratory-based techniques, a method of flow visualisation is typically used. For liquid fluid flow investigations, two main method categories are identified (Merzkirch 1987; Post and Van Walsum 1993):

a) Particle tracer methods

This method is based upon the assumption that small solid particles added to the flow will follow fluid streamlines; therefore particle density is an important factor when considering the appropriate particles to use. The visualisation process is typically achieved by illuminating the flow domain to highlight the particles, assuming that there is sufficient colour contrast between the particles and the fluid. The flow visualisation is captured via computer imaging software via a camera or camera-microscope setup. Aside from providing a visualisation of flow patterns, this approach can be applied to techniques such as particle velocimetry to characterise flow velocity (Buzzaccaro *et al.* 2013).

b) Optical methods

Optical methods of flow visualisation utilise the luminescence and light refraction properties of the fluid under analysis, or of solutions added to the fluid. Common approaches include:

- **Flow fluorescence**

The luminescence properties of fluorescent dyes mixing with a non-fluorescent fluid are exploited for the imaging of flow and mixing patterns using video image capture. The fluorescence is controlled through illumination with lasers or other light sources (this subject is considered in greater detail in Section 2.6.2.2).

- **Shadowgraphs**

Temporal variations in density, caused by flow features, are expressed as changes in the light refraction index of a fluid. The resultant shadowgraphs (light and dark areas corresponding to variations in density) are captured on a photographic film in response to the passing of a parallel light source through the flowing fluid (Post and Van Walsum 1993).

- **Interferometry**

Interferometry flow visualisation also utilises density variations in flowing fluids. However, measurement is obtained by using phase shift to calculate refractive indexes, rather than measuring the refractive index directly. This is achieved by splitting a laser beam, into a main and reference beam. The main beam is passed through the flowing fluid and the reference is used to measure the phase shift (Brownlee *et al.* 2011).

2.6.2.2 *Flow fluorescence*

The flow fluorescence optical technique is selected as the most practical for use in laboratory based flow visualisation methods to be employed in this study. Therefore it is important to briefly consider this method in some further detail, particularly with respect to those considerations which may affect accuracy of data obtained through the method.

Firstly, the main components required to make fluorescence-based measurements are:

- **Fluorescent dye** – commonly used dyes include fluorescein, rhodamine and cyanine.
- **Illumination source** - e.g. lasers, mercury lamp. The choice of illumination source should be made to ensure that the light wavelength spectra of the source is appropriate to the excitation wavelength range of the fluorescent dye being used (see 'excitation bandpass filter' below). Specifically, consideration needs to be given to the relative output strength of the illumination source within the excitation spectra of the dye.
- **Excitation bandpass filter** – Each different dye will have a specified wavelength range at which excitation of the fluorescent molecules occurs, consisting of a peak excitation wavelength and a wavelength range either side of the peak (e.g. 494nm peak excitation for fluorescein). A filter restricts the transmission of light to a narrow range of wavelengths appropriate to the excitation spectra of the fluorescent dye being used. This filter is placed between the light source and the fluorescent target.
- **Fluorescent target** – the target for which the fluorescence method is being used e.g. fluid solution containing fluorescent dye for flow visualisation experiments, fluorescently labelled molecules (e.g. proteins, antibodies, and amino acids) for microscopy studies.
- **Emission bandpass filter** – Excitation of the fluorescent molecules leads to emission of light at a specific wavelength range (e.g. ~520nm peak emission for fluorescein, in the yellow-green part of the electromagnetic spectrum). This filter limits the transmission of light to a narrow range of wavelengths appropriate to the emission spectra of the fluorescent dye being used. This filter is placed between the fluorescent target and the measurement medium.

- **Measurement medium** – Fluorescence can be measured directly with a purpose-specific device, a fluorometer. Alternatively camera-microscope imaging can be used and fluorescence analysed via a combination of image capture and programming computer software (e.g. LabVIEW and Matlab respectively). The latter is more appropriate for flow visualisation, as it allows for analysis of spatial fluorescence variations with time (within a flow cell for example).

The basic relationship between the excitation of a fluorescent dye, such as fluorescein or rhodamine, and the fluorescent dye solution concentration is described by equation 2-9 (Crimaldi 2008):

$$F \propto \frac{I}{1+I/I_{sat}} C \quad (2-9)$$

where F is fluorescence (fluorescent intensity), I is the intensity of the excitation light source, I_{sat} is the excitation light source intensity at which fluorescence saturation occurs, and C is the concentration of the fluorescent dye. Fluorescence saturation occurs when all fluorophore molecules in the path of the light source are excited, and F becomes independent of I (Walker 1987). In cases where $I \ll I_{sat}$ equation 2-9 can be simplified to equation 2-10 (Crimaldi 2008):

$$F \propto IC \quad (2-10)$$

However, this relationship typically only holds true for low concentrations of the fluorescent dyes mentioned above (and many others). When conducting a flow fluorescence investigation it is therefore necessary to establish the range of concentrations for which fluorescent intensity is proportional to the fluorescent dye concentration (for a given light source intensity below I_{sat}).

There are two additional factors which can influence accuracy and reliability for flow fluorescence investigations:

a) *pH Dependency*

The impact of solution pH upon fluorescence intensity for fluorescent dyes such as fluorescein is well established (Martin and Lindqvist 1975; Diehl and

Markuszewski 1989; Mota *et al.* 1991; Zhu *et al.* 2005). The relationship between pH and fluorescent intensity for the fluorescent dye fluorescein, as determined by Diehl and Markuszewski (1989), is presented in Figure 2-19. In that study fluorescent intensity was effectively zero below pH 3, reached a maximum intensity at around pH 8, and remained consistent at > pH 8. Similar results were presented by Zhu *et al.* (2005), although the pH level corresponding to maximum fluorescent intensity ranged from ~pH 7.5 to ~pH 9.0. Also, Zhu *et al.* (2005) identified a minor relationship between fluorescein concentration and the pH level corresponding to maximum fluorescent intensity.

b) *Photobleaching and fluorophore decay*

Photobleaching describes the process of fluorophore molecule destruction in response to excitation via an illumination source (Saylor 1995). Individual fluorophore molecules are photochemically destroyed, and the photobleaching effect describes the cumulative effect of multiple destructions over time.

Photobleaching is distinct from the process of *fluorophore decay* for which the fluorescent properties of the fluorophore molecules deteriorate over time, largely independent from the light source illumination intensity. The photobleaching process however is directly related to light source intensity. For a mercury arc lamp, photobleaching effects are typically measured on the scale of seconds to minutes, whilst for laser light sources photobleaching processes are usually observed at the microsecond scale (Song *et al.* 1995). Therefore, light source selection and luminescent intensity regulation are potential methods of controlling or limiting photobleaching effects for flow fluorescent experiments.

Cont'd over...

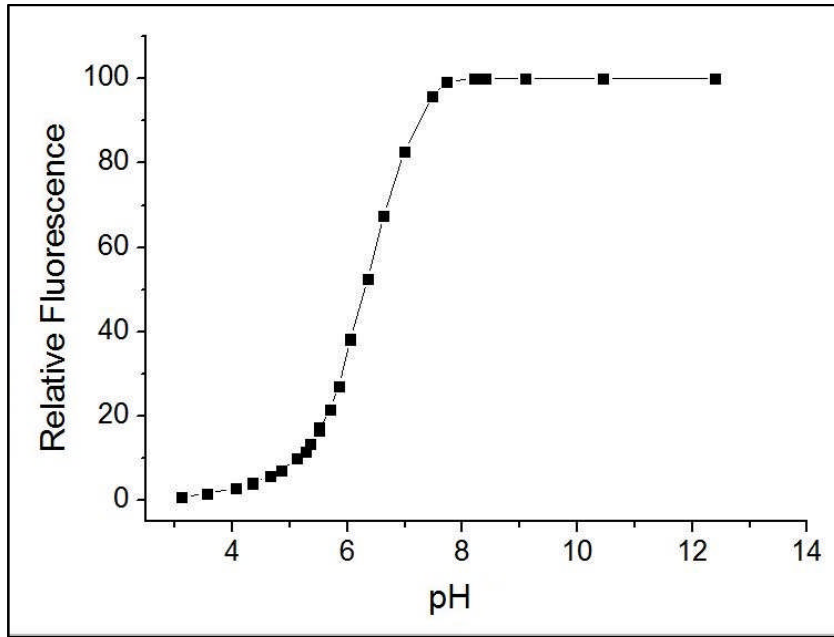


Figure 2-19 Fluorescent intensity of fluorescein as a function of pH. Data is normalised with respect to maximum fluorescent intensity at pH 8. Re-drawn from data presented by Diehl and Markuszewski (1989). The concentration of fluorescein used for this study was 6 μ M.

2.7 Chapter summary

2.7.1 Project background

A legacy of land and water contaminated through the activities associated with industries related to nuclear energy and weapons development and operation still exists today. Aqueous uranium (uranyl) is one of the contaminants associated with this legacy, particularly associated with uranium mining and milling for nuclear power and weapons use. Contaminated land and water resources therefore provide a continuing risk to human health and the environment.

Traditional contamination monitoring approaches required the labour intensive collection of samples and subsequent laboratory testing and analysis. More recently, methodologies have been developed for the real-time monitoring of potentially contaminated water resources in particular (e.g. rivers, lakes, and groundwater). These include wireless sensor network systems, and automated water sampling systems. Such systems for the accurate and timely monitoring of target contaminants are much sought after by industries and government bodies tasked with the monitoring and remediation of contaminated sites. They offer a potentially cost effective and readily manageable monitoring system with respect to the migration of contamination plumes, and the effectiveness of remediation strategies.

Biosensors are identified as a cost effective method of analyte detection. Much biosensor development work is related to applications in medical diagnostics, but examples of biosensors for environmental contaminant detection can also be found. Specifically, Conroy *et al.* (2010) developed a biosensor for aqueous uranyl ions (UO_2^{2+}). However, this biosensor was established as a laboratory proof-of-concept only, and the development of a robust and optimised deployment method is required to establish a transition to the sensor's practical use in real-world monitoring situations.

2.7.2 Implications for current research investigations

2.7.2.1 Cross-disciplinary research

From a skills development point of view for the researcher employed on this study (i.e. the author), knowledge and skills development areas were identified that cross disciplinary boundaries:

- Biosensor construction techniques
- Biosensor operational theory
- Electrochemical analysis techniques and theory
- Fluid delivery system design principles
- Channel flow theory and principles
- Fluid flow investigative and analysis techniques

2.7.2.2 Identifying the knowledge gap

The most significant knowledge gap identified through this literature review and background study relates to the design of minifluidic (i.e. at the ~mm scale) flow cell devices for the deployment of biosensors. Specifically, no previous studies were identified which systematically investigated the impact of flow cell geometry on the analyte concentration in the active region of a biosensor cell. Additionally, whilst the proof-of-concept work for the uranyl biosensor by Conroy established a working sensor under laboratory conditions, no investigations were conducted into the operation of the biosensor under conditions applicable to potential real world contaminant monitoring deployment. Also, issues such as biosensor reusability within a deployment system were not explicitly investigated as part of the proof-of-concept work for the sensor.

In summary therefore, two main elements are identified for the investigations that will contribute and/or supplement existing scientific knowledge:

- 1) The development of an optimised channel flow cell design and operational protocol for biosensor integration.
- 2) A clear assessment of the factors and challenges associated with the flow cell integration and repeatable deployment and operation of robust biosensors.

Furthermore, these two elements should be viewed as contributions to a potentially continuous strand of research, the aim of which is the development of a modular automated remotely controlled water monitoring system (see conceptual model presented in Section 1.4).

CHAPTER 3

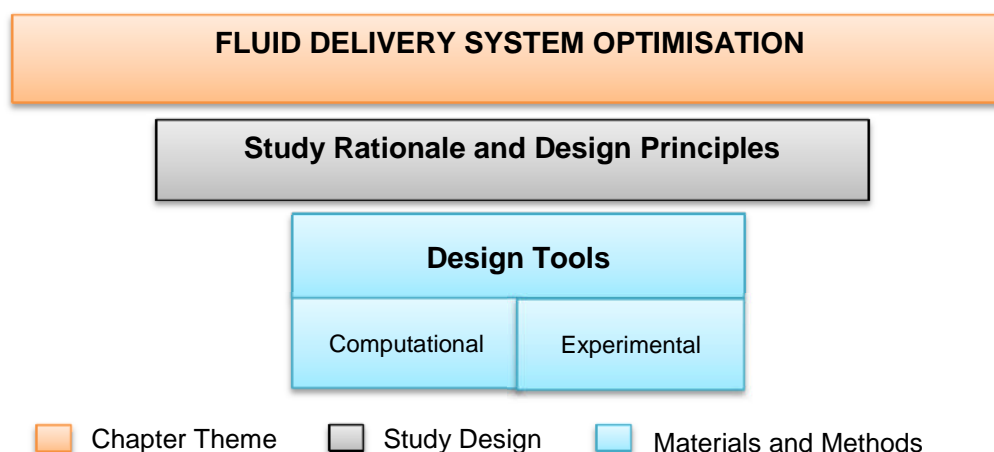
Flow cell design for effective
biosensing – investigation
design

Chapter 3 **Flow cell design for effective biosensing – investigation design**

3.1 Chapter introduction

Chapters 3 and 4 describe the rationale, methodology and investigation results with respect to the development and optimisation of a fluid delivery system for the uranyl biosensor described in Section 2.4.3. This chapter specifically considers the development of a study and process design rationale, and fluid delivery system design principles, that would underpin the study objectives presented in Section 1.2 (3.2.1 and 3.2.2). This rationale then informed the development of an optimisation investigative process for the fluid delivery system, outlined in Section 3.2.3. Finally, a guiding investigative strategy is presented for the fluid delivery system optimisation process (Section 3.2.4).

Chapter Outline Map



3.2 Fluid delivery system optimisation process

3.2.1 Optimisation process design

3.2.1.1 Rationale for study

The traditional laboratory 3-electrode electrochemical cell set up utilised by Conroy (2012) for the development of the uranyl biosensors is not readily amenable to field deployment of biosensors (Section 2.4.3), particularly with respect to ultimate integration into an automated and remotely controlled monitoring system.

Although an initial investigation into the use of screen-printed electrodes for biosensor construction by Conroy (2012) was deemed to be unsuccessful (Section 2.4.3), the application of screen-printed electrodes for this purpose remains a compact and complete electrochemical unit ideally suited for incorporation into a fluid delivery device. Therefore it is justified that screen-printed electrodes were considered for further investigation as part of this project. A commercially available flow cell produced specifically to incorporate screen-printed electrodes (Figure 2-13), was purchased from Dropsens (Oveido, Spain) for this purpose.

However, the outcome of preliminary flow tests on the commercial flow cell indicated the prevalence of low or static flow zones ('dead zones') in this type of flow cell at low flow rates (e.g. 1-2 mL min⁻¹). This, combined with the outcome of the literature review relating to flow cell design (Section 2.7), contributed to the determination that the investigation of biosensor integration with respect solely to the commercially sourced flow cell type was not sufficient.

Therefore, a study was developed that would consider the influence of flow domain geometry and flow conditions upon flow cell efficiency within a flow channel type flow cell (Figure 2-14C). The aim of the study was therefore to develop an optimised protocol for the design and operation of a flow cell for the purposes of biosensor deployment. The study would also be designed to enable flow efficiency comparison between a bespoke flow cell to be developed for the study, and the commercially sourced Dropsens flow cell.

3.2.1.2 Optimisation process design strategy

The starting point for the design of an optimisation process for the biosensor deployment fluid delivery system (flow cell) was identification of the key principles applicable to flow cell design (Section 3.2.2). With consideration of these principles, tools were identified that would enable investigation of the influence of flow channel geometry and flow conditions upon flow cell performance (Section 3.2.3). A dual approach of computational modelling and laboratory-based optical flow experimentation was used, as this would provide an in-built comparative validation process to the study and therefore ensure a robust approach to the development of an operational flow-biosensor protocol.

The computational modelling tool would allow for the development of flow simulations and, once models were developed, would therefore provide a flexible tool enabling manipulation of flow channel geometry and flow control parameters. The experimental tool would provide not only a validation method for the numerical models, but would itself provide data that would practically and theoretically inform flow cell design. Following selection of appropriate investigative tools, a bespoke flow cell for use in the experimental investigation was designed and suitable computational fluid dynamics software was selected for use in for the computational modelling (Section 3.2.3).

The approach to developing an investigation procedure for this study was to identify an overall strategy that could be applied to results created using both the computational tool, and the experimental method. The outline optimisation process developed is presented in Figure 3-1.

Cont'd over....

Fluid Delivery System Optimisation Process

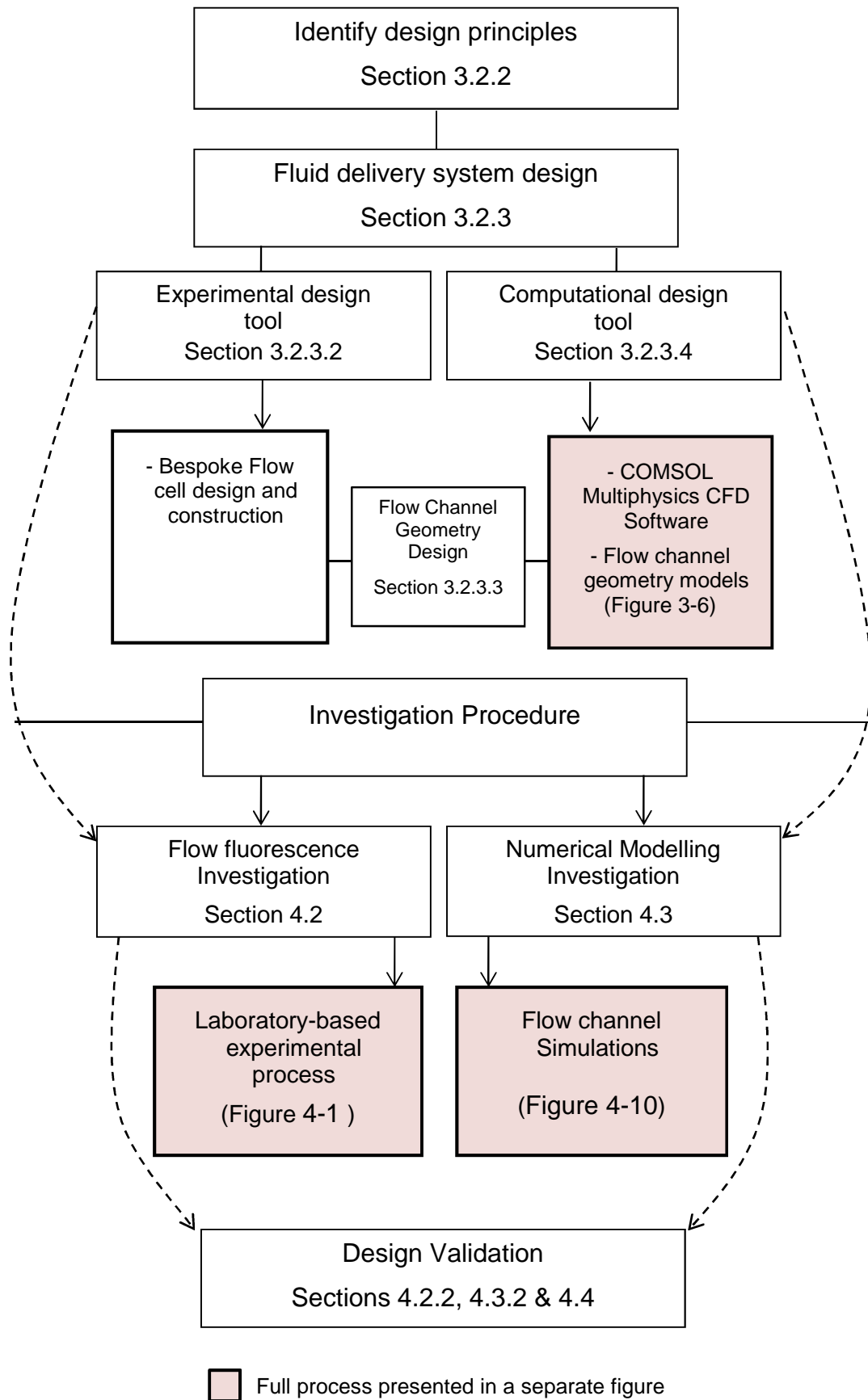


Figure 3-1 Fluid delivery system optimisation process outline

3.2.2 Fluid delivery system design principles

The key design principles and operational requirements for the fluid delivery system were defined within two distinct categories: a) the design, structure and analytical process requirements of the uranyl biosensor and b) the operational requirements for a biosensor system deployed within an automated and remotely controlled water monitoring system.

Biosensor design, structure and analytical process considerations:

- Impedance-based uranyl biosensor requiring integration with an analytical instrument permitting impedance measurements (e.g. potentiostat).
- Biosensor to be constructed upon a transducer surface (e.g. screen-printed gold electrodes) requiring integration into the fluid delivery system.
- Aqueous measurement sample to be delivered to the biosensor surface.
- A period of equilibration of analyte within the flow domain with the active element of the biosensor (e.g. 20-30 minutes for the uranyl biosensor) prior to making an electrochemical measurement.

Operational requirements for biosensor deployment within remote monitoring system:

- Compatibility with remotely operated flow control systems.
- Optimisation of the fluid delivery system with respect to understanding and therefore controlling the concentration of a target analyte within the flow domain of the fluid delivery system as a known proportion of the analyte concentration as it is delivered into the system inlet.
- Requirement for delivery of buffer solution (e.g. phosphate buffer solution, PBS) to regenerate the biosensor surface (Conroy *et al.* 2010), and for in-situ wet storage of the biosensor within the deployed monitoring system.

- Optimisation of fluid control operations to minimise the volumes of sample and buffer solutions to be stored as waste materials. This would help to minimise the number of routine maintenance visits to the site of the remotely controlled water monitoring system.
- A robust and water-tight construction to withstand repeated use within a field setting.
- Some practical consideration with respect to minimising the need for regular routine maintenance and replacement of fluid delivery system components.
- Some consideration with respect to minimising manufacturing costs, whilst not negatively influencing system performance and accuracy.

3.2.3 Fluid delivery system design

3.2.3.1 Design approach

A parallel approach was employed in the design and development of the fluid delivery system, which incorporated both design tools (experimental and computational). However, for reasons of clarity, the development of each tool is described separately here. The experimental design tool was developed primarily through the construction of a bespoke flow cell (Section 3.2.3.2), whilst the computational tool involved the development of flow channel computational models (Section 3.2.3.4). The development of different flow channel geometries is also described separately (Section 3.2.3.3). The design principles presented in Section 3.2.2 were used as the common basis of design.

3.2.3.2 Experimental design tool

A bespoke flow cell was designed and developed solely for suitability in conducting flow analysis experiments. However, a flow chamber maximum width of 8 mm was determined for the flow cell, such that the circular active area (i.e. the region containing the working, reference and counter electrodes) of a commercially available screen-printed electrode (e.g. Figure 2-9, Section 2.4.4) could ultimately be accommodated. The flow cell would

be later modified to accommodate screen-printed electrodes (and an alternative bespoke electrode), for the development of the integrated uranyl biosensor (Section 5.3).

The flow channel length (L , Figure 3-2) was set at 30 mm between the extremities of the inlet and outlet ports. This allowed for the development of small rectangular flow channels of 1 mm width (h , Figure 3-2) which joined the inlet and outlet ports, positioned either side of an expanded central region of 8 mm maximum height (H , Figure 3-2). This provided a channel expansion ratio (CER) of 8:1. The depth of the flow channel was fixed at 1.5 mm since preliminary experiments demonstrated this to be a lower limit beyond which practical operation (e.g. bubble entrapment, filling) became difficult. Figure 3-2 represents the case of maximum channel expansion (and contraction) rate.

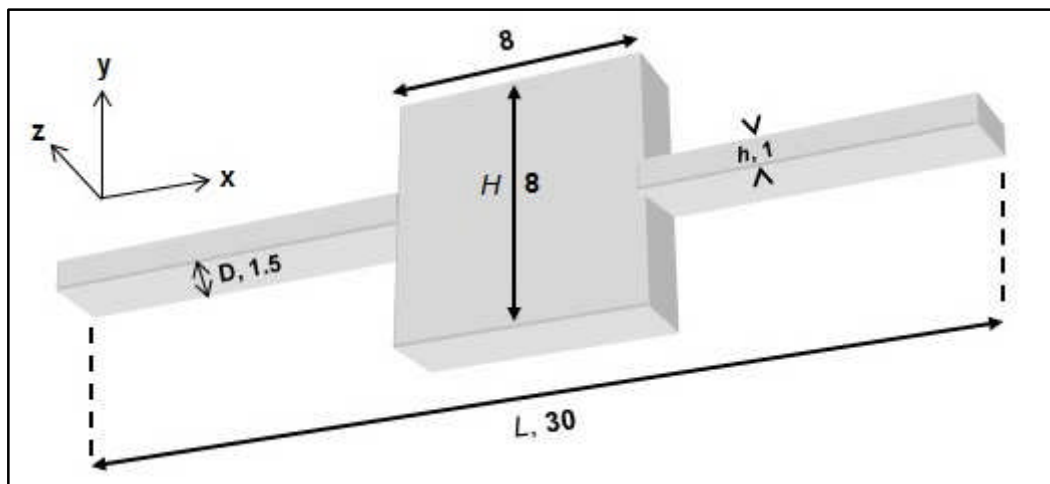


Figure 3-2 3D representation of fundamental flow domain dimensions for experimental flow cell. CER 8:1. All stated measurements in mm.

The experimental flow cell was manufactured from two transparent Polymethylmethacrylate (PMMA, Perspex) blocks of dimensions 60 x 30 x 10 mm with a 1.5 mm thick Polytetrafluoroethylene (PTFE, Teflon) gasket placed between them, into which the flow channel geometry was cut. Six M4 socket hex-cap screws were used to sandwich the PTFE gasket between the two blocks thus creating a seal. Inlet and outlet holes of diameter 1 mm were drilled into the base of the uppermost PMMA block, and counterbored to 6 mm diameter at the top to ultimately accommodate $\frac{1}{4}$ "-28 UNF threaded nuts for the connection of fluidic tubing (Figure 3-3, Figure 3-4).

PMMA was selected as the flow cell body material primarily because a transparent material was required for the fluorescence-based optical flow analysis. Additionally, the transparency of the material also allowed for easy diagnosis of flow cell performance issues such as the development of air bubbles within the flow domain. In comparison to other transparent hard plastics such as polycarbonate (PC), PMMA is less likely to reduce transparency through coloration over time.

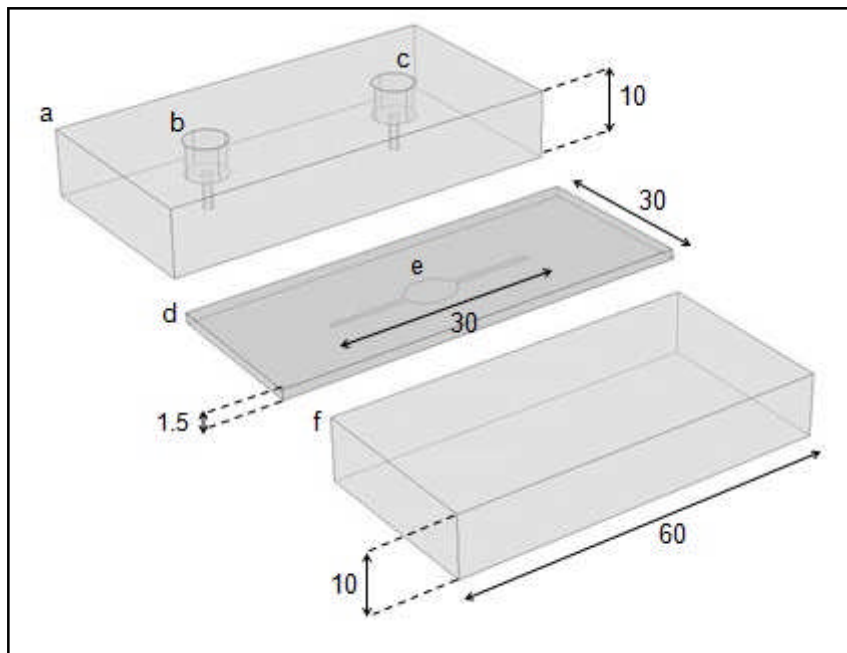


Figure 3-3 Bespoke flow cell construction schematic diagram: a) PMMA top block with b) inlet and c) outlet holes. Inlet and outlet accommodate $\frac{1}{4}$ "-28 threaded nuts at the top and feature 1mm openings at the fluid inlet/outlet point; d) PTFE gasket with e) 30mm cut-out flow domain section; f) PMMA base block. Bolt holes used to secure the flow cell unit are not shown for clarity. All stated measurements in mm.

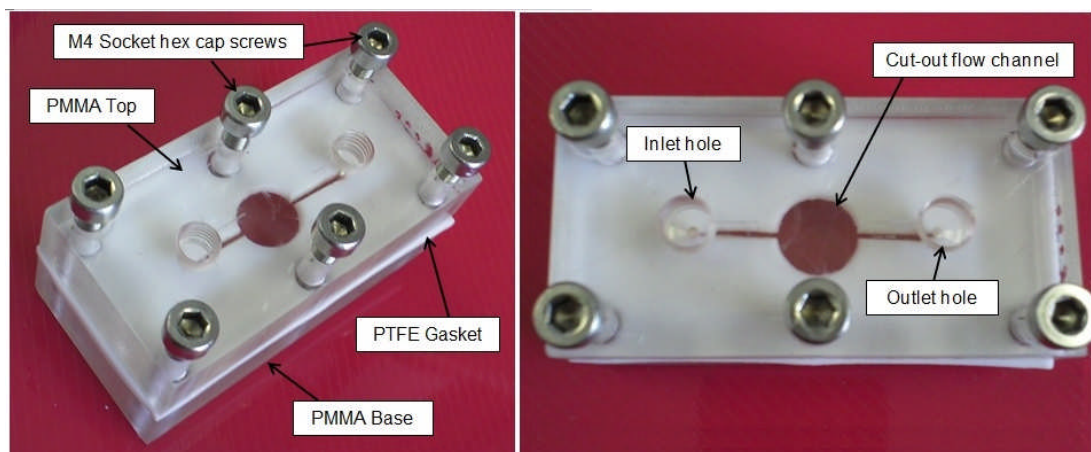


Figure 3-4 Images of bespoke flow cell (experimental design tool)

Polycarbonate does have a marginally higher general chemical resistance than PMMA, but the chemical resistance of the flow cell construction materials does not need to be particularly high. This is because the likelihood of highly corrosive materials in potential natural water samples is low. PMMA however is typically easier to handle and machine than polycarbonate, and usually lower in cost.

The selected material for the flow channel gasket was PTFE (Teflon). PTFE is a relatively soft plastic (at a thickness of 1.5 mm). It is therefore readily amenable to the cutting of flow channel geometries within a rectangular piece cut to the dimensions of the flow cell (Figure 3-3, Figure 3-4). Crucially for the purposes of use as a flow cell gasket, PTFE retains its shape and integrity when loaded but demonstrates enough flexibility to provide a watertight seal for the cell.

Another method for construction of the flow channel was briefly considered. This would have involved cutting the flow channel geometry directly into the hard plastic body of the flow cell (either the top or the base), and achieving a watertight seal with the use of rubber O-rings. This method was discounted for two reasons. Firstly, this approach would require the construction of a number of different flow cell tops (or bases) to enable the study of different flow channel geometries. The use of removable flexible gaskets therefore reduces the cost and ease of manufacture. Secondly, the rubber O-rings could potentially trap small amounts of fluid and soluble material between the ring and the hard body of the flow cell. This could lead to unexpected diffusion of material into the fluid flow between flow cell flushes, and therefore small measurement errors. This would not be an issue with the PTFE gaskets, where the flow channel is cut directly from the plastic.

3.2.3.3 Flow channel geometry design

As mentioned in the previous sub-section, the main practical advantage of using a removable gasket for construction of the flow channel is the ability for easy replacement with flow channels of a different geometry.

The work of Acrivos and Schrader (1982) amongst others showed how regions of recirculation (eddies) can develop within laminar flow in an

expanding channel (Section 2.5.2). The development of eddies affects the efficiency of the flow cell by influencing the relationship between advective flow and diffusion with respect to the equilibration of a target analyte within the flow cell. The aim therefore was to develop a range of different flow channel geometries to investigate the influence of geometry, and flow rate on the development of eddies and ultimately the efficiency of the flow cell.

Specifically, the approach was to consider variations in flow cell geometry that included a variation in the rate of channel expansion (and symmetrical contraction) for a channel with a channel expansion ratio of 8:1. Three different geometries were considered in which the geometry of the central expanded region of the channel was varied. The central region geometries developed were (in cross-section) a square, a circle and a more gradually expanding and contracting geometry (Figure 3-5). The square shape reflected the case of maximum expansion for a channel flow cell, as considered for the studies of 'flow over a backward step' described in Section 2.5.2. This design was expected to be the least efficient of the geometries studied, and therefore represented a 'worst case scenario' against which the performance of the other two geometries could be compared. The volumetric capacity for each of the flow chamber geometries is presented in Table 3-1.

The more gradually expanding channel, termed the iCell due to its similarity to the shape of an eye, was developed from a 3rd order polynomial. One quarter of the profile (Figure 3-5C, dark line) is given by the local x, y coordinate positions (mm) described in equations 3-1 to 3-3:

$$y = (C_1 x^3 + C_2 x^2 + C_3 x + 0.5), (0 \leq x \leq 9) \quad (3-1)$$

where, $C_1 = - (2b/a^3)$ (3-2)

and, $C_2 = (3b/a^2)$ (3-3)

and, $C_3 = 0$

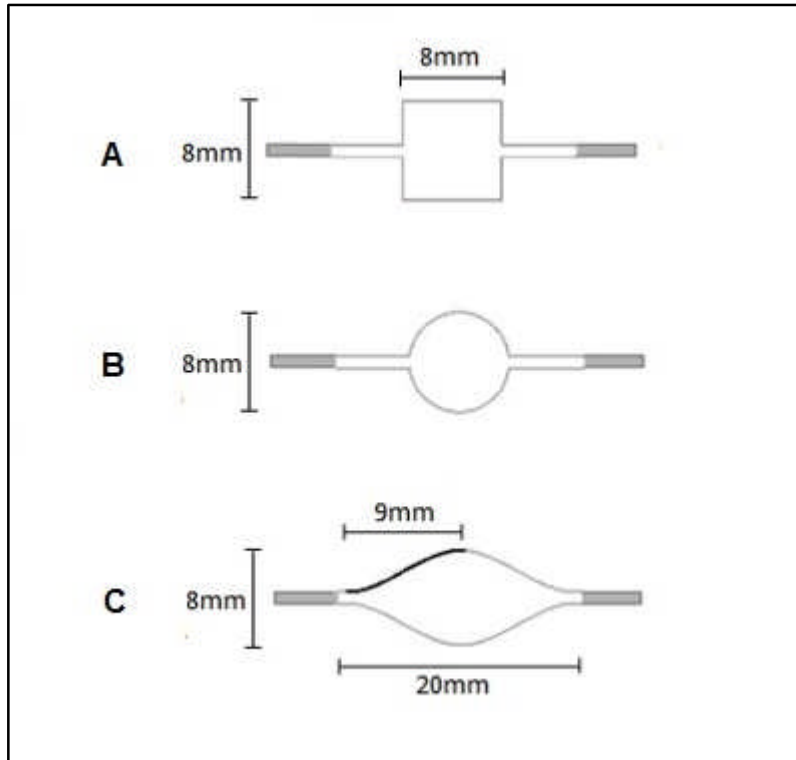


Figure 3-5 Flow channel geometries: **A)** Sudden channel expansion (square central region), **B)** Circular central region, **C)** iCell bespoke channel design.

The polynomial expression was subjected to the size constraints presented in Figure 3-5C, such that $a = 9.0$ mm and $b = 3.5$ mm. This curve was reflected about the vertical ($x = 9$) and horizontal planes ($y = 0$) to give the final geometry of the central part of the flow cell. The geometry of the entire channel was completed by appending 6 mm long channels of 1 mm width at each end of the centrally expanded region. Specific values of C_1 and C_2 used to develop the one-quarter curve are included in Table 3-1.

As described in Section 2.5.2, the Reynolds number (Re) represents the ratio of inertial to viscous forces within a fluid flow, and can be used to predict whether flow will be laminar or turbulent under prevalent conditions. Reynolds numbers were calculated at minimum and maximum channel widths for a flow channel with an expansion ratio of 8:1, and for flow velocities based upon inlet flow rates of 1, 5 and 10 mL min⁻¹ (Table 3-2).

Table 3-1 Volumetric flow chamber capacity for three flow channel geometries, based upon a flow channel depth of 1.5 mm. Plus, component values for iCell development (shown to 6 decimal places).

Central expanded channel Geometry	Volumetric Flow Chamber Capacity (mL)	C ₁ (iCell only)	C ₂ (iCell only)
Square (Figure 3-5, A)	0.096	-	-
Circle (Figure 3-5, B)	0.075	-	-
iCell (Figure 3-5, C)	0.120	-0.010289	0.138889

Table 3-2 Estimated maximum and minimum Reynolds numbers (Re) for flow cell flow channel, at three selected inlet flow rates (converted to bulk linear velocities).

Cell Width min and max (m)	Reynolds number (Re) at three selected bulk linear velocities		
	0.014 m s⁻¹	0.106 m s⁻¹	0.142 m s⁻¹
0.001	17	85	170
0.008	36	179	358

In the field of fluid mechanics, a common assumption is made that the transition from laminar to fluid flow occurs at $Re \sim 2000$ (Douglas *et al.* 2005), for flow within a pipe. Although the geometries considered in this study feature a step change, therefore deviating from simple pipe geometry, there is no published evidence to indicate that a step change would in itself lead to a significant increase in Re and therefore a transition to turbulent conditions. Therefore, because the calculated Reynolds numbers presented in Table 3-2 are significantly lower than 2000, they could safely be considered predictors of laminar flow for the range of flow conditions described.

3.2.3.4 *Computational design tool*

The process outline for developing the computational design tool is summarised in Figure 3-6. The first step in developing a computational design tool was to produce a conceptual framework. This involved the identification of the key requirements of such a tool with respect to the investigation of flow channel design:

- Numerical framework for the simulation and analysis of laminar fluid flow, to model the flow field of aqueous solutions into the bespoke flow cell (simulating flow conditions within which flow can be assumed to be laminar, as discussed in Section 3.2.3.3). Thus, the numerical modelling software would allow for the application of steady-state Navier-Stokes equations for laminar flow.
- Enable the development of 3D models of each of the three flow cell geometries.
- Capability for the simulation of dilute species transport, to model the flow into the wet flow chamber of an aqueous solution containing a target analyte. Thus, the numerical tool would allow for the application of advection-diffusion equations for an incompressible flow.
- Include the specification of flow boundary conditions, such as at flow channel walls, and inlet and outlet conditions.
- Permit the selection and adjustment of key flow conditions and flow parameters, such as flow rate and flow pressure conditions.
- Permit the selection and adjustment of fluid and fluid interaction characteristics to include fluid density, temperature, dynamic viscosity, and diffusion coefficients.

Computational Design Tool

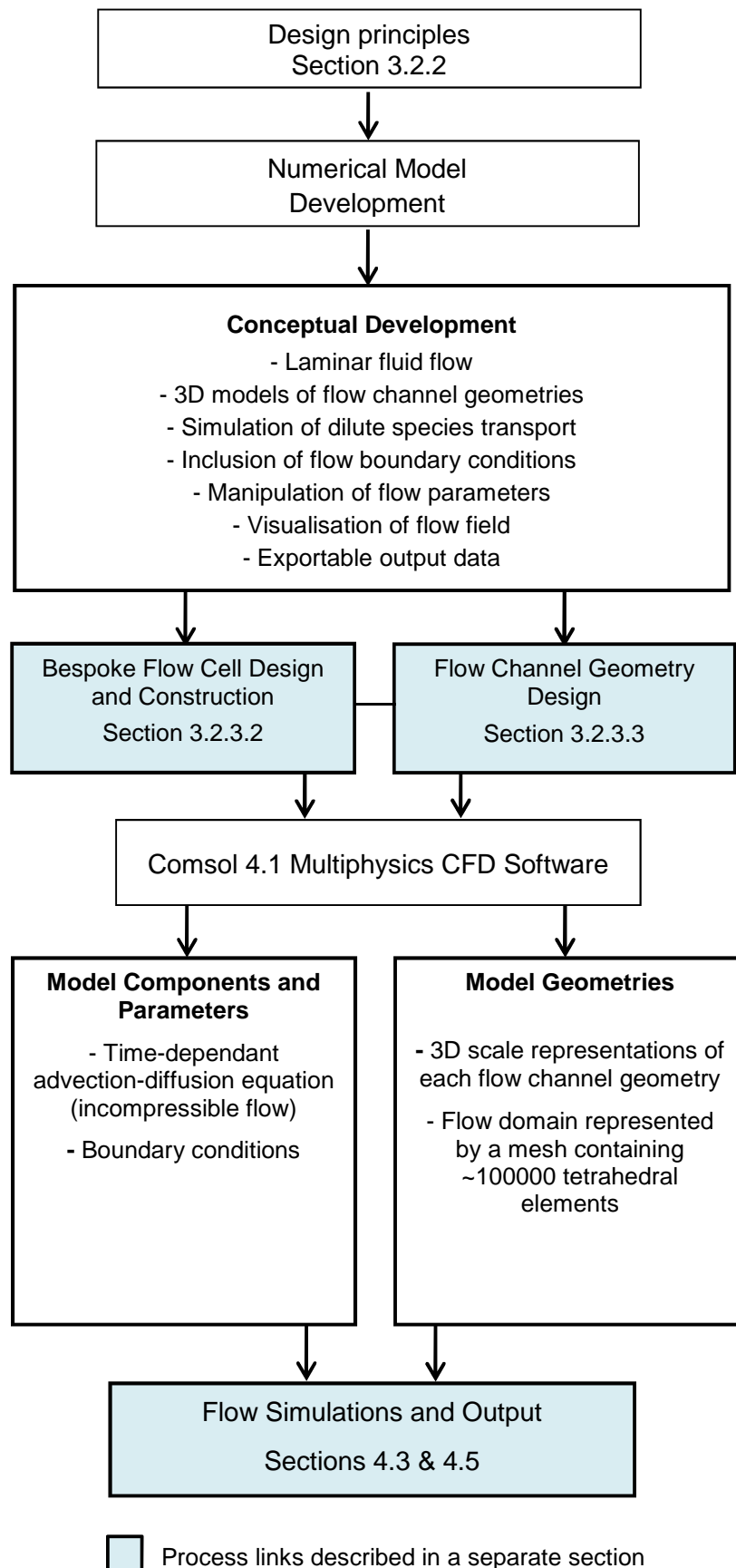


Figure 3-6 Computational design tool developmental process

A commercially available software package was chosen to develop the numerical models and conduct the computational investigation, COMSOL Multiphysics (version 4.1). Comsol Multiphysics utilises the finite element method (Section 2.6.1), to develop solutions and analysis for physics and engineering numerical applications. Specifically, the software package incorporates a computational fluid dynamics (CFD) module that provides the capabilities required by the conceptual framework list presented above. The rationale for selection of this software was described in Section 2.6.1.

Firstly, 3D models of each of the three flow channel geometries were developed, to match the flow channel geometries to be used in the experimental investigation, and using the real channel dimensions (in mm). This was achieved using a geometric domain method within the software, where individual 2D geometric elements were joined in union to create the entire required geometry. The 2D geometry was then extruded to a height of 1.5 mm, representing the depth of the flow channel. In a separate work plane, a 5 mm circular tube was incorporated to represent a portion of fluidics tubing into the inlet hole (Figure 3-7). Although unionised with respect to developing model simulations, the individual geometric elements were set within the model builder to be retained also as individual components. This would allow for both targeted variation across the flow cell in constructing a geometric mesh for numerical investigation, and also the selection of individual components for the analysis of numerical solutions.

The flow chamber was represented by a mesh of 3D tetrahedral elements, for which the software allowed for selection from predefined size settings. Table 3-3 presents the element size parameters for a selection of predefined mesh sizes, along with the approximate number of tetrahedral elements with respect to the entire geometry shown in Figure 3-7. The utilisation of multiple mesh sizes within one flow channel geometry, through the use of individual geometric units within the design, is demonstrated in Figure 3-8. The approach to the selection of mesh size and distribution will be discussed further in Section 4.3.2.

Table 3-3 Element size parameters and approximate number of elements for predefined size settings for the entire circular flow channel geometry, COMSOL Multiphysics 4.1.

Predefined Element Size Category	Maximum Element Size (mm)	Minimum Element Size (mm)	Maximum Element Growth Rate	Approx. No. of elements
Extra Fine	0.145	0.00949	1.08	~960,000
Finer	0.234	0.0253	1.1	~687,000
Fine	0.335	0.0632	1.13	~128,000
Normal	0.424	0.126	1.15	~42,000
Coarse	0.632	0.19	1.2	~14,000
Coarser	0.822	0.253	1.25	~6,000
Extra Coarse	1.26	0.316	1.3	~3,500

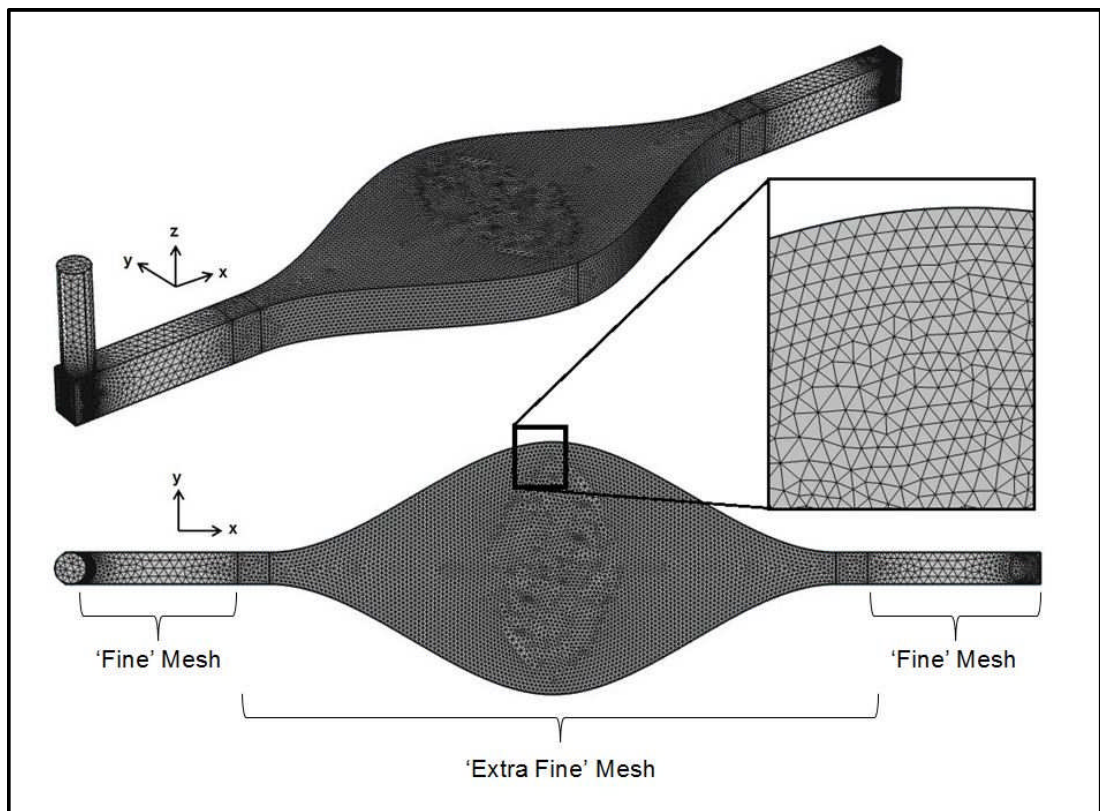


Figure 3-8 Flow channel model 3D tetrahedral mesh, for iCell geometry. Comsol 4.1 Multiphysics. Mesh size details are given in Table 3-3.

Numerically, the time-dependant advection-diffusion equation for an incompressible flow (equation 3-4) was used to simulate the transport of a dilute species, through a solvent (water) due to the processes of advection and diffusion. Specifically, this would simulate the transport of sodium fluorescein in water observed in the experimental design tool investigation (Section 4.2.3).

The advection diffusion equation is given by (Bird *et al.* 2007):

$$\underbrace{\frac{\partial c}{\partial t}}_{\text{variation of concentration with time}} = \underbrace{D\nabla^2 c}_{\text{diffusion term}} - \underbrace{\mathbf{v} \cdot \nabla c}_{\text{advection term}} \quad (3-4)$$

where c is concentration, t is time, D is the diffusion coefficient, v is velocity field; and ∇ is the del operator.

Transport due to diffusion is controlled by the gradient in concentration at any given location and regulated by the diffusion coefficient of the analyte within the solvent. Transport due to advection is governed by the underlying flow field. This is determined through solution of a steady-state Navier-Stokes equation, subject to appropriate boundary conditions, which models the laminar fluid flow. This is summarised in (equation 3.5), for an incompressible flow (Acheson and Acheson 1990):

$$\underbrace{\rho \mathbf{v} \cdot \nabla \mathbf{v}}_{\text{acceleration}} = \underbrace{-\nabla p}_{\text{pressure gradient}} + \underbrace{\mu \nabla^2 \mathbf{v}}_{\text{viscous}} \quad (3-5)$$

$$\nabla \cdot \mathbf{v} = 0$$

where ρ is fluid density, p is fluid pressure, and μ is the coefficient of dynamic viscosity.

Additional to the models of the three flow channel geometries, a model of the flow domain of a commercially available flow cell of a different design (Dropsens 'FLWCL', Figure 2-13, Section 2.5.1) was also developed. This design featured an impinging jet design, which would facilitate fluid delivery

from the inlet directly onto the surface of a screen-printed electrode (Figure 3-9). Incorporating this model into the study would allow for a direct comparison of flow cell performance of the three channel geometries against a commercially available design.

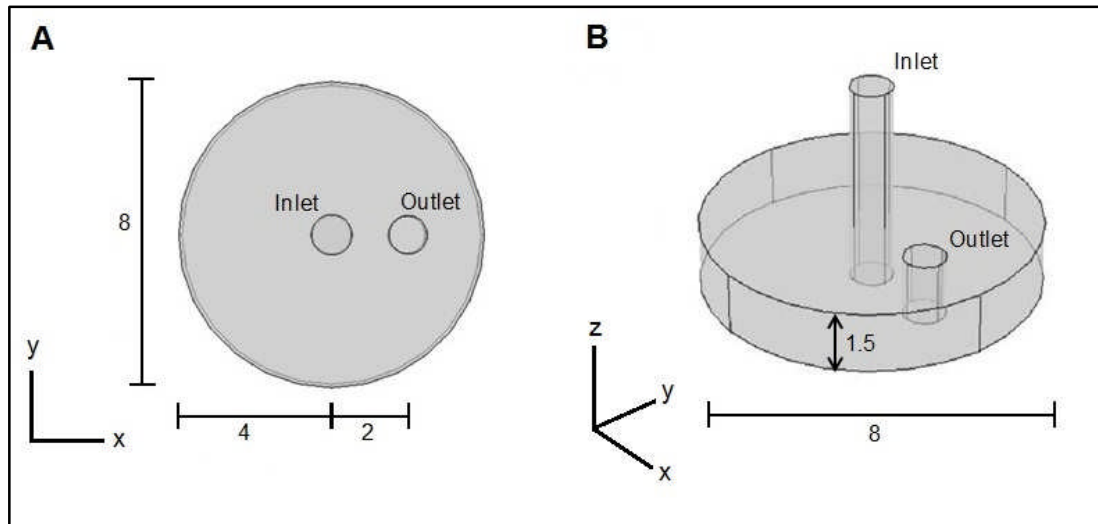


Figure 3-9 Model of commercial flow cell flow domain (Dropsens, FLWCL). A) Plan outline view, B) 3D Model outline view. All measurements in mm.

3.2.4 Guiding investigative strategy

To achieve a robust investigation, it was essential to identify an overall investigative strategy that could be applied, as much as was practically possible, to both the experimental and computational design tools. This can be summarised as follows:

- A range of flow rates that could be utilised in whole or in part across the two investigative approaches. Note: for practical purposes with regards to investigative time management, a greater number of flow rates would be utilised in the numerical modelling approach as compared to the experimental approach.
- Flow analysis experiments and flow simulations to be run for the same length of time for each investigative approach.
- Numerical model to reflect physical properties of fluids used in the experimental investigation e.g. diffusion coefficient of inlet fluids with relation to the bulk fluid present in the flow channel.

- A method of integral validation for the experimental flow analysis approach to be used (Section 4.2.2).
- A method of integral validation for the numerical modelling approach to be used (Section 4.3.2).
- Commutable method (or methods) of data analysis with respect to the two investigative approaches, that will enable a valid quantifiable comparison to be made between them.

3.3 Chapter summary

This chapter presented an approach for the investigation of the optimisation of a fluid delivery system that could be utilised in the deployment of a specific analytical biosensor system. The development of this optimisation process was described with respect to both a design rationale that focussed on the ultimate use of the fluid delivery system (i.e. biosensor deployment), and design principles that were drawn out of this rationale. Specifically, the design principles included the optimisation of fluid delivery to enable controlled equilibration of solute concentration within a 'wet' flow cell with that entering the inlet of the cell.

Parallel investigation procedures were developed to inform the fluid delivery system design, an experimental approach and a computational approach. For the experimental approach, a bespoke flow channel flow cell was developed that included flow channels of three different geometries. The geometries were varied based upon the rate of expansion from a narrow inlet channel to an expanded channel region that would allow for ultimate incorporation of a biosensor unit. The computational investigation procedure was developed using commercially available software with computational fluid dynamics (CFD) capabilities (COMSOL 4.1). Geometrically accurate models of the three flow channels considered in the experimental investigation were developed, to enable flow simulations to be run across a wide range of inflow rates. Additionally, the flow domain of a commercially available flow cell of a different design was modelled for comparative purposes.

CHAPTER 4

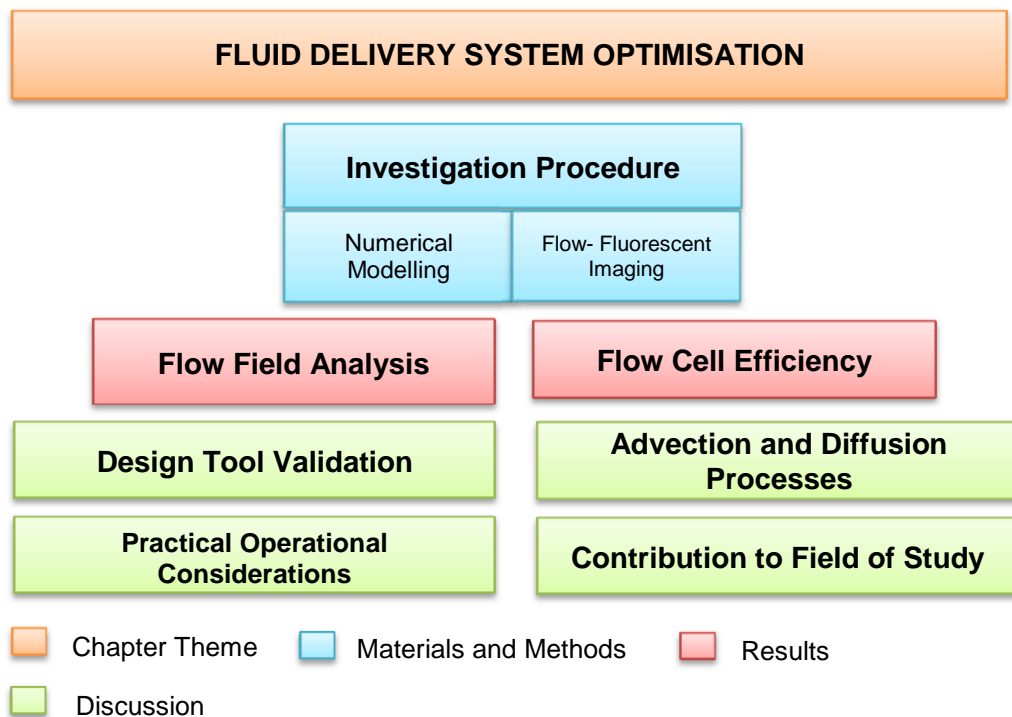
Flow cell design for effective
biosensing – investigation
process, results and discussion

Chapter 4 **Flow cell design for effective biosensing - investigation process, results and discussion**

4.1 Chapter introduction

This chapter presents the application methods for the fluid delivery system optimisation process developed in Chapter 3 (Sections 4.2 to 4.4). Additionally, the results of the developed investigations are presented (Section 4.5), followed by discussion of these results with respect to the development of an optimised fluid delivery system (flow cell) design, and operational protocol (Section 4.6).

Chapter Outline Map



4.2 Experimental investigation procedure

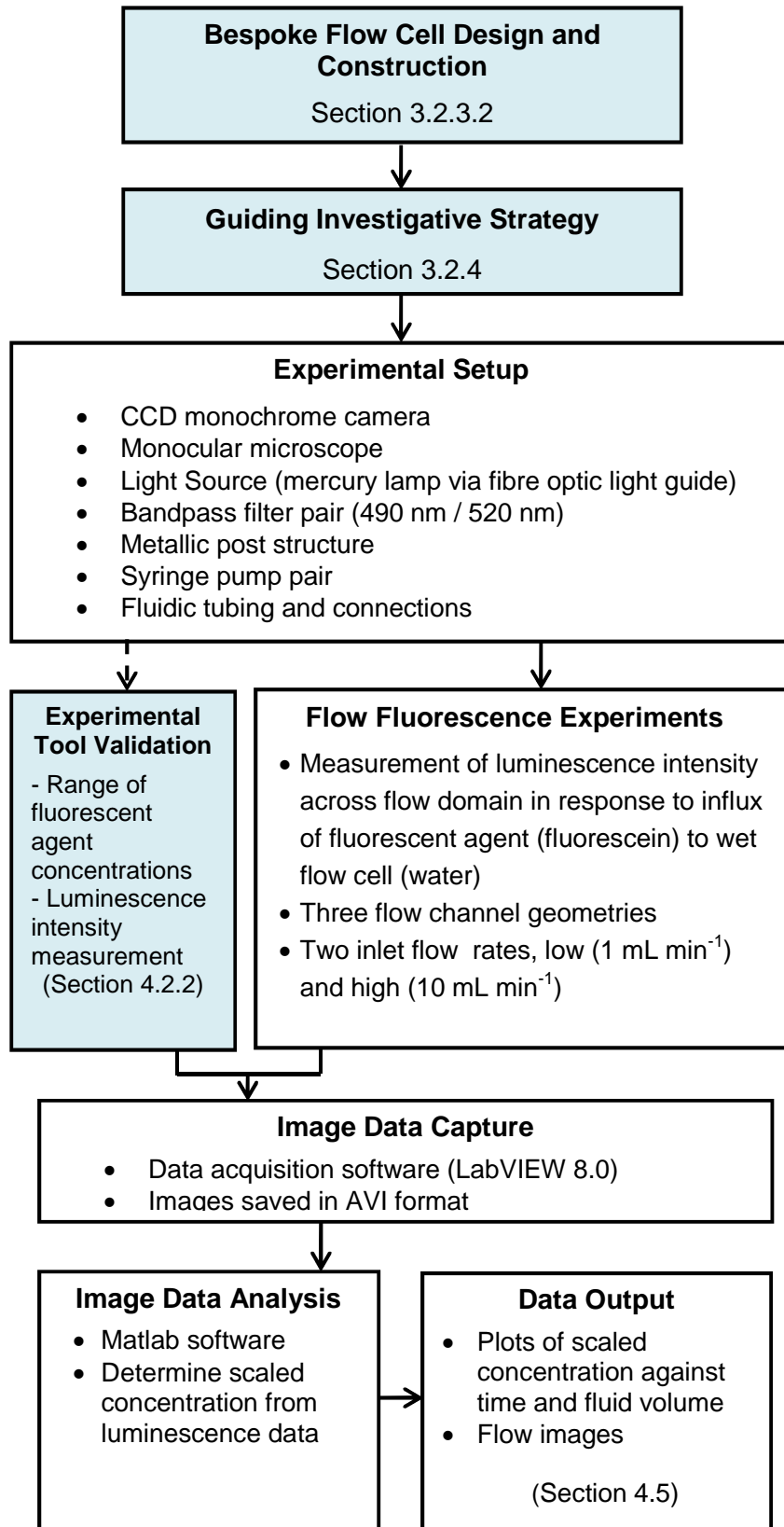
The process outline for investigation using the experimental design tool is summarised in Figure 4-1 .

4.2.1 Experimental setup

A laboratory-based experimental rig was developed for the investigation. A CCD monochrome camera (Adimec 1000 m) was attached to a monocular microscope, and connected to a personal computer that incorporated data acquisition software (LabVIEW 8.0, National Instruments). The camera-microscope was clamped in position to sit vertically above a specially constructed metal post framework. This framework was used to hold the transparent bespoke flow cell in vertical alignment with the camera-microscope, with a pair of bandpass filters positioned below (CW 490 nm \pm 2 nm FWHM 10 nm \pm 2 nm) and above (CW 520 nm \pm 2 nm FWHM 10 nm \pm 2 nm) the cell. A mercury lamp (Dolan Jenner MHR 100) fitted with a fibre optic light guide was positioned at the base of the rig to shine vertically upwards through the flow cell.

A pair of syringe pumps (Aladdin) was each fitted with a 10 mL syringe, and these were connected to the inlet of the bespoke flow cell via a tee-piece to allow easy switchover between the fluid initially used to fill the cell and the influent. The distance between the outlet of the tee piece and the flow cell was minimized (55 mm) to limit mixing of these fluids outside of the flow cell.

Investigation using Experimental Design Tool



□ Process links described in a separate section

Figure 4-1 Experimental design tool investigation process

Fluid conveyance was achieved using 1/8" OD PTFE tubing (ID 1.59 mm), and connections made using threaded nuts and ferrules to ensure a robust seal. A schematic of the experimental rig is presented in Figure 4-2.

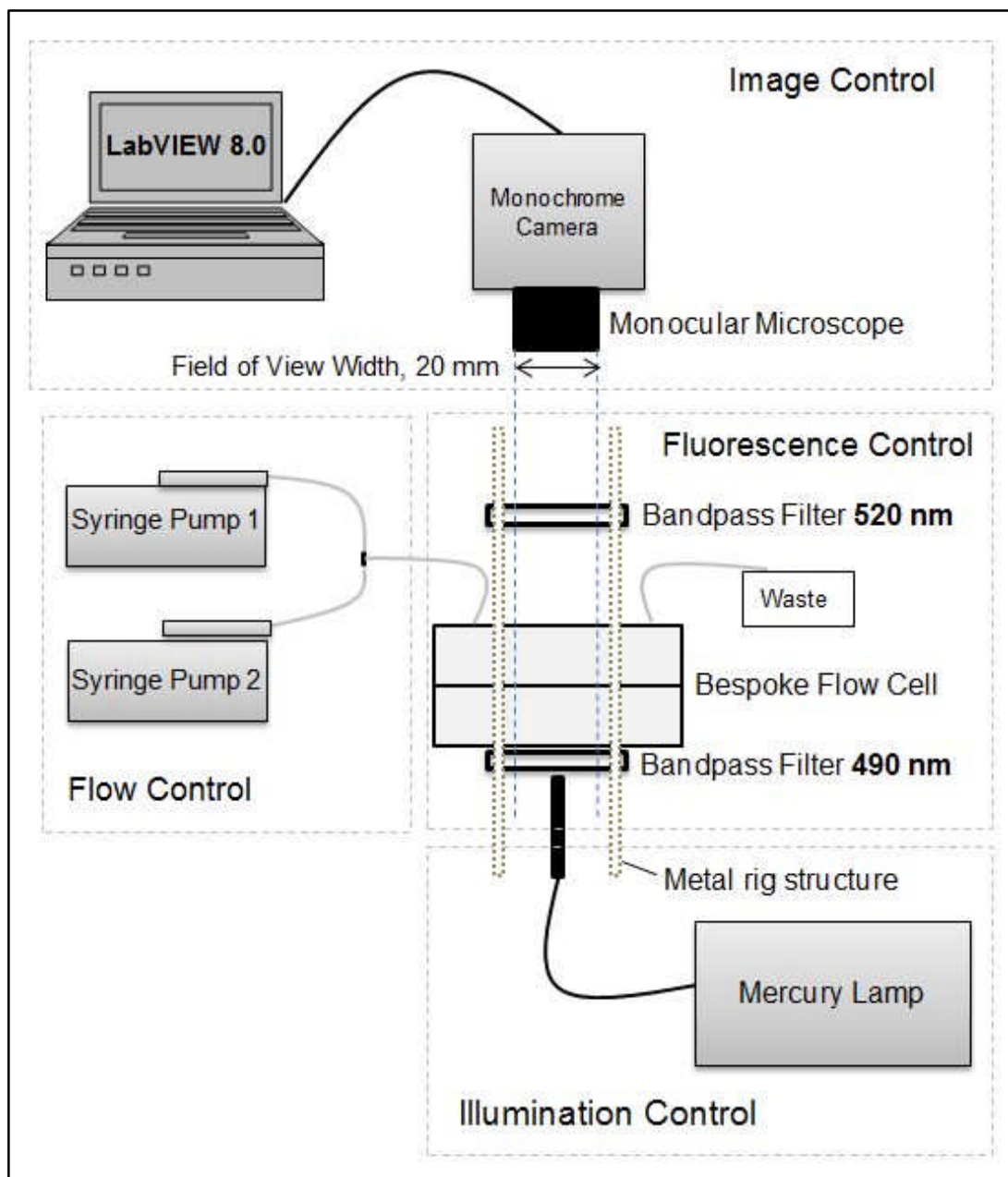


Figure 4-2 Schematic diagram of experimental flow analysis setup

Fluorescein sodium salt solution ($C_{20}H_{10}Na_2O_5$) was used as the fluorescent agent in the flow-fluorescent experiments. Fluorescein has a peak excitation wavelength of 494 nm and a Thorlabs FB490-10 bandpass filter permits approximately 20% light transmission at this wavelength (compared to a maximum transmission of around 50% for the filter) (Figure 4-3).

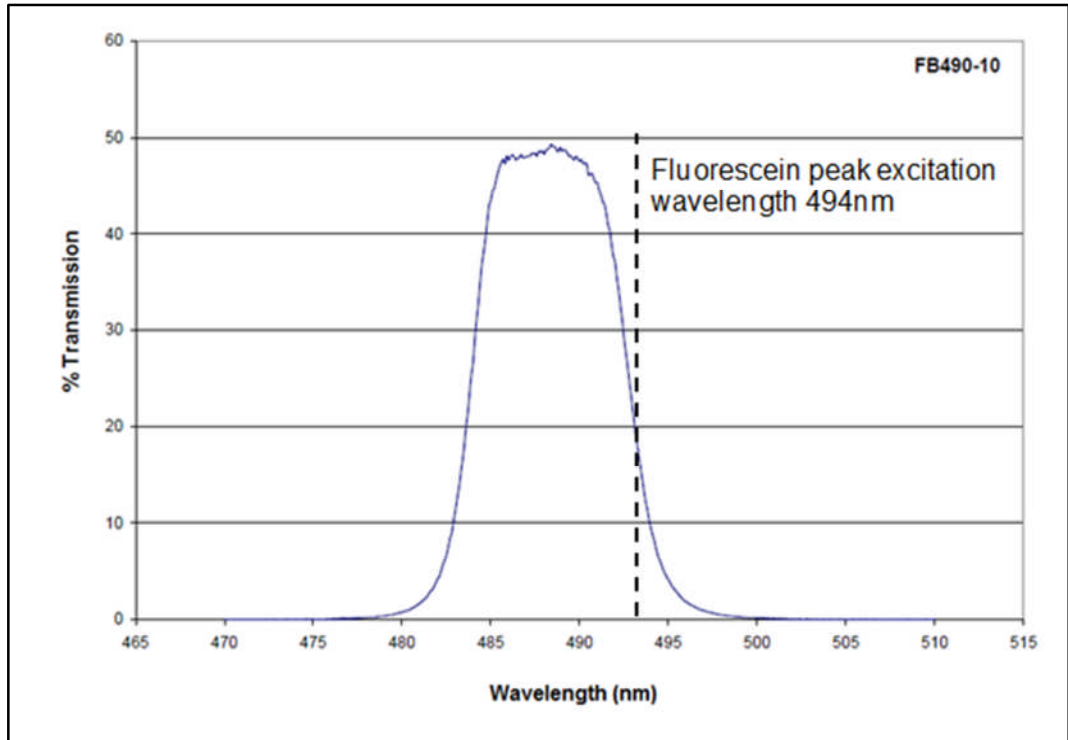


Figure 4-3 Light transmission spectra for 490 nm bandpass filter (Thorlabs.com 2011a)

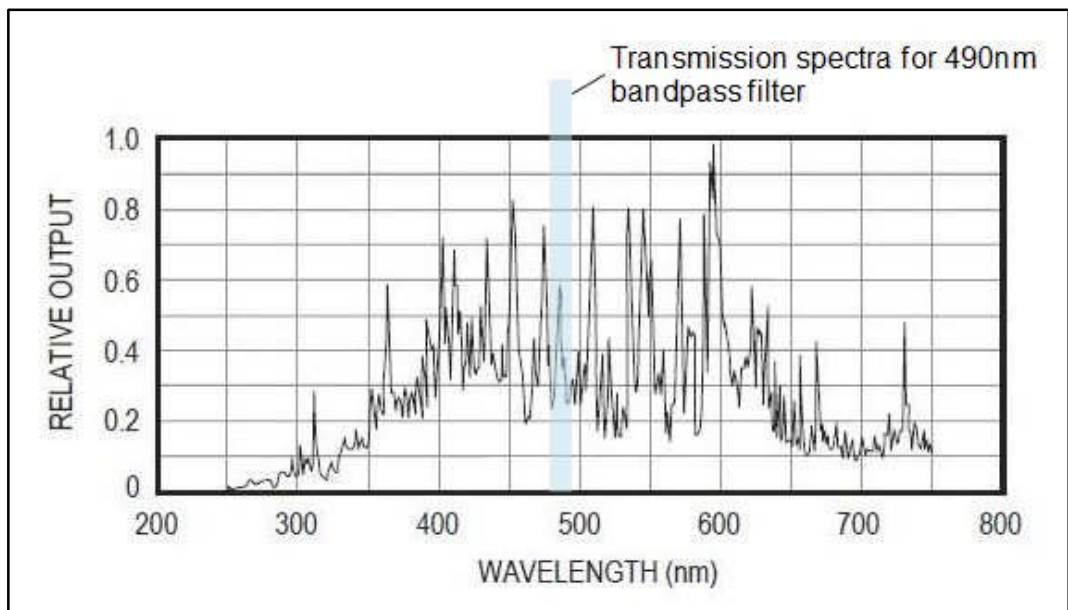


Figure 4-4 Light transmission spectra for Dolan Jenner mercury lamp MHR-100 (Dolan Jenner Industries 2011)

However, some excitation was expected to also occur at wavelengths below 490nm, and the bandpass filter provides maximum transmission between approximately 486 nm and 492 nm (Figure 4-3). The mercury lamp emits light at a broad range of wavelengths including the range 490-495 nm, and

therefore covering the maximum excitation range of fluorescein, albeit at approximately 30% of relative output (Figure 4-4).

It can be determined from Figure 4-3 and Figure 4-4 therefore that approximately 9-15% of light transmission would be utilised in the excitation of the fluorescein solution with the setup described. Additionally, the peak emission wavelength for fluorescein is 520 nm, and a Thorlabs FB520-10 bandpass filter permits approximately 55% light transmission at this wavelength (Figure 4-5). Preliminary tests of the experimental setup indicated that utilising the mercury lamp at approximately 75% of maximum output, provided a more than sufficient luminescence range to conduct detailed flow analysis. This was demonstrated in the experimental results presented in Section 4.5.

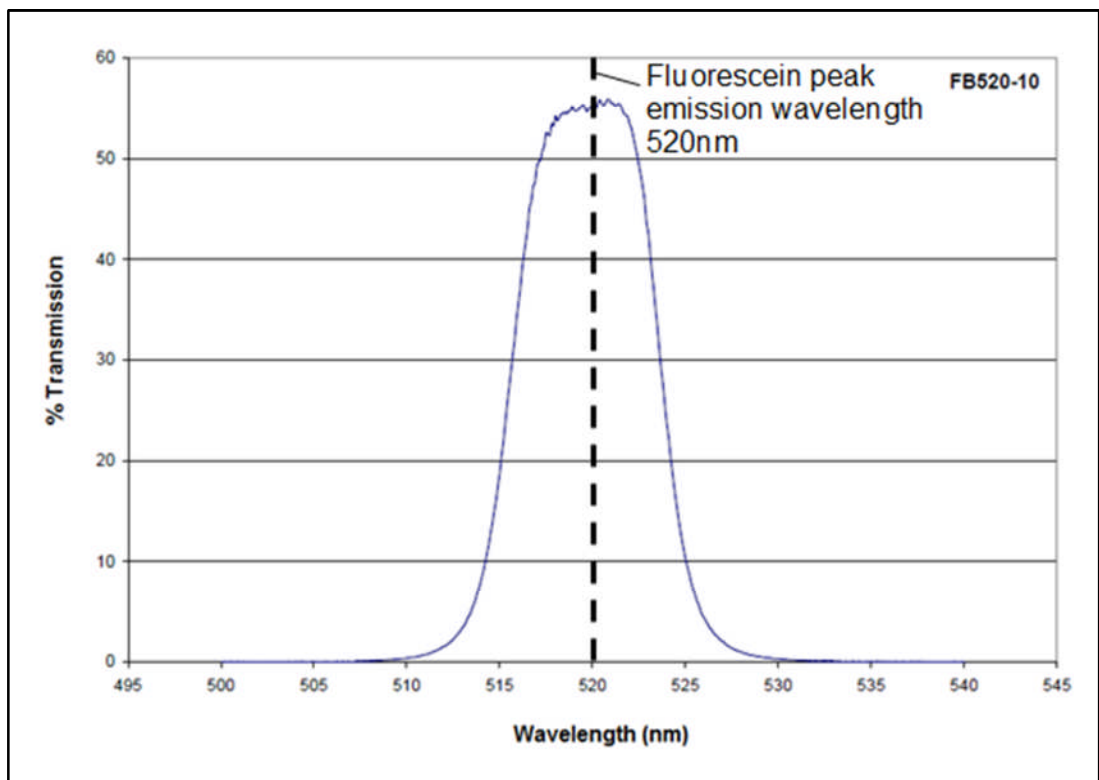


Figure 4-5 Light transmission spectra for 520 nm bandpass filter (Thorlabs.com 2011b)

The key parameter settings for the image capture software (LabVIEW 8.0) are presented in Table 4-1. The use of a monochrome camera (Adimec 1000M) and a grayscale luminescence intensity range of 0,255 were chosen because of enhanced image clarity in comparison to a colour camera

(Adimec 1000C) with a RGB range of 0,255 during preliminary testing of the experimental setup.

Table 4-1 Image capture software (LabVIEW 8.0) key parameter settings and selections

Parameter	Selected Setting (units)
Image Recording Format	Audio Video Interleave, AVI
Recording Rate	25 (Frames per second)
Luminescence Range of Output Images	0,255 (Grayscale)
Resolution	1004 x 1004 (Pixels)
Pixel Size	7.4 (μm)

4.2.2 Validation of the experimental tool

To ensure the integrity of the experimental design tool, an approach was developed that could demonstrate the applicability of the flow-fluorescence method in representing flow characteristics. Specifically, the relationship between the fluorescent agent (fluorescein sodium salt) concentration and luminescence intensity was investigated with the experimental setup presented in Figure 4-2. A range of eleven fluorescein concentrations between 0 μM (deionised water only) and 200 μM were investigated.

The bespoke flow cell was filled with aqueous fluorescein sodium salt ($\text{C}_{20}\text{H}_{10}\text{Na}_2\text{O}_5$) solution of known concentration using one of the two syringe pumps, and the pump was then halted. AVI images of the fluorescent flow channel were then captured, for 50 seconds duration at a frame rate of 25 frames per second. This was repeated for the concentration range described above, at 20 μM intervals. Because of the reported influence of fluorescent dye solution pH conditions upon fluorescence intensity (Zhu *et al.* 2005, section 2.6.2.2), the pH of each solution was measured and recorded. The pH across all solution concentrations was observed to be within a narrowly

defined range of pH 7.2 – 7.3, and would not therefore be regarded as a significant factor for these experiments.

Processing of the images was conducted using Matlab (Mathworks) programming software. Firstly, a region of interest (ROI) was defined by the application of a 'mask' that corresponded to the channel region only whilst excluding all regions of the image outside of the flow channel (Figure 4-6).

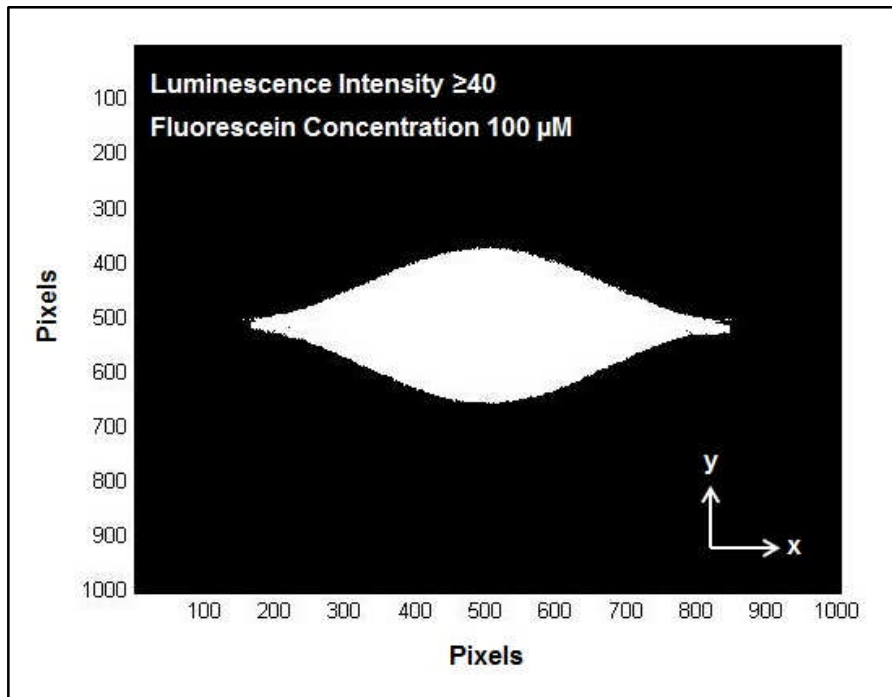


Figure 4-6 Mask applied to image of an iCell flow channel containing 100 μM fluorescein sodium solution. Light area represents the region of interest; dark area represents the applied mask. Mask is based upon a luminescence intensity threshold of 40 (Grayscale 0,255). Masks based upon the same principles were applied to the other two flow channel geometries.

The mask was defined by determining the minimum luminescence intensity, for a selected linear region of the channel to account for any small variation in intensity across the flow channel. A mean intensity for the ROI was then calculated, representing the mean of the sum total luminescence intensity of each pixel within the masked area. The data was normalised with respect to the background luminescence intensity i.e. fluorescein concentration at 0 μM (deionised water only). The Matlab program written to interrogate the fluorescence-intensity relationship is presented in Appendix A1 (Figure A-1). The resultant mean luminescence for each fluorescein concentration was plotted. A linear response was observed for the fluorescence concentration

range 0-100 μM , beyond which saturation of the fluorescence intensity was observed (Figure 4-7).

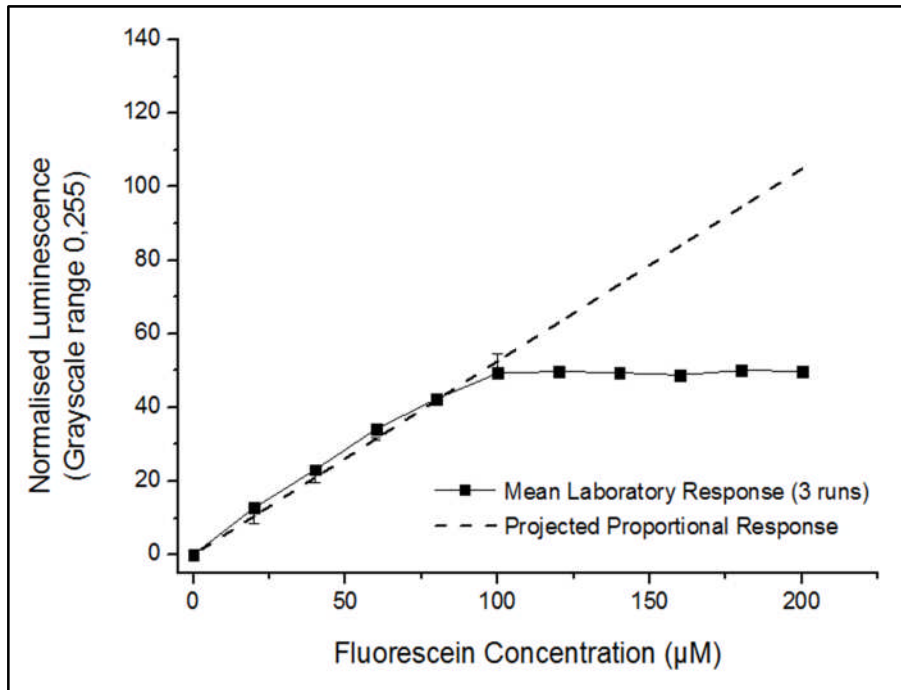


Figure 4-7 Normalised luminescence response to fluorescein sodium salt solution concentration, and projected linear response based upon best-fit line for concentration range 0-100 μM .

Additionally, a separate program was run that investigated the mean luminescence intensity within the region of interest over time. This was done to serve as a check that a statistically significant change in static luminescence (i.e. without the presence of any flow conditions) would not be a factor during the flow-fluorescence experiments. Indeed, this was confirmed by the resultant plot of mean intensity against time for which variation in intensity was within a 1 point luminescence range on the 0,255 grayscale (Figure 4-8).

Cont'd over.....

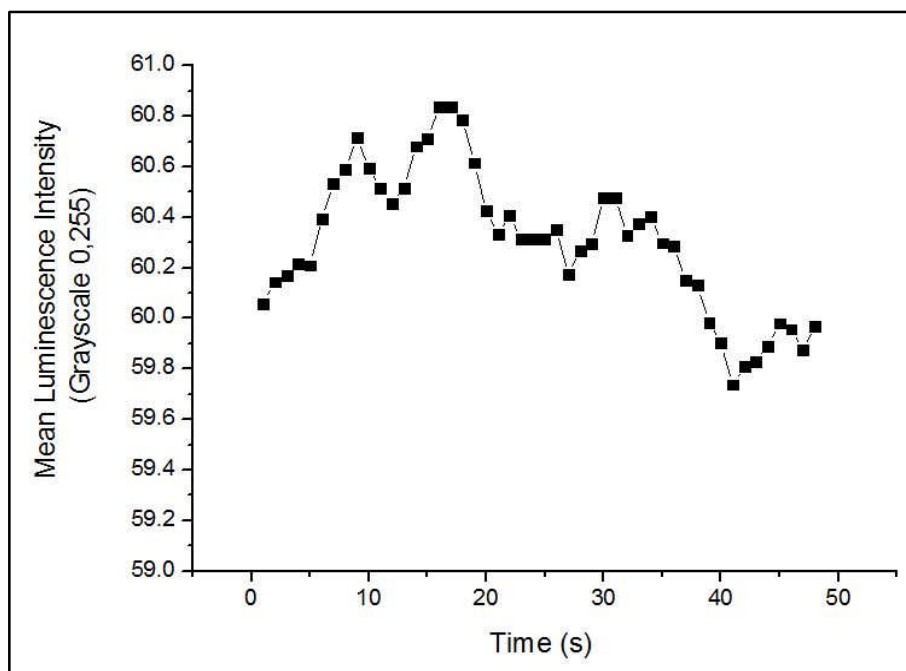


Figure 4-8 Mean luminescent intensity against time for a flow channel (Figure 4-6) containing 100 μM fluorescein sodium solution.

4.2.3 Flow-fluorescence experiments

Before the commencement of each flow experiment, the flow cell (contained within the experimental setup presented in Figure 4-2) was slowly filled with deionised water, using one of the two syringe pumps. For the cell filling, an inlet flow rate of 0.2 mL min^{-1} was used as this aided the prevention of air bubble formation and trapping within the flow channel.

Each experiment commenced with the simultaneous starting of the image capture software and the pump containing 100 μM fluorescein sodium salt solution at a predetermined flow rate. For these experiments, the fluorescein was used to model an analyte of interest. Flow rates of 1 mL min^{-1} and 10 mL min^{-1} were chosen to represent 'low' and 'high' flow rates within the range that would be considered for the numerical modelling investigation (Section 4.3). Flow experiments were conducted at these two flow rates for each of the three flow channel geometries, and the duration of each experiment was determined visually via the image capture software display. The pump and the image capture were halted when no change was observed between subsequent images, and this took between 35 and 165 seconds depending on flow rate and flow cell geometry.

Processing of the raw image capture data was conducted using Matlab (Mathworks) programming software. Firstly, individual frames of the video sequence were selected by identification of a) that which represented the commencement of fluorescein solution inflow, and b) that which represented the maximum concentration of fluorescein solution. The former was achieved by running a Matlab program which interrogated a time series of images representing the flow experiment. A circular region of interest (ROI) of 4 pixels radius positioned at the inlet of the flow channel images was interrogated, and the mean luminescence intensity at each single frame was then determined. A selected number of sequential frames from the start of the video were considered, with the number of frames based upon on a visual estimate of the time taken for the fluorescein solution to enter the flow cell. The Matlab program output was a plot of video frame number against mean luminescence intensity for the ROI (Figure 4-9). The video frame selected to represent the maximum fluorescein concentration was the last frame in the video sequence.

Secondly, a further Matlab program was developed to analyse each pixel within the flow channel region for the video duration between the inflow of the fluorescein solution and the last image of the video. The Matlab code for this program is presented in Appendix A2 (Figure A-2). Once again, a region of interest (ROI) for analysis was determined by the application of a mask. For this program the mask was evaluated by firstly calculating the difference between the luminescent intensity of the final video frame (representing maximum fluorescein concentration) and the background luminescence intensity. The resultant image was then displayed and a threshold intensity value determined based upon the luminescence intensity for a selected linear region of the flow channel. An image of the applied mask was then displayed to check the quality of the defined ROI, and the mask threshold value was amended if necessary.

Cont'd over....

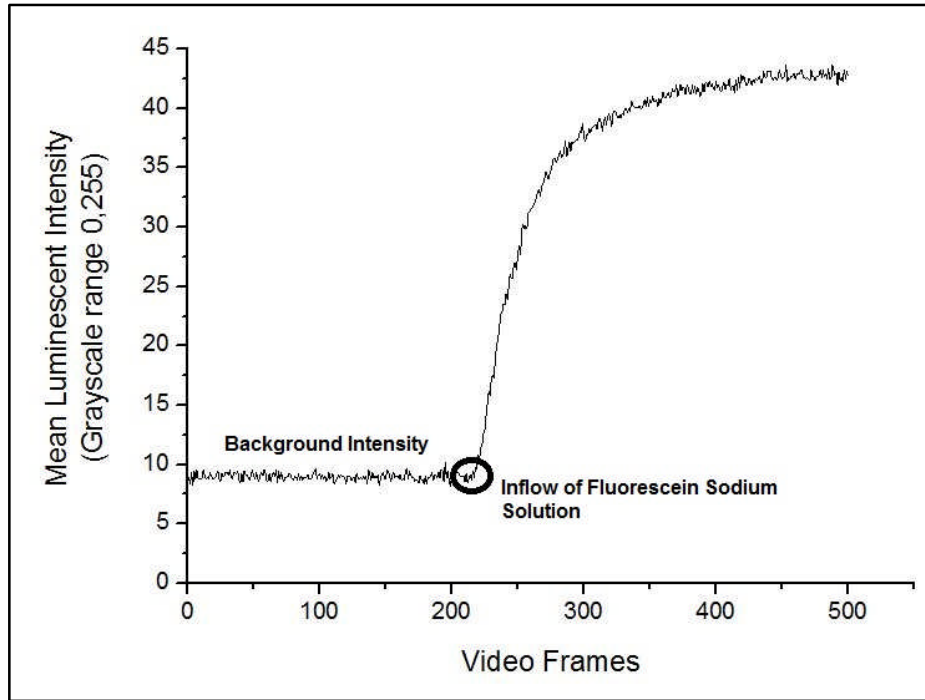


Figure 4-9 Luminescent intensity response to inflow of fluorescein sodium solution for circular geometry channel @ 1 mL min⁻¹ inflow rate. Mean intensity relates to a circular ROI of 4 pixels radius, positioned at the inlet of the flow channel. Processed from video images recorded at 25 frames per second.

For the region of interest, each pixel within the flow domain was analysed to determine a scaled concentration, C_{ratio} , where 0 corresponds to no analyte and 1 corresponds to the maximum concentration of analyte. A measurement frequency of every 25 frames, representing one measurement per second, was chosen. Because fluorescence intensity is linearly related to concentration for these experiments (Section 4.2.2), the concentration ratio is related to the relative fluorescent intensity by equation 4-1.

$$C_{ratio} = (I - I_0) / (I_{end} - I_0) \quad (4-1)$$

where I_0 is the background intensity of each pixel at the start of the flow experiment and I_{end} is the fluorescence intensity of that same pixel at the end of the flow experiment. In addition to determining the local concentration ratio, the mean concentration ratio within the flow cell was calculated. A plot of mean scaled intensity against time was produced through the Matlab program as a check against program errors. Output data, the flow cell mean concentration ratio against time, was then exported to graphing data analysis software (Origin 8.6_64 bit).

4.3 Computational investigation procedure

The process outline for investigation using the computational design tool is summarised in Figure 4-10.

4.3.1 Investigation setup

A range of ten simulated inflow rates were selected for the investigation, to include the flow rates considered as part of the experimental investigation (1 and 10 mL min⁻¹). The selected volumetric flow rates were 0.1, 0.25, 0.5, 1.0, 1.75, 2.5, 3.75, 5.0, 7.5, and 10 mL min⁻¹. This range was chosen to purposely expand beyond the range of flow rates 'typically' used for biosensor (and other sensor) flow cell experiments i.e. 0.5 – 1.5 mL min⁻¹. A consistent set of fluid materials, fluid properties, boundary condition types, and dilute species properties were determined for use across all of the numerical models.

Water was selected as the fluid (Figure 4-11A), to replicate the materials used in the experimental investigation. The fluid material temperature was set at 293.15 K (20°C), to replicate the conditions under which the experimental investigation was conducted. Other fluid properties were determined as a function of the user-defined temperature, and the resultant values are presented in Table 4-2.

The volumetric flow rate and boundary conditions were specified for each model through laminar flow controls (Figure 4-11A). Boundary conditions for the numerical models were selected to represent the prevalent conditions of the experimental investigation. Three types of boundary condition were defined, and set for the inlet, outlet, and walls:

A) Inlet Boundary Condition

The flow inlet was isolated within the model geometry construction, to which an inlet boundary condition was applied for each model. The inlet boundary was defined by the simulated laminar inflow of fluid at the inlet. This was the

Investigation using Computational Design Tool

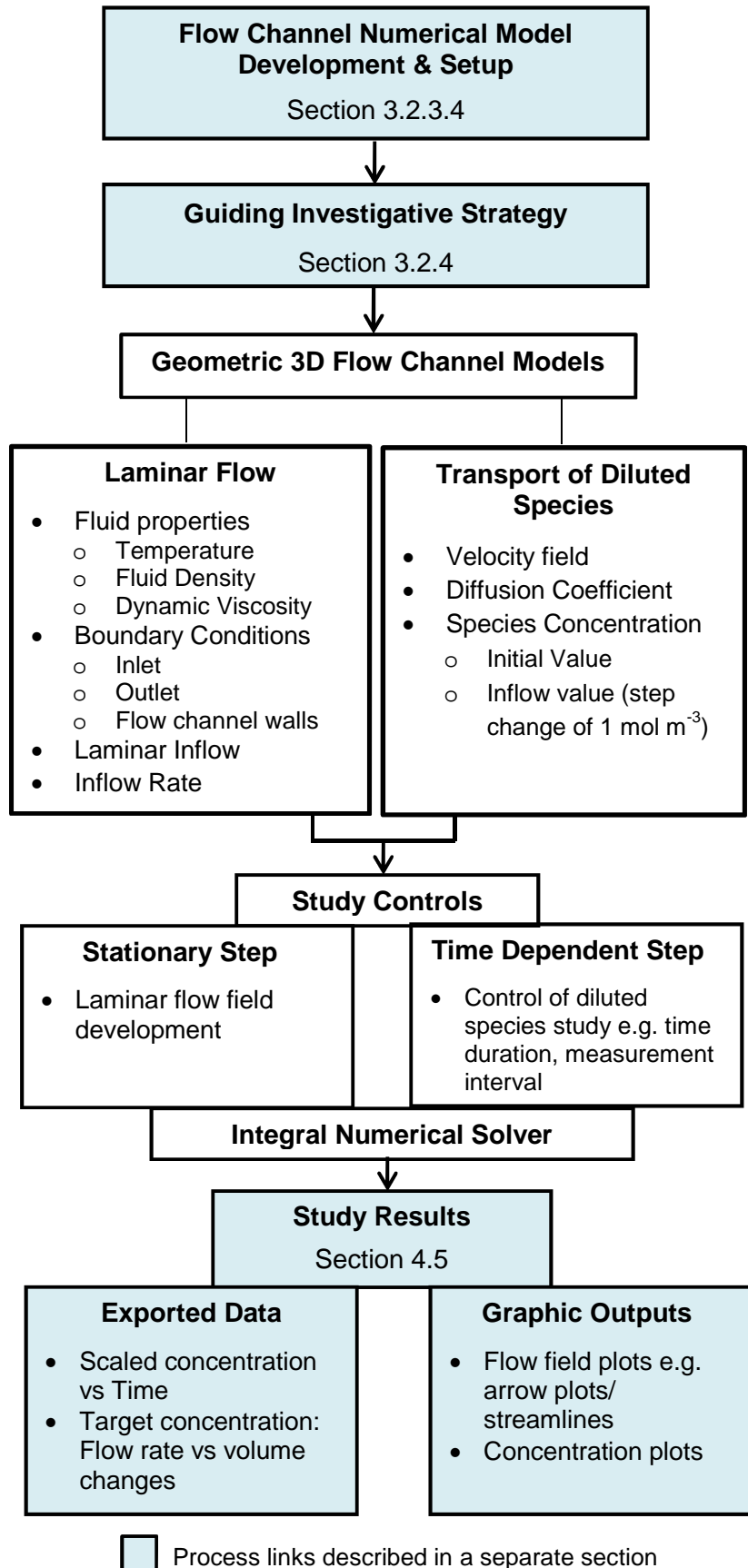


Figure 4-10 Computational design tool investigation process

Table 4-2 Selected material (water) property values used for computational models within COMSOL 4.1 software.

Property	Value	Units
Temperature (T)	293.15	K
Dynamic Viscosity (μ)	0.001	Pa s
Density	999.62	kg m ⁻³

most suitable boundary condition because the volumetric inflow rate was explicitly known. The specific inlet boundary conditions therefore varied between different models, according to the specification within the model of the volumetric inflow rate. The volumetric inflow rate was selected in each case from the range of flow rates presented above.

B) Outlet Boundary Condition

The flow outlet was also isolated within the construction geometry, to which an outlet boundary condition was applied for each model. This boundary was set with respect to the pressure (no viscous stress) conditions at the outlet. Specifically, the fluid pressure at the outlet was set at zero Pa.

C) Wall Boundary Condition

A no-slip boundary condition was used with respect to all walls of the flow channel models. This set a zero velocity for the fluid at the boundary. The wall boundary condition was over-ridden at the inlet and outlet by those independently defined boundary conditions.

The advection-diffusion equation for the models was solved subject to a velocity field defined under the flow conditions described above, through model settings that controlled the conditions of the transport of a dilute species (simulating sodium fluorescein transport)(Figure 4-11A). A diffusion coefficient of $5 \times 10^{-10} \text{ m}^2 \text{ s}^{-1}$ was specified to match that of sodium fluorescein in water (Walker 1987). The initial concentration throughout the

flow domain was set to 0, and at time zero the concentration at the inlet was set to $c = 1$.

The tetrahedral mesh settings were also defined at this stage through the model development controls (Figure 4-11A). Uniform mesh size settings were selected for use across all of the numerical models. The dependence of the model response upon mesh configuration was determined through a separate validation process, and this is described in detail in Section 4.3.2. This process was then used to select an appropriate mesh setting for the models.

The model simulation controls were composed of three elements; two study configuration components and a solver configuration component (Figure 4-11B). The study configuration consisted of a stationary study step through which the underlying laminar flow field was developed, and a time-dependent step through which the transport of diluted species was analysed.

Cont'd over....

4.3.2 Computational tool validation

A study was conducted to examine the extent of the dependence of model numerical output upon the size of mesh and mesh element distribution. Additionally the influence of inflow rate and was also considered with respect to mesh sensitivity.

Two inflow rates were selected; 0.1 mL min^{-1} and 1 mL min^{-1} , and model simulations were run for 500s and 200s respectively. These two inflow rates were chosen to investigate whether any mesh sensitivity was related to variation in simulated flow rate, whilst minimising the computational time required to conduct the study. The study durations were chosen following preliminary simulations used to identify the minimum time taken for dilute species concentration within the flow channel to approach 100% of the influent. It should be noted that these study durations were slightly different to those used in the main computational investigation (Section 4.3.3, Table 4-5). This is because this validation study did not include investigation of the commercial flow cell design.

Six different mesh settings were considered, with successive settings determined by a 250,000 increase in the total number of tetrahedral elements for the whole geometry (Table 4-3). The mesh configuration was determined by the use of both the pre-determined in-built model mesh settings (Table 3-3) and custom mesh settings (Table 4-4), either independently or in combination.

Cont'd over....

Table 4-3 Mesh settings for computational tool validation process.

Mesh Setting (MS)	Detail (Pre-defined mesh settings detailed in Table 3-3, Section 3.2.3.4. Custom mesh settings are detailed in)	Approx. total number of tetrahedral elements
1	Custom 1 mesh for ROI, Fine mesh for remainder	250,000
2	Custom 2 mesh for ROI, Fine mesh for remainder	500,000
3	Custom 3 mesh for ROI, Custom 4 mesh for remainder	750,000
4	Custom 3 mesh : entire flow geometry	1,000,000
5	Custom 5 mesh for ROI, Extra Fine mesh for remainder	1,250,000
6	Custom 6 mesh for ROI, Extra Fine mesh for remainder	1,500,000

Table 4-4 Custom mesh configuration parameter settings.

Custom Mesh	Maximum Element Size (mm)	Minimum Element Size (mm)	Maximum Element Growth Rate	Resolution of Curvature	Resolution of Narrow Regions
1	0.210	0.0120	1.090	0.350	0.920
2	0.156	0.0099	1.080	0.300	0.950
3	0.147	0.0095	1.080	0.300	0.950
4	0.159	0.0140	1.084	0.340	0.920
5	0.124	0.0032	1.06	0.27	0.97
6	0.117	0.0030	1.05	0.26	0.98

The custom mesh settings were derived through the adjustment of pre-determined mesh settings. Mesh configurations were also either a single mesh size for the entire geometry, or different mesh sizes for the analytical region of interest (ROI) and the remainder of the geometry. The ROI related to a 3D 20 mm length section of flow channel within the central region of the channel geometry. This ROI was purposely isolated within the geometric construction to enable the utilisation of different mesh settings, and to provide a region for analysis that would correspond with the ‘field of view’ of the experimental setup (Section 4.2.1).

The study was conducted by running flow simulations at each of the mesh settings and inflow rates using the circular flow channel geometry (Figure 3-5B, Section 3.2.3.3). The mean dilute species concentration for the ROI (c_{roi}) was then calculated using a volume integration function within the Comsol 4.1 software (summarised in equation 4-2).

$$c_{roi} = \int \frac{c}{V} dv \quad (4-2)$$

where c is the dilute species concentration, and V is the total mesh volume for the ROI. Because the dilute species concentration for the model was set to achieve a step change of 1 (mol m³)(Section 4.3.1), this provided a cell concentration ratio (CCR) between 0 and 1 at each time step. Computed results were taken every second for both of the inflow rates.

Two methods of analysis were used for this aspect of the study. Firstly, c_{roi} was plotted against time for each mesh setting, and for the two flow rates considered. This enabled a direct comparison between each mesh setting (Figure 4-12). Additionally, target CCR values of 0.95 and 0.99 (i.e. 95% and 99%) were selected and the time taken to reach each target was plotted for each mesh setting at the two flow rates (Figure 4-13). The largest discrepancy between all successive mesh settings was observed in the initial stages of flow. Differences of up to 40% were observed for the low flow rate, and differences of up to 3% for the higher flow rate. It should be noted however that these higher differences related to c_{roi} values of less than 0.1 in each case. Additionally, it was clear from these results that mesh sensitivity with respect to the target concentration ratios was most statistically

significant between MS1 and MS2 for the higher flow rate and between MS2 and MS3 for the lower flow rate (Figure 4-12 & Figure 4-13).

Beyond the initial stages of flow, differences between successive mesh settings at both flow rates were typically below 1% at each time step for the four finer mesh settings (MS3-MS6).

Based on this validation exercise, mesh setting 3 (MS3, Table 4-3) was adopted for use in the flow simulations. This is because beyond mesh setting 3 the impact upon results were maintained within a reasonable level (less than 5% difference in total between mesh setting 3 and mesh setting 6) for both flow rates considered.

Cont'd over....

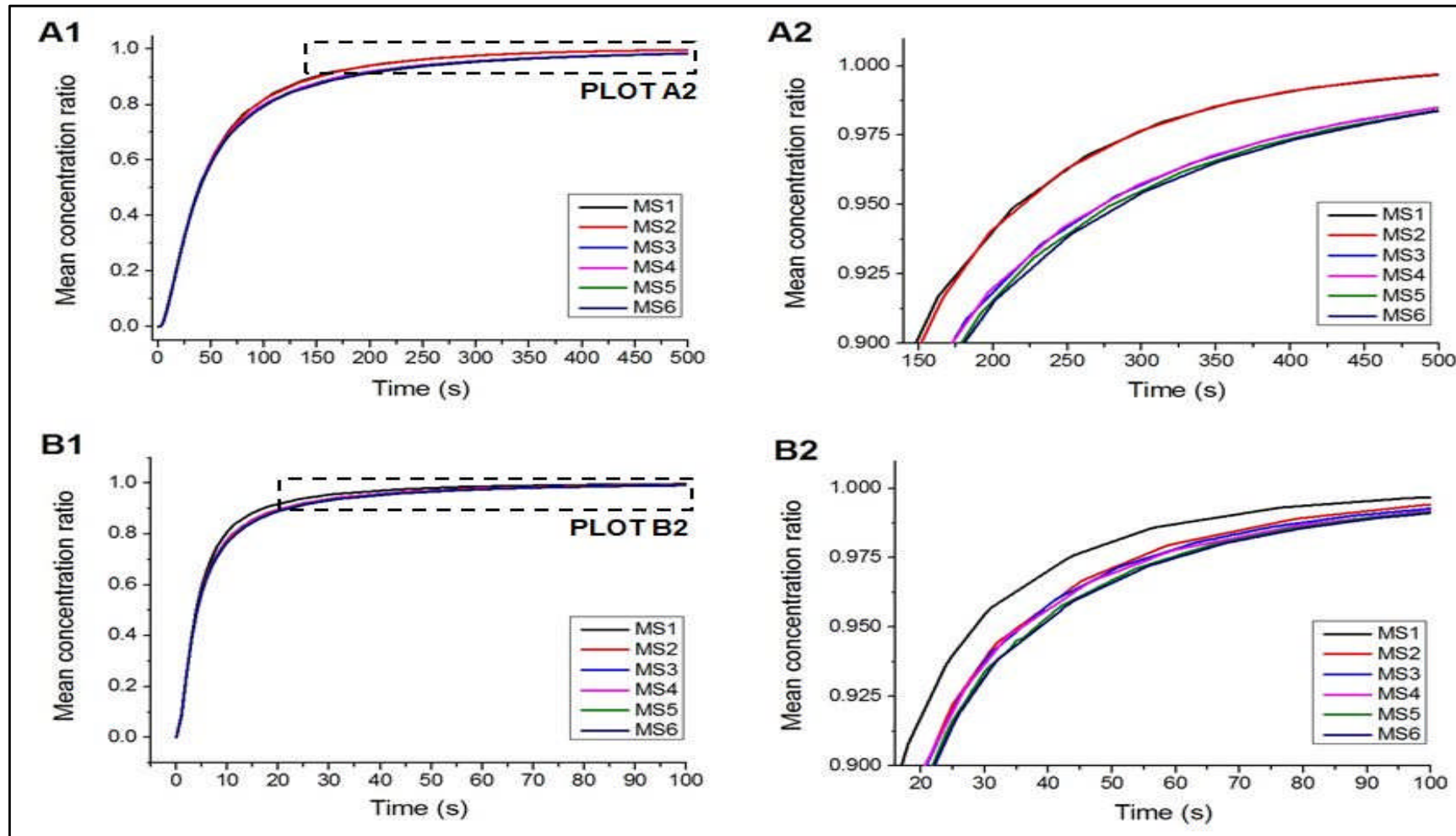


Figure 4-12 Mesh sensitivity analysis 1. Mean concentration ratio against time for each of the six mesh settings (MS): A) Inflow rate 0.1 mL min⁻¹, B) Inflow rate 1 mL min⁻¹. Plots A2 and B2 show isolated regions of plots A1 and B1.

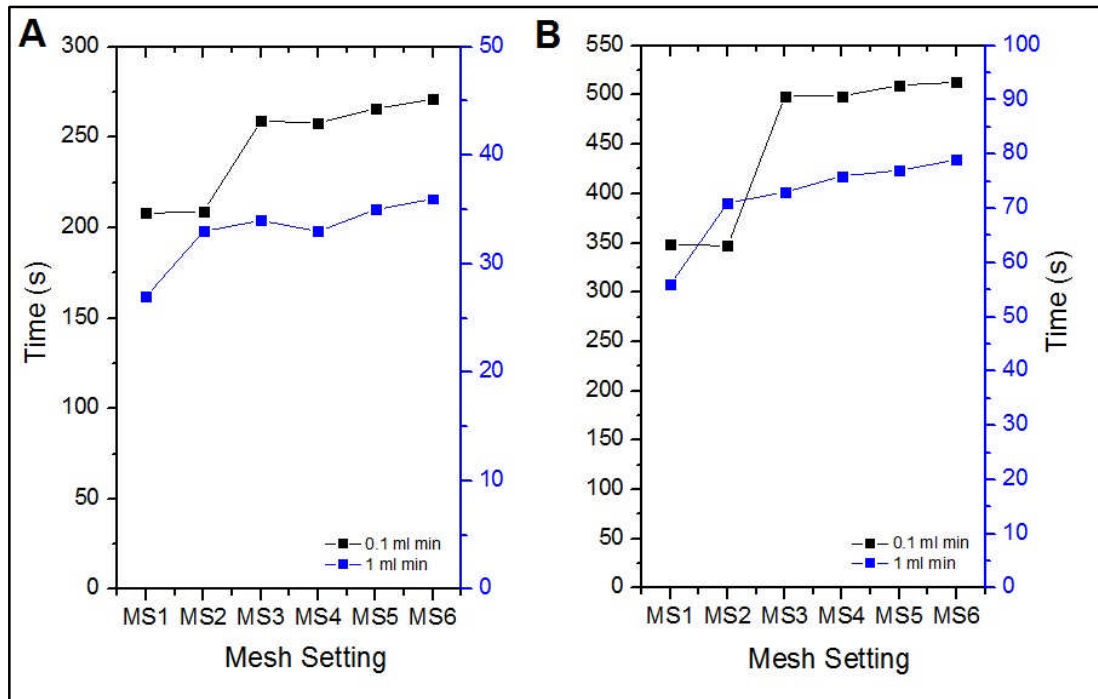


Figure 4-13 Mesh sensitivity analysis 2. Time taken to reach target mean dilute species concentration within flow domain: A) 95%, B) 99%.

4.3.3 Computational flow simulations

Flow simulations were run using the model settings described in Section 4.3.1, and using mesh setting 3 (Table 4-3) as recommended in Section 4.3.2. Models were run for the three channel geometries and the commercial flow cell geometry at each of the ten study inflow rates; and the simulation duration and measurement step were varied dependent upon the inflow rate (Table 4-5). The study duration and measurement steps were determined following preliminary simulations used to identify the minimum time taken for dilute species concentration within the flow channel to approach 100% of the influent. It should be noted that length of time over which the concentration was studied for the inflow rates of 1.0 and 10.0 mL min⁻¹ was slightly longer than those used in the experimental investigation. This is solely because of the inclusion of the commercial flow cell geometry for the computational investigation.

Cont'd over....

Table 4-5 Study duration for flow simulations

Inflow Rate (mL min ⁻¹)	0.1	0.25	0.5	1.0	1.75	2.5	3.75	5.0	7.5	10.0
Study Duration (s)	750	500	500	300	250	200	150	120	100	50

A range of methods were utilised in the analysis of numerical solutions:

- 1) Calculation of the mean dilute species concentration for the analytical region of interest (c_{roi} , Eq. 3-7), at each time step. The ROI was the 3D 20 mm central section of the flow channel (as defined in Section 4.3.2).
- 2) From concentration-time data, calculation of :
 - a. A non-dimensional parameter ($v/v_{flowcell}$) at each time point giving the flow volume expressed as number of flow cell changes.
 - b. Total inflow volume at each time step.Plots of concentration against fluid volume/volume changes were then produced.
- 3) Determination of dilute species concentration with time for selected single points within the 3D flow domain.
- 4) Flow field graphic plots:
 - a. Arrow plots indicating direction of flow and proportional velocity across the flow channel ROI, for a 2D horizontal plane of the flow channel at half of the flow channel depth.
 - b. Streamlines indicating the mean direction of flow across the flow channel ROI, for a 2D horizontal plane of the flow channel at half of the flow channel depth.
- 5) Concentration colour maps representing the dilute species concentration distribution for each flow simulation, at each time measurement step.

4.4 Comparative validation

It was important to consider methods that would enable validation of the fluid delivery system optimisation process investigation as a whole.

This was done by conducting a direct comparison of data from the experimental and computational investigations. This was an appropriate validation method because of the parallel approach taken in the development of the experimental and computational investigations, as described across Sections 4.2 and 4.3.

Two analytical approaches were employed in the comparative validation process. Analysis results for both methods are presented here for the 20 mm length region of interest of the *circular* flow channel geometry, and for inflow rates of 1 mL min⁻¹ & 10 mL min⁻¹. It should be noted that the comparative investigation process was conducted for all three of the flow channel geometries considered in this study. However, the comparative results were similar for each and it was decided to present in this thesis results only for the circular channel geometry to provide a more concise narrative. The circular geometry was chosen for this purpose because it represents the midpoint of the range of channel expansions considered in the study. The two inflow rates used in the process were selected because they were the two rates used in the experimental investigation (Section 4.2.3).

1) Qualitative Approach

Comparison of processed images from the experimental investigation with modelled concentration maps. Images and model plots were obtained for the 20 mm length region of interest of the circular flow channel geometry at four time steps: 3, 5, 10 & 20 seconds.

2) Quantitative Approach

Plots of mean concentration ratio against time for both investigation methods were produced and plotted together for each of the two flow rates. Experimental data was shown as a mean of triplicate experiments with standard error also plotted.

4.5 Investigation results

4.5.1 Comparative validation results

The qualitative validation approach provided a good match at both flow rates with respect to the overall shape and extent of the flow field at each of the studied time steps. The variation in concentration across the flow channel can also be matched reasonably well for the two investigative methods, although the numerical model concentration maps do provide greater detail and clarity with respect to the concentration change. For the higher flow rate, the progressive development of flow features (i.e. regions of recirculation, eddies) were clearly observed in both the experimental and computational investigations (Figure 4-14).

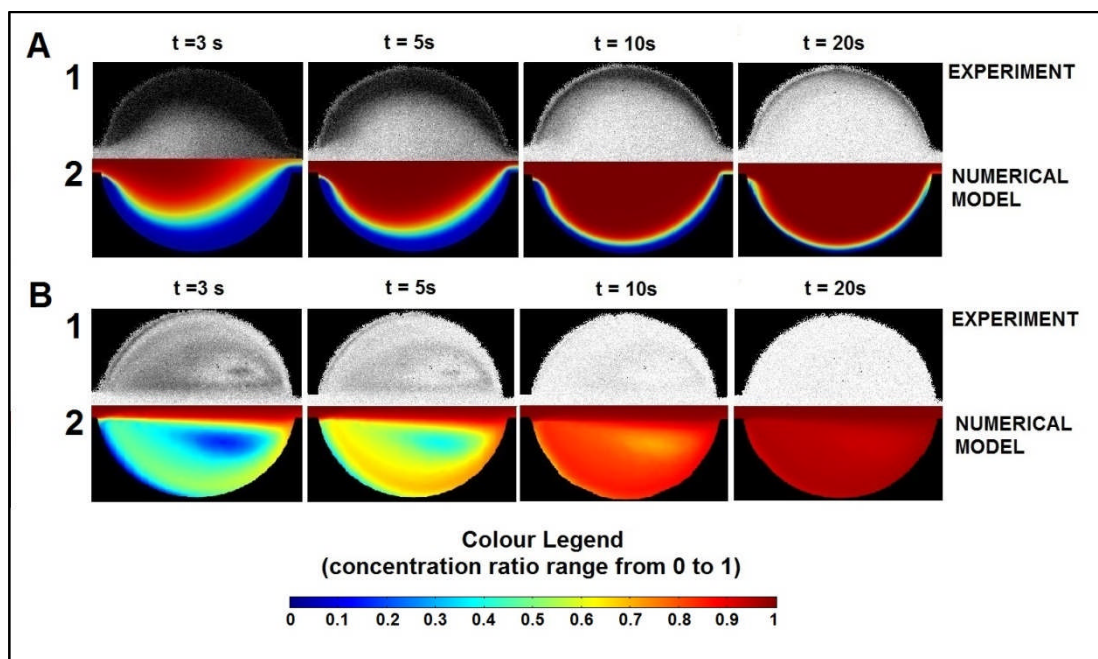


Figure 4-14 Comparative validation 1. Performance of the circular flow cell when the flow rate was A) 1 mL/min, and B) 10 mL min⁻¹. (1) Processed experimental images, where black is low concentration and white is high concentration, (2) Predicted concentration maps.

Similarly, the concentration ratio plots demonstrate a good match between the experimental and computational investigation for both flow rates (Figure 4-15). The difference in mean concentration ratio at each measurement step was less than 5% at the low flow rate, and less than 2%

at the higher flow rate, whilst the standard error on the mean of three experimental runs was in the 0-5% range across both flow rates.

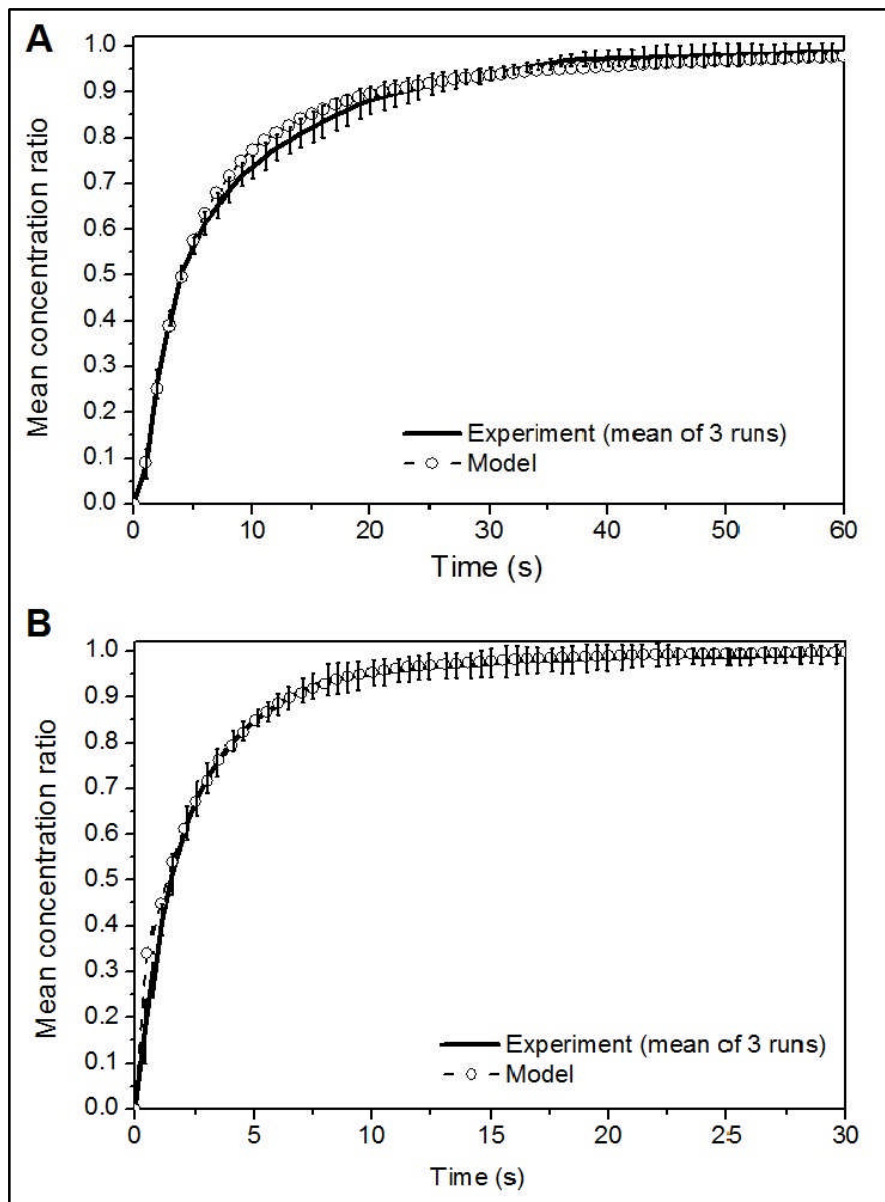


Figure 4-15 Comparative validation 2. Mean concentration ratio within the circular flow cell as a function of time for A) 1 mL min⁻¹, and B) 10 mL min⁻¹.

4.5.2 Flow field

4.5.2.1 Flow field development

The flow field describes the resultant flow response to the external pressures, fluid properties and flow domain geometry. The flow fields of the flow cell geometries studied in these investigations are considered here by

examining the proportional distribution of flow velocity, and flow direction for each case.

Figure 4-16 shows arrow velocity plots for two low flow rates (and therefore relatively low Reynolds Numbers, Re), 0.1 mL min^{-1} and 1 mL min^{-1} , for each of the four different flow cell geometries considered in the investigation. The arrow velocity plots present the predominant direction of flow across the flow domain, along with an indication of proportional flow velocity (indicated by the size of each arrow). For the three flow channel geometries (Figure 4-16 a-c) the flow can generally be described as following the contours of the flow cell from inlet to outlet. However, regions of relative low velocity can be seen in each case and for both flow rates. These are particularly prevalent, for example, in the corners of the square channel geometry. In this case, the plots also show that the size of these regions of relative low velocity increase with the increase in flow velocity.

The distribution of flow velocity can be examined more clearly by producing plots of the ratio of flow velocity in the x direction (u , i.e. direction of flow directly from inlet to outlet) to the maximum flow velocity (u_{max}) along a line that cuts the flow cell geometry in the y direction. Figure 4-17 shows such plots for three cut-lines at a single selected flow cell depth (0.5 flow cell total depth), whilst Figure 4-18 presents plots for a single cut-line at three different flow cell depths (0.25, 0.5 and 0.75 of flow cell total depth). Both Figure 4-17 and Figure 4-18 consider only the larger of the two flow rates considered in Figure 4-16.

These plots also provide information on the direction of flow, where a positive value indicates normal advective flow in the x direction and negative values indicate flow back towards the inlet, and thus the presence of circulatory flow. One purpose of producing these plots therefore is to examine whether the regions of low velocity observed in Figure 4-17 include regions of circulatory flow not readily visible from the arrow plots. The square flow channel geometry does demonstrate a distribution of flow velocity that is not steadily proportional across the flow channel width at the cut-line closest to the inlet (Figure 4-17A, line A), but no circulatory regions are indicated for any of the cut-lines. This indicates that circulatory regions (eddies) have not

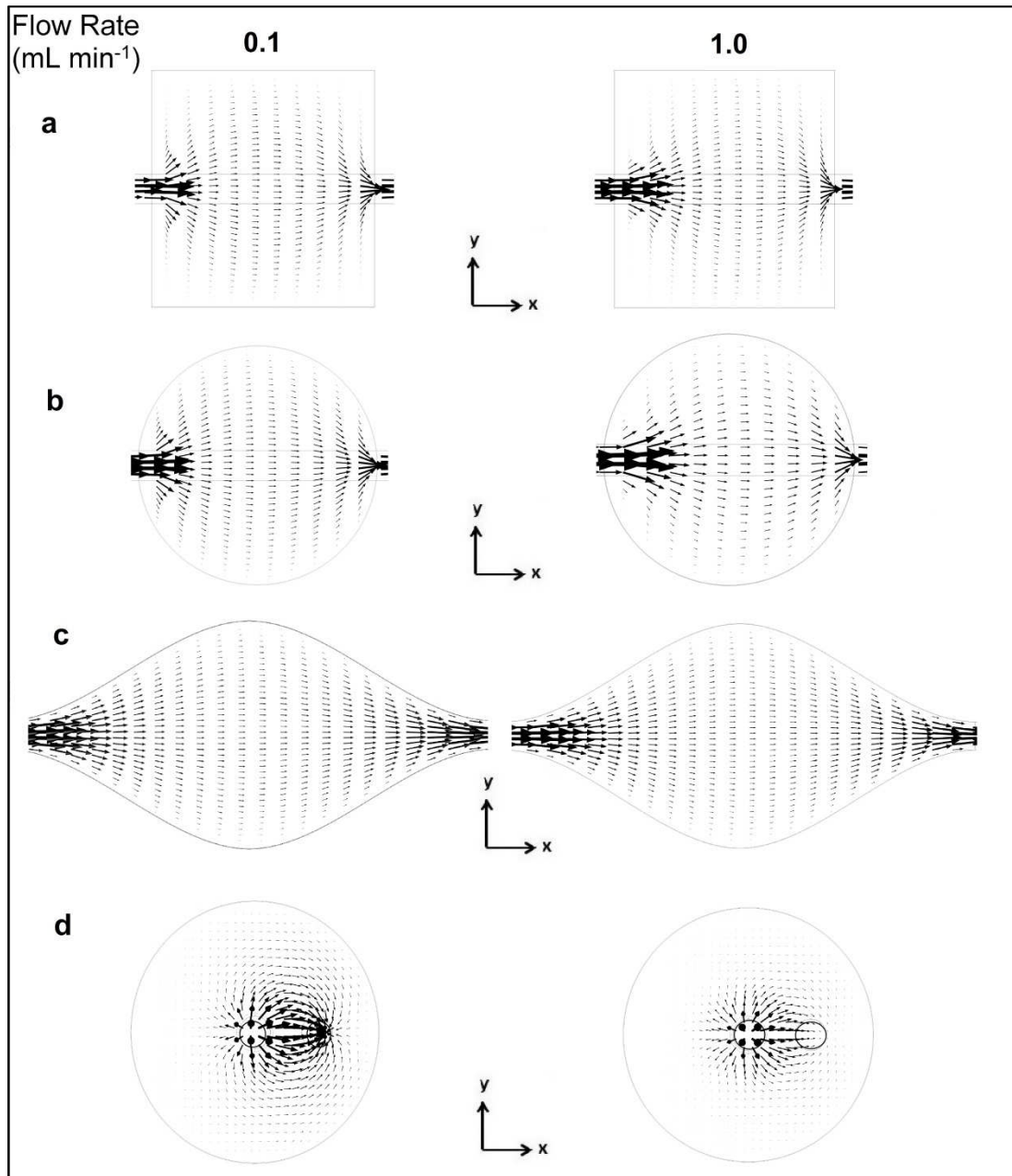


Figure 4-16 Arrow velocity plots at two selected 'low' flow rates. The same configuration settings were used to produce the arrow plots in each case.

developed to the extent of the flow domain represented by the cut-lines considered. It does not however exclude the possibility that the process of eddy development has commenced in the corners of the square geometry at this flow rate (1 mL min⁻¹) (this issue will be considered further in Section 4.5.2.2). The channel geometries featuring a more gradual rate of channel expansion (and contraction) do also show regions of relative low velocity (Figure 4-17b-c). However, the decreases in velocity from the channel centre line to the channel walls for these geometries are much

closer to the proportional velocity change that would be expected for laminar tubular flow, than is the case for the square geometry.

For comparison the results for the commercial flow cell geometry are also included in Figure 4-16 - Figure 4-18. It should be remembered that the geometry for this flow cell is quite different from the three channel geometries. The flow inlet is central to the flow domain and the outlet is positioned 2 mm from it in the x direction (e.g. Figure 4-17C). The flow field that develops is more complex than those of the flow channel geometries for these lower flow rates. Flow exits the inlet hole in all directions and this leads to flow both directly from the inlet to outlet in the central section of the flow domain, and flow from the inlet initially in the opposition direction from the outlet. For the latter flow, flow direction then reverses and accesses the outlet via the outer regions of the flow channel (Figure 4-16d & Figure 4-17C).

Because of the 3D nature of the flow domain, the flow field should also be considered with respect to any variation in flow at different flow domain depths (Figure 4-18). Two of the flow channel geometries and the commercial flow cell geometry were evaluated with respect to three-dimensional flow for a selected cut-line in the y direction (at 0.5 of the full length of the flow domain for the channel geometries, and at 0.25 of the full length of the flow domain for the commercial flow cell), and at three flow domain depths (0.25, 0.5 and 0.75 of the flow domain thickness). No significant variation in flow velocity distribution and flow direction (for the element of flow in the x direction, u) was observed between the three flow channel depths for the two channel geometries considered (Figure 4-18A-B). However, some variation in velocity distribution was observed for the commercial flow cell. In particular, a decrease in u/u_{max} was observed with respect to an increase in channel depth position for the flow towards the outlet at the outer regions of the flow domain (Figure 4-18C).

Cont'd over....

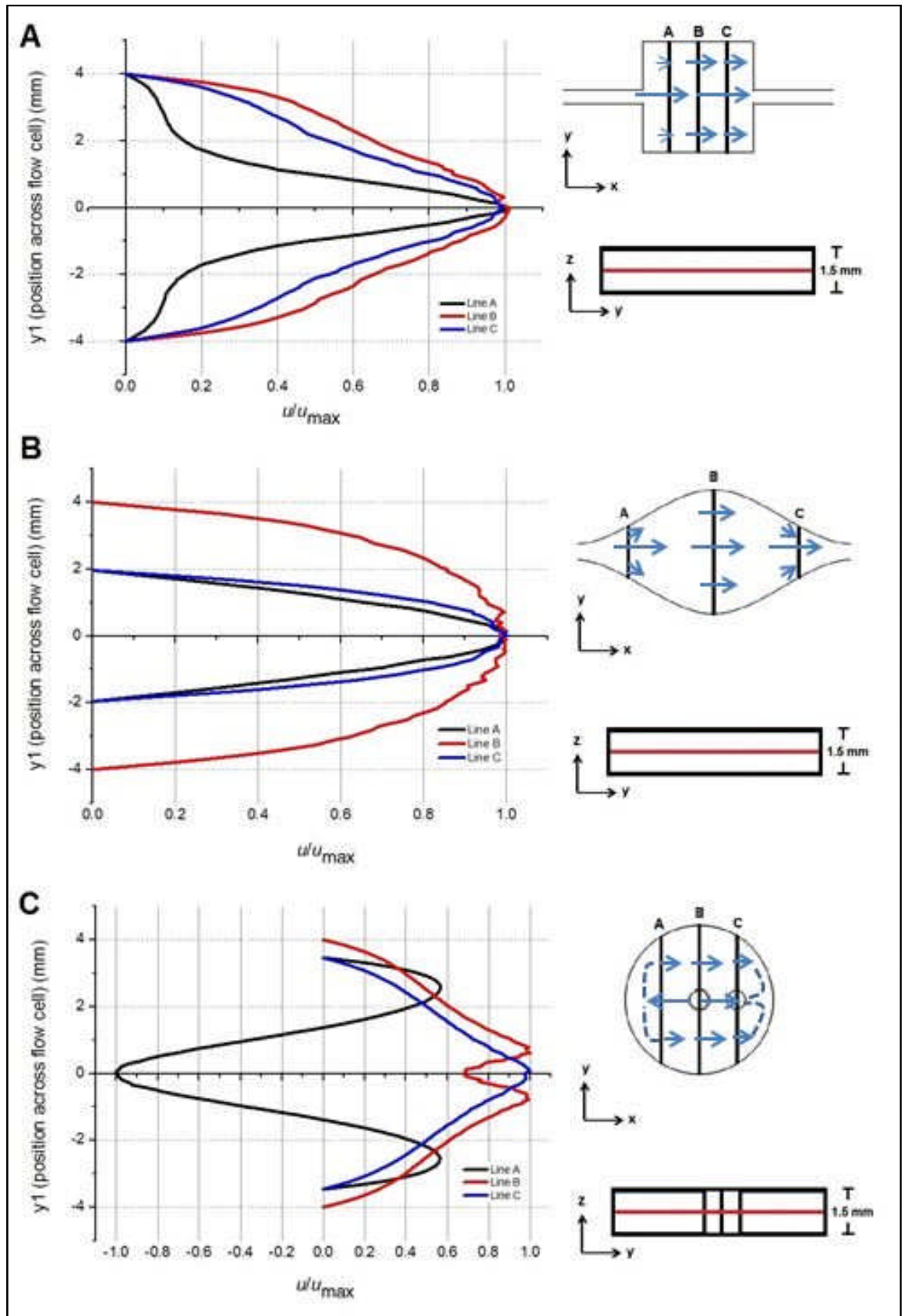


Figure 4-17 Flow velocity plots at an inlet flow rate of 1 mL min^{-1} . Flow velocity plotted as a ratio of flow velocity in the x direction and the maximum flow velocity along a line cutting the flow channel perpendicular to the flow, and at mid-depth of the 3D channel.

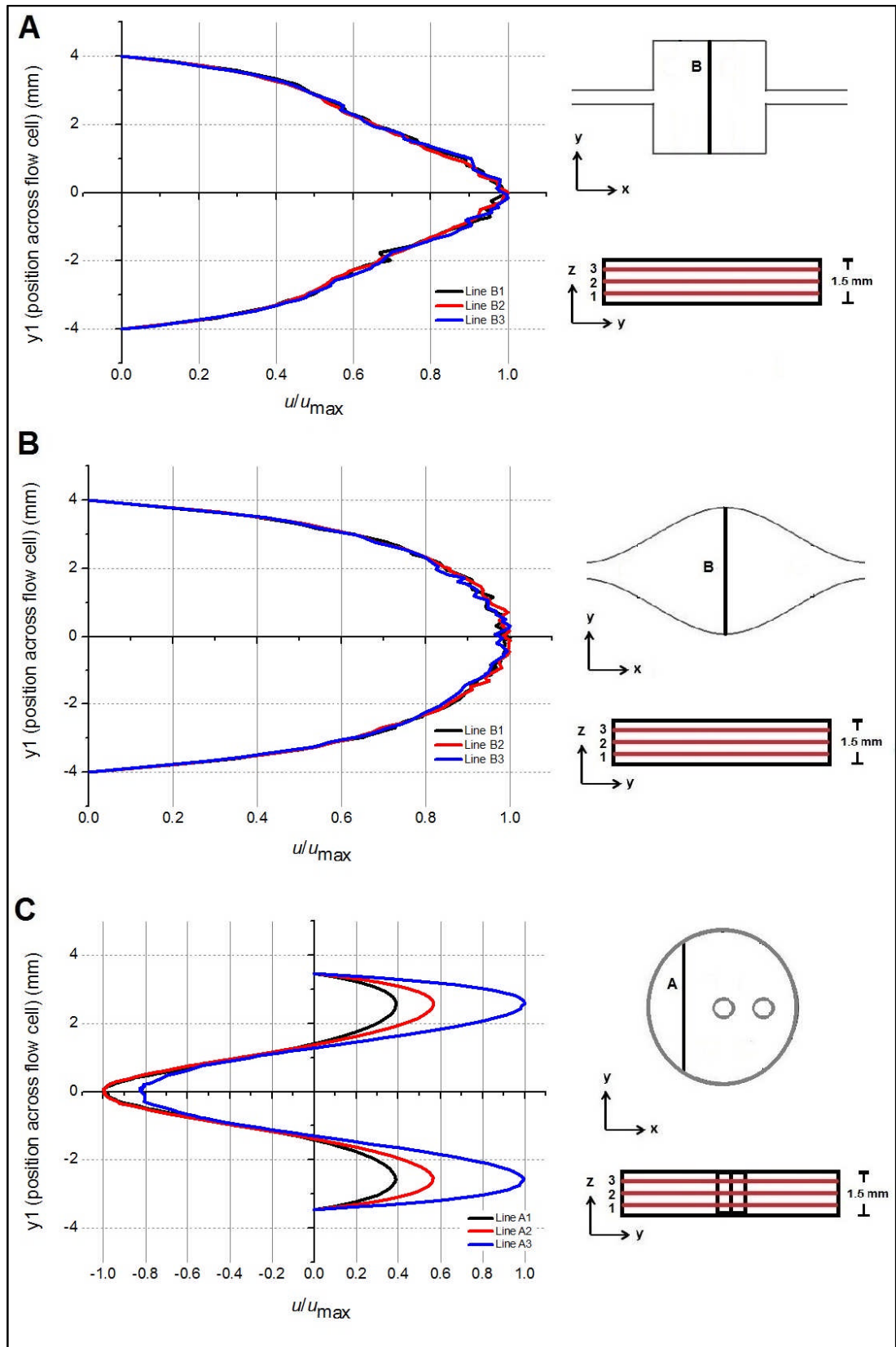


Figure 4-18 Flow velocity plots at an inlet flow rate of 1 mL min^{-1} . Flow velocity plotted as a ratio of flow velocity in the x direction and the maximum flow velocity along a line cutting the flow channel perpendicular to the flow, and at three selected channel depths.

4.5.2.2 Eddy and 3D flow development

The key observable feature in the flow channel geometries with increasing flow rate is the clear development of regions of recirculation (eddies), with development occurring either side of the central high velocity flow channel region (Figure 4-19, Figure 4-21A). It is clear also that eddy size increases with increasing flow rates, limited only by the dimensions of the constraining flow channel geometry (Figure 4-19). A comparison of the circular and iCell geometries indicates that, particularly at lower to medium flow rates, the relatively more gradual expansion (and contraction) of the iCell leads to a restriction in the rate of eddy growth with respect to increasing flow rate, although it clearly does not exclude eddy development altogether (Figure 4-19). Figure 4-21A highlights the very low relative velocity of the flow within these eddies, as presented here for the iCell geometry.

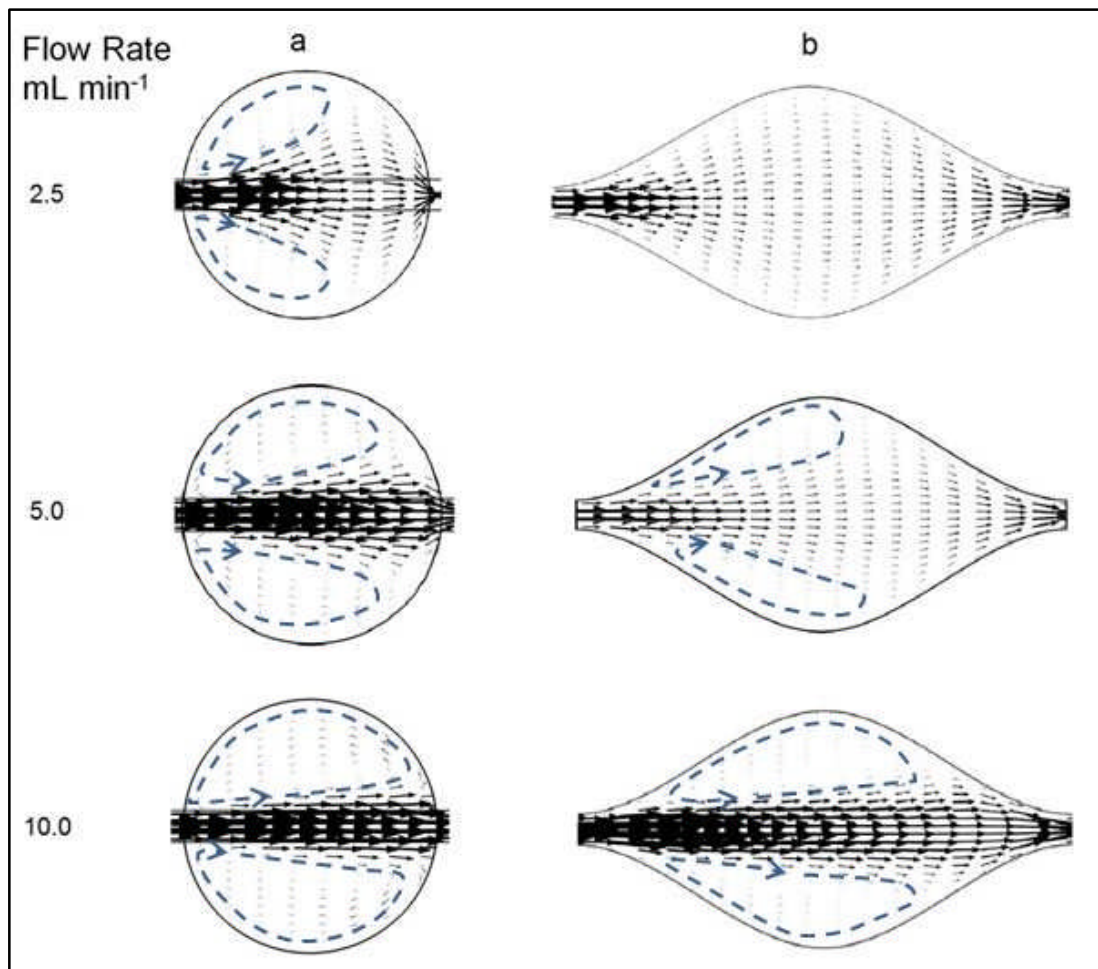


Figure 4-19 Arrow velocity plots at three selected 'medium' to 'high' flow rates, and for two selected flow channel geometries. The outline of eddies are superimposed to aid clarity.

For the square channel geometry, and by considering flow velocity along a cut-line within the expanded channel region that is close to the inlet channel, it can be seen (as suggested in Section 4.5.2.1) that regions of extremely low velocity eddies have developed within the corners of the flow channel at a low flow rate of 1 mL min^{-1} (Figure 4-20A). It is clear at the low flow rate the eddy is restricted to the corner region of the geometry, and does not extend further into the flow channel (Figure 4-20A). However, at the higher inflow rate of 5 mL min^{-1} the eddies within the corner are no longer distinct from larger eddies that extend to cover more than half of the length of the expanded flow channel region.

At higher flow rates, for example 7.5 mL min^{-1} , flow is observed within the commercial flow cell design that can perhaps be described as '3-dimensional flow'. By plotting flow velocity distribution at three flow channel depths, it can be seen that flow is predominantly in opposite directions at the deepest flow channel depth as compared to the shallowest (Figure 4-21B, Lines A1 & A3). This effectively suggests a 'turnover' of flow in the x direction of the flow domain. Meanwhile, the flow at the central channel depth demonstrates elements of lateral circulatory flow (Figure 4-21B, Line A2). In comparison, no difference is observed in flow velocity distribution between the three different flow channel depths at this higher flow rate for the iCell geometry. This indicates that eddies that have developed within the iCell flow channel are two dimensional only, with no apparent vertical component (Figure 4-21A).

Cont'd over.....

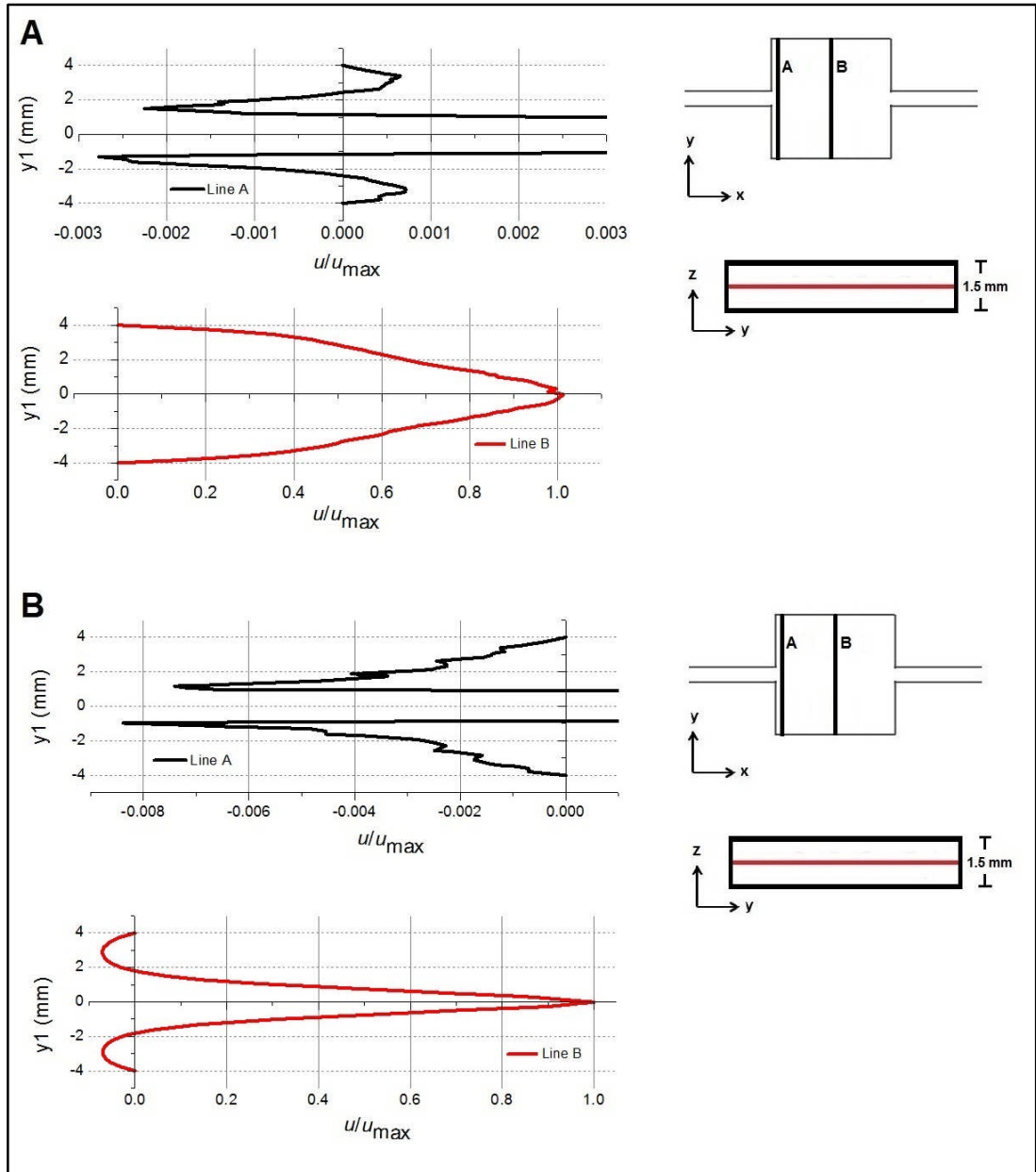


Figure 4-20 Flow velocity plots at an inlet flow rate of **A)** 1 mL min⁻¹ and **B)** 5 mL min⁻¹ for the square channel geometry.

Cont'd over.....

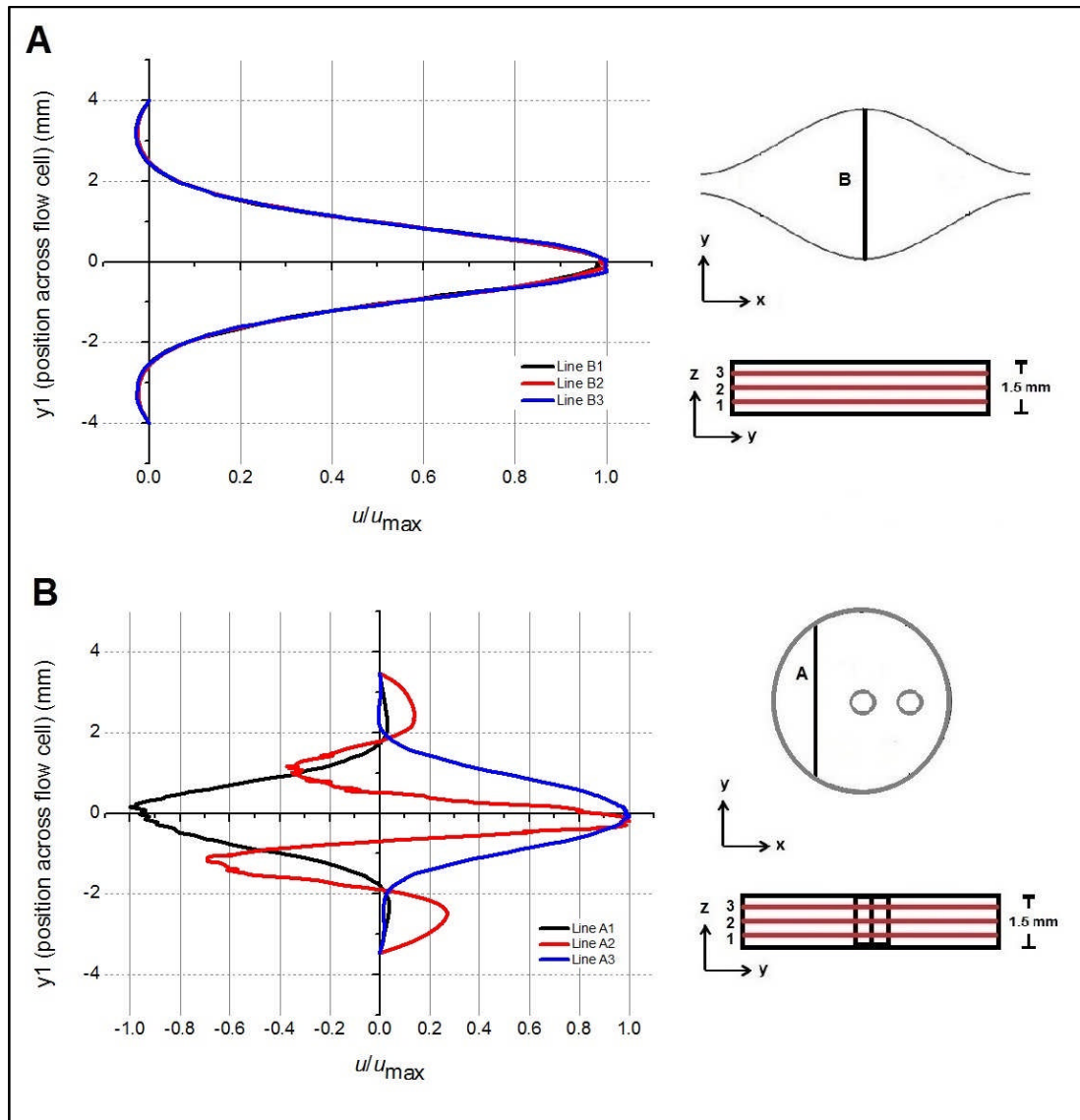


Figure 4-21 Flow velocity plots at an inlet flow rate of 7.5 mL min^{-1} . Flow velocity plotted as a ratio of flow velocity in the x direction and the maximum flow velocity along a line cutting the flow channel perpendicular to the flow, and at three selected channel depths.

Although a comprehensive study of the clearly complex flow field generated within the commercial flow cell is beyond the scope of this study, it is useful for comparative purposes to consider the three-dimensional aspect of the flow in a little more detail. Specifically, by examining flow velocity plots for a selected cut plane in depth view (i.e. in the 'z' direction), a preliminary assessment can be made of the nature of the flow 'turnover' established for a high flow rate as indicated in Figure 4-21. Figure 4-22 provides a 'side-on' view of the flow field at a low (1 mL min^{-1}) and high (7.5 mL min^{-1}) flow rate. Circulatory regions of flow in the depth plane were clearly observed at the higher flow rate (Figure 4-22B), and these are wholly absent at the low flow

rate (Figure 4-22A). Figure 4-22B suggests that there are three or four distinct circulatory regions for the cut-plane considered, but that they may be connected. A very preliminary assessment would be that that these are open eddies within the vertical 'depth plane'. However, much more detailed studies (beyond the scope of this study) would be required to confirm this and to provide a much more detailed picture of flow field development within the commercial flow cell.

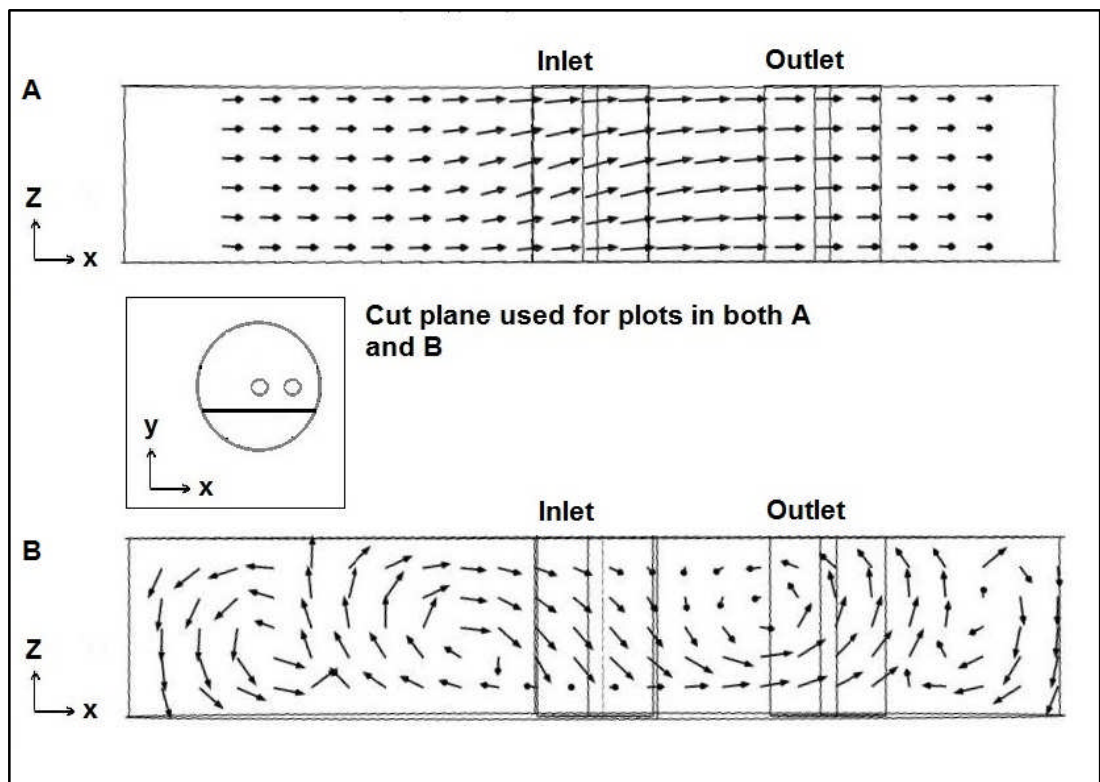


Figure 4-22 Normalised arrow velocity plots for the commercial flow cell at two selected flow rates: A) 1 mL min^{-1} , and B) 7.5 mL min^{-1}

4.5.2.3 Dilute species response to flow field

Finally with respect to assessing flow field development, it is useful to examine the response of the modelled dilute species to the underlying flow field under varying flow conditions. Figure 4-23 presents colour concentration maps for the three flow channel geometries, and for four selected flow rates. The underlying flow field is represented in the images by flow streamlines (the bottom half of each image), and all images represent a 'snapshot' of the flow simulation determined by considering the time taken for five flow cell volumes to have passed through the flow domain.

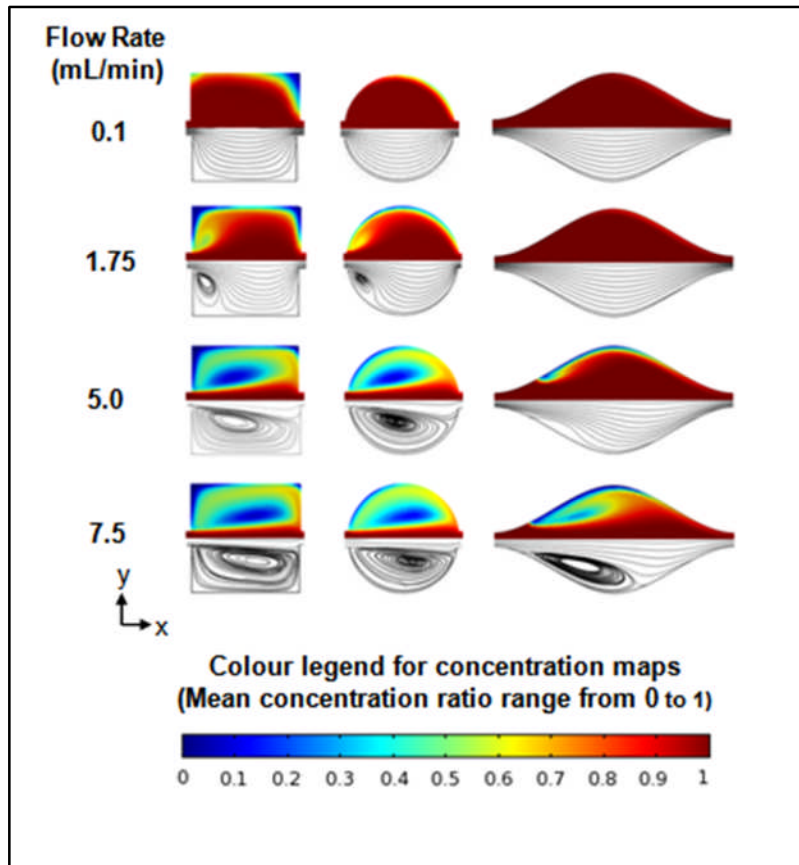


Figure 4-23 Computational results showing concentration maps (top) and streamlines (bottom), after 5 flow cell volume changes and taken through the mid-plane for four selected flow rates.

In general terms, there is a good correlation between the underlying flow fields and the pattern of dilute species concentration ratio distribution. For example, the low velocity regions within the corners of the square geometry (as identified by white space between streamlines) correspond well with low concentration areas in those regions. These plots also demonstrate clearly how the development and growth of eddies with increasing flow rate lead to the development of ‘islands’ of relatively low dilute species concentration. For the flow rates considered, eddy size increases with increasing flow rate (observable for the square and circular geometries in particular). Finally, the influence of flow cell geometry upon eddy development is also reinforced by these images. In particular, the development of eddies occurs at higher flow rates for the more gradually expanding iCell channel in comparison to either the square or the circular channel geometries (Figure 4-23).

4.5.3 Flow cell efficiency

The flow field responses presented in Figure 4-23 suggested that eddy development is restricted through the iCell design up to a flow rate of 1.75 mL/min. However, this is not sufficient in itself to provide evidence that this flow cell design and flow rate combination provides a 'better performing' flow cell. Therefore, it is still important to determine in a quantifiable way what impact the prevailing flow field development has upon the mean cell concentration of a target analyte in a real analytical flow cell system (which modelling of a dilute species represents), and for the full range of flow rates considered.

It is useful to think of the analyte response in terms of the efficiency of the flow cell in equilibrating the concentration of the analyte within the flow domain with that injected at the inlet of the flow cell. The mean analyte concentration within the flow domain as a ratio of the concentration is termed the cell concentration ratio (CCR). The 'efficiency' of the flow cell geometries with respect to the response to the injection of a dilute species (i.e. analyte) can be analysed in a number of ways. Three analytical approaches have been adopted here:

1) **Time study analysis** – the change in analyte concentration with respect to time for each of the geometries at a range of inflow rates. The performances of the four geometries are directly compared against each other.

2) **Flow throughput analysis** – the change in analyte concentration with respect to the number of fluid changes within the flow domain. This has the advantage of accounting for the differences of flow cell volume when conducting a comparative analysis. This analysis was also conducted with respect to the influence of changing flow conditions on each of the flow cell geometries separately, rather than being directly comparative. It therefore allows for an assessment of change in performance with increasing flow rates in each case.

3) **Time to reach a given concentration** – this allows a comparison of the four flow cell geometries across all of the flow rates considered in the study. Here the time and volume to reach a given target cell concentration ratio

(CCR) as a function of flow rate was examined. The target CCR's considered were 75% and 99% of analyte concentration within the flow domain with respect to that entering the flow cell at the inlet. The CCR of 99% was selected here to represent a CCR state approaching 100%, which would naturally be the aspiration for most biosensor analyses. The selection of a CCR of 75% was made to represent those occasions where it may be desirable to operate a deployed biosensor to the attainment of a lower CCR. The potential reasons for doing this will be discussed in Section 4.6.3.

4.5.3.1 Time study analysis

At the lowest flow rates (0.1 & 1 mL min⁻¹), the performance of the circular and iCell geometries are very similar, whilst the square geometry shows decreasing relative performance to these two geometries with an increase in flow rate from 0.1 mL min⁻¹ to 1 mL min⁻¹. The commercial flow cell geometry is significantly less efficient at these flow rates when compared to the three channel geometries (Figure 4-24A-B).

At a 'medium' flow rate of 5 mL min⁻¹ the iCell geometry once again provides the most efficient response, although here the commercial cell is competitive in terms of performance with the circular geometry and with the square cell performing badly (Figure 4-24C). However, at a relatively high flow rate of 7.5 mL min⁻¹ the performance benefits demonstrated by the iCell are no longer prevalent when compared to both the circular geometry and the commercial flow cell (Figure 4-24D).

Cont'd over...

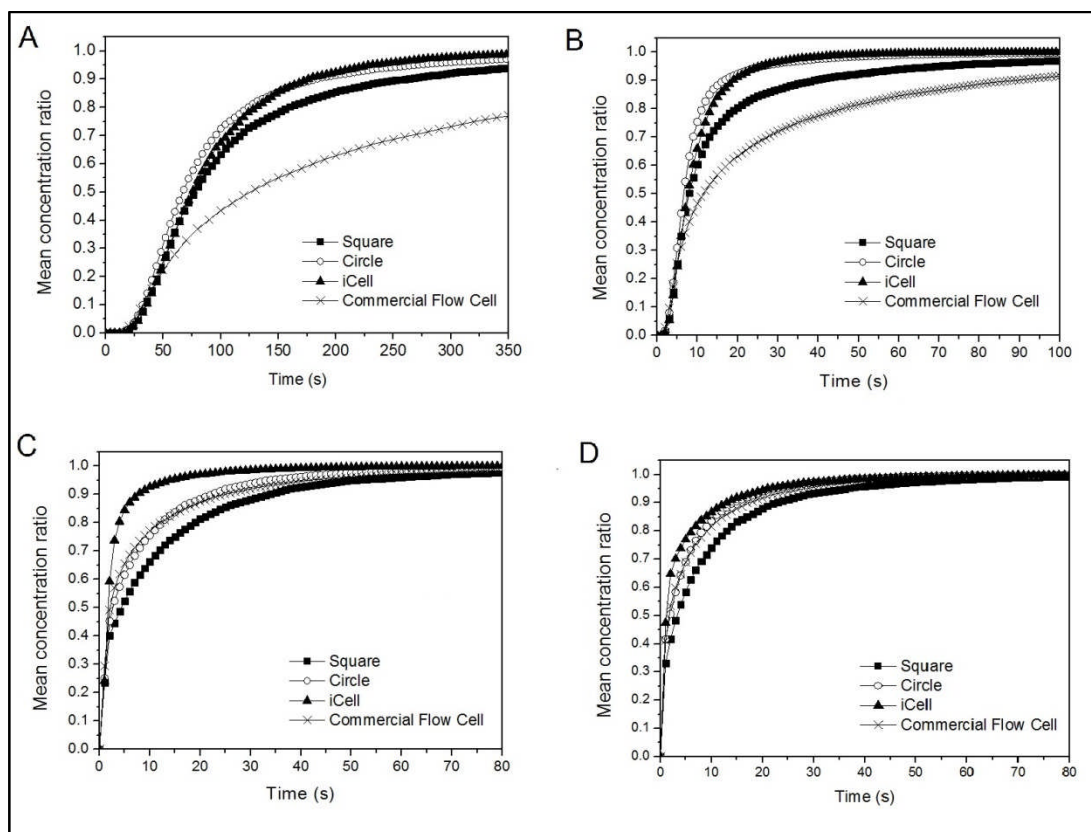


Figure 4-24 Temporal response of flow cell to injection of analyte for the four flow cell geometries at flow rates of (A) 0.1 mL min^{-1} , (B) 1 mL min^{-1} , (C) 5 mL min^{-1} , and (D) 7.5 mL min^{-1} .

4.5.3.2 Flow throughput analysis

Analysing flow throughput rather than response over time is a more accurate method of evaluating flow cell efficiency in this case, because it normalises the data with respect to fluid volume (which varies slightly across the different geometries). The efficiency of both the square and circular flow cell decreases with increasing flow rate for the lower range of flow rates considered (0.1 , 1 , and 5 mL min^{-1} in this case) but reaches what can be described as a ‘steady-state’ between 5 and 7.5 mL min^{-1} .

The iCell retains its performance level for the two lower flow rates, whilst the extent of decreasing efficiency at the two higher flow rates is lower than when compared to the other two flow channel geometries (Figure 4-25C). With regards to the commercial flow cell, a steady decrease in efficiency is observed across the four flow rates considered (Figure 4-25D). The commercial flow cell performance, whilst typically less efficient than the channel geometries is however more consistent in performance level across

the flow rates considered here. In all cases recirculatory flows (eddies) have a negative effect on the performance.

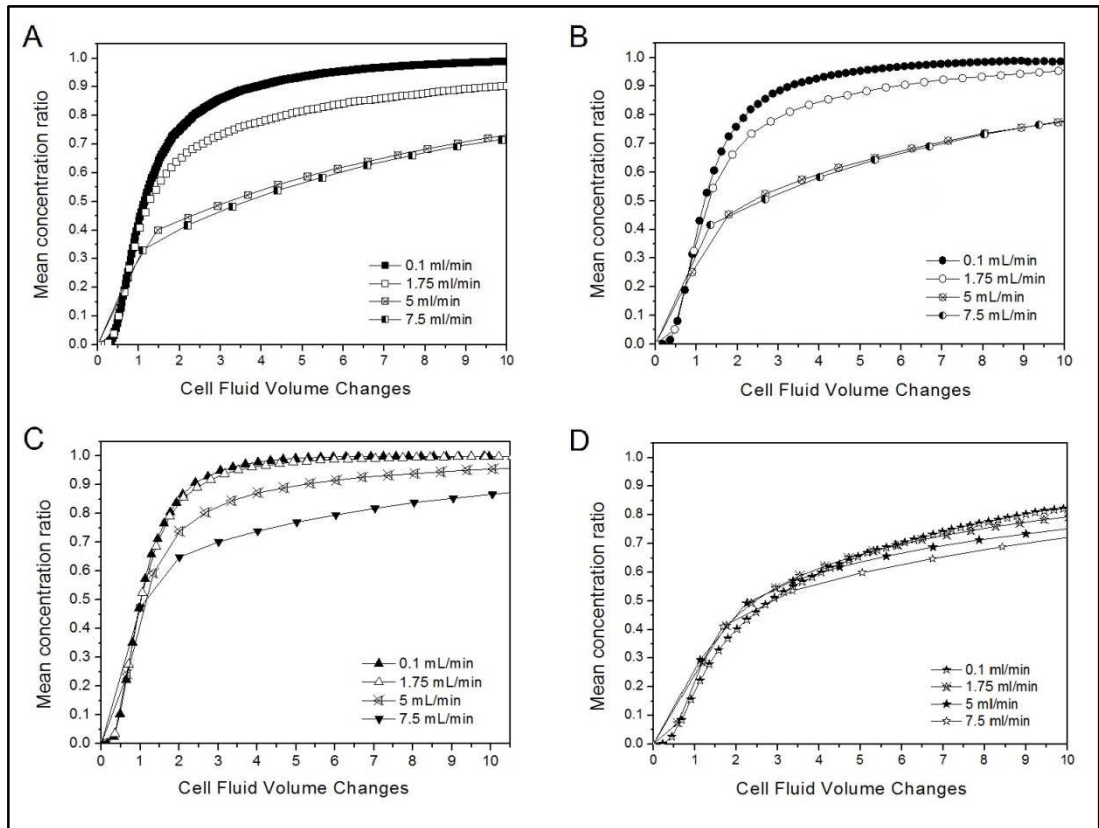


Figure 4-25 Fluid volume response of flow cell to injection of analyte at four selected inflow rates for (A) Square channel geometry, (B) Circular channel geometry, (C) iCell channel geometry, and (D) Commercial flow cell.

4.5.3.3 Time to reach a given concentration

The consideration of flow cell response for specified target cell concentration ratios (CCR's) allows for a direct comparison of flow cell performance across all of the inflow rates considered for this investigation (Figure 4-26).

The mean performances of the circular and iCell geometries are very similar up to an including a flow rate of 1 mL min^{-1} , after which there is a relative decrease in efficiency of the circular geometry up to and including a flow rate of 5 mL min^{-1} . The square geometry has a lower performance level than the other two flow channel geometries at all inflow rates. Also, the square geometry shows a rather gradual decrease in efficiency up to a flow rate of 2.5 mL min^{-1} followed by a sharp decrease beyond this flow rate (most noticeable in Figure 4-26B2).

At flow rates below 2.5 mL min^{-1} the commercial flow cell is much less efficient than all of the flow channel geometries, but is more efficient than the square channel geometry beyond 2.5 mL min^{-1} . The commercial cell is marginally the most efficient of all flow cell designs at the highest study flow rate of 10 mL min^{-1} , although the efficiency of all flow cell designs at this flow rate are much lower than at lower flow rates.

At all flow rates some regions within any given cell geometry will reach a given concentration of analyte quicker than others (e.g. locations aligned with the inlet respond more quickly than locations towards the edge of the cell). This is illustrated in Figure 4-26(A2) which compares the concentration of the analyte at the centre point of the flow cell to the mean whole-cell response for the circular and iCell designs.

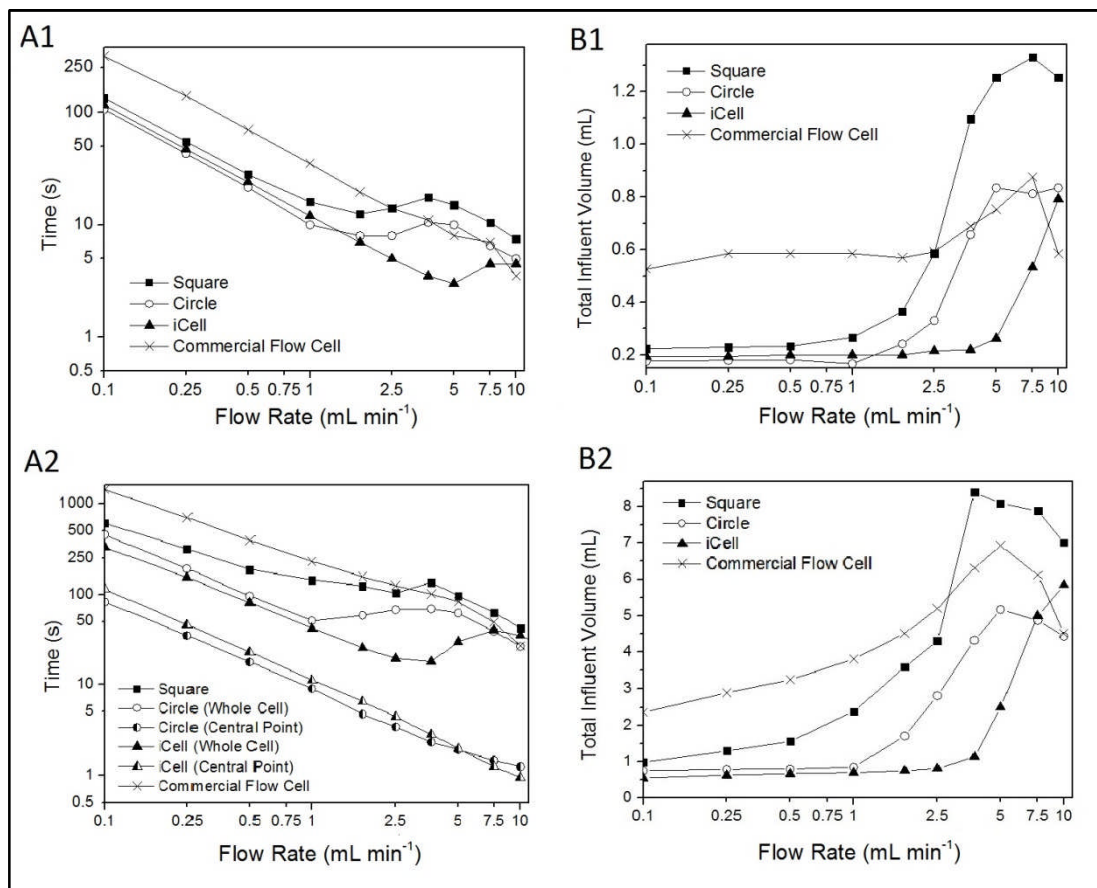


Figure 4-26 (A) Time taken and (B) required influent volume for cell concentration ratios of (1) 75% and (2) 99% of that of injected fluid (as a function of inlet flow rate). Also shown for (A2) is the response for a single point at the centre of the flow domain for the iCell and the circular cell.

4.6 Discussion

4.6.1 Validity of investigative approach

With the dual nature of this study, i.e. computational and experimental, it was vital that the independent validity of each of the investigative approaches could be established. This in turn allowed for a much stronger comparative validation process between the two investigative approaches.

For the experimental investigation, a linear response of measured illuminance with increasing fluorescent agent concentration was established for the concentration range of 0-100 μM (Section 4.2.2). Additionally, it was determined that the impacts of fluid pH variation and photobleaching upon the fluorescence response of fluorescein sodium effects were negligible in this study (Section 4.2.2). These outcomes provided confidence that the flow-fluorescence approach would provide a defensible and robust method of visualising and quantifying the flow response to variation in flow cell geometry and flow conditions.

For the computational investigation an extensive range of six different mesh configurations were considered in a mesh sensitivity study, and a preferred mesh setting selected (Section 4.3.2). With mesh studies further possible model accuracy gains have to be balanced in relation to computing time and computer memory needs. Although very small accuracy gains would most likely have been possible with access to even higher power computing (available high powered computers were used anyway for the finer mesh configurations), the mesh configurations had reached a sensitivity level that could be described as being within a 'reasonable margin of error'. Operation at the preferred mesh setting would therefore provided confidence that the computational results would be largely independent of mesh size. This in turn would allow for focus to be on ensuring that the numerical models were a strong representation of real flow channel geometries and real flow conditions.

The overall validity of the investigative approach was confirmed by directly comparing results from the experimental investigation with those of the computational investigation. Both qualitative and quantitative results

demonstrated a strong agreement between the two investigative methods (Section 4.4).

This provided overall confidence therefore that the investigative procedures used for the development of the flow cell design were robust in their development, and provided valid tools for the investigation conducted.

4.6.2 Advection and diffusion processes

4.6.2.1 Advection and diffusion relationship

The performance of each of the flow cell geometries is dependent primarily upon the relationship between advection and diffusion processes within the flow regime. Because diffusion is typically a relatively slow process (when compared to advection for channel flows of the dimensions used in this study), a flow regime for which solute diffusion is the dominant process will demonstrate a lower level of performance than a flow regime for which advection is dominant. It should be remembered that, in a flow channel, diffusion processes become more significant with the development and growth of eddies within the laminar flow because the transport of an analyte (i.e. the solute) into eddies can only occur through diffusion. However, when eddies are minimised or absent advection will be the dominant process (Section 2.5.2).

4.6.2.2 Flow domain geometry

For the three flow channel geometries at low flow rates, the flow largely follows the contours of the flow channel (4.5.2.1, Figure 4-16). For these flow conditions therefore advection will be the dominant process, and diffusion into eddies will be restricted to the very small eddies starting to develop within the corners of the square channel geometry (as identified in Figure 4-20A). However, the impact of the corner eddy development (and general low velocity corner flow) in the square geometry upon relative flow channel performance at 'low' flow rates of 0.1 and 1 mL min⁻¹ is already prevalent (Figure 4-24A-B).

With increasing flow rate, diffusion processes become more dominant as eddies develop and grow within each of the flow channel geometries. For the

circular and iCell geometries the process of eddy development is different to that of the square channel geometry. For these more gradually expanding channels, eddy development relates to a separation of flow beyond a critical flow rate and can be described as 'inertial eddies' (Scholle *et al.* 2008). This process of eddy development is typically preceded by the growth of regions of low relative velocity at the extremities of the expanded flow channel (as demonstrated for the circular and iCell geometries between flow rates of 0.1 and 1 mL min⁻¹ in Figure 4-16b-c). Eddies within the square channel geometry originate and expand from the corners of the flow channel, and can be described more accurately as 'corner eddies' (Moffatt 1964; Biswas *et al.* 2004).

What is clear from both consideration of flow field development (Section 4.5.2), and the subsequent flow cell performance (Section 4.5.3), is that the more gradual expansion of the iCell geometry restricts the growth of eddies relative to the other two flow channel geometries. Therefore, the iCell can be operated at higher flow rates, with no loss in flow cell efficiency, than either the circular or square geometries. Optimum operational flow rates for each will be presented in Section 4.6.3.1.

The performance of the commercially available flow cell was significantly poorer than either the circular cell or the iCell for all but the highest flow rate despite the cell having a smaller internal volume. It was apparent for the commercial cell that large regions of relatively low velocity flow develop within the flow domain at lower flow rates (e.g. Figure 4-16d). It is a reasonable assumption therefore that diffusion of analyte is a more important process for solute transport into these low velocity areas. At the highest flow rates considered however, the 'turnover' of flow in the commercial flow cell, identified preliminarily as open eddies in the vertical plane (Section 4.5.2.2), does provide marginal performance advantages when compared to the flow channel geometries dominated by eddies in the horizontal plane at these higher flow rates.

4.6.3 Practical operational considerations

4.6.3.1 Flow cell operations

There are clear advantages to operating a flow cell close to the optimum point prior to eddy development. The cell response will be independent of the diffusion coefficient of the analyte, and relatively insensitive to slight variations in flow rate. For the circular flow cell this optimum occurred at a flow rate of 1 mL min^{-1} , when the total influent volume was 0.85 mL and the injection time was 51 seconds. For the iCell the optimum was at a flow rate between 1.75 and 2.5 mL min^{-1} , when the total influent volume was between 0.75 & 0.81 mL and the injection time was between 26 and 20 seconds. Thus the iCell performed best out of the cell geometries considered, both in terms of the smallest influent volume required (least waste produced) and shortest injection time (the period for which the biosensor is exposed to a varying analyte concentration).

An additional consideration when optimising a flow cell operating protocol for practical deployment is the operating environment. Automated systems which are to be deployed remotely in the field, for example, will be constrained by the need to minimise effluent volumes (since this may have to be stored, depending on local regulations) and power usage.

4.6.3.2 Implications for sensor operation

The selection of an appropriate operating protocol for a flow cell will depend on a proper understanding of the biosensor kinetics. The rates of ligand-receptor association (k_a) and dissociation (k_b) must be considered relative to the flow cell response rate. Where k_a and k_b are of similar magnitude (whether fast or slow relative to the flow cell response rate, e.g. Dai *et al.* 2008; Conroy *et al.* 2010) the biosensor will equilibrate with the final cell concentration, and a robust measurement can be made. Therefore the main operational consideration is to ensure that the desired CCR is reached (e.g. 99% of influent concentration). A sensor with fast kinetics relative to the flow cell response rate will respond “instantaneously” to the cell concentration, but when the kinetics are slow (e.g. Stubenrauch *et al.* 2009) time for equilibration must be allowed once the cell reaches the desired CCR.

Sensors where ligand-receptor association is fast in comparison with ligand-receptor dissociation are more problematic. The ratio k_a/k_b (equal to the distribution coefficient, K_d) is a measure of how the analyte partitions between the sensor surface and the solution when equilibrium is reached. A high k_a/k_b value implies more analyte association with the sensor for a given solution concentration than a low k_a/k_b value. Thus high degrees of surface association, where the sensor becomes less sensitive to differences in solution concentration, can be reached with relatively modest solution concentrations. Operating this type of sensor with modest or high solution concentrations at a high CCR will give a small dynamic range. However, with better understanding of the flow dynamics within the cell it may be possible to operate such sensors as “accumulation sensors” where the flow cell is briefly operated for achievement of a lower CCR value, flow is ceased and the sensor is allowed to equilibrate. The solution concentration can then be estimated from the sensor response using a cell factor.

4.6.4 Contribution to field of study

4.6.4.1 Expansion of subject knowledge

The investigations conducted as part of this study apply the principles of channel flow and eddy development to the design geometry and performance efficiency of flow cells for the first time. Demonstrated here is that the flow channel geometry is an important consideration in flow cell design. Additionally, it has been shown through a comparative study, a well-designed flow channel flow cell has operational performance advantages over a commercially available ‘wall-jet’ style flow cell.

Cooper and Compton (1998) considered the impact of analyte diffusion to the electrode surface on biosensor response. For their work however, flow velocity was assumed to vary parabolically with distance from the sensor surface (at the centre of the flow domain). This study has confirmed that this is not an unreasonable assumption at low flow rates (i.e. low Re), albeit that it introduces an implicit margin of error with respect to flow cell performance. Additionally, it is clear that the work of Cooper and Compton (1998) did not consider the impact upon sensor equilibration of the mean analyte/solute

concentration of the entire flow domain (as has been done here). Their focus was upon diffusion effects in the immediate vicinity of the active sensor surface. These investigations expand on Cooper and Compton (1998) work by explicitly considering the influence of flow channel geometry on understanding mean flow domain analyte concentration for given flow conditions (within a defined range of flow rates). Furthermore, an inverse correlation between the rate of flow channel expansion and the growth of eddies with increasing flow rate that had not previously been specified in publication has been established.

With respect to the (validated) numerical modelling approach to flow design, previous studies have focussed primarily on the reaction kinetics of a specific biosensor system (e.g. Lammertyn (2006)) rather than taking a more general view on the influence of flow cell design upon cell performance.

4.6.4.2 Scope of investigations

One potential limitation to these investigations relates to access to higher powered computing (HPC) for the computational investigation. However, it should be noted that high powered computing was utilised for those simulations featuring finer mesh sizes, and further gains could only be achieved by access to HPC resources not readily available at the time of the study. Furthermore, the results that were obtained from the computational validation exercise did demonstrate a good level of mesh independency and any further gains would be small.

Other aspects of the investigations which may be identified as limiting the scope of the study are the range of flow conditions (i.e. inflow rates) utilised in the numerical and experimental investigations, and the range of flow cell geometries considered in the study. The range of inflow rates selected for the computational investigation was chosen purposely to exceed the range of flow rates 'typically' used for flow cell sensor investigations. Typical rates used were in the range 1-2 mL min⁻¹ (but universally without any scientific rationale for their use), based upon the author's own personal lab experience and a range of published literature. The computational investigation for study considered flow rates in the range 0.1 – 10 mL min⁻¹. Since the experimental investigation was a much more time intensive

process, two flow rates that represented both the extremes of the computational investigation range, and included at least one flow rate that was 'typically' utilised in flow cell investigations (1 mL min^{-1}) were selected.

The main focus of the fluid delivery system optimisation process was to investigate flow cells of the flow channel type, and in particular the influence of varying rates of flow channel expansion. The three different channel designs, which included the sharp channel expansion case (i.e. the square geometry), a medium rate of channel expansion (the circular geometry) and a bespoke design with a more gradual expansion rate (the iCell design) were sufficient to demonstrate the extent of any influence. In addition, a commercially available Dropsens flow cell design was specifically chosen for inclusion in the study because it was probably the most well-known commercial flow cell product currently on the market, and its design was significantly different to that of the flow channel geometries considered here.

4.7 Chapter summary

4.7.1 General summary

Each of the two investigation procedures for the fluid delivery system optimisation process was carefully designed to ensure that the two approaches were demonstrably compatible, and would enable both qualitative and quantitative comparison of investigative results for validation of the overall investigation process. Additionally, independent validation processes for each of the two investigation procedures were built into the fluid delivery system optimisation process. The results of both the independent validation processes for each investigation procedure and the overall comparative validation provided evidence that the investigative approach was quantifiably robust.

The experimental and numerical results showed that the behaviour of a flow cell, measured in terms of its response to the incoming fluid, is critically dependant on both the shape of the flow cell and the flow rate of the influent.

If a channel flow cell is operated beyond an optimum flow rate, the development of regions of circulatory flow (eddies) will occur and the increasing influence of diffusion processes (over advection processes) will lead to a decrease in flow cell performance. By controlling the rate of flow channel expansion, the development of eddies can be restricted at lower flow rates, leading to a more efficient flow cell.

4.7.2 Operational protocol recommendations

The headline operational protocol recommendations identified through the investigations described in this chapter are summarised below:

- The **flow channel design is recommended** above the commercially available 'wall-jet' flow cell design, because of demonstrated enhanced relative performance across a broad range of operational flow rates.
- Of the flow channel geometries considered, the more gradual expansion and contraction of **the iCell design is recommended**,

because of its relative higher performance due to relatively restricted eddy development with increasing flow rate.

- An operational **flow rate range for the iCell of 1 to 2.5 mL min⁻¹ is recommended**, because of the consistent performance in terms of fluid volume throughput to achieve target analyte concentration ratios within this range. Lower flow rates could be utilised for very similar performance achievement, but would add unnecessary operational time.

CHAPTER 5

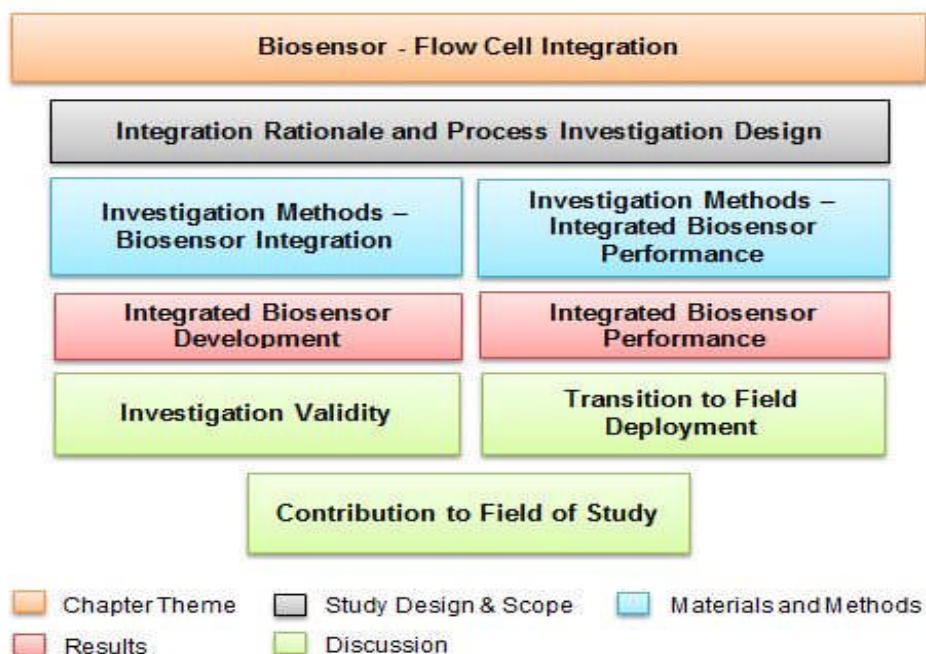
Biosensor – flow cell integration

Chapter 5 Biosensor-flow cell integration

5.1 Chapter introduction

Following the development of the optimised fluid delivery system (Chapter 3), the next step towards the development of an automated water monitoring system is to consider the integration of a specific sensor within the fluid delivery unit. The sensor selected for this purpose was the uranyl biosensor developed by Conroy *et al.* (2010), and as described in Section 2.4.3. This part of the project was initially approached in a manner similar to that used for the fluid delivery system optimisation process, by constructing an informed rationale for the integration process and the identification of the key drivers and principles for the integration investigation process. However, whilst a general outline for the integration investigation was developed at the planning stage, the results of preliminary biosensor performance investigations were to play a much more significant role in influencing the nature and direction of the investigation (particularly when compared to the fluid delivery system investigation process).

Chapter Outline Map



5.2 Biosensor-flow cell integration process design

5.2.1 Rationale for integration, and investigative scope

The uranyl biosensor to be deployed was developed by Conroy (2012) as described in Section 2.4.3. The construction and analytical protocol developed by Conroy (2012) for the biosensor therefore naturally provides a suitable basis for investigation into the integration of the sensor unit into the optimised fluid delivery system. However, the investigations conducted by Conroy (2012) did not extend to full trials into methods of practical deployment. A limited study into biosensor development on screen-printed electrodes was completed, but the results did not replicate those achieved using a more traditional electrochemical investigation setup (Section 2.4.3).

Also, for the main biosensor development work using P3 silicon wafer gold electrodes, the mean analyte-impedance response presented by Conroy effectively showed a saturation of the sensor at analyte concentrations beyond $\sim 10^{-9}$ M (Section 2.4.3, Figure 2-8). However, these investigations were conducted within a vessel containing a relatively large volume (~ 30 mL) of analyte solution, which may have contributed to this response. Therefore, an investigation that examined the biosensor analyte-impedance response within the substantially smaller flow cell volume (~ 0.2 mL) was appropriate.

Furthermore, the transition from a laboratory-tested device (proof of concept) to practical field deployment for biosensors, and impedimetric biosensors in particular, clearly presents continuing challenges (as outlined in Section 2.4.6). Therefore, a rationale for integration and scope for investigation was developed that identified those areas of biosensor construction and operation which provide the most likely barriers to successful biosensor-flow cell integration:

A) Physical transducer

It is important to differentiate between a physical transducer and the biosensor which is based upon it. The transducer converts a biorecognition event on the surface of the biosensor into a measurable signal which can be

read and analysed via an analytical instrument (e.g. a potentiostat). In the case of the uranyl biosensor, the biorecognition event is the binding of the uranyl ion analyte to the JG-A12 surface layer protein, which acts as the bioreceptor element of the biosensor (Section 2.4.3).

The uranyl biosensor is an impedimetric biosensor (the different types of electrochemical biosensor were described in Section 2.4.2). This means that the analytical measurement is based upon a change in impedance due to the biorecognition event, as measured through the biosensor/transducer unit.

The type of physical transducer (electrode) used to integrate the biosensor into the flow cell was identified as a valid area of investigation. Firstly, because the investigation of uranyl biosensor construction upon screen-printed electrodes (SPE's) by Conroy (2012) was limited to study of a single batch of electrodes, it was decided that some further investigation of SPE's was appropriate. Furthermore, because early SPE investigations by Conroy (2012) showed significant batch variability, and electrode degradation, with respect to electrode cleaning processes the study was never developed into one which examined complete uranyl biosensors constructed upon SPE's (Conroy 2012). Whilst offering such an opportunity, the investigation for this study would also be conducted in a manner that specifically considered biosensor quality and performance, with respect to deployment within the optimised flow cell unit from the outset.

After an unsuccessful trial of uranyl biosensor development upon screen-printed electrodes by Conroy (2012), this study went on to investigate an alternative transducer surface (Section 5.3.1.1).

B) Biosensor Construction

The development of the uranyl biosensor by Conroy (2012) with respect to selection of chemical platform for the biorecognition element, and the biorecognition element itself, had included comprehensive investigations towards an optimal design. Furthermore, Conroy (2012) presented the results of successful trials of this optimal design (summarised in Section 2.4.3). Therefore the investigative plan for this study did not include any

substantial revisiting of the biosensor construction approach, as this would have required a separate full project.

Additionally, the scope of this investigation did not extend to any consideration of developing alternative sensors (to Conroy's uranyl biosensor) for aqueous uranyl measurement, of either the same or different biosensor types. This again would have required an entirely new full study.

C) Biosensor Performance

Biosensor performance was identified as the key area for investigation for this study. First, the investigation considered whether a calibratable electrochemical biosensor response to target analyte concentration (uranyl solutions), could be developed within the optimised flow cell unit. Furthermore, the regeneration capabilities of the biosensor were investigated as part of this process. For the deployment of the biosensor within an automated monitoring system, regeneration was a key factor in determining whether such biosensors could produce reliable measurement results with repeated use, or if they were restricted to being single-use units. Along with the consideration of performance repeatability of biosensors constructed upon different electrode chips, this investigation also examined regeneration of the biosensor upon a single electrode chip, through the complete removal of the biosensor and regeneration of the surface. This was because Conroy (2012) did not investigate this aspect.

5.2.2 Integration process design strategy

Due to uncertainties associated with the integration of the uranyl biosensor into the optimised flow cell (as described in Section 5.2.1), the integration process needed to be more flexible than that used in the flow cell design optimisation process (Chapter 3). An outline investigative structure was developed that could accommodate changes in investigative direction based upon preliminary results (Figure 5-1).

Flow Cell-Biosensor Integration Investigation Process

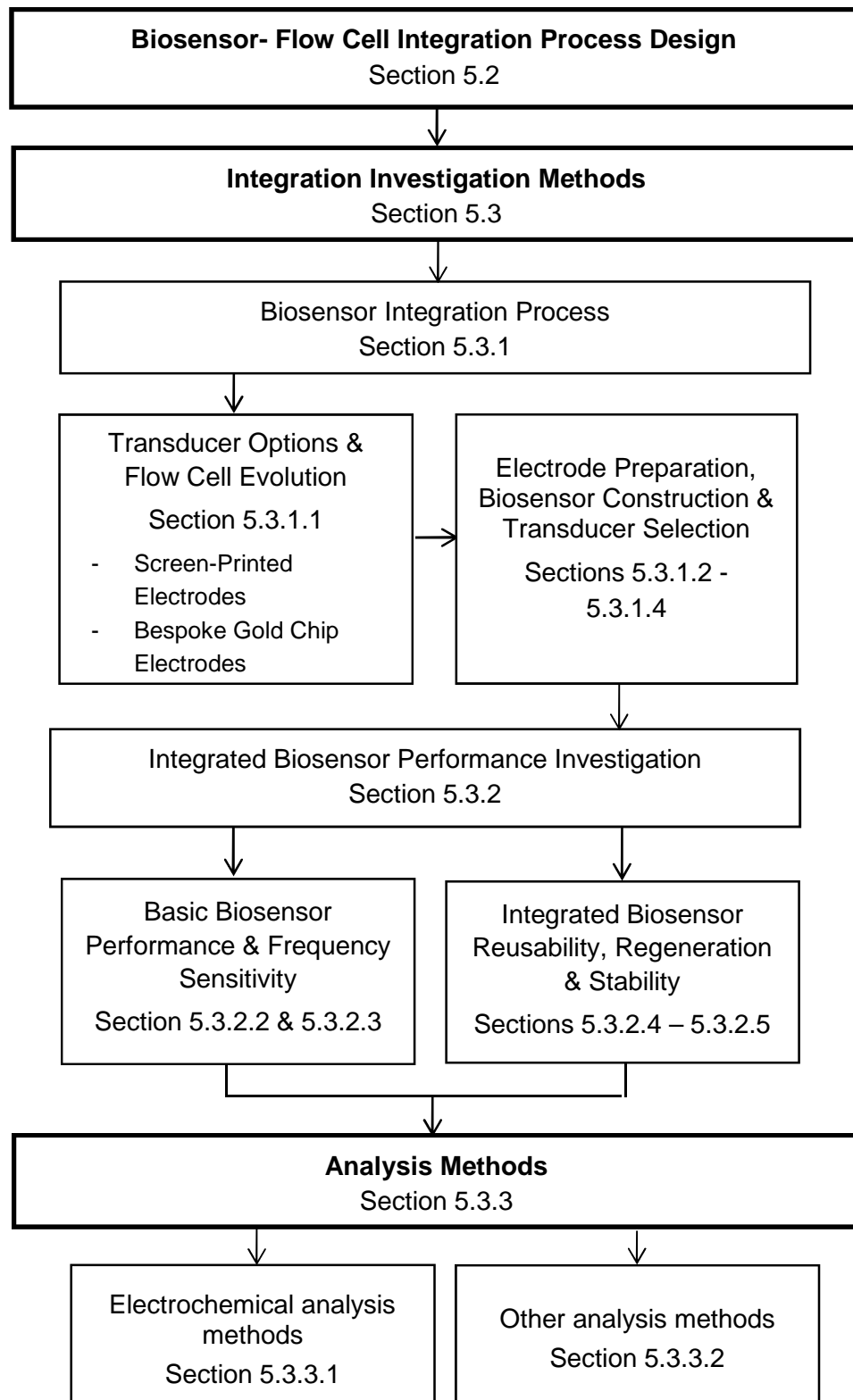


Figure 5-1 Flow cell-biosensor integration investigation process outline

5.3 Integration investigation methods

5.3.1 Biosensor integration process

The investigation into the biosensor integration process had two components:

- *Physical transducer options and flow cell evolution*

A consideration of two different types of physical transducer through which to integrate the biosensor into the flow cell unit, and the associated necessary development of the bespoke optimised-design flow cell (Chapter 3).

- *Physical transducer selection method*

An investigation was conducted using fully constructed uranyl biosensors upon each of the two electrode types, and a preferred method was selected. The preferred physical transducer option was then employed for all subsequent investigations i.e. those related to biosensor performance.

The methodology applied to these two components is presented in the following sub-sections. This includes the electrode preparation and biosensor construction methods employed.

5.3.1.1 *Physical transducer options and flow cell evolution*

It should be noted that the term *physical transducer* here refers to the three electrode system used to transform the biosensor-analyte binding event into a measurable signal (see Section 2.4.1), and includes the working electrode *transducer base or substrate* upon which the biosensor is constructed.

The two different physical transducer types considered for the biosensor integration process were a) custom-made commercially-sourced screen-printed electrodes (self-contained three electrode units), and b) bespoke gold chip electrodes set within a polycarbonate block. The latter was operated together with reference and counter electrodes independent of the working electrode block (described in further detail below).

Custom-made commercially-sourced screen-printed electrodes

Screen-printed electrodes were sourced from Dropsens (Oveido, Spain). The electrode design was based upon a commercially available electrode (Dropsens C223AT, Section 2.4.4), featuring a 1.6 mm diameter gold working electrode upon which the uranyl biosensor would be constructed. A gold counter electrode and a silver/silver chloride reference provided an 8 mm diameter 'active region' that, together with the working electrode, completed the *three electrode system* (Section 2.4.2). However, to ensure that the electrode provided an uninterrupted flow surface within the iCell flow cell design, a bespoke-sized ceramic substrate was designed. The bespoke substrate developed measured 30 mm x 30 mm, whilst electrode thickness was retained at 0.5 mm (Figure 5-2).

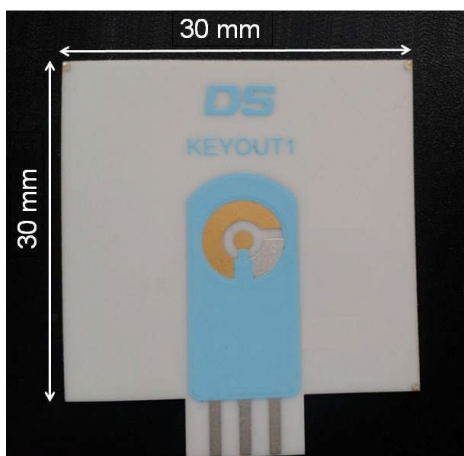


Figure 5-2 Dropsens C223AT screen-printed electrode on bespoke 30 mm x 30 mm ceramic substrate. The thickness of the electrode was 0.5 mm.

A new flow cell was constructed to accommodate the bespoke-size screen-printed electrode, for which a 0.5 mm thick recess was cut into a polyoxymethylene (POM) base (Figure 5-3A). A recess of 1.5mm thickness with dimensions 30 mm x 20 mm was cut into the underside of a PMMA flow cell top. Into this recess a PTFE gasket with matching dimensions was fitted, into which the optimised iCell flow channel geometry was cut (Figure 5-3B). Inlet and outlet holes of 1 mm diameter were drilled into the PMMA flow cell top block, with these holes expanding to 6mm diameter at the top to ultimately accommodate ¼"-28 UNF threaded nuts for the connection of

fluidic tubing. The flow cell/electrode unit was sealed watertight with four M6 socket hex-cap screws (Figure 5-3C).

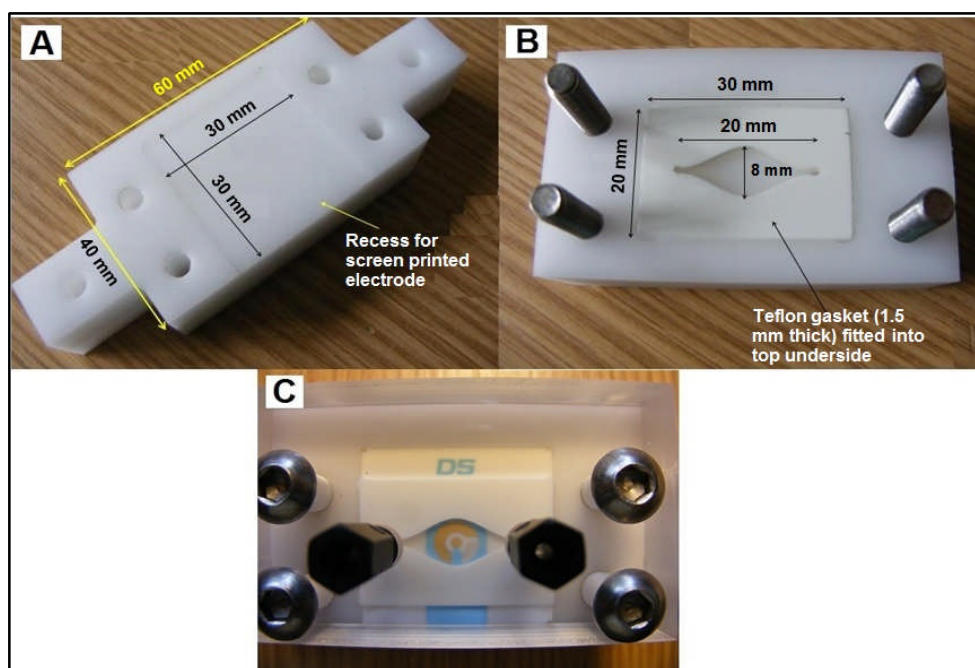


Figure 5-3 Flow cell evolution 1. Integration of bespoke screen-printed electrode: A) base, B) top, C) plan view of complete flow cell-electrode unit.

Bespoke gold chip electrodes

The bespoke electrodes featured a 1.6 mm diameter gold chip set centrally within a polycarbonate (PC) block of dimensions 30mm x 30 mm x 5 mm. The gold chip was set into the block using an epoxy resin, and a pure copper connector was soldered onto the gold chip (Figure 5-4).

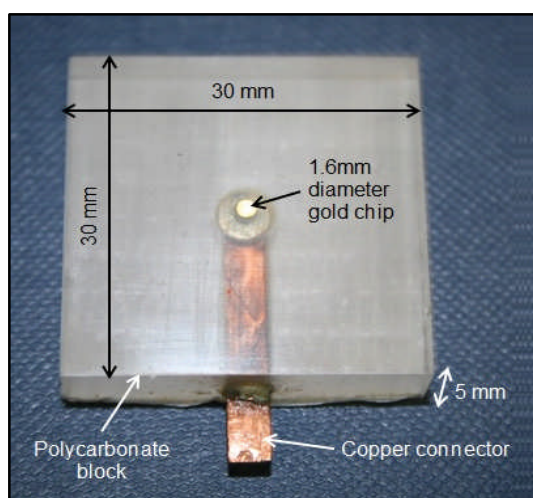


Figure 5-4 Bespoke electrode unit featuring a gold chip embedded into a polycarbonate block.

Clearly, unlike the screen-printed electrode, this bespoke electrode unit did not constitute a complete three-electrode electrochemical transducer. It was therefore necessary to further modify the flow cell unit to incorporate a counter and reference electrode, to form a self-contained electrochemical cell (Figure 5-5). Additionally, the recess within the flow cell base was deepened to accommodate the thicker bespoke gold chip electrode. For the counter electrode a ~2 mm diameter hole was drilled through the flow cell top unit and a 2 mm diameter platinum rod of 2.5 mm length was fixed into position using epoxy resin. For the reference electrode, a ~2.5 mm diameter hole was drilled through the flow cell unit top at the bottom of which was placed a small rubber O-ring. This hole would be used to accommodate a removable glass-barrelled micro reference electrode, sourced from Microelectrodes Inc. The counter and reference electrode holes were drilled to be positioned 1 mm either side of the gold chip working electrode, in a direction perpendicular to direct flow between the inlet and outlet, once the whole electrochemical flow cell was assembled (Figure 5-5).

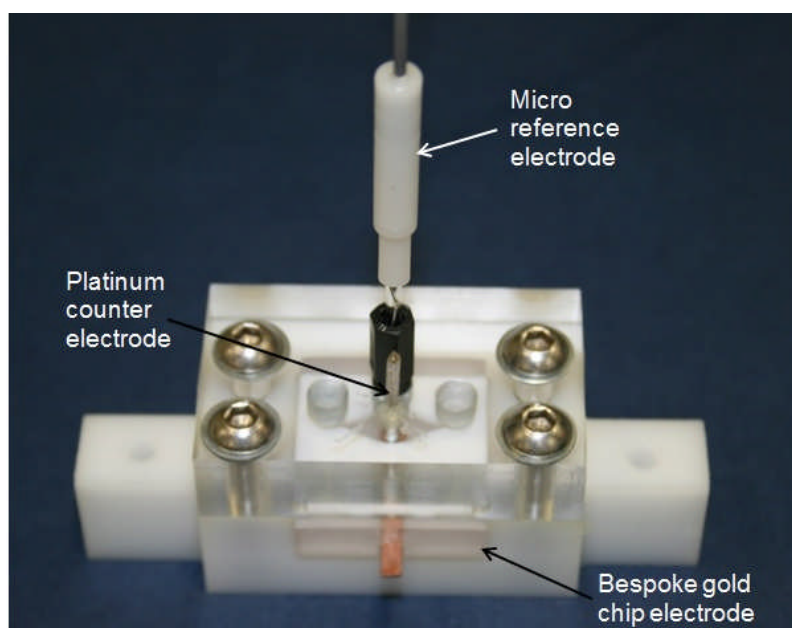


Figure 5-5 Flow cell evolution 2. Electrochemical flow cell - integration of bespoke gold chip electrode.

5.3.1.2 Electrode preparation method

The following electrode preparation methods were used for this study:

A) Electrochemical cleaning plus sonication (screen-printed electrodes)

Electrodes were connected to a potentiostat (GPES software on an Autolabs potentiostat), and 12 cycles of cyclic voltammetry (CV) were performed in 0.1 M sulphuric acid (H_2SO_4) as an electrode cleaning step. A starting potential of -0.4 V was used, together with a vertical potential range of 1.4 V and -0.4 V. CV scans were conducted at a scan rate of 50 mV s^{-1} . This was followed by a five minute sonication bath in ethanol for each electrode.

B) Mechanical cleaning and polishing, plus electrochemical cleaning and sonication (bespoke gold chip electrodes)

This approach combines the mechanical cleaning and polishing of gold chip electrodes (recommended as a preferred method by Tkac and Davis (2008)), and the electrochemical cleaning method outlined in (A)(recommended as a preferred cleaning method for gold chip electrodes by Campiña *et al.* (2008)).

First, the electrode block (Figure 5-4) was ground and polished according to the regime outlined in Table 5-1. This regime was based upon the method described by Tkac and Davis (2008), and also developed with reference to gold chip grinding and polishing guidelines published by Struers Ltd (Struers Ltd 2014). The electrode was rinsed with ethanol and dH_2O between each grinding and polishing step. A twin wheel rotating disk hand polishing and grinding machine was used. Polishing cloths, silicon carbide papers, diamond abrasive solution, and polishing lubricant fluid were all sourced from Struers Ltd (Rotherham, UK).

Subsequently, the method described in (A) for the screen-printed electrodes was applied in full.

Each of the preparation methods were analysed using both cyclic voltammetry and electrochemical impedance spectroscopy.

Table 5-1 Grinding and polishing process for bespoke gold chip electrode

Grinding	Grinding Step			
	Grind 1	Grind 2	Grind 3	Grind 4
Surface	SiC paper #400	SiC paper #1000	SiC paper #2000	SiC paper #4000
Lubricant Type	Water	Water	Water	Water
Rotation speed (rpm)	300	300	300	300
Time (s)	4 x 25	4 x 25	4 x 25	4 x 50
Rotation after each 25s/50s time step	90°	90°	90°	90°
Polishing	Polishing Step			
	Polish 1			
Surface	Polishing Cloth			
Abrasive Type	Diamond Suspension ¼ µm			
Lubricant Type	Struers DP-Red			
Rotation speed (rpm)	150			
Time (s)	180			

5.3.1.3 Biosensor construction method

A standard method of uranyl biosensor construction was used for each of the investigations described in this sub-chapter. The general method was adopted from Conroy *et al.* (2010), but is briefly outlined here for clarity.

Firstly, the electrode surface was prepared using the preferred method identified in the investigation described in Section 5.3.1.2. A self-assembled monolayer was constructed upon the gold electrode surface by incubating

the electrode in a 10mM solution of 4-aminothiophenol (4-ATP) in ethanol for 4 h. A chemical linker was attached to the SAM through incubation in 5mM sulfo-SMCC solution for 1 h. The sulfo-SMCC was first dissolved in dimethyl sulfoxide (DMSO), and the final solution comprised 20% (v/v) stock DMSO solution and 80% (v/v) 10 mM phosphate buffered saline (PBS) solution at pH 7.4. The PBS used in this study was prepared in dH_2O from tablets sourced from Sigma Aldrich. One tablet dissolved in 200 mL of deionized water (dH_2O) yielded 10 mM phosphate buffer, with 2.7 mM KCl and 137 mM NaCl, pH 7.4 at 25 °C (Sigma Aldrich 2014a). Finally, the biorecognition element was attached by incubating the biosensor unit in 1 mg mL^{-1} JG-A12 surface layer protein solution in 10 mM PBS at pH 7.4 for 1 h. Electrochemical impedance spectroscopy and cyclic voltammetry analysis was conducted after each construction stage to provide analysis and assessment of biosensor quality (analysis methods are described in full in Section 5.3.3).

5.3.1.4 Physical transducer selection method

Preliminary electrochemical experiments were conducted in order to determine a preferred physical transducer type, from the two options described in Section 5.3.1.1, to use in the subsequent investigations into biosensor performance.

Uranyl biosensors were constructed upon each type of electrode using the methodology described in Section 5.3.1.3, and investigations were conducted in triplicate (i.e. three different electrodes of each type). Cyclic voltammetry analysis was used both after the electrode preparation stage, and upon completion of biosensor construction for each electrode. The analysis results were subsequently used to inform the choice of preferred electrode type. Additionally, surface investigation methods were used to characterise electrode surface topography for the two types of electrodes. Specifically, scanning electron microscope (SEM) and coherence scanning interferometry (CSI) techniques were employed (Section 5.3.3.2).

5.3.2 Integrated biosensor performance

Through the transducer selection investigation, the bespoke gold chip electrode and electrochemical cell approach was identified as the preferred method (the results that led to this selection are presented in Section 5.4.1). Therefore, all subsequent investigations into biosensor performance were based upon this method of biosensor-flow cell integration.

There were three main elements to the biosensor performance investigations:

- *Biosensor system frequency sensitivity*

An investigation was conducted to determine whether the biosensor-analyte response was sensitive to any specific applied voltage frequency or range of frequencies (when using the electrochemical impedance spectroscopy analysis method described in Section 5.3.3.1).

- *Biosensor stability*

For any sensor system it was important to determine to what extent signal drift may apply within the typical conditions that the sensor will be operated.

- *Biosensor regeneration (reusability)*

The term biosensor regeneration is used here to describe a range of approaches that sought to establish the extent to which the integrated uranyl biosensor, and the transducer unit upon which it was constructed, was reusable (as opposed to being single-use calibrated sensors).

The methodology employed for each of these elements will be described fully in the following sub-sections.

5.3.2.1 *Experimental setup*

All investigations into biosensor performance were conducted with the biosensor integrated into the electrochemical cell setup described in Section 5.3.1.1 and shown in Figure 5-5. The full experimental setup is

described schematically in Figure 5-6. Two syringe pumps were used to control the flow of a) target analyte solutions (uranyl solutions) and b) buffer solutions. Flow was regulated by means of a manual control valve unit, which served the purposes of both enabling switching of flow between analyte and buffer solutions and in limiting any potential 'back diffusion' to the length of the connecting flow tubing. Additionally, an inline bubble trap was placed between the syringe flow and the flow cell inlet as a precaution against the development of air bubbles within the flow domain.

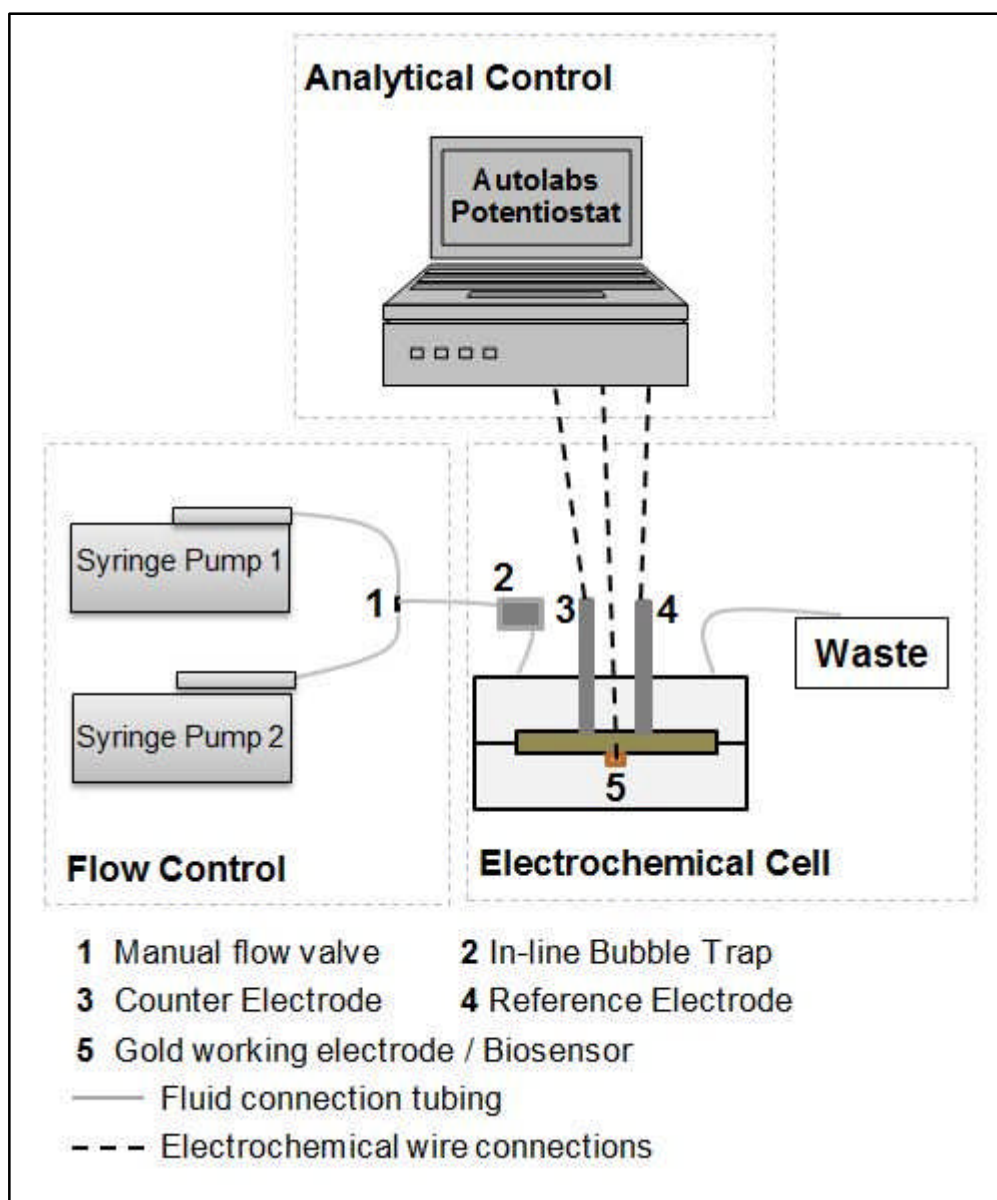


Figure 5-6 Schematic diagram showing the setup for biosensor performance investigations, using bespoke gold chip electrode and modified flow cell.

5.3.2.2 *General biosensor performance investigative approach*

This sub-section describes the general methodology employed in the investigations into biosensor performance. Where alterations were made to this methodology for any specific investigation, this is specified in the text relating to that investigation.

First, uranyl biosensors were constructed using the method described in Section 5.3.1.2, and integrated into the bespoke flow cell unit within the experimental setup described in Section 5.3.2.1. Uranyl nitrate ($\text{UO}_2(\text{NO}_3)_2$) solutions were prepared in 10 mM phosphate buffer saline (PBS) at pH 7.4 (Conroy 2012), across a concentration range of 10^{-12} to 10^{-6} M. This range was selected to include the range of aqueous uranium concentrations identified in a real contaminated site (10^{-8} to 10^{-6} M), as described for the Pécs (Hungary) mining legacy site in Section 2.2.2.

One 10 mL plastic syringe was filled with 10 mM PBS at pH 7.4, and a second syringe was filled with the lowest concentration of uranyl-PBS solution. Using one of the two syringe pumps (Figure 5-6), the electrochemical flow cell was initially filled with PBS buffer solution. This was done to replicate the pre-use wet storage of the uranyl biosensor within a deployed automated monitoring system. Next, the second syringe pump was used to flow the uranyl solution into the flow cell. The pump was operated at a flow rate of 1.75 mL min^{-1} for 45 seconds to ensure that an analyte cell concentration ratio of at least 99% was achieved, based upon the optimised flow cell operational protocol recommendation presented in Section 4.7.2. The analyte concentration at the sensor surface was left to equilibrate with the bulk fluid analyte concentration for a period of 20 minutes, after which electrochemical impedance spectroscopy analysis was conducted.

The flow cell was subsequently 'flushed' with PBS, at a flow rate of 1.75 mL min^{-1} for 60 seconds. The intended purpose of this step was two-fold: complete flushing of the analyte solution from the flow cell, and achieving the dissociation of the uranyl analyte from the biorecognition element of the biosensor. The process was subsequently repeated for each analyte concentration, in increasing concentration order.

5.3.2.3 *Biosensor frequency sensitivity*

The complete methodology described in Section 5.3.2.2 was used for the investigation into biosensor frequency sensitivity. The electrochemical impedance spectroscopy analysis focused upon the impedance response to analyte-biosensor binding across the full range of frequencies used in the analysis (as described in Section 5.3.3.1). This was achieved by plotting analyte concentration against both the real and imaginary components of impedance for selected frequencies. The purpose of this investigation was to isolate a specific frequency or range of frequencies for which subsequent biosensor performance investigations could be focussed upon i.e. those to which the analyte-biosensor response was deemed to be most sensitive.

5.3.2.4 *Biosensor regeneration (reusability)*

For a sensor to be practically useful for point-of-use deployment, and particularly when commercial prospects are considered, the regeneration of the sensor for repeated use is important. For this study, two aspects of biosensor regeneration were investigated:

- *Chip-to-chip repeatability*

The repeatability of the integrated biosensor-analyte response was investigated between biosensors constructed upon three different previously unused gold chip bespoke electrodes.

- *Single chip regeneration*

The repeatability of the integrated biosensor-analyte response was investigated between three biosensors constructed upon the same single bespoke gold chip electrode. The electrode was re-generated between the construction of each biosensor using the preferred electrode preparation method (as determined in the investigation described in Section 5.3.1.2).

5.3.2.5 *Biosensor storage stability*

It is important to understand the stability of an integrated point-of-use biosensor with respect to, as much as possible from laboratory based investigation, the conditions within which the sensor would be deployed. The term 'stability' here relates specifically to the extent to which the impedance signal of the biosensor unit drifts when stored within a buffer solution prior to the delivery of an analyte solution for analysis. The stability of the integrated biosensor was assessed by analysing the impedance response to exposure to 10 mM PBS solution at pH 7.4 only. Hence, only the first part of the methodology described in Section 5.3.2.2 was employed i.e. no analyte was delivered to the sensor surface. The biosensor was exposed to PBS for a total of 2 hours, and electrochemical impedance spectroscopy scans were performed at 40 minute intervals.

5.3.3 **Analysis methods**

The analysis methods utilised in these investigations can be categorised into 'electrochemical' and 'non-electrochemical' methods.

5.3.3.1 *Electrochemical analysis methods*

Different electrochemical analysis methods were used for different aspects of the investigation. Each electrochemical analysis (EA) method along with the main settings utilised are outlined below, and the aspects of the investigations for which they were used are summarised in Table 5-2.

EA1 – Cyclic Voltammetry (CV)

The cyclic voltammetry technique was described in detail in Section 2.4.5, and was used in these investigations primarily for assessing electrode preparation techniques, and biosensor construction layers (biosensor quality). All cyclic voltammetry analysis was conducted using GPES software on an Autolabs potentiostat, and scans were between potentials of 0.7 V and -0.4 V at a scan rate of 50 mV s⁻¹. Scans were conducted in 10 mM ferrocyanide/ferricyanide (Fe (CN)₆^{3-/4-}) electrolyte solution (in 10 mM PBS at pH 7.4) unless otherwise stated (Conroy 2012).

EA2 – Electrochemical Impedance Spectroscopy (EIS), Broad Frequency Range

Electrochemical impedance spectroscopy techniques were described in detail in Section 2.4.5, and were used primarily for assessing biosensor quality and biosensor performance. EIS analysis was conducted using FRA software on an Autolabs potentiostat, with 51 measurements taken using an alternating amplitude of ± 10 mV set around a background potential of 0V (against Ag/AgCl reference electrode), and for a frequency range of 25000 Hz to 0.25 Hz. Scans were conducted using 10 mM ferrocyanide/ferricyanide ($\text{Fe}(\text{CN})_6^{3-/4-}$) electrolyte solution (in 10 mM PBS at pH 7.4) unless otherwise stated (Conroy 2012).

EA3 - Electrochemical Impedance Spectroscopy (EIS), Limited Frequency Range

Following initial biosensor performance analysis, it was possible to identify a limited range of frequencies that were more sensitive to the analyte-bioreceptor association activity (Section 5.4.2.1). A more focused analysis could then be applied to various aspects of biosensor performance investigation. EIS analysis was conducted using FRA software on an Autolabs potentiostat, with 10 measurements taken using an alternating amplitude of ± 10 mV set around a background potential of 0V (against Ag/AgCl reference electrode), and for a frequency range of 100 Hz to 0.25 Hz. Scans were conducted using uranyl nitrate ($\text{UO}_2(\text{NO}_3)_2$) solutions of various concentrations (in 10 mM PBS) unless otherwise stated.

5.3.3.2 Non-electrochemical analysis methods

Two non-electrochemical methods were used to provide information relating to the surface microstructure of the gold working electrodes of both types of electrode considered in this study. This information was then used to aid analysis of the quality of constructed biosensors, through assessment of the impact of surface topography upon self-assembled base layer formation for example.

NEA1 – Coherence Scanning Interferometry (CSI)

Interferometry is a non-contact method, utilising light source beam splitting and re-integration to provide information about the topography of material surfaces. This method was used in this study for providing information on both the bespoke gold chip electrodes and screen-printed electrode surfaces upon which the uranyl biosensor would be constructed. The analysis was carried out using an NP-FLEX optical profiling machine.

NEA2 - Scanning electron microscopy (SEM)

Scanning electron microscopy utilises the back scattering of a focussed beam of electrons directed at a surface, or secondary electrons emitted as a result of interactions between the electron beam and atoms of the surface material(s). The back-scattered or secondary electrons are detected and utilised to produce an image of the surface. For this study, this approach was used to provide additional surface information about the screen-printed gold working electrodes. However, this method was not suitable for the relatively bulky polycarbonate block of the bespoke gold chip electrodes, because of thickness restrictions of the SEM sample chamber.

Cont'd over.....

Table 5-2 Analysis methods for the different aspects of biosensor-flow cell integration investigation.

Aspect of Investigation	EA1	EA2	EA3	NEA1	NEA2
<u>Biosensor Development</u>					
- Electrode Preparation	✓				
- Biosensor Quality	✓	✓		✓	✓
<u>Biosensor Performance</u>					
- Basic Biosensor Performance		✓	✓		
- Single Chip Regeneration		✓			
- Chip-to-chip reusability		✓			

EA1 – Cyclic Voltammetry

EA2 – Electrochemical Impedance Spectroscopy, Broad Frequency Range

EA3 – Electrochemical Impedance Spectroscopy, Limited Frequency Range

NEA1 – Coherence Scanning Interferometry

NEA2 – Scanning Electron Microscopy

5.4 Investigation results

5.4.1 Physical transducer selection

Cyclic voltammetry (CV) was used to compare the quality of uranyl biosensors constructed upon screen-printed electrodes and bespoke gold chip electrodes. The investigative method described in Section 5.3.1.4 was employed, and the CV settings described in Section 5.3.3.1 were used for analysis. Three separate new (i.e. previously unused) electrodes of each type were used for each investigation, to provide triplicate results.

Figure 5-7 presents comparative CV results. In both cases the electrochemical response to the presence of a fully constructed biosensor is compared to the electrochemical response of the bare prepared (i.e. cleaned) electrode.

The most noticeable feature of the cyclic voltammetry investigation was the distinct difference in response to the construction of the full biosensor upon the electrode surface between the two different electrode types (Figure 5-7A-B). For the bespoke gold chip electrodes, the presence of the uranyl biosensor had a clear insulating effect on the electrochemical circuit. Current peak values reduced from $\pm 40\text{-}50\ \mu\text{A}$ for the bare cleaned electrode to $< \pm 10\ \mu\text{A}$ for the biosensor-functionalised electrode. Additionally for the bespoke gold chip electrodes, the distinct electrolyte oxidation and reduction peaks (explained in Section 2.4.5.3) identifiable for the bare electrode are no longer distinguishable following the construction of the uranyl biosensor (Figure 5-7B). For the screen-printed electrodes however, whilst a small decrease in peak currents of typically $5\text{-}10\ \mu\text{A}$ was observed this was significantly less than for the bespoke gold chip electrodes as described above. Overall, the insulating properties of the uranyl biosensor were much less apparent with the screen-printed electrodes, with the distinct oxidation and reduction peaks still being clearly distinguishable following biosensor construction (Figure 5-7A).

Additional to the electrochemical analysis, brief investigations were conducted into the surface topography of the non-functionalised (i.e. bare cleaned) electrodes. This helped to provide some context with respect to the

electrochemical results. The coherence scanning interferometry (CSI) method was used to provide surface topography detail for both of the electrode types. The CSI results are presented in Figure 5-8 for the screen-printed electrodes and Figure 5-10 for the bespoke gold chip electrodes. Both electrodes show topographical variation or features across the extent of the surface considered, and both at the $\sim\mu\text{m}$ scale, but the nature of this topography differed between the two electrode types.

The screen-printed electrodes showed a topography consisting of 'clusters' of peaks and troughs (Figure 5-8), with the bulk of topographical variance within $\pm 1\mu\text{m}$ of a set datum. Scanning electron microscope images of the same electrode surface suggested that these 'topographical clusters' are nodules of material protruding from the electrode surface (Figure 5-9). A likely explanation is the globulisation of the ink used in screen printing the gold electrode surface (discussed further in Section 5.5.1). The topographical features of the bespoke gold electrode however, were more linear in nature, and consistent with the mechanical process of cleaning and polishing used to prepare the electrode surface for biosensor construction (Section 5.3.1.2). The peaks and troughs were, on average, at a marginally smaller scale than those observed for the screen-printed electrodes, with the bulk of topographical variance within 300 nm of the datum.

Cont'd over.....

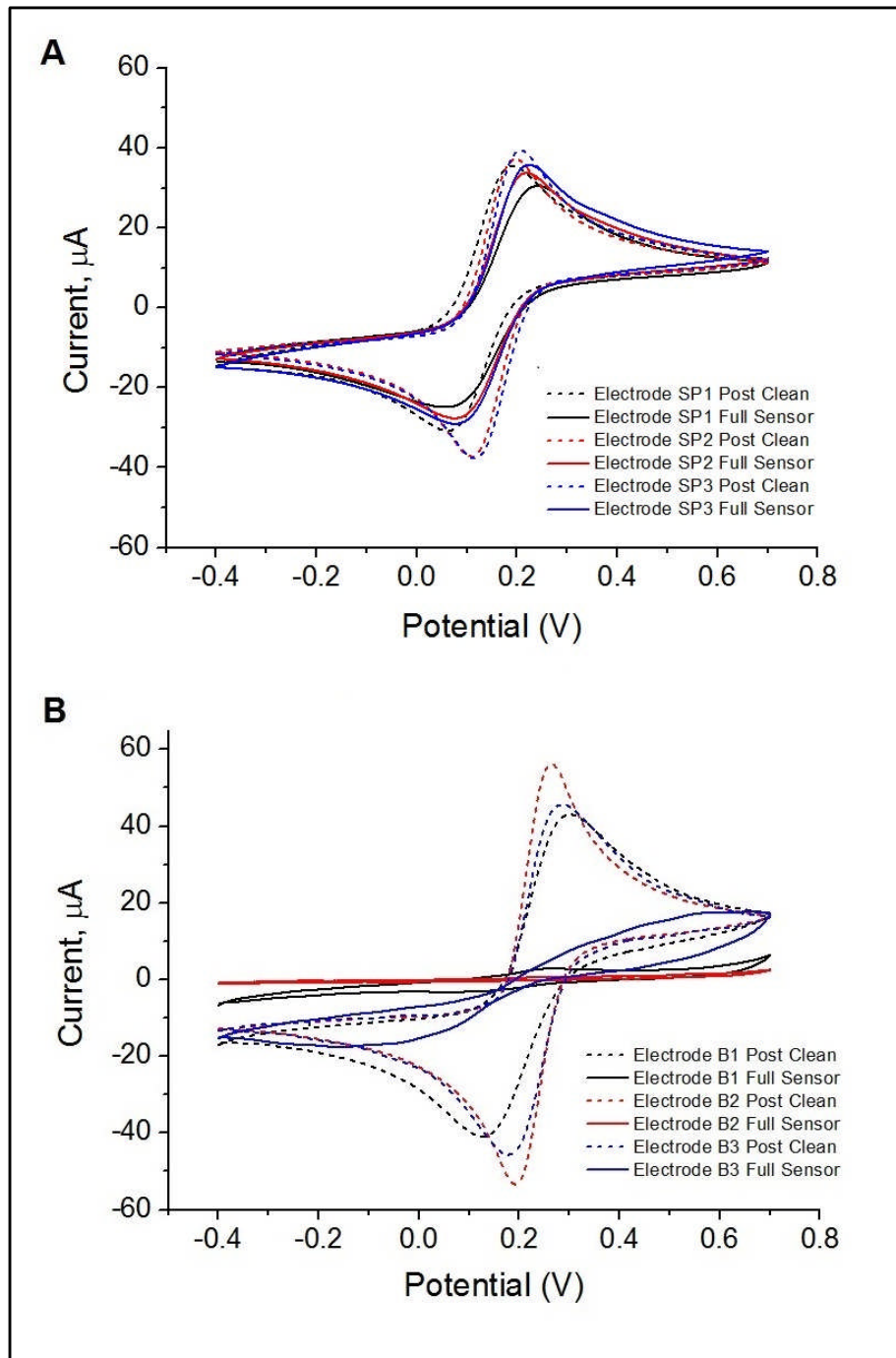


Figure 5-7 Transducer selection investigation results: A) CV scans screen-printed electrodes in triplicate, B) CV scans bespoke gold chip electrodes in triplicate. Analysis conducted post electrode cleaning/preparation, and upon the completion of biosensor construction for each electrode. Electrochemical analysis was conducted in 10mM ferrocyanide/ferricyanide ($\text{Fe}(\text{CN})_6^{3-/4-}$) electrolyte solution (in 10 mM PBS at pH 7.4).

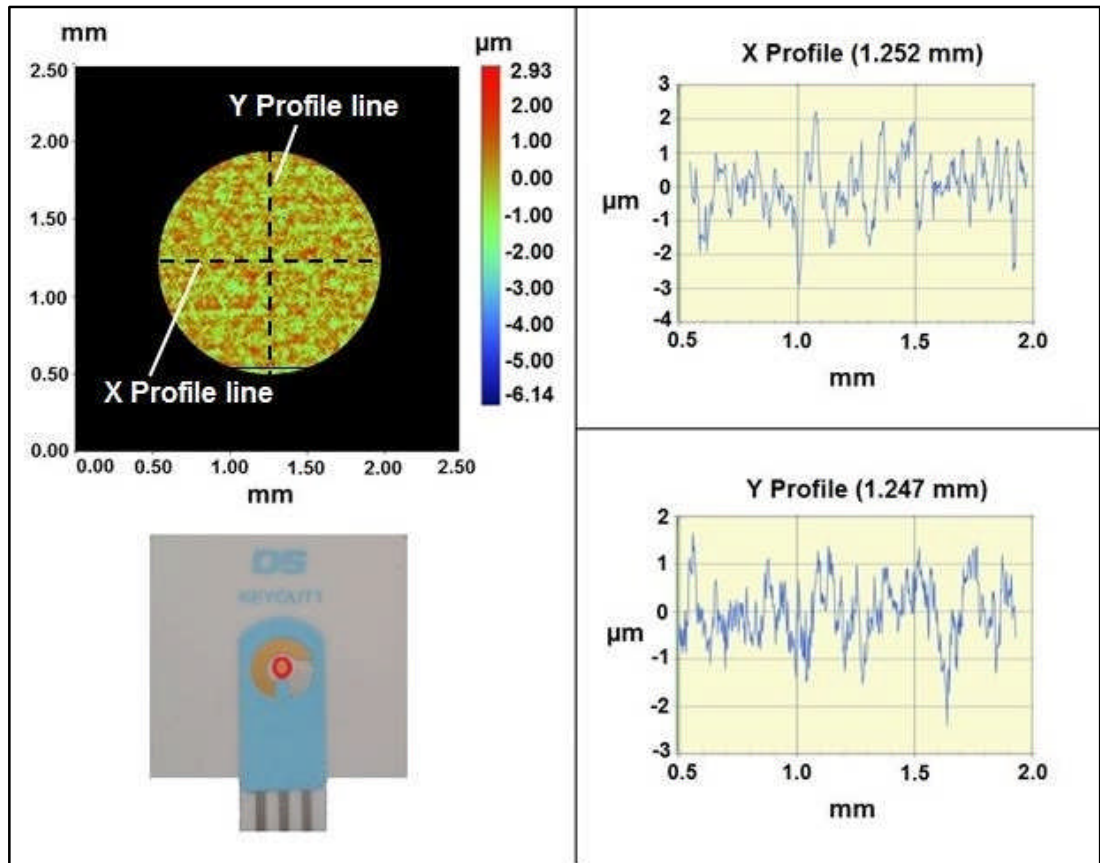


Figure 5-8 Coherence scanning interferometry (CSI) analysis of the gold working electrode of a Dropsens screen-printed electrode. The type of electrode analysed is shown, and the area of the electrode which contains the study area is highlighted with a red border.

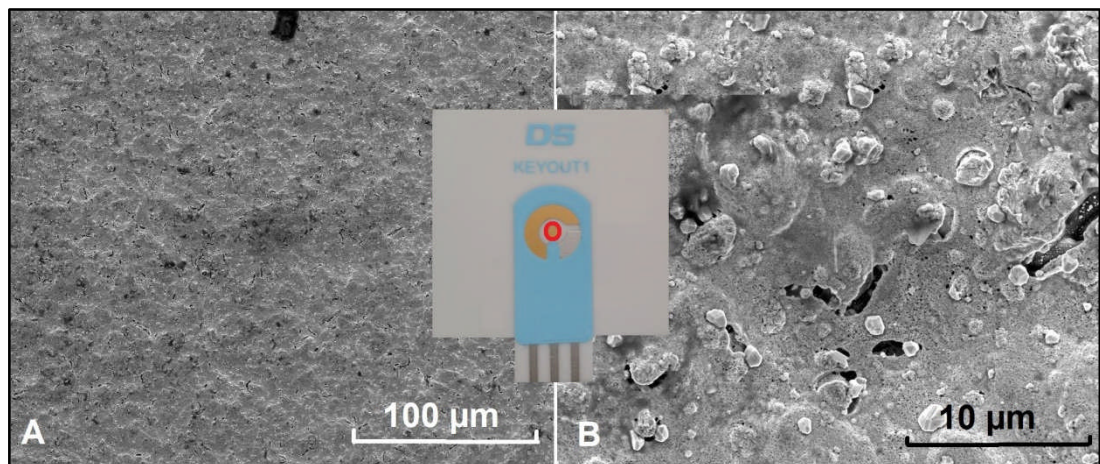


Figure 5-9 Scanning electron microscope (SEM) images of the gold working electrode of a Dropsens screen-printed electrode at A) 1000x magnification, and B) 5000x magnification. The type of electrode analysed is shown, and the area of the electrode which contains the study area is highlighted with a red border.

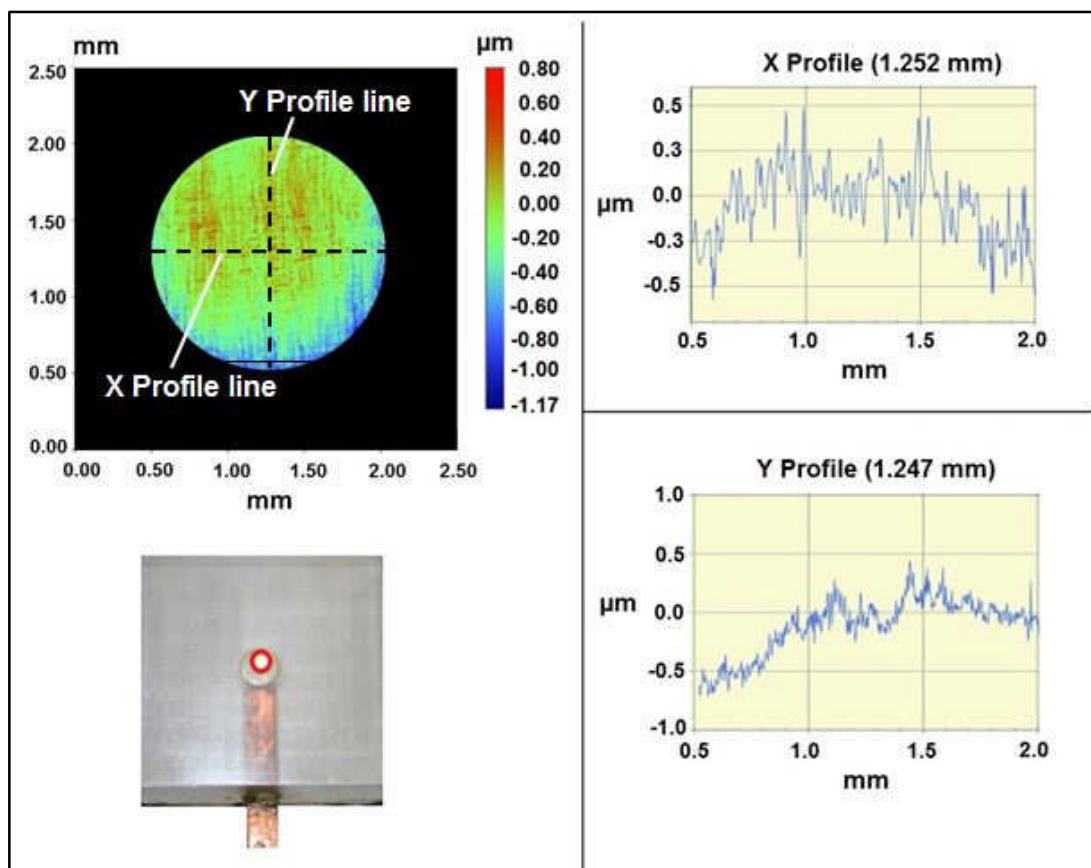


Figure 5-10 Coherence scanning interferometry (CSI) analysis of the working electrode of a bespoke gold chip electrode. The type of electrode analysed is shown, and the working electrode study area highlighted with a red border.

Ultimately, the bespoke gold chip electrodes were selected as the electrode of choice for use in the biosensor performance investigations. The full rationale behind this choice will be included in the discussion sub-chapter (Section 5.5.1).

5.4.2 Integrated biosensor performance

5.4.2.1 System frequency sensitivity

From Section 2.4.5 (Figure 2-11 in particular) it was clear that different equivalent circuit components are represented by electrochemical impedance spectroscopy measurements taken at different frequencies. Specifically, the solution resistance is determined at high frequencies (i.e. left-hand side of Nyquist plot), and charge-transfer resistance at lower frequencies (i.e. right-hand side of Nyquist plot).

It is useful therefore for any impedimetric biosensor to establish the relationship between the biosensor-analyte impedance response and the frequency at which the impedance measurements are taken. Specifically with respect to the accurate and practical operation of a point-of-use deployed sensor, it was necessary to establish a frequency or range of frequencies at which the change in impedance corresponding to the change in analyte is represented.

Figure 5-11 presents the impedance response (both the real component (Figure 5-11A) and imaginary component (Figure 5-11B) to a range of analyte concentrations for three selected measurement frequencies.

For a functioning analyte-specific biosensor, an impedance response that is fully or partially proportional to a change in analyte concentration would be expected. A partially proportional response relates to the case where a response analogous or associated with analyte saturation of the sensor receptor sites occurs (this will be discussed in further detail in Sections 5.5.4.2 and 5.5.4.3). Of the three frequencies considered, the most proportional response was observed at the lowest frequency (0.25 Hz) for both the real and imaginary components of impedance (Figure 5-11). The reason for this is most likely the result of providing a longer measurement time in relation to the rate of electron transfer. Additionally, the lower frequency measurements correspond more to the interrogation of mass transfer of analyte from the bulk solution to the sensor surface rather than the electron-transfer dominance observed at higher frequencies (Conroy 2012).

From this, a more focused measurement frequency range of 0.25 to 100 Hz could be employed for the subsequent biosensor performance investigations (as described in Section 5.3.3.1). The presentation of the results of these biosensor performance investigations (Sections 5.4.2.2 and 5.4.2.3 in particular) will include further consideration of the frequency sensitivity of biosensor-analyte response for this narrower range of frequencies.

Cont'd over.....

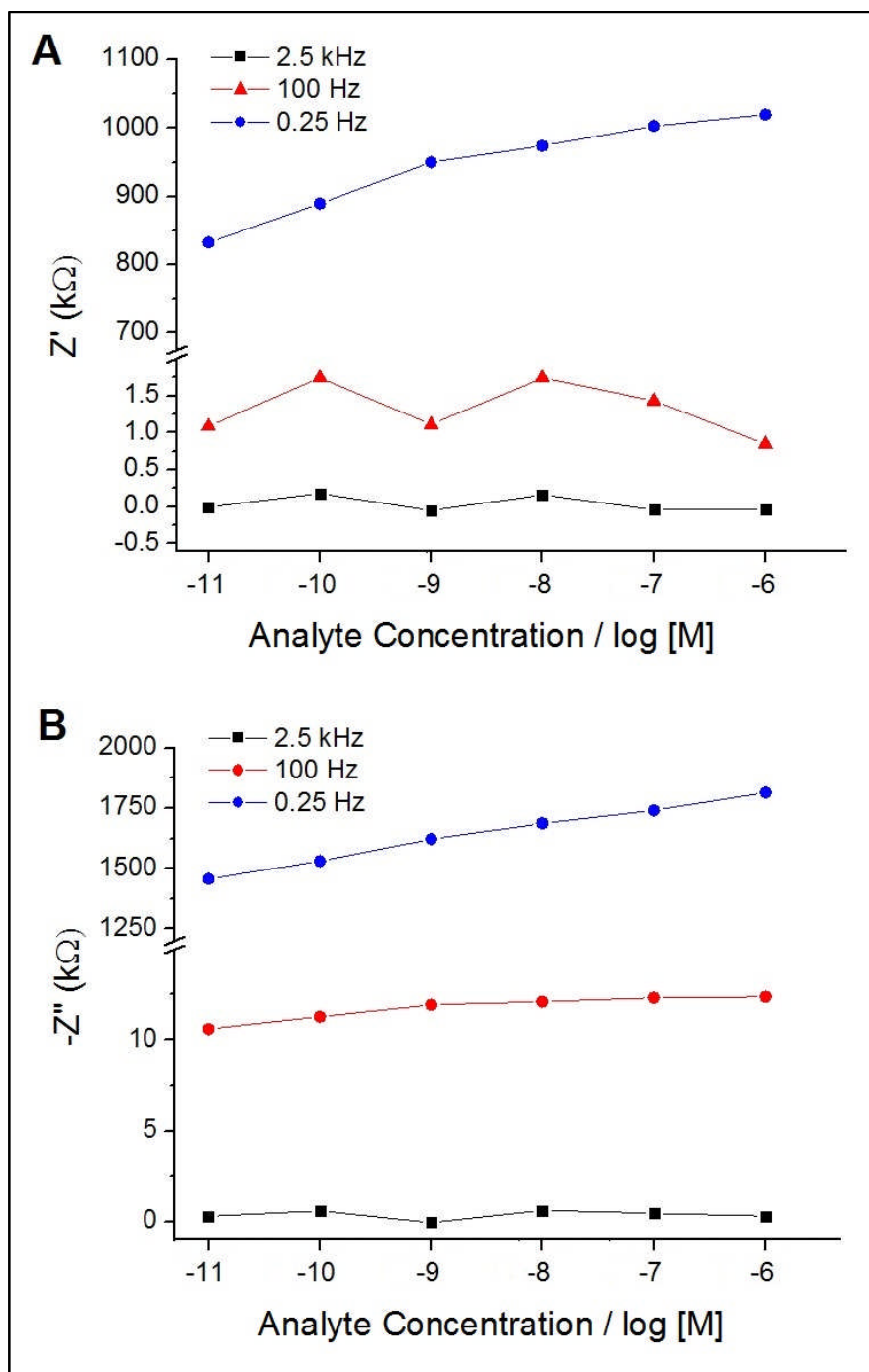


Figure 5-11 Frequency sensitivity of full uranyl biosensor constructed upon a bespoke gold chip electrode. Impedance response to change in uranyl nitrate ($\text{UO}_2(\text{NO}_3)_2$) (in 10 mM PBS) analyte concentration at three selected frequencies; 2.5 kHz, 100 Hz & 0.25 Hz: A) Real component of impedance (Z'), B) Imaginary component of impedance ($-Z''$).

5.4.2.2 Integrated biosensor single chip regeneration

The impedance response to analyte delivery for integrated uranyl biosensors constructed upon the same physical transducer surface is presented in Figure 5-12. The regeneration of the electrode surface was achieved by re-

applying the electrode preparation method for the bespoke gold electrodes described in 5.3.1.2. The results shown represent the mean of triplicate experiments where the electrode surface was regenerated after each series of impedance measurements and a new biosensor constructed upon it. Uranyl nitrate ($\text{UO}_2(\text{NO}_3)_2$) solution was used as the analyte for the investigations. The data is presented in form of the change of impedance that results from the biosensor-analyte interaction, and measured against a baseline impedance taken prior to the delivery of analyte to the sensor surface (i.e. the biosensor in buffer solution only). The standard error of measurements on the triplicate sensors is presented in the form of error bars on each of the plots, which present results for three selected measurement frequencies (0.25, 1 and 10 Hz). Linear fit plot lines have also been added to the plots where a relationship between impedance and analyte concentration approximated a linear relationship for the range of analytes considered.

The range of mean impedance changes, against a starting baseline impedance, was 10% - 35% across the measurement frequencies used and for both components of impedance (Figure 5-12). The lower figure represented the change in impedance for the lowest analyte concentration (10^{-12} M), and the higher figure represented the highest analyte concentration (10^{-6} M).

However, the most striking aspect of these results is the extent of the error bars, which represent the degree of repeatability in the triplicate experiments (Figure 5-12). When considered as a percentage of the mean change in impedance value at each analyte concentration, the standard error was consistently around 40% across all frequencies and for both components of impedance. Because of this large error across the triplicate results, it is useful to consider a repeat experiment for one selected frequency in isolation and in detail. This is presented for a measurement frequency of 0.25 Hz in Figure 5-13.

From Figure 5-13 it is clear that there was a degradation of the impedance signal with repeated regeneration of the same electrode surface for biosensor construction. This degradation was more marked for the real component of impedance (i.e. Z' , representing primarily resistive elements of

the analyte-sensor interaction) than for the imaginary component (i.e. Z'' representing primarily capacitive elements of the analyte-sensor interaction). For the first use of the electrode, a proportional impedance response was identified with respect to increasing analyte concentration. This constitutes a change in impedance range of ~10% to ~50% for Z' and ~15% to ~60% for Z'' . For the change in impedance per decade log increase in analyte concentration for Z' , two separate linear slopes were fitted representing an average change of ~10% and ~4% respectively. For Z'' an average change of ~7% was determined across the full range of analyte concentrations considered.

Cont'd over....

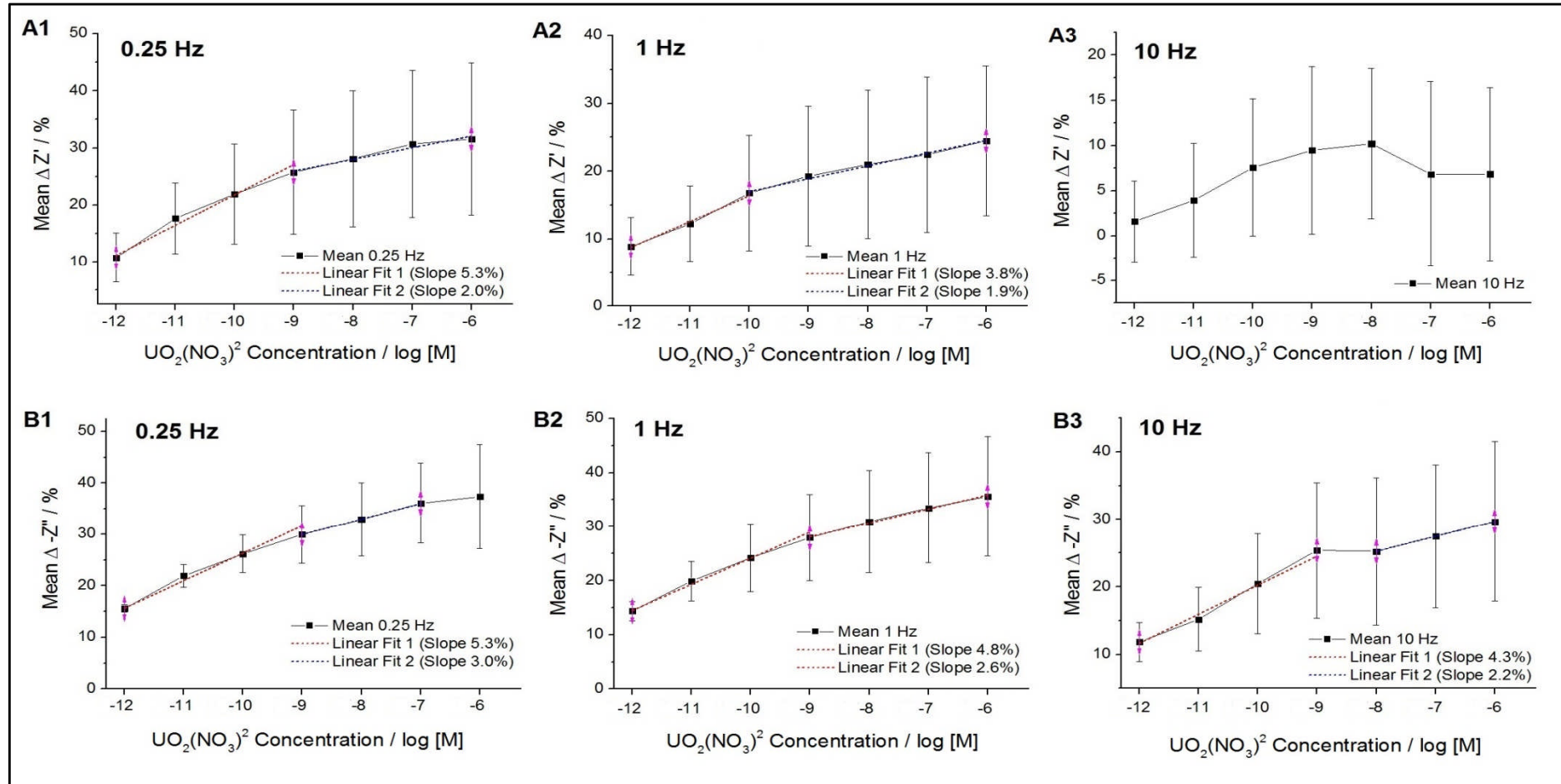


Figure 5-12 Impedance response to biosensor-analyte interaction for three selected frequencies for the regeneration of a single biosensor chip (i.e. uranyl biosensor constructed three times upon the same electrode, and electrode surface regenerated after each use). Results presented as the mean of triplicate experiments, with error bars representing the standard error in each case. A) Real component of impedance, B) Imaginary component of impedance.

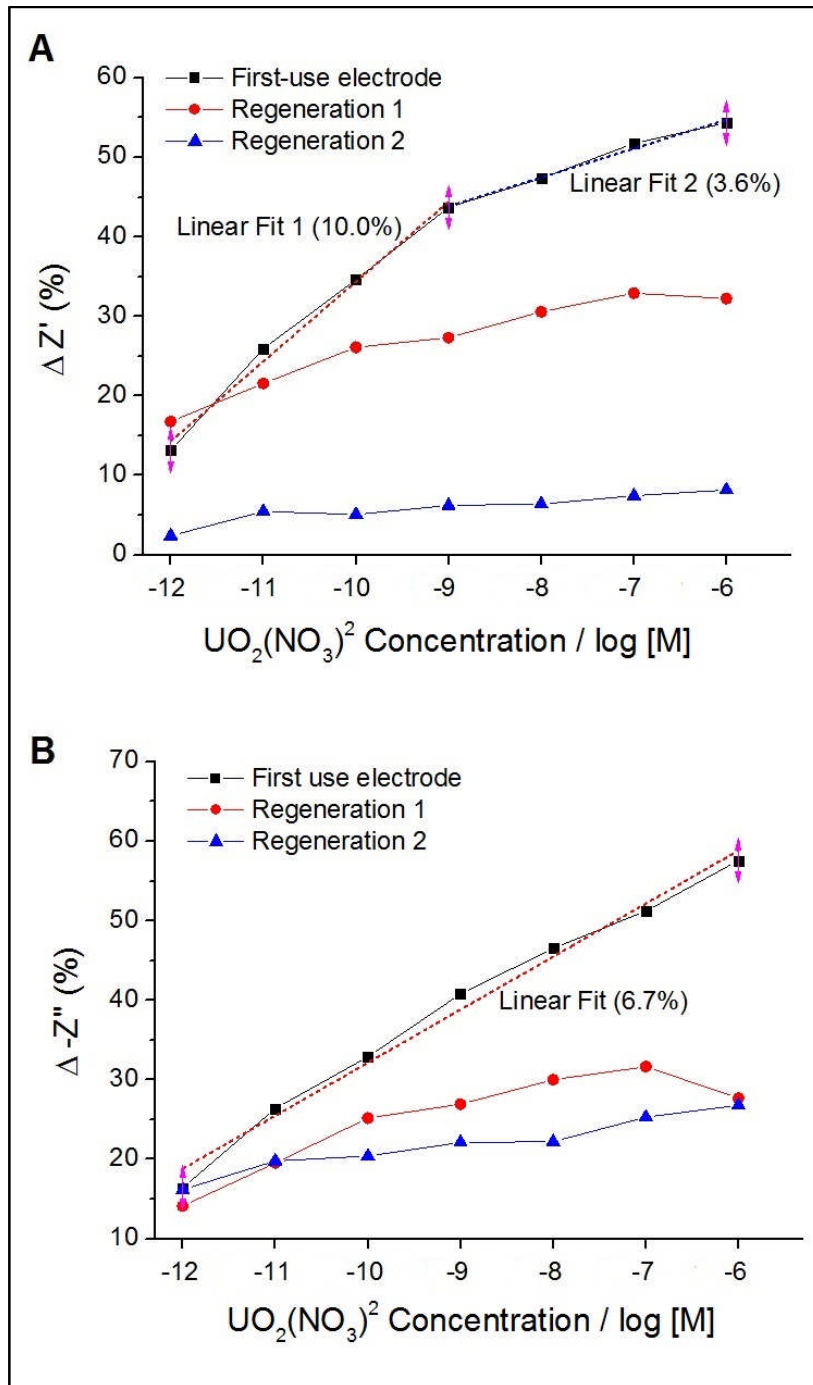


Figure 5-13 Triplicate regenerated uranyl biosensor chip impedance response to uranyl nitrate ($\text{UO}_2(\text{NO}_3)_2$) analyte. Results expressed as a change of impedance against a baseline impedance measurement. A) Real component of impedance, B) Imaginary component of impedance. Measurements taken at 0.25 Hz for a potential perturbation of ± 10 mV around a background voltage of 0V.

Cont'd over....

5.4.2.3 Integrated biosensor chip-to-chip repeatability

The impedance response to analyte delivery for integrated uranyl biosensors constructed upon different, previously unused, physical transducer surfaces is presented in Figure 5-14. The results presented represent the mean of triplicate investigations i.e. three new electrodes to develop the uranyl biosensors. Uranyl nitrate ($\text{UO}_2(\text{NO}_3)_2$) solution at a range of concentrations (10^{-12} to 10^{-6} M) was used as the analyte for the investigations.

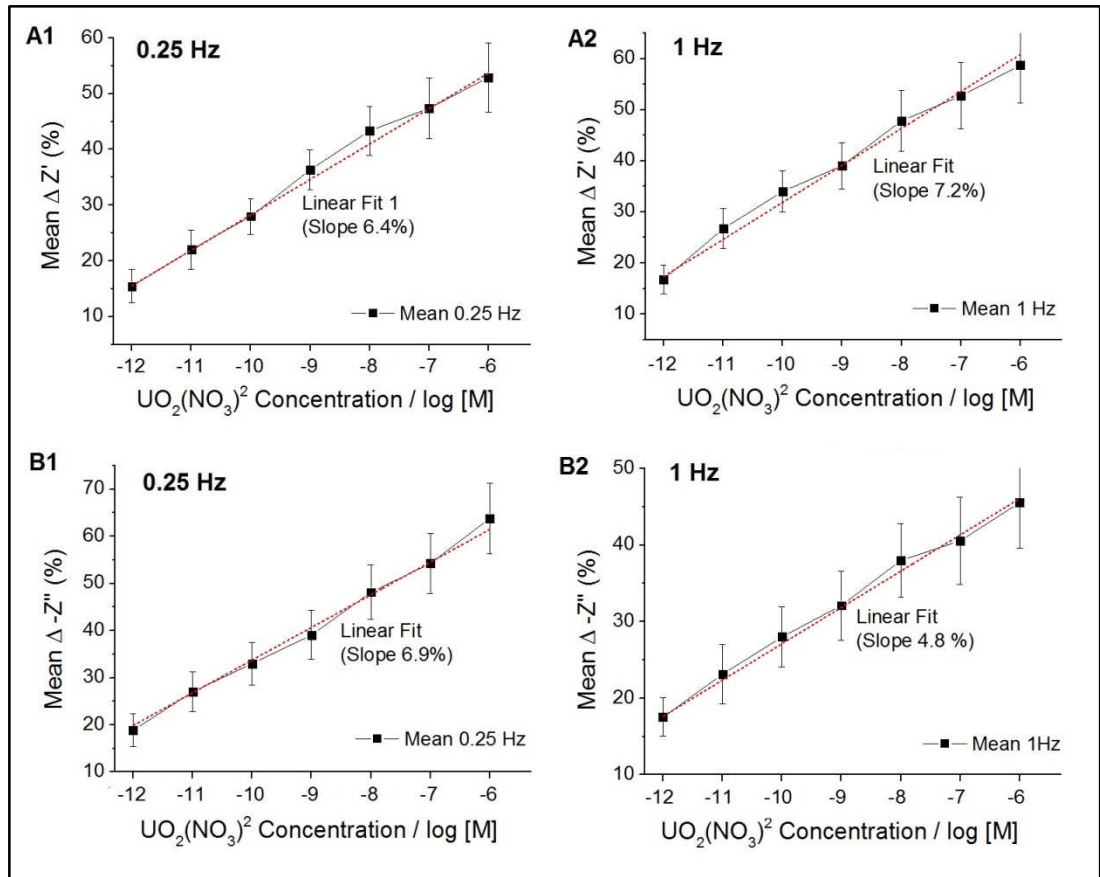


Figure 5-14 Impedance response to biosensor-analyte interaction for two selected frequencies for biosensors constructed upon three different (previously unused) electrode chips. Results presented as the mean of triplicate experiments, with error bars representing the standard error in each case. A) Real component of impedance, B) Imaginary component of impedance.

Once again, the data is presented as a change in impedance resultant from the biosensor-analyte interaction, and measured against a baseline impedance taken prior to the delivery of analyte to the sensor surface (i.e. the biosensor in buffer solution only). The standard error of the mean

impedance from triplicate measurements is presented in the form of error bars on each of the plots, which present results for two selected measurement frequencies (0.25 & 1 Hz). As used for the single chip regeneration investigation (Section 5.4.2.2), linear fit plot lines were added to the plots where a linear relationship between impedance response and analyte concentration was identified.

In comparison to the results from the biosensors constructed upon regenerated single chip, the resultant impedance was a much more clearly defined proportional relationship in each case. For the real component of impedance (Z'), the mean change in impedance ranged from ~15% at the lowest analyte concentration to 55% at the highest analyte concentration across both measurement frequencies. The average increase of change in impedance per tenfold increase in analyte concentration for Z' was ~6.5% at 0.25 Hz and ~7% at 1 Hz (Figure 5-14A). For the imaginary component of impedance (Z''), the mean change in impedance ranged from ~20% at the lowest analyte concentration to 65% at the highest analyte concentration. However, there was a small difference between the two different measurement frequencies, with a marginally smaller range observed at the higher frequency (~45% at the highest analyte concentration). The average increase of change in impedance per tenfold increase in analyte concentration for Z'' was ~7% at 0.25 Hz and ~5% at 1 Hz (Figure 5-14B).

As observed for the single chip regeneration investigation (Section 5.4.2.2), noticeable error bars are presented on Figure 5-14. These error bars represent the variability of the impedance response to a change in analyte concentration across the three different electrode chips, expressed as the standard error of a triplicate mean. However, the margin of error was in a range of 10-15% for both components of impedance and across the two frequencies, when expressed as a percentage of the mean impedance response for each analyte concentration. This was significantly lower than the range of error observed for the single chip regeneration investigation (Section 5.4.2.2).

5.4.2.4 Integrated biosensor storage stability

The impedance response to an integrated uranyl biosensor stored in 10 mM phosphate buffer saline (PBS, pH 7.4) for 2 hours, is presented in Figure 5-15. The impedance response was considered at two different measurement frequencies. The choice of buffer and buffer concentration reflected the recommendation made by Conroy (2012) for the long term storage of the uranyl biosensors.

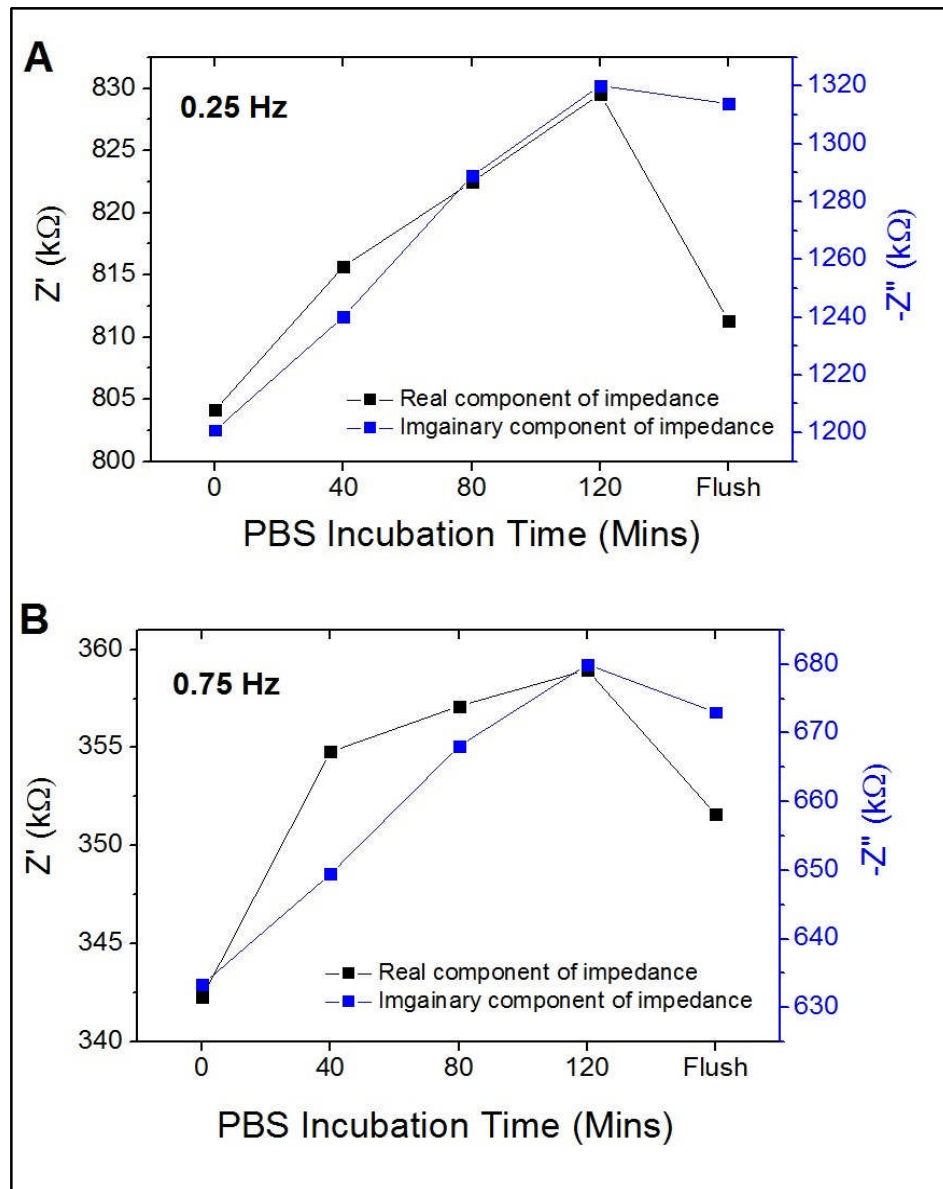


Figure 5-15 Integrated uranyl biosensor stability analysis. The biosensor was incubated in 10 mM phosphate buffer solution (PBS) for 2 hours, and impedance measurements taken at 40 minute intervals. After 2 hours, the flow cell was flushed with fresh PBS, and a final impedance measurement taken. A) measurements taken at 0.25 Hz B) measurements taken at 0.75 Hz

The results indicate that signal drift did occur over the timescale investigated. The impedance responses shown in Figure 5-15 represent a total change in impedance of ~10% at 25 Hz for the imaginary component of impedance (Z'') across the full duration of the investigation, and ~3% for the real component of impedance (Z'). At 75 Hz, these values are marginally higher for the real component (~5%), and marginally lower for the imaginary component (~8%).

The implications of these results upon integrated biosensor operation will be considered in the discussion sub-chapter (Section 5.5.3).

5.5 Discussion - transition to field deployment

5.5.1 Physical transducer selection

The investigation of two different physical transducers (i.e. electrode types), with respect to their suitability for integrating the uranyl biosensor into the optimised ICell flow cell, served two purposes. Firstly, by providing a choice based upon electrochemical and surface topography data, a more robust investigation was developed than if an arbitrary choice of one electrode type was made. Secondly, the results produced from this investigation provided an early insight into the extent of the challenges involved in the integration of biosensors, and impedimetric biosensors in particular, into fluid delivery systems. Consideration of Figure 5-7 for example highlights not only the differences in electrochemical response between the two electrode types, but also the variability of responses between triplicate experiments of the same electrode type.

Ultimately the bespoke gold chip electrode and modified electrochemical cell system was chosen as the preferred method of biosensor integration, to be used for all subsequent investigations. The rationale for this choice was based upon both the electrochemical and surface topography results produced through this investigation (Figure 5-7 to Figure 5-10), but with specific reference to the original uranyl biosensor development investigations conducted by Conroy *et al.* (2010).

The biosensor development results presented by Conroy described the full biosensor as an insulating surface that produced a 'flattened' cyclic voltammogram, very similar to that produced through electrochemical analysis of the bespoke gold chip electrodes (Figure 5-7B). The more defined oxidation and reduction peaks of the cyclic voltammograms representing biosensors constructed upon screen-printed electrode suggested a more conductive surface than biosensors constructed upon either the bespoke gold chip electrodes, or the P3 gold-silicon wafer electrodes used by Conroy. The inference from these results is that a more complete and uniform biosensor was deposited onto the bespoke gold chip electrodes than for the screen-printed electrodes.

The differences in surface topography between the two electrode types (Figure 5-8 to Figure 5-10) may provide some explanation for the electrochemical results discussed above. Both exhibited topographical features, although the features observed for the bespoke gold chip electrodes were on a marginally smaller scale (bulk of features ± 300 nm for a selected cross-section, Figure 5-8) than those observed for the screen-printed electrodes (bulk of features $\pm 1\mu\text{m}$ for a selected cross-section, Figure 5-8). However, the main difference between the two electrode types related to the nature of the topographical features. The bespoke electrode exhibited linear features, most likely resultant from the mechanical polishing process used to prepare the surface for biosensor construction (Figure 5-10).

Conversely, the SPE exhibited clusters of topographical peaks and troughs leading to a 'speckled' appearance on the coherence scanning interferometry visual representation (Figure 5-8). This 'clustering' was also visible on scanning electron microscope images of the SPE surface (Figure 5-9), and was attributed to globulisation of the gold ink used in the screen printing process. The composition of gold ink for the electrode screen printing process, and for other electronic component printing processes such as inkjet methods, typically consists of gold nanoparticles encapsulated in a mixture consisting of a polymeric binder, plus other additives (Huang *et al.* 2003). These additives are used to improve dispersion of the gold particles, and to aid the printing and adhesion process. However, the exact chemical composition of the ink is not typically disclosed by electrode manufacturing companies (Hayat and Marty 2014). One other possibility for the difference in electrochemical analysis results for the two electrode types therefore is chemical interference or chemical incompatibility disrupting the binding of the biosensor base self-assembled layer to the gold surface, related to the non- gold constituents of the screen printing ink.

A full study linking electrode surface topography and biosensor quality was beyond the scope of this investigation. However, in summary, the experiments that have been carried out highlight a number of key factors that may impact the quality of the uranyl biosensors: (i) The globulisation

effect of screen-printed electrode surface topography, related to the use of gold nanoparticles in screen printing inks; (ii) possible chemical interference associated with non-gold constituents of the screen printing ink; (iii) alteration of the surface properties of gold chip electrodes through mechanical polishing methods.

In any event the electrochemical results, supported by the surface topography studies and reference to the original investigations by Conroy (2012), was deemed sufficient to confidently propose a more comprehensive and uniform electrode surface coverage of the biosensor deposition layers for the bespoke gold chip electrodes. This electrode type was therefore selected as the preferred option for use in all subsequent investigations.

5.5.2 Integrated biosensor regeneration

Before considering specific discussion points relating to the regeneration and reusability of the integrated uranyl biosensor, it is useful to consider the preferred range of measurement frequencies at which these investigations were conducted.

A proportional impedance response to increasing uranyl analyte was observed only at lower frequency measurements, i.e. those below 100 Hz, and the most proportional response was observed for the frequencies <10Hz. This was demonstrated through the biosensor performance results presented throughout Section 5.4.2 (e.g. Figure 5-11 to Figure 5-14 inclusive). The reason for this is most likely that lower frequencies provide a longer measurement time in relation to the rate of electron transfer. Additionally, the lower frequency measurements correspond more to the interrogation of mass transfer of analyte from the bulk solution to the sensor surface rather than the electron-transfer dominance observed at higher frequencies (Conroy 2012). The preferred operational frequency range was identified as 0.25 – 1.0 Hz. As discussed in Section 2.4.6 successful practical biosensor field deployment requires a sensor unit that has demonstrable repeatable performance.

The size of the error associated with the single chip regeneration investigation (Figure 5-12), around 40% error around the mean of three

experiments, effectively means that the biosensor is not practically reusable using this method. Although the same method was used to prepare the electrode surface for each biosensor construction upon the same chip, the inference from these results is that the regeneration process does impact upon the impedance of the biosensor unit. Other published studies have reported that the methods used to regenerate gold electrodes functionalised with biosensor structures, can lead to changes in the microstructure/topography and surface area of the gold surface. These studies also support the hypothesis, offered above, that such factors can influence the impedance response of biosensor systems constructed upon these surfaces, typically leading to a decrease in the impedance signal with repeated regeneration (Carvalho *et al.* 2005; e.g. Bhalla *et al.* 2010).

The chip-to-chip repeatability investigation indicated that there is also significant error associated with the comparison of uranyl biosensor performance for sensors constructed upon three different (previously unused) electrode chips (Figure 5-14). Once again, the same preparation method was used for each separate biosensor chip construction. However, the margin of error, at a range of 10-15% of the mean impedance response, was significantly lower than for the single chip regeneration. Of the two methods of attempting repeatable uranyl biosensor analysis, the use of individual new electrode chips for each is new biosensor is clearly preferable.

Overall, the results from these investigations provide good support for the link between biosensor quality and the surface properties of the electrode chip upon which the biosensor is constructed. With respect to biosensor performance therefore, the conclusion can be drawn that performance is highly dependent upon the electrode surface topography and microstructure.

5.5.3 Integrated system storage stability

The reason for storing the integrated biosensor in buffer solution, between measurements within an automated water monitoring system for example, is to provide a stable range of pH conditions. This is required to discourage the denaturing of the S-layer protein biorecognition element of the uranyl

biosensor. Phosphate buffer solution (PBS) at pH 7.4 was used for this purpose in this study.

The results of electrochemical analysis clearly showed an impedance response over time to the integrated biosensor in buffer solution (Figure 5-15). It is important to clarify at this point that the investigation was conducted within an enclosed environment, inside a closed Faraday cage, and was therefore isolated from any potential outside influences upon the impedance signal. The inference therefore is that the observed increase in impedance over time is caused by the presence of the buffer solution and/or interaction of the buffer with the biosensor. However, flushing the flow cell with a supply of fresh buffer solution did lead to some correction of this signal drift. The correction was more significant for the real component of impedance (Z') than for the imaginary component of impedance (Z''). The implication of this is an indication that the real component of impedance (Z') provides a more reproducible signal within a deployed integrated system.

5.5.4 Integrated biosensor practical operation

5.5.4.1 Optimised flow cell

The first point of discussion concerning the practical operation of the integrated uranyl biosensor relates to the operation of the optimised iCell flow cell. In terms of providing a trial of flow cell operations, the investigations described and presented in this chapter were wholly successful. The flow cell remained watertight throughout all investigations, and the development of air bubbles was readily controlled through the insertion of the inline bubble trap (as shown in Figure 5-6). The incorporation of a platinum counter and Ag/AgCl reference electrode into the flow cell unit, and subsequent integration with a potentiostat controller was also successful. This was determined by both preliminary electrochemical test analyses, and the investigative results themselves. The operational protocol for the flow cell, developed through the investigations presented in Chapter 3, was easy to implement through the experimental setup shown in Figure 5-6 and pump control operations.

5.5.4.2 *Integrated biosensor performance overview*

In terms of the practical operation of the integrated uranyl biosensor, the challenges associated with biosensor regeneration and repeatability as described in Section 5.5.2 are clearly problematic. However, it is worth taking an holistic view of the investigation results to try and identify any prevalent defensible relationship between the integrated sensor impedance response and analyte concentration.

Firstly, by considering the mean impedance response to analyte concentration for the single chip regeneration and chip-to-chip repeatability investigations (Figure 5-13 & Figure 5-14), a relationship is identified. That is, at frequencies of 0.25 and 1.0 Hz in particular, an increase in analyte concentration correlates generally with an increase in both components of impedance (Z' and Z''). Because of the significantly large error associated with the single chip regeneration results (Figure 5-13) however, the results from the chip-to-chip repeatability investigation (Figure 5-14) are arguably more reliable in terms of starting to try and define the impedance-analyte relationship further. Comparison of the mean impedance response of Figure 5-14 and the response for the first-use electrode from the single chip regeneration investigation (Figure 5-13) allows for a tentative defined relationship to be proposed. A slope of ~6-7%, representing the change in impedance per log cycle of uranyl concentration, is observed for the imaginary component of impedance at a measurement frequency of 0.25 Hz across both plots. The error associated with Figure 5-14 would limit the certainty with which this relationship could be used as a calibration tool for practical integrated biosensor operation, but it is a useful guide nevertheless.

At this point, it is useful to make a direct comparison of the biosensor performance investigation results presented in this chapter and the calibration curve presented by Conroy *et al.* (2010). Conroy's 'calibration curve' was reprinted in Section 2.4.3 of this thesis (Figure 2-8), but it is repeated below for reader convenience. It should be noted that Figure 2-8 provided an average impedance response to uranyl analytes, and also compared that response to those for potentially interfering ions. Also, these

results were presented only for the imaginary component of impedance (Z''), so the comparison with results from this study will be made on that basis.

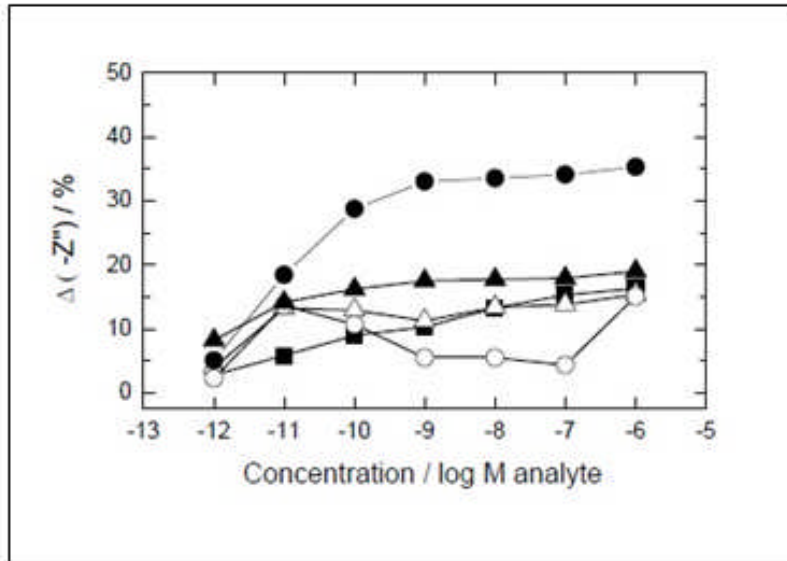


Figure 2-8 Response of uranyl biosensor to uranyl analyte, compared to the response to potential interfering ions. ● Average uranyl response, ▲ cobalt chloride, △ calcium sulphate, ■ nickel nitrate, ○ cadmium nitrate (Conroy 2012).

(Chapter 2 figure repeated for reader convenience)

The first point of note is that there is a difference in the range of impedance values (i.e. the dynamic range of the sensor) between the average biosensor impedance response of Figure 2-8 and those of Figure 5-13 & Figure 5-14. For Conroy's results, the change in impedance range was ~5% - 35%, and for this study the observed range was ~20% to 60%. A possible explanation for this however is a difference in background impedance levels, e.g. related to the different electrode configurations, and perhaps a larger measurement solution volume for Conroy's investigation. A difference in inherent system background impedance between the two experimental setups would lead to an impact upon the change in impedance values for the two sets of data.

Of more significance is that Conroy's calibration curve (Figure 2-8) exhibited a flattening of an initial proportional response, beyond a uranyl analyte concentration of $\sim 10^{-10}$ M. Conversely, the results presented in this study approximated a linear response for the entire range of analyte concentrations considered (e.g. Figure 5-14).

5.5.4.3 Adsorption models

To seek to understand the different impedance responses between the two studies it is useful to consider potentially suitable models for the signal response (impedance) to the association of uranyl ions with the S-layer protein bioreceptor of the biosensor. The Langmuir adsorption equation (commonly known as the Langmuir isotherm) describes the relationship between adsorption of molecules onto a solid surface and the concentration of a medium above the solid surface for a given temperature (Eq. 5-1)(Adamson and Gast 1967).

$$\theta = \frac{\alpha \cdot c}{1 + \alpha \cdot c} \quad (5-1)$$

where θ is the fractional coverage of the surface, c is the concentration of the medium (analyte) in the bulk solution above the surface, and α is an adsorption/equilibrium constant. Whilst originally developed for adsorption of gas molecules, the isotherm is now commonly applied to adsorption from all fluids (Gerringa *et al.* 1995; e.g. Choy *et al.* 2000).

The term adsorption with respect to models such as this can relate to a) physisorption processes - adsorption through primarily van der Waals' forces, not involving chemical bonding; or b) chemisorption processes - adsorption through chemical bonding (e.g. covalent or ionic). Chemisorption bonds are typically (although not universally) stronger than those for physisorption (Ibach 2006). The proposed model for the binding of the uranyl ion to the JG-A12 S-layer protein (Section 2.4.3, Figure 2-7) would suggest that the latter is applicable to the uranyl biosensor. It is appropriate therefore to consider the Langmuir isotherm model when assessing the analyte-signal (impedance) response of the uranyl biosensor. In doing so, the impedance axis of the biosensor-analyte response plots will serve as a proxy for sensor surface coverage of the Langmuir model. This is because impedance is expected to change with the amount of binding occurring at the sensor surface as described in Section 2.4.5.

Figure 5-16 presents a Langmuir isotherm fitted to the concentration range applicable to the uranyl biosensor investigations conducted in this study and by Conroy, using a log-scale for concentration.

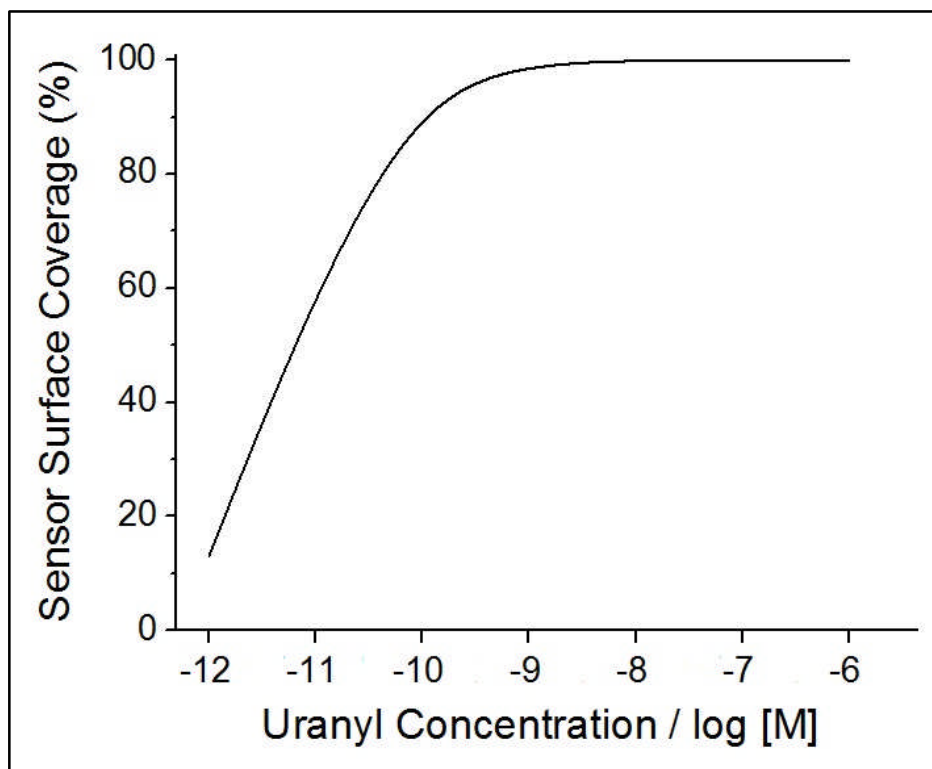


Figure 5-16 Idealised Langmuir isotherm with a logarithmic concentration scale (x-axis), fitted to uranyl-biosensor binding for an analyte concentration range of 10^{-12} M to 10^{-6} M.

There is a very good match between the Langmuir isotherm presented in Figure 5-16 and the analyte-impedance response presented by Conroy in Figure 2-8. That is, the sensor surface coverage distribution response to increasing analyte concentration of the idealised Langmuir isotherm corresponds well with the impedance response to increasing analyte concentration of the uranyl biosensor as presented by Conroy. Beyond an analyte concentration of 10^{-10} M for both the Langmuir model and Conroy's experimental data the sensor surface is assumed to be close to full analyte coverage.

The analyte-impedance response plots presented in this study are typically more linear across the range of analyte concentrations studied (e.g. Figure 5-14). One possible explanation for the apparently different analyte-impedance responses for this study and that conducted by Conroy relates to

the measurement approaches used. Conroy conducted electrochemical investigations by using a traditional three electrode electrochemical cell within a glass vessel containing ~30 mL electrolyte/analyte solution (Section 2.4.3). This study was conducted in the iCell flow cell with a sample volume of ~0.2 mL. This represents a scaling down factor of the measurement environment of ~150. The potential relevance of this is that it is possible that the binding process within the flow cell results in a decrease in the concentration of the bulk solution in the cell due to the very small volume. In the larger electrochemical cell used by Conroy, the significantly larger volume would mean that this effect is very unlikely to occur. An additional possible important factor is that for Conroy's experiment the analyte solution concentration was gradually increased by adding an aliquot of uranyl analyte of fixed concentration before each measurement. For the investigations in this study, the sensor surface was 'washed' with buffer solution after each measurement, potentially leading to some dissociation of uranyl bound to the sensor surface, and before the delivery of a higher concentration analyte to the sensor surface.

One final possible, relatively minor, factor with respect to the different impedance-analyte responses is electrode surface area. The P3 electrodes utilised by Conroy as the physical transducer base of the sensor had a marginally smaller surface area (~0.8 mm²) than the bespoke gold chip electrode used in this study (area ~2 mm²). That represents a maximum scaling up of the sensor surface of 2.5. The larger surface area of the bespoke gold chip electrodes potentially provides more binding sites. A recent experimental study by Das *et al.* (2009) presented a relationship between biosensor surface area and a reduced dynamic range (DR) for the sensor. Specifically, a reduction in surface area was observed to lower the higher detection limit (HDL) of the biosensor, through the reduction of the sensor's saturation level.

An alternative model to the Langmuir isotherm is the Freundlich adsorption isotherm, which is an empirical equation (the Langmuir isotherm is derived theoretically)(Eq. 5-2)((Freundlich and Hatfield 1926; Yang 1998):

$$\frac{x}{m} = Kc^{\frac{1}{n}} \quad (5-2)$$

where x is the mass of the adsorbate, m is the mass of the adsorbent, c is the concentration of the medium (analyte) in the bulk solution above the surface, and K and n are constants representing the adsorbate and adsorbent properties respectively. By fitting the concentration range applicable to the uranyl biosensor investigations conducted in this study and by Conroy to the Freundlich isotherm model (with a log-scale for concentration), an adsorption coverage response that approximates more to the response obtained in this study is observed (Figure 5-17).

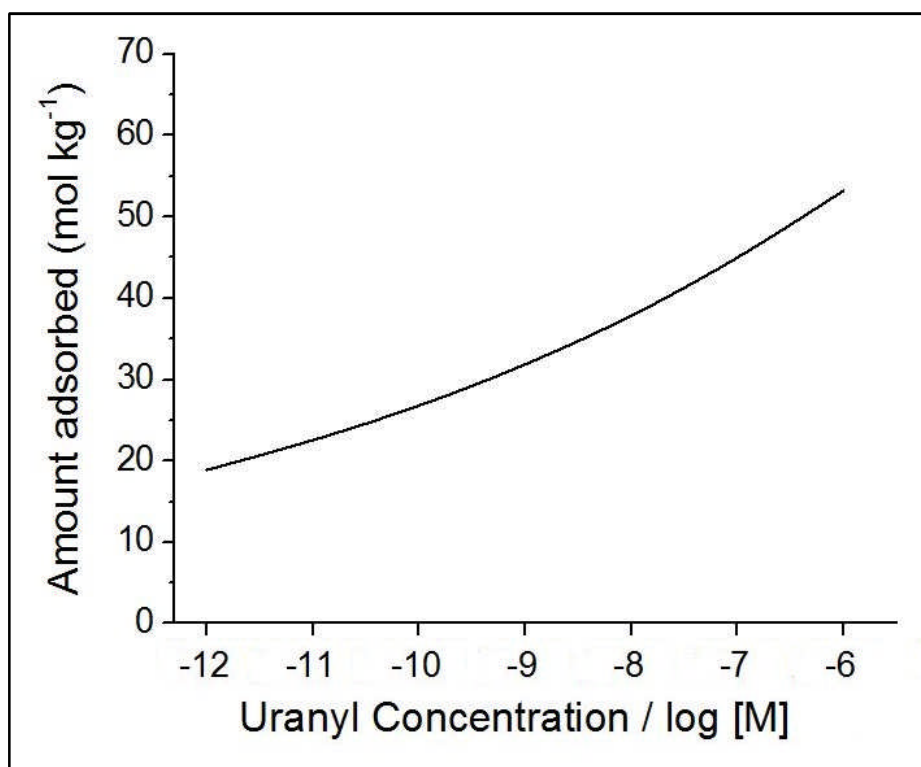


Figure 5-17 Idealised Freundlich adsorption isotherm with a logarithmic concentration scale (x-axis), fitted to uranyl-biosensor binding for an analyte concentration range of 10^{-12} M to 10^{-6} M.

There is no intended implication from the preceding discussion that the binding mechanism of the uranyl ion to the protein bioreceptor of the sensor is changed in any way through the process of integrating the sensor into the flow cell. Rather, the impedance-analyte response for the uranyl biosensor is determined primarily by the proportional sensor surface adsorption coverage

with increasing analyte concentration. In turn, this is potentially dependent on a number of factors including the ratio of sample volume to sensor surface area, measurement approach, and the sensor surface area itself. Moreover, for the two investigation approaches discussed here the theoretical Langmuir isotherm adsorption model provides a best fit to the traditional large sample volume – analyte accumulation approach to impedance measurements of Conroy. Conversely, the Freundlich isotherm adsorption model provides a closer approximation of the smaller scale biosensor-analyte response measurements investigated for this study.

To finalise the discussion of the practical operation of the integrated uranyl biosensor, the operation of the integrated sensor as part of an automated and remotely controlled water monitoring system for real-world contaminated sites is to be considered. This will be done in the further discussion chapter (Section 6.2).

5.6 Chapter summary

The process of sensor integration into the optimised iCell flow cell developed in Chapter 3 was investigated through the integration of a biosensor for the detection of uranyl ions in aqueous solutions. The relative success of the integration process was considered primarily in terms of the practical operation of the integrated sensor, specifically the following:

- Analyte solution delivery control
- Integration with signal measurement and processing equipment (i.e. a potentiostat)
- Sensor-analyte signal calibration
- Signal response repeatability/sensor reusability

The operation of the iCell flow cell with respect to analyte solution delivery control and integration with signal measurement equipment was successfully achieved. The iCell flow cell was operated in accordance with the operational protocol presented in Section 4.7.

The uranyl biosensor was successfully integrated into the iCell flow cell through the development of bespoke gold chip electrodes embedded into small polycarbonate blocks, and the associated modification of the flow cell to incorporate a platinum counter electrode and an Ag/AgCl reference electrode. The bespoke electrodes and electrochemical flow cell were identified as the preferred biosensor integration method over commercially available screen-printed electrodes.

Additionally, the investigations presented in this chapter have advanced the understanding of the practical operation of the uranyl biosensor. Specifically, the analyte-impedance responses observed in this study and for the original uranyl biosensor development work conducted by Conroy (Conroy 2012) were compared and fitted to two different surface adsorption models. The different models were used to broadly represent factors that influence the impedance response of the biosensor with increasing analyte concentration, which potentially led to observed differences in the biosensor response between the two different studies. These factors included the ratio of sample volume to sensor surface area, measurement approach, and the sensor surface area itself

Also, the investigation highlighted the challenges associated with biosensor/electrode surface regeneration and associated measurement repeatability. This was represented by the significant error margins associated with biosensors constructed upon both one single regenerated gold chip electrode, and upon previously unused different gold chip electrodes. This aspect of the investigation will be discussed further in Chapter 6 (Section 6.3), with specific reference to working towards the provision of robust and repeatable measurements with the integrated uranyl biosensor incorporated as part of an automated and remotely controlled water monitoring system.

CHAPTER 6

Further discussion

Chapter 6 Further discussion

6.1 Chapter introduction

This chapter provides discussion about the issues associated with ultimately incorporating the integrated uranyl biosensor into a remotely operated automated water monitoring system. This is done specifically with respect to providing robust and reliable aqueous uranyl concentration measurements within such a system.

Firstly, consideration is given to how the two main elements of the investigations conducted for this study, flow cell optimisation and biosensor integration, could be brought together to provide operational protocols for robust sensor measurements (Section 6.2).

Next, the integration of the uranyl biosensor into the optimised iCell flow cell clearly highlighted some of the challenges associated with the integration of sensor units into fluid delivery systems. In particular, the regeneration and reusability of an impedimetric biosensor constructed upon gold electrodes clearly presented its own specific challenges (Chapter 5). Therefore, brief further consideration is given here to the batch variability of gold electrode surfaces for sensor construction (Section 6.3).

Finally, the development of the optimised iCell flow cell through this study has led to two associated small projects/investigations. A brief overview of these is presented in this chapter to provide both additional support to the relevance of the output from this study, and as an introduction to the opportunities afforded by the development of the optimised flow cell design (Section 6.4). Both projects can also be viewed as developments associated with working towards incorporation of an integrated sensor-flow cell unit into an automated water monitoring system.

6.2 Robust measurements from uranyl biosensors deployed on real contaminated sites

This section seeks to assess the progress achieved towards the development of a robust deployed measurement device for the detection of uranyl ions in real water samples, and to identify operational protocols which could be used to make robust measurements as part of an automated and remotely controlled water monitoring system.

6.2.1 Early warning sensor system

In considering to what extent progress has been made towards making robust uranyl measurements from real, potentially contaminated, water samples it is first useful to re-state and summarise some relevant points developed in this thesis.

In Section 2.2.2 the uranium concentration in groundwater for the Pécs contamination site in Hungary was identified as being in the range $10 \mu\text{g L}^{-1}$ to 0.5 mg L^{-1} (equating to 10^{-8} to 10^{-6} M for uranyl nitrate for example). The lower figure represented the background uranium level for the area. The mean impedance response presented in Figure 5-14 (Section 5.4.2) for this study was ~6-7% per log cycle of uranyl concentration for measurements made at 0.25 Hz, for both components of impedance (Z' & Z''). The error margin for measurements taken for concentrations in the range 10^{-8} M and 10^{-6} M was 10-15% of the mean impedance value, and this equated to a change in impedance of ~4-5% (Section 5.4.2). As a comparison, the precision of the integrated uranyl biosensor should be viewed with reference to the precision of a laboratory standard aqueous uranium measurement. The between-run precision level of a commonly used standard method for the detection of uranium in water samples, solid fluorimetry with either laser excitation or ultraviolet light, was reported as being up to ~6% (WHO 2004). Finally, the mean change in impedance for an analyte concentration of 10^{-8} M in this study was 43% for the real component of impedance (Z') and 48% for the imaginary component of impedance (Z'')(Figure 5-14).

The first point of note from the above summary statements is that the error margin for chip-to-chip biosensor performance (for sensors constructed on different previously unused sensor surfaces), was only 4-9% higher than the upper error margin level of the most commonly used laboratory standard measurement method. Therefore, if improvements could be achieved in biosensor chip batch variability, most likely through robust and repeatable electrode surface preparation and regeneration methods, the integrated uranyl biosensor performance level could become comparable to the standard laboratory methods used. The issue of batch variability will be discussed further in Section 6.3. The batch variability margin observed in this study suggests that providing single *accurate* measurements of the analyte concentration of a given sample, i.e. operating the sensor unit as a simple '*detection sensor*', would currently be problematic. A reasonable level of accuracy for such measurements would be within 6% error for repeated measurements, to at least match the laboratory standard. Although, the observed impedance response for this study of ~6-7% per log cycle of uranyl concentration, would indicate that a precision level significantly below 6% would be required to operate the integrated sensor unit as a simple '*detection sensor*'.

Potentially a more appropriate operational protocol for the current integrated biosensor system would be operation as a *threshold sensor*, which could also be described as an *early warning sensor system*. Using the mean change in impedance measurements for an analyte concentration of 10^{-8} M as stated above, representing the background water uranium for the example site at Pécs, threshold change in impedance values of 50% for Z' and 55% for Z'' could be employed. Operating the biosensors using measurements related to the real component of impedance would be preferable, due to better control of signal drift control identified in Section 5.5.3. Once the threshold impedance response had been identified for a particular monitoring station (e.g. a groundwater borehole), more traditional sampling methods could be employed and supporting analysis conducted using laboratory standard measurements (e.g. solid fluorimetry). The integrated biosensor measurements, whilst providing the option of remote monitoring of contamination plume development and/or the

effectiveness of remediation approaches for example, would not be relied upon as the sole source of uranyl contamination measurements.

For any given potentially contaminated site therefore it would be possible to first determine the background uranyl concentration in water samples through standard measurement methods. A threshold impedance response for the integrated biosensor, applicable to uranyl concentrations above the background level could then be determined from a calibration analyte-impedance plot such as that presented in Figure 5-14.

An alternative to the threshold sensor protocol described above, is one where the sensor system takes regular measurements e.g. three to four times a day, and readings are transferred to a human for inspection. Any significant noticeable change in impedance over time, with a *significant* change being determined through operator experience and not defined explicitly, would trigger the 'early warning system'. This would in turn initiate the additional investigations using traditional sampling and analytical methods.

For both of the above operational protocols, sample management and flow control would be essential. This would include ensuring that the measured water sample is flushed each time from the flow cell following completion of the measurement, using buffer solution. Also, the water reservoir being sampled (e.g. groundwater aquifer) should be isolated from the integrated biosensor-flow cell unit through a valve control system to prevent analyte or interfering ion diffusion to the sensor between measurements.

6.2.2 Integrated biosensor measurement optimisation

Following on from Section 6.2.1, a natural question to raise is whether the characterisation of the optimised iCell flow cell, and investigation of the biosensor-flow cell integration process, can be applied in a particular way that would potentially improve sensor accuracy and reliability. Namely, can an operational protocol be developed that would ultimately justify the application of the integrated uranyl biosensor as the sole source of uranyl

contamination information (i.e. without support from manual sampling and standard laboratory analysis)?

A potential operational protocol which may provide development towards this is considered below:

Proposed Optimisation Protocol – Operating as an accumulation sensor

In Section 5.5.4 analyte accumulation upon the uranyl biosensor surface, leading to a state approximating full sensor surface coverage (i.e. approaching the occupation of all binding sites) at analyte concentrations above 10^{-10} M UO_2^{2+} , was identified for the biosensor calibration investigations conducted by Conroy (2012) as part of the original development of the uranyl biosensor. This behaviour provided a strong fit to the Langmuir isotherm adsorption model for a uranyl analyte concentration of 10^{-12} M to 10^{-6} M (with concentration presented on a log-scale). For the flow cell integrated biosensor investigated in this study however, full sensor surface coverage was not observed for the range of analyte concentrations studied. Also, the impedance-analyte concentration response was a better fit to a different adsorption model (Freundlich isotherm).

A major proposed contributing factor to the different impedance-analyte concentration responses of the two studies was that the measurement within a small sample volume for the integrated biosensor led to a decrease in the bulk solution concentration above the sensor surface (Section 5.5.4). However, despite the observed differences between studies there was no indication that any fundamental change in the analyte-bioreceptor binding mechanism had occurred due to the sensor integration process.

Therefore the expectation is that for a given uranyl concentration (above 10^{-10} M UO_2^{2+}), a state approximating full sensor surface coverage will eventually occur with the integrated uranyl biosensor if the flow cell chamber is repeatedly re-filled with analyte solution. Furthermore, the expectation is that a lower total volume of analyte solution will be required to achieve sensor surface saturation for higher analyte concentrations. Thus, a calibration plot could be developed for the uranyl analyte solution volume required to achieve (near) surface saturation (x-axis) and uranyl analyte

concentration (y-axis). Ultimately, practical operation of the deployed integrated biosensor would involve a series of impedance measurements following the re-filling of the flow cell chamber with analyte solution. Using the flow pump control component of the measurement setup, the volume of analyte solution required to achieve full sensor surface coverage could be determined, and matched to the calibration plot. An estimate for uranyl analyte concentration of the sample would be determined from the calibration plot. A more detailed protocol for this approach is specified below:

- 1) Integrated uranyl biosensor is stored in buffer solution between measurements.
- 2) Take a baseline impedance measurement using attached potentiostat (e.g. measurement may be controlled remotely if integrated sensor is part of an automated water monitoring system)
- 3) Fill the iCell flow cell with the pumped analyte sample solution to be measured (e.g. from groundwater borehole) according to the optimised flow cell protocol for a minimum cell concentration ratio (CCR) of 99%, as developed in Chapter 3. That is, operate at a flow rate between 1.75 mL min^{-1} and 2.5 mL min^{-1} for a minimum of 30 seconds (Section 4.6.3).
- 4) Wait for a fixed time duration, to allow for analyte solution-sensor equilibration. An equilibration time of 30 minutes was used in this study for sensor calibration purposes, but shorter equilibration periods could be used for an accumulation sensor.
- 5) Take impedance measurement using attached potentiostat, and calculate the change in impedance (%) using the baseline measurement taken in (2).
- 6) Repeat steps (3) to (5) until the change in impedance of a given measurement does not significantly change from the preceding measurement e.g. change in measurement $<2\%$ across 3-4 measurements.
- 7) Utilise the pump control function of the monitoring system to estimate the volume of analyte solution sample required to reach stage 6.

- 8) Fit the volume of solution used to a calibration plot of uranyl analyte solution volume (required to achieve full sensor surface coverage) to determine the uranyl analyte concentration.

The proposed protocol utilises the optimised iCell flow cell operational protocol to indirectly measure uranyl analyte concentration in an 'unknown' sample.

It should be noted that this approach would still be subject to margins of error associated with uranyl biosensors constructed upon different electrode chips. For this reason, it is not currently realistic to propose that this operational protocol method is used as a stand-alone approach to uranyl measurements as part of an automated water monitoring system. However, should improvements in chip-to-chip sensor reusability be achieved in the future, this method of operation may be preferable to the 'early warning system' described in Section 6.2.1 for deployment on some sites. This is primarily because it would no longer necessitate a threshold measurement level, and therefore a need to explicitly know the background aqueous uranium concentration of a site (or part of a site). Furthermore, in the event of improved sensor repeatability, with levels comparable to standard laboratory aqueous uranium detection methods, trials would be recommended to determine a preferred operational method between the one described above and operation as a simple detection sensor (i.e. simply measure the change in impedance against a background level and use a calibration plot to equate the measured value to an analyte concentration, or range of concentrations).

6.3 Biosensor/electrode batch variability

The results of the biosensor-flow cell integration investigations presented in Chapter 5 demonstrated that biosensor quality is impacted by electrode surface properties e.g. surface nano-topography and chemical composition (particularly for screen-printed electrodes in the latter case). Consequently, variations in electrode surface between different electrode chips contributes to batch variability in uranyl biosensor performance.

This section therefore very briefly re-visits the literature to provide some context to this issue, with respect to future progress towards achieving repeatable and robust uranyl biosensor measurements as part of an automated water monitoring system.

In Section 2.4.4, results of a review (Table 2-3) was presented of electrode preparation methods used specifically for preparation of solid gold electrodes for the deposition of self-assembled monolayers (SAM's), and methods for the regeneration of electrode surfaces following SAM deposition (i.e. SAM removal). For the review, six different peer-reviewed papers were examined and in total these featured twelve different electrode preparation methods. The first standout point of note regarding this review of gold electrode preparation methods is the clear lack of agreement between authors with respect to both the range of preparation methods considered for their studies, and the choice of recommended best preparation method (or combination of methods). Recommended methods included (as sole recommended method or as part of a combined method approach) flame annealing desorption (Campaña *et al.* 2008), chemical cleaning (e.g. piranha solution (Carvalho *et al.* 2005)), electrochemical oxidative desorption in acidic solution (Carvalho *et al.* 2005), electrochemical reductive desorption in alkaline solution (Tkac and Davis 2008), mechanical polishing (Tkac and Davis 2008), and electrochemical oxidative cleaning in buffer solution (Bhalla *et al.* 2010). A selection of these recommended methods were employed for preparation of the gold chip bespoke electrodes in this study.

The implication of this review is that the link between electrode surface preparation and the quality of chemical or biochemical surfaces deposited on

them is well made in the literature. It is also an indication that the issue of biosensor batch variability as a result of surface topographical variations between electrode chips is an ongoing one not limited to this study.

6.4 Associated work

During this study, two associated projects/investigations were conducted. These were not conducted by the author (of this thesis), but are described here as a) a demonstration of the potential commercial opportunities related to the flow cell design and development work described in this thesis, and b) an indication of the additional integration process required to complete the transition from sensor laboratory proof of concept to deployment within an automated remotely controlled water monitoring system.

Specifically, the two projects/investigations were:

- **Production Flow Cell Development**

The iCell flow cell that was designed and optimised through this study, as described in Chapters 3 and 4, was developed further into a design suitable for mass production.

- **Pump and Flow Control System**

A short project was conducted, by an undergraduate student at the University of Leeds, which investigated the development of a modular pump and flow control system incorporating sensor calibration and signal readout capabilities.

6.4.1 Production flow cell

The iCell flow cell design developed and optimised through the investigations described in Chapters 3 and 4 was developed into a flow cell design suitable potentially for commercial production. This process of flow cell design development was driven by Professor Nik Kapur, one of the supervisors on this project.

It is important to stress that the basic geometry and relative dimensions of the optimised iCell flow domain, and the basic method of operation, was not altered in any way by the re-design process. Instead, design alterations focussed primarily upon the achievement of improvements in the ease-of-use of the unit as a whole, whilst also arguably achieving improvements in

design aesthetics (Figure 6-1). The main features of the re-designed cell were:

- Hinged flow cell base and top (instead of isolated top and base)
- Easy to use locking mechanism to effect a watertight seal (instead of 4-6 locking nuts)
- Reorientation of the base recess for electrode fitting, such that inserted electrodes sit parallel to the direction flow instead of perpendicular to the direction of flow.

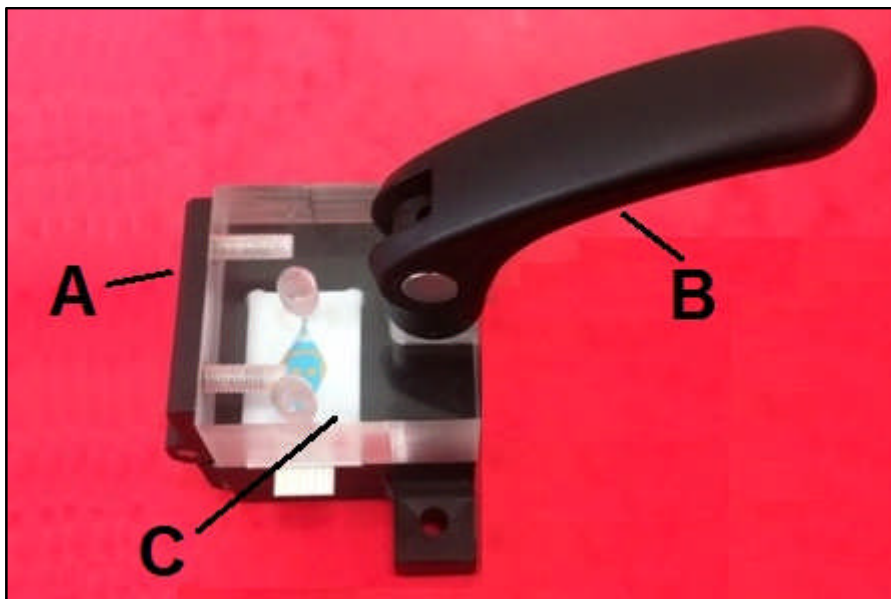


Figure 6-1 Production iCell flow cell design, with hinged top and base (A) and easy-to-use locking mechanism (B). The new design also featured a re-orientation of the electrode with respect to the direction of flow (C).

6.4.2 Automated pump and flow control system

As part of an undergraduate level 3 student project, a study was conducted to investigate the development of an automated pump and flow control system, which also included data transmission and measurement result display capabilities. The initial development work on the system was conducted by a School of Mechanical Engineering student at the University of Leeds, Thomas Pollard, under the supervision of Professor Nik Kapur. Further developments to the system, specifically incorporation of peristaltic

pumps and pump motor controls, were conducted by Professor Nik Kapur. The initial project to develop the system is described fully in Pollard (2014).

Such a system could ultimately be integrated with the electrochemical iCell flow cell and incorporated biosensor (Figure 6-2) as part of a real-time automated monitoring system.

The prototype system was developed using off-the-shelf commercially available components. The main elements of the control system are shown in Figure 6-2A-B. These were:

- **Arduino Uno R3 microcontroller** – enabled control of sample acquisition (including pump control), and sample signal measurement.
- **Arduino GSM* Shield** – connected to the R3 microcontroller, provided remote transmission of data between an internet based data service. The unit makes transmissions via the GPRS (General Packet Radio Service) wireless network. *GSM – Global system for mobile communications. The transmissions were received through a RS232 (serial protocol) module by the internet based data service.
- **Two miniature peristaltic pumps** (with inbuilt stepper motors) - in operational mode these would be conducted to a buffer solution and the water sample to be analysed respectively
- **Switching valve** – Provided switching capabilities between the pump delivering buffer solution and the pump delivering the sample to be measured
- **Stepper motor controllers** – connected to R3 controller, controlled the operation of the peristaltic pumps and switching valve.
- **LCD Display** – although the system was designed to transmit measured data to a remote web service, a local display was also included.

The signal measurement control and data transmission elements of the system were successfully tested using a pH sensor operated locally. However, the pump control functionality was not demonstrated as part of this initial project. Additionally, this initial system was programmed to make

scheduled automated sensor measurements; further developments could include remote control functionality.

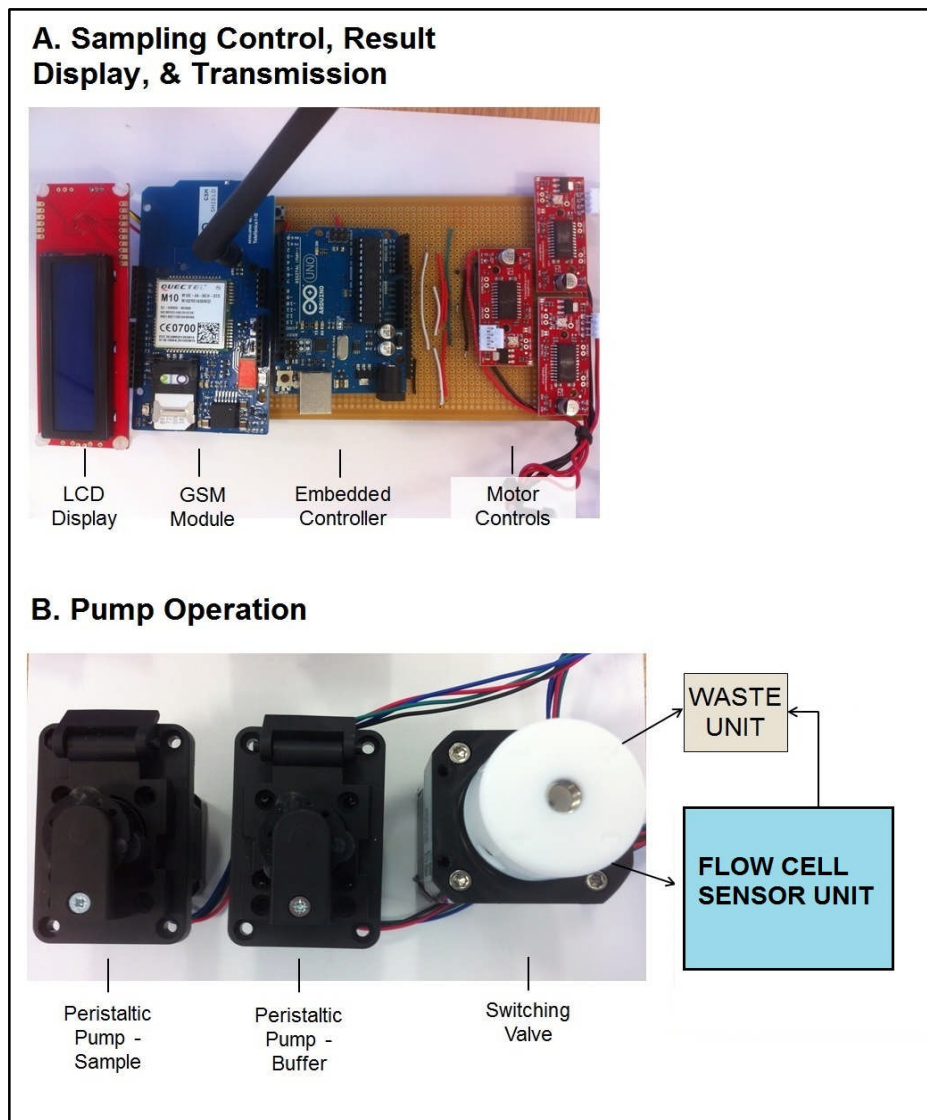


Figure 6-2 Early prototype automated pump and flow control system with data transmission capabilities, developed by Pollard and Kapur.

Overall therefore, this system presents very early stage development work with respect to the progression to a fully automated and remotely controlled water monitoring system. However, it does demonstrate that the technology required to make this transition is currently available. Further work will be required to enable the successful integration of the biosensor-flow cell unit developed through this study, for real-time contamination monitoring. For example, in the development system described above the Arduino microcontroller (via the GSM shield) communicated with an internet based

service via a rs232 (serial protocol) module. For a full-functioning water monitoring system, incorporating a flow cell integrated biosensor, communication could be made instead with a potentiostat for the control of electrochemical measurements.

CHAPTER 7

Conclusions

Chapter 7 **Conclusions**

This final chapter presents the main conclusions identified through the research investigations. Specifically, the project conclusions are outlined with respect to the project objectives developed in Chapter 1 (Section 7.1), and the contribution made to subject knowledge and practice is specified (Section 7.2). Finally, recommendations for further research are outlined (Section 7.3).

7.1 Project outcomes with respect to research aim and objectives

First, a reminder of the research study aim and objectives:

AIM

Develop a fluid delivery system for sensor units, and biosensors specifically, for which the geometrical design and operational protocol are optimised to enable control over the equilibration of the sample analyte concentration within the flow cell with that within the influent. Such a fluid delivery system would be designed to ultimately form a modular component of an automated water monitoring system.

OBJECTIVES

- 1)** Investigate and quantify an optimal design for a fluid delivery system (flow cell) that will contribute to the transition of laboratory proof-of-concept biosensors for point-of-use deployment.
- 2)** Develop specific recommendations for an operational protocol for the optimally-designed flow cell unit.
- 3)** Investigate and quantify the successful integration of a specific biosensor unit, a biosensor for the detection of aqueous uranyl ions, into the optimally-designed flow cell unit.

4) Develop specific recommendations for a successful biosensor integration approach, and for an operational protocol for the integrated biosensor-flow cell unit.

An optimal flow cell design and recommended operational protocol (objectives 1 and 2) was achieved through the application of established fluid mechanics principles and investigative techniques, specifically numerical flow modelling and experimental flow visualisation approaches. The suitability of the design investigation with respect to the stated objectives was measured through strong quantitative validation results for both of the two investigative tools (numerical models of flow cell geometries and flow fluorescence investigations). Additionally the validity of the overall investigation was determined through strong comparative results, incorporating both qualitative and quantitative analysis, of the two different investigative methods. The preferred design, the iCell geometry, was ultimately selected through comparative analysis of a range of quantitative flow analysis results for three different flow channel geometries, along with comparison of results against a commercially available flow cell of a different design (Chapters 3 and 4).

A biosensor for the detection of uranyl ions was successfully integrated into the optimised iCell flow cell (objective 3). Success in this sense relates first to the modification of the flow cell to incorporate a bespoke gold chip working electrode, and separate counter and reference electrodes. Additionally, the integrated system was operated successfully to produce coherent analytical electrochemical results, broadly comparable to those presented by Conroy (2012) for the original biosensor development investigation. That is, for the integrated uranyl biosensor a relationship was identified between uranyl solution concentration and impedance electrochemical response for an analyte concentration range of 10^{-12} M to 10^{-6} M (Chapter 5). However, the results of this study demonstrated the achievement of an extension to the operational range (i.e. sensor dynamic range) of the uranyl biosensor from that presented by Conroy (2012). That is, the range of analyte concentrations detected by the sensor before surface coverage saturation occurred was extended from $10^{-12} - 10^{-10}$ M UO_2^{2+} for

Conroy's calibration plot, to 10^{-12} - 10^{-6} M UO_2^{2+} for this study. This represents a minimum extended dynamic range of four orders of magnitude (this is a *minimum* because surface coverage saturation was not demonstrated for the range of analyte concentrations considered in this study).

Finally, recommendations for the operational protocols of an integrated uranyl biosensor incorporated within an automated and remotely controlled water monitoring system were developed (objective 4). Specifically, these considered operation of the integrated sensor within the restrictions provided by margins of error associated with repeatable sensor performance for units constructed upon different electrode chips. Two different operational protocol approaches were proposed. First, a protocol was described for which the uranyl sensor was operated as an *early warning sensor* by identifying a threshold change of impedance level. System measurements beyond the threshold level would trigger secondary water sampling using traditional manual sampling methods, followed by supporting analysis using standard laboratory techniques (e.g. solid fluorimetry). Secondly, an operational protocol was proposed for which the uranyl biosensor was operated as an *accumulation sensor* and calibration was related to the volume of analyte solution required to achieve (near) full sensor surface adsorption coverage for a given analyte concentration.

7.2 Contribution to knowledge and practice

Firstly, the following general recommendations were identified for the design and operation of flow cells for the integration of biosensor units. It should be remembered that the term cell concentration ratio (CCR) describes the ratio of the mean analyte concentration within the flow cell to the analyte concentration of the influent:

- **Select a flow cell design and operational protocol that prevents the development of regions of flow recirculation (eddies).**
 - This limits the influence of slower diffusion processes and therefore allows for the minimisation of fluid volume and time required to reach

a desired cell concentration ratio (CCR). The minimisation of fluid volume, both measurement samples and buffers/reagents, potentially minimises costs and reduces the requirement for waste retrieval (particularly useful for remotely operated automated systems).

- This can be achieved by the combined effect of reducing the rate of channel expansion and contraction, and maintaining a flow rate below which the onset of eddies arise.

- **Flow cell performance should always be fully characterised for a range of flow rates and cell concentration ratios (CCR's) before being used for the integration of biosensors (or other sensor types)**

- This is because it is important to recognise that (a) the mean concentration of analyte within the flow cell will differ from that within the influent, and (b) the time required to reach the CCR is in part a function of the cell geometry

- This enables the development of an operational protocol that provides flow controls suitable to the operational mechanics (i.e. biosensor binding association and dissociation rates, sensor-analyte reaction kinetics) and practical operational purpose of the specific biosensor-flow cell integrated unit under consideration.

Additionally, with respect to the integration of the uranyl biosensor into the optimised flow cell the following contributions to the understanding of biosensor development and operation were identified:

- 1) **Uranyl biosensor quality, and biosensor performance, is dependent on biosensor surface quality**

- Bespoke gold chip electrodes (as part of an electrochemical flow cell) were demonstrated to be preferable to commercially sourced screen-printed electrodes for the construction of the uranyl biosensors. The relatively poor performance of the screen-printed electrodes was associated with the surface nano-topography and/or chemical composition of ink employed in the screen printing process.

However, further development work is still required to improve the biosensor performance of the integrated uranyl biosensor (Section 7.3).

2) An understanding of how to utilise the chemical equilibrium between analyte bound to the biosensor surface and analyte free in solution to extend the dynamic range of the uranyl biosensor.

- The extension of the dynamic range of the uranyl biosensor described in Section 7.1 was achieved by understanding the benefits of scaling down the operation of the uranyl biosensor in terms of the sample volume to which the sensor surface was exposed during measurements. The Langmuir isotherm adsorption model proved to be a good predictor of bound analyte surface coverage of the uranyl biosensor for biosensor performance investigations conducted by Conroy in a relatively large sample volume (~30 mL). The sensor surface was effectively 'saturated' with analyte for UO_2^{2+} concentrations beyond 10^{-10} M. However, by integrating the biosensor into the optimised iCell flow cell (sample volume ~0.2 mL) a response not predicted by the Langmuir model for the range of analyte concentrations considered was observed. Instead, a different adsorption model (Freundlich adsorption isotherm) proved to be a better fit. This was primarily attributed to a decrease in analyte concentration within the flow cell bulk solution due to analyte binding on the biosensor surface. In other words, the cell concentration ratio (CCR) established through the flow cell operational protocol was changed by analyte adsorption to the sensor surface. This meant that saturation of the sensor surface did not occur for the range of analyte concentrations considered, thus extending the operational dynamic range of the sensor.

Cont'd over....

3) An understanding of how to utilise the chemical equilibrium between analyte bound to the biosensor surface and analyte free in solution as a means of calibrating the uranyl biosensor for optimised field deployment operation

- An extension to point (2) above was the identification of an operational protocol (summarised in Section 7.1) which capitalised on the biosensor-analyte adsorption behaviour predicted by the Langmuir model. That is, repeated filling of the iCell flow cell would ultimately lead to (near) full sensor surface analyte coverage, approximating sensor saturation, for analyte concentrations above 10^{-10} M. This would allow for the development of a calibration plot of total analyte solution volume required to achieve 'saturation' against analyte concentration.

7.3 Recommended further research

Recommendations for further research are considered separately with respect to the two main elements of the study (from Section 1.4):

- Design of an optimised flow cell for biosensor point-of-use deployment
- Integration of a selected biosensor, for the detection of aqueous uranyl ions, into the optimally-designed flow cell

Optimised flow cell research development

A) Integration with automation and remote control technology

In Chapter 6, an early stage project was outlined that used off-the-shelf electronic components to develop a data control and transmission platform, towards the development of an automated monitoring system. The next step is to fully integrate the iCell flow cell with this platform, and with remotely operated sample pumping and flow controls. Ideally, such a system would be tested using a calibrated biosensor or other sensor type.

B) Healthcare applications

Whilst the focus of this study has been on integration into the optimised flow cell of a biosensor for environmental monitoring, a significant amount of current biosensor research is related to medical diagnostics. The iCell flow cell could therefore be considered for the integration of biosensors towards the development of point-of-care diagnostic tools. The iCell design principles would apply to the type of samples applicable to healthcare applications, such as blood, urine, and surgical drain fluids. However, further research work would be required to model the flow cell response, and to develop specific operational protocols, for fluids of the range of viscosities appropriate to these types of sample.

Uranyl biosensor deployment research development

C) Full studies related to robust integrated uranyl biosensor repeatability

Methods were proposed in this thesis for the robust operation of the integrated uranyl biosensors as part of an automated water monitoring system (Chapter 6). However, these were developed within the limitations provided by errors associated with chip-to-chip repeatability. Therefore, it logically follows that future improvements in sensor chip-to-chip margin errors, through alternative preparation methods for the gold chip electrodes and/or alternative gold electrode surfaces, would also potentially improve sensor reliability.

Additionally, an operational protocol for integrated uranyl biosensor measurements was proposed in Section 6.2, for which the unit was operated as an accumulation sensor. Unfortunately, time did not permit calibration investigations for this proposed method to be conducted as part of this study. They are therefore recommended here as forming part of any future work.

REFERENCES

- Abbot Laboratories, Abbot Point Of Care*. 2013. [online]. [Accessed 24/05/2013]. Available from: <http://www.abbotpointofcare.com/>.
- ACHESON, D. J. and D. ACHESON. 1990. *Elementary fluid dynamics*. Clarendon press Oxford.
- ACRIVOS, A. and M. L. SCHRADER. 1982. Steady flow in a sudden expansion at high Reynolds numbers. *Physics of Fluids*, **25**(6), pp.923-930.
- ADAMSON, A. W. and A. P. GAST. 1967. *Physical chemistry of surfaces*.
- AKYILDIZ, I. F., W. SU, Y. SANKARASUBRAMANIAM and E. CAYIRCI. 2002. Wireless sensor networks: a survey. *Computer Networks*, **38**(4), pp.393-422.
- BANICA, F.-G. 2012. *Chemical Sensors and Biosensors: Fundamentals and Applications*. John Wiley & Sons.
- BARD, A. J. and L. R. FAULKNER. 1980. *Electrochemical methods: fundamentals and applications*. Wiley New York.
- BARKLEY, D., M. G. M. GOMES and R. D. HENDERSON. 2002. Three-dimensional instability in flow over a backward-facing step. *Journal of Fluid Mechanics*, **473**, pp.167-190.
- BATAILLARD, P., F. GARDIES, N. JAFFREZIC-RENAULT, C. MARTELET, B. COLIN and B. MANDRAND. 1988. Direct detection of immunospecies by capacitance measurements. *Analytical Chemistry*, **60**(21), pp.2374-2379.
- BEATON, A. D., V. J. SIEBEN, C. F. A. FLOQUET, E. M. WAUGH, S. ABI KAED BEY, I. R. G. OGILVIE, M. C. MOWLEM and H. MORGAN. 2011. An automated microfluidic colourimetric sensor applied in situ to determine nitrite concentration. *Sensors and Actuators B: Chemical*, **156**(2), pp.1009-1014.
- BELKIN, S. 2006. Genetically engineered microorganisms for pollution monitoring. *Soil and Water Pollution Monitoring, Protection and Remediation*. Springer, pp.147-160.
- BHALLA, V., S. CARRARA, C. STAGNI and B. SAMORÌ. 2010. Chip cleaning and regeneration for electrochemical sensor arrays. *Thin Solid Films*, **518**(12), pp.3360-3366.
- BIRAN, A., P. RAMI, S. BUCHINGER, R. GEORG and S. BELKIN. 2009. Genetically Engineered Bacteria for Genotoxicity Assessment. In: D. BARCELÓ and P.-D. HANSEN, eds. *Biosensors for Environmental Monitoring of Aquatic Systems*. Springer Berlin Heidelberg, pp.161-186.
- BIRD, R. B., W. E. STEWART and E. N. LIGHTFOOT. 2007. *Transport phenomena*. John Wiley & Sons.
- BISWAS, G., M. BREUER and F. DURST. 2004. Backward-Facing Step Flows for Various Expansion Ratios at Low and Moderate Reynolds Numbers. *Journal of Fluids Engineering*, **126**(3), pp.362-374.

- BITTON, G. and B. KOOPMAN. 1992. Bacterial and enzymatic bioassays for toxicity testing in the environment. *Reviews of environmental contamination and toxicology*. Springer, pp.1-22.
- BOEHM, D. A., P. A. GOTTLIEB and S. Z. HUA. 2007. On-chip microfluidic biosensor for bacterial detection and identification. *Sensors and Actuators B: Chemical*, **126**(2), pp.508-514.
- BROWNLEE, C., V. PEGORARO, S. SHANKAR, P. S. MCCORMICK and C. D. HANSEN. 2011. Physically-based interactive flow visualization based on schlieren and interferometry experimental techniques. *Visualization and Computer Graphics, IEEE Transactions on*, **17**(11), pp.1574-1586.
- BURGE, S. R. and J. MAY. 2005. Automated ground water sampling and analysis of trichloroethene using a "universal" sampling/analytical system. *Ground Water Monitoring & Remediation*, **25**(1), pp.113-122.
- BUZZACCARO, S., E. SECCHI and R. PIAZZA. 2013. Ghost Particle Velocimetry: Accurate 3D Flow Visualization Using Standard Lab Equipment. *Physical Review Letters*, **111**(4), p048101.
- CAMPIÑA, J. M., A. MARTINS and F. SILVA. 2008. A new cleaning methodology for efficient Au-SAM removal. *Electrochimica Acta*, **53**(26), pp.7681-7689.
- CANTU-PEREZ, A., S. BARRASS and A. GAVRIILIDIS. 2010. Residence time distributions in microchannels: Comparison between channels with herringbone structures and a rectangular channel. *Chemical Engineering Journal*, **160**(3), pp.834-844.
- CAPELLA, J. V., A. BONASTRE, R. ORS and M. PERIS. 2013. In line river monitoring of nitrate concentration by means of a Wireless Sensor Network with energy harvesting. *Sensors and Actuators B: Chemical*, **177**(0), pp.419-427.
- CARVALHAL, R. F., R. SANCHES FREIRE and L. T. KUBOTA. 2005. Polycrystalline Gold Electrodes: A Comparative Study of Pretreatment Procedures Used for Cleaning and Thiol Self-Assembly Monolayer Formation. *Electroanalysis*, **17**(14), pp.1251-1259.
- CHIKKAVEERIAIAH, B. V., H. LIU, V. MANI, F. PAPADIMITRAKOPOULOS and J. F. RUSLING. 2009. A microfluidic electrochemical device for high sensitivity biosensing: Detection of nanomolar hydrogen peroxide. *Electrochemistry Communications*, **11**(4), pp.819-822.
- CHOI, A., J.-S. PARK and H.-I. JUNG. 2009. Solid-medium-integrated impedimetric biosensor for real-time monitoring of microorganisms. *Sensors and Actuators B: Chemical*, **137**(1), pp.357-362.
- CHOI, S., M. GORYLL, L. SIN, P. WONG and J. CHAE. 2011. Microfluidic-based biosensors toward point-of-care detection of nucleic acids and proteins. *Microfluidics and Nanofluidics*, **10**(2), pp.231-247.
- CHOY, K. K. H., J. F. PORTER and G. MCKAY. 2000. Langmuir Isotherm Models Applied to the Multicomponent Sorption of Acid Dyes from Effluent onto Activated Carbon. *Journal of Chemical & Engineering Data*, **45**(4), pp.575-584.

COLDRICK, Z., P. STEENSON, P. MILLNER, M. DAVIES and A. NELSON. 2009. Phospholipid monolayer coated microfabricated electrodes to model the interaction of molecules with biomembranes. *Electrochimica Acta*, **54**(22), pp.4954-4962.

COMSOL. 2012. COMSOL Multiphysics User's Guide. [online]. Available from:
[http://nf.nci.org.au/facilities/software/COMSOL/4.3a/doc/pdf/mph/COMSOLM
ultiphysicsUsersGuide.pdf](http://nf.nci.org.au/facilities/software/COMSOL/4.3a/doc/pdf/mph/COMSOLM%20multiphysicsUsersGuide.pdf).

CONROY, D. 2012. *Nanostructured surfaces for sensing heavy metals and radionuclides in aqueous systems*. PhD thesis, The University of Leeds.

CONROY, D. J. R., P. A. MILLNER, D. I. STEWART and K. POLLMANN. 2010. Biosensing for the Environment and Defence: Aqueous Uranyl Detection Using Bacterial Surface Layer Proteins. *Sensors*, **10**(5), pp.4739-4755.

COOPER, J. A. and R. G. COMPTON. 1998. Channel Electrodes — A Review. *Electroanalysis*, **10**(3), pp.141-155.

CRANÇON, P., A. MANGERET and L. DE WINDT. 2012. Assessing Migration of Uranium through Chalk Substrate: Field Study and Reactive Transport Modelling. *Journal ISSN*, **1929**, p2732.

CREW, A., D. LONSDALE, N. BYRD, R. PITTSOON and J. P. HART. 2011. A screen-printed, amperometric biosensor array incorporated into a novel automated system for the simultaneous determination of organophosphate pesticides. *Biosensors and Bioelectronics*, **26**(6), pp.2847-2851.

CRIMALDI, J. 2008. Planar laser induced fluorescence in aqueous flows. *Experiments in Fluids*, **44**(6), pp.851-863.

CRUICKSHANK, J. 2012. Findings of the Sellafield Contaminated Land & Groundwater Management Project and the Next Steps for the Land Quality Programme. [online]. Available from:
<http://www.sellafielddesites.com/land/documents/Signpost%20Report.pdf>.

CSŐVÁRI, M., Z. BERTA, J. CSICSÁK and G. FÖLDING. 2005a. Chapter 9 Mecsek Ore, Pécs, Hungary case study. *In*: T. M. F. G. S. K.E. ROEHL and D. I. STEWART, eds. *Trace Metals and other Contaminants in the Environment*. Elsevier, pp.211-259.

CSŐVÁRI, M., J. CSICSÁK, G. FÖLDING and G. SIMONCSICS. 2005b. Chapter 10 Experimental iron barrier in Pécs, Hungary. *In*: T. M. F. G. S. K.E. ROEHL and D. I. STEWART, eds. *Trace Metals and other Contaminants in the Environment*. Elsevier, pp.261-281.

DAI, Z., H. BAI, M. HONG, Y. ZHU, J. BAO and J. SHEN. 2008. A novel nitrite biosensor based on the direct electron transfer of hemoglobin immobilized on CdS hollow nanospheres. *Biosensors and Bioelectronics*, **23**(12), pp.1869-1873.

DAS, N. 2012. Remediation of Radionuclide Pollutants through Biosorption— an Overview. *CLEAN—Soil, Air, Water*, **40**(1), pp.16-23.

DAS, S., H. VIKALO and A. HASSIBI. 2009. On scaling laws of biosensors: a stochastic approach. *Journal of Applied Physics*, **105**(10), p102021.

DEFRA. 2007. *Policy for the Long Term Management of Solid Low Level Radioactive Waste in the United Kingdom*. London, UK: Department for Environment Food and Rural Affairs,.

DEFRA. 2012. *Environmental Protection Act 1990: Part 2A Contaminated Land Statutory Guidance* Online: HM Government.

DIEHL, H. and R. MARKUSZEWSKI. 1989. Studies on fluorescein—VII: The fluorescence of fluorescein as a function of pH. *Talanta*, **36**(3), pp.416-418.

DOLAN JENNER INDUSTRIES. 2011. *Replacement Lamps* [online]. [Accessed 06/07/2011]. Available from: <http://www.dolan-jenner.com/Catalog/PDFs/Lamps.pdf>.

DOMINGO, J. L. 2001. Reproductive and developmental toxicity of natural and depleted uranium: a review. *Reproductive Toxicology*, **15**(6), pp.603-609.

DOUGLAS, J. F., J. M. GASORIEK, J. A. SWAFFIELD and L. B. JACK. 2005. *Fluid Mechanics*. Fifth ed. Harlow, Essex, England: Pearson Education Limited.

DROPSSENS. 2011a. *Flow-Cell for Screen-Printed Electrodes (ref. FLWCL)* [online]. [Accessed 06/06/2011]. Available from: http://www.dropsens.com/en/pdfs_productos/flowcell.pdf.

DROPSSENS. 2011b. *Screen-Printed Electrodes* [online]. [Accessed 03/06/2011]. Available from: http://www.dropsens.com/en/screen_printed_electrodes_pag.html.

DU, D., J. WANG, J. N. SMITH, C. TIMCHALK and Y. H. LIN. 2009. Biomonitoring of Organophosphorus Agent Exposure by Reactivation of Cholinesterase Enzyme Based on Carbon Nanotube-Enhanced Flow-Injection Amperometric Detection. *Analytical Chemistry*, **81**(22), pp.9314-9320.

EL GHONEMY, H. 2004. ***Sellafield Groundwater Conceptual Model***. BNFL, Nuclear Sciences & Technology Services, 2004.

ERICKSON, K. A. and P. WILDING. 1993. EVALUATION OF A NOVEL POINT-OF-CARE SYSTEM, THE I-STAT PORTABLE CLINICAL ANALYZER. *Clinical Chemistry*, **39**(2), pp.283-287.

FERZIGER, J. H. and M. PERIĆ. 2002. *Computational methods for fluid dynamics*. Springer Berlin.

FREDRICKSON, J. K., J. M. ZACHARA, D. L. BALKWILL, D. KENNEDY, S. M. W. LI, H. M. KOSTANDARITHES, M. J. DALY, M. F. ROMINE and F. J. BROCKMAN. 2004. Geomicrobiology of high-level nuclear waste-contaminated vadose sediments at the Hanford Site, Washington State. *Applied and Environmental Microbiology*, **70**(7), pp.4230-4241.

FREUNDLICH, H. and H. S. HATFIELD. 1926. Colloid and capillary chemistry.

FRISBIE, S. H., E. J. MITCHELL and B. SARKAR. 2013. World Health Organization increases its drinking-water guideline for uranium. *Environmental Science: Processes & Impacts*, **15**(10), pp.1817-1823.

- FU, E., T. LIANG, J. HOUGHTALING, S. RAMACHANDRAN, S. A. RAMSEY, B. LUTZ and P. YAGER. 2011. Enhanced Sensitivity of Lateral Flow Tests Using a Two-Dimensional Paper Network Format. *Analytical Chemistry*, **83**(20), pp.7941-7946.
- GARTIA, M. R., B. BRAUNSCHWEIG, T.-W. CHANG, P. MOINZADEH, B. S. MINSKER, G. AGHA, A. WIECKOWSKI, L. L. KEEFER and G. L. LIU. 2012. The microelectronic wireless nitrate sensor network for environmental water monitoring. *Journal of Environmental Monitoring*, **14**(12), pp.3068-3075.
- GAVRILESCU, M., L. V. PAVEL and I. CRETESCU. 2009. Characterization and remediation of soils contaminated with uranium. *Journal of Hazardous Materials*, **163**(2-3), pp.475-510.
- GERRINGA, L. J. A., P. M. J. HERMAN and T. C. W. POORTVLIET. 1995. Comparison of the linear Van den Berg/Ružić transformation and a non-linear fit of the Langmuir isotherm applied to Cu speciation data in the estuarine environment. *Marine Chemistry*, **48**(2), pp.131-142.
- GIBB, T. R., A. P. IVANOV, J. B. EDEL and T. ALBRECHT. 2014. Single Molecule Ionic Current Sensing in Segmented Flow Microfluidics. *Analytical Chemistry*, **86**(3), pp.1864-1871.
- GLAVAN, A. C., R. V. MARTINEZ, E. J. MAXWELL, A. B. SUBRAMANIAM, R. M. NUNES, S. SOH and G. M. WHITESIDES. 2013. Rapid fabrication of pressure-driven open-channel microfluidic devices in omniphobic RF paper. *Lab on a Chip*, **13**(15), pp.2922-2930.
- GORAL, V., Q. WU, H. SUN and Y. FANG. 2011. Label-free optical biosensor with microfluidics for sensing ligand-directed functional selectivity on trafficking of thrombin receptor. *FEBS Letters*, **585**(7), pp.1054-1060.
- GRENTHE, I., J. DROŹDŹYŃSKI, T. FUJINO, E. BUCK, T. ALBRECHT-SCHMITT and S. WOLF. 2006. Uranium. In: L. MORSS, N. EDELSTEIN and J. FUGER, eds. *The Chemistry of the Actinide and Transactinide Elements*. Springer Netherlands, pp.253-698.
- GRIESHABER, D., R. MACKENZIE, J. VOEROES and E. REIMHULT. 2008. Electrochemical biosensors-Sensor principles and architectures. *Sensors*, **8**(3), pp.1400-1458.
- GUEDRI, H. and C. DURRIEU. 2008. A self-assembled monolayers based conductometric algal whole cell biosensor for water monitoring. *Microchimica Acta*, **163**(3-4), pp.179-184.
- HAYAT, A. and J. L. MARTY. 2014. Disposable Screen Printed Electrochemical Sensors: Tools for Environmental Monitoring. *Sensors*, **14**(6), pp.10432-10453.
- HELALI, S. 2013. *Impedimetric Immunosensor for Pesticide Detection*. State of the Art in Biosensors - Environmental and Medical Applications.
- HNAIEN, M., S. BOURIGUA, F. BESSUEILLE, J. BAUSELLS, A. ERRACHID, F. LAGARDE and N. JAFFREZIC-RENAULT. 2011. Impedimetric microbial biosensor based on single wall carbon nanotube modified microelectrodes for trichloroethylene detection. *Electrochimica Acta*, **56**(28), pp.10353-10358.

- HOOGVLIET, J. C., M. DIJKSMA, B. KAMP and W. P. VAN BENNEKOM. 2000. Electrochemical Pretreatment of Polycrystalline Gold Electrodes To Produce a Reproducible Surface Roughness for Self-Assembly: A Study in Phosphate Buffer pH 7.4. *Analytical Chemistry*, **72**(9), pp.2016-2021.
- HUANG, D., F. LIAO, S. MOLESA, D. REDINGER and V. SUBRAMANIAN. 2003. Plastic-compatible low resistance printable gold nanoparticle conductors for flexible electronics. *Journal of the Electrochemical Society*, **150**(7), pp.G412-G417.
- HYATT, N. C., S. R. BIGGS, F. R. LIVENS, J. C. YOUNG and N. EVANS. 2009. DIAMOND: academic innovation in support of UK radioactive waste management. *In: Scientific Basis for Nuclear Waste Management XXXII, Boston, MA, USA* Materials Research Society.
- IBACH, H. 2006. *Physics of surfaces and interfaces*. Springer.
- ISLAM, K., Y.-C. JANG, R. CHAND, S. K. JHA, H. H. LEE and Y.-S. KIM. 2011. Microfluidic Biosensor for β -Amyloid (1-42) Detection Using Cyclic Voltammetry. *Journal of nanoscience and nanotechnology*, **11**(7), pp.5657-5662.
- IVNITSKI, D., I. ABDEL-HAMID, P. ATANASOV and E. WILKINS. 1999. Biosensors for detection of pathogenic bacteria. *Biosensors & Bioelectronics*, **14**(7), pp.599-624.
- JADIA, C. D. and M. FULEKAR. 2009. Phytoremediation of heavy metals: Recent techniques. *African journal of biotechnology*, **8**(6).
- JOKERST, J. C., J. M. EMORY and C. S. HENRY. 2012. Advances in microfluidics for environmental analysis. *Analyst*, **137**(1), pp.24-34.
- KADEMANI, B. S., G. SURWASE, A. SAGAR, L. MOHAN and K. BHANUMURTHY. 2013. Research trends in radioactive waste management: a global perspective. *International Journal of Low Radiation*, **9**(1), pp.59-94.
- KISSINGER, P. T. and W. R. HEINEMAN. 1983. Cyclic voltammetry. *Journal of Chemical Education*, **60**(9), p702.
- KOBLIZEK, M., J. MALY, J. MASOJIDEK, J. KOMENDA, T. KUCERA, M. T. GIARDI, A. K. MATTOO and R. PILLOTON. 2002. A biosensor for the detection of triazine and phenylurea herbicides designed using Photosystem II coupled to a screen-printed electrode. *Biotechnology and Bioengineering*, **78**(1), pp.110-116.
- KOCSIS, A. and H. MOLNAR. 2009. *Genotoxicity: Evaluation, Testing and Prediction*. Nova Biomedical Books.
- KOMAITIS, E., E. VASILIOU, G. KREMMYDAS, D. G. GEORGAKOPOULOS and C. GEORGIOU. 2010. Development of a fully automated flow injection analyzer implementing bioluminescent biosensors for water toxicity assessment. *Sensors*, **10**(8), pp.7089-7098.
- KONCKI, R. 2007. Recent developments in potentiometric biosensors for biomedical analysis. *Analytica Chimica Acta*, **599**(1), pp.7-15.
- KORHONEN, R. K., P. JULKUNEN, L. LI and C. C. VAN DONKELAAR. 2013. Computational Models of Articular Cartilage. *Computational and mathematical methods in medicine*, **2013**.

- KOROTCENKOV, G. 2010. *Chemical Sensors: Fundamentals of Sensing Materials Volume 1: General Approaches*. Momentum Press.
- KOTAMÄKI, N., S. THESSLER, J. KOSKIAHO, A. O. HANNUKALA, H. HUITU, T. HUTTULA, J. HAVENTO and M. JÄRVENPÄÄ. 2009. Wireless in-situ sensor network for agriculture and water monitoring on a river basin scale in southern Finland: Evaluation from a data user's perspective. *Sensors*, **9**(4), pp.2862-2883.
- KOTSILIERIS, T. and G. T. KARETSOS. 2008. A Mobile Agent Enabled Wireless Sensor Network for River Water Monitoring. *In: Wireless and Mobile Communications, 2008. ICWMC '08. The Fourth International Conference on*, July 27 2008-Aug. 1 2008, pp.346-351.
- KURTTIO, P., H. KOMULAINEN, A. LEINO, L. SALONEN, A. AUVINEN and H. SAHA. 2005. Bone as a possible target of chemical toxicity of natural uranium in drinking water. *Environmental health perspectives*, **113**(1), p68.
- KWAKYE, S., V. N. GORAL and A. J. BAEUMNER. 2006. Electrochemical microfluidic biosensor for nucleic acid detection with integrated minipotentostat. *Biosensors and Bioelectronics*, **21**(12), pp.2217-2223.
- LAMMERTYN, J., P. VERBOVEN, E. A. VERAVERBEKE, S. VERMEIR, J. IRUDAYARAJ and B. M. NICOLAÏ. 2006. Analysis of fluid flow and reaction kinetics in a flow injection analysis biosensor. *Sensors and Actuators B: Chemical*, **114**(2), pp.728-736.
- LASIA, A. 2002. *Electrochemical impedance spectroscopy and its applications*. Springer.
- LI, G. and P. MIAO. 2013. Theoretical Background of Electrochemical Analysis. *Electrochemical Analysis of Proteins and Cells*. Springer, pp.5-18.
- LIN, R. H., L. J. WU, C. H. LEE and S. Y. LIN-SHIAU. 1993. Cytogenetic toxicity of uranyl nitrate in Chinese hamster ovary cells. *Mutation Research/Genetic Toxicology*, **319**(3), pp.197-203.
- LUPPA, P. B., L. J. SOKOLL and D. W. CHAN. 2001. Immunosensors—principles and applications to clinical chemistry. *Clinica Chimica Acta*, **314**(1–2), pp.1-26.
- MACDONALD, J. 1992. Impedance spectroscopy. *Annals of Biomedical Engineering*, **20**(3), pp.289-305.
- MACY, M. W. and J. SKVORETZ. 1998. The evolution of trust and cooperation between strangers: A computational model. *American Sociological Review*, pp.638-660.
- MARK, D., S. HAEBERLE, G. ROTH, F. VON STETTEN and R. ZENGERLE. 2010. Microfluidic lab-on-a-chip platforms: requirements, characteristics and applications. *Chemical Society Reviews*, **39**(3), pp.1153-1182.
- MARLE, L. and G. M. GREENWAY. 2005. Microfluidic devices for environmental monitoring. *TrAC Trends in Analytical Chemistry*, **24**(9), pp.795-802.
- MARTIN, H., B. M. PATTERSON, G. B. DAVIS and P. GRATHWOHL. 2003. Field Trial of Contaminant Groundwater Monitoring: Comparing Time-

Integrating Ceramic Dosimeters and Conventional Water Sampling. *Environmental Science & Technology*, **37**(7), pp.1360-1364.

MARTIN, M. M. and L. LINDQVIST. 1975. The pH dependence of fluorescein fluorescence. *Journal of Luminescence*, **10**(6), pp.381-390.

MATATAGUI, D., J. FONTECHA, M. J. FERNÁNDEZ, M. J. OLIVER, J. HERNANDO-GARCÍA, J. L. SÁNCHEZ-ROJAS, I. GRÀCIA, C. CANÉ, J. P. SANTOS and M. C. HORRILLO. 2013. Comparison of two types of acoustic biosensors to detect immunoreactions: Love-wave sensor working in dynamic mode and QCM working in static mode. *Sensors and Actuators B: Chemical*, **189**(0), pp.123-129.

MCGRAW, C. M., S. E. STITZEL, J. CLEARY, C. SLATER and D. DIAMOND. 2007. Autonomous microfluidic system for phosphate detection. *Talanta*, **71**(3), pp.1180-1185.

MERROUN, M. L., J. RAFF, A. ROSSBERG, C. HENNIG, T. REICH and S. SELENSKA-POBELL. 2005. Complexation of uranium by cells and S-layer sheets of *Bacillus sphaericus* JG-A12. *Applied and Environmental Microbiology*, **71**(9), pp.5532-5543.

MERZKIRCH, W. 1987. *Flow visualization*. Elsevier.

MICHELINI, E., L. CEVENINI, M. CALABRETTA, S. SPINOZZI, C. CAMBORATA and A. RODA. 2013. Field-deployable whole-cell bioluminescent biosensors: so near and yet so far. *Analytical and Bioanalytical Chemistry*, **405**(19), pp.6155-6163.

MISHRA, R. K., R. B. DOMINGUEZ, S. BHAND, R. MUÑOZ and J.-L. MARTY. 2012. A novel automated flow-based biosensor for the determination of organophosphate pesticides in milk. *Biosensors and Bioelectronics*, **32**(1), pp.56-61.

MIZUSHIMA, J. and Y. SHIOTANI. 2001. Transitions and instabilities of flow in a symmetric channel with a suddenly expanded and contracted part. *Journal of Fluid Mechanics*, **434**, pp.355-369.

MOFFATT, H. K. 1964. Viscous and resistive eddies near a sharp corner. *Journal of Fluid Mechanics*, **18**(1), pp.1-18.

MOTA, M. C., P. CARVALHO, J. RAMALHO and E. LEITE. 1991. Spectrophotometric analysis of sodium fluorescein aqueous solutions. Determination of molar absorption coefficient. *International Ophthalmology*, **15**(5), pp.321-326.

MUKHOPADHYAY, M. 2005. *Mechanics of composite materials and structures*. Universities press.

NDA. 2006. *NDA Strategy*. UK HM Government.

NDA. 2011. *Radioactive Wastes in the UK: A Summary of the 2010 Inventory*. UK HM Government.

NEUFELD, T., I. ESHKENAZI, E. COHEN and J. RISHPON. 2000. A micro flow injection electrochemical biosensor for organophosphorus pesticides. *Biosensors and Bioelectronics*, **15**(5-6), pp.323-329.

- NEWMAN, J. D. and A. P. F. TURNER. 2005. Home blood glucose biosensors: a commercial perspective. *Biosensors & Bioelectronics*, **20**(12), pp.2435-2453.
- NEWSOME, L., K. MORRIS and J. R. LLOYD. 2014. The biogeochemistry and bioremediation of uranium and other priority radionuclides. *Chemical Geology*, **363**(0), pp.164-184.
- NIEDERBACHER, P. and M. NAHOLD. 2005. Chapter 11 Installation and operation of an Adsorptive Reactor and Barrier (AR&B) system in Brunn am Gebirge, Austria. In: T. M. F. G. S. K.E. ROEHL and D. I. STEWART, eds. *Trace Metals and other Contaminants in the Environment*. Elsevier, pp.283-309.
- O'FLYRM, B., R. MARTINEZ, J. CLEARY, C. SLATER, F. REGAN, D. DIAMOND and H. MURPHY. 2007. SmartCoast: a wireless sensor network for water quality monitoring. In: *Local Computer Networks, 2007. LCN 2007. 32nd IEEE Conference on: IEEE*, pp.815-816.
- O'HARA, M. J., S. R. BURGE and J. W. GRATE. 2009. Automated radioanalytical system for the determination of ⁹⁰Sr in environmental water samples by ⁹⁰Y Cherenkov radiation counting. *Analytical Chemistry*, **81**(3), pp.1228-1237.
- OKAWA, Y., H. KOBAYASHI and T. OHNO. 1995. Direct and simultaneous determination of uric acid and glucose in serum with electrochemical filter/biosensor flow-injection analysis system. *Analytica Chimica Acta*, **315**(1-2), pp.137-143.
- OLANIRAN, A. O., L. HIRALAL and B. PILLAY. 2011. Whole-cell bacterial biosensors for rapid and effective monitoring of heavy metals and inorganic pollutants in wastewater. *Journal of Environmental Monitoring*, **13**(10), pp.2914-2920.
- OLIVER, I. W., M. C. GRAHAM, A. B. MACKENZIE, R. M. ELLAM and J. G. FARMER. 2007. Assessing depleted uranium (DU) contamination of soil, plants and earthworms at UK weapons testing sites. *Journal of Environmental Monitoring*, **9**(7), pp.740-748.
- ORAZEM, M. E. and B. TRIBOLLET. 2011. *Electrochemical impedance spectroscopy*. John Wiley & Sons.
- POLLARD, T. 2014 *An Autonomous Pumping System for Remote Sampling and "The Web of Things"*. School of Mechanical Engineering, University of Leeds, Undergraduate Project Dissertation, MECH 3810, Unpublished.
- POLLMANN, K., J. RAFF, M. MERROUN, K. FAHMY and S. SELENSKA-POBELL. 2006. Metal binding by bacteria from uranium mining waste piles and its technological applications. *Biotechnology Advances*, **24**(1), pp.58-68.
- PORTA, L., T. H. ILLANGASEKARE, P. LODEN, Q. HAN and A. P. JAYASUMANA. 2009. Continuous plume monitoring using wireless sensors: Proof of concept in intermediate scale tank. *Journal of Environmental Engineering*, **135**(9), pp.831-838.
- POST, F. H. and T. VAN WALSUM. 1993. *Fluid flow visualization*. Springer.

- POWELL, J. H., C. N. WATERS, D. MILLWARD and N. S. ROBINS. 2010. *Managing Radioactive Waste Safely: Initial Geological Unsuitability Screening of West Cumbria*. Keyworth, Nottingham: Natural Environment Research Council (NERC)/British Geological Survey.
- PRODROMIDIS, M. I. 2010. Impedimetric immunosensors—A review. *Electrochimica Acta*, **55**(14), pp.4227-4233.
- PRODROMIDIS, M. I. and M. I. KARAYANNIS. 2002. Enzyme based amperometric Biosensors for food analysis. *Electroanalysis*, **14**(4), pp.241-261.
- REYES, D. R., D. IOSSIFIDIS, P.-A. AUROUX and A. MANZ. 2002. Micro Total Analysis Systems. 1. Introduction, Theory, and Technology. *Analytical Chemistry*, **74**(12), pp.2623-2636.
- RIPPETH, J. J., T. D. GIBSON, J. P. HART, I. C. HARTLEY and G. NELSON. 1997. Flow-injection detector incorporating a screen-printed disposable amperometric biosensor for monitoring organophosphate pesticides. *Analyst*, **122**(11), pp.1425-1429.
- RIVET, C., H. LEE, A. HIRSCH, S. HAMILTON and H. LU. 2011. Microfluidics for medical diagnostics and biosensors. *Chemical Engineering Science*, **66**(7), pp.1490-1507.
- ROEHL, K. E., K. CZURDA, T. MEGGYES, F.-G. SIMON and D. I. STEWART. 2005. Chapter 1 Permeable reactive barriers. In: T. M. F. G. S. K.E. ROEHL and D. I. STEWART, eds. *Trace Metals and other Contaminants in the Environment*. Elsevier, pp.1-25.
- RON, H., S. MATLIS and I. RUBINSTEIN. 1998. Self-Assembled Monolayers on Oxidized Metals. 2. Gold Surface Oxidative Pretreatment, Monolayer Properties, and Depression Formation. *Langmuir*, **14**(5), pp.1116-1121.
- RONKAINEN, N. J., H. B. HALSALL and W. R. HEINEMAN. 2010. Electrochemical biosensors. *Chemical Society Reviews*, **39**(5), pp.1747-1763.
- ROY, D. K. and A. P. PENTLAND. 2002. Learning words from sights and sounds: A computational model. *Cognitive science*, **26**(1), pp.113-146.
- RUSHWORTH, J. V., N. A. HIRST, J. A. GOODE, D. J. PIKE, A. AHMED and P. MILLNER. 2013. *Impedimetric Biosensors for Medical Applications: Current Progress and Challenges*. Momentum Press.
- SAENKO, V., V. IVANOV, A. TSYB, T. BOGDANOVA, M. TRONKO, Y. DEMIDCHIK and S. YAMASHITA. 2011. The Chernobyl Accident and its Consequences. *Clinical Oncology*, **23**(4), pp.234-243.
- SAFAVIEH, M., M. U. AHMED, M. TOLBA and M. ZOUROB. 2012. Microfluidic electrochemical assay for rapid detection and quantification of *Escherichia coli*. *Biosensors and Bioelectronics*, **31**(1), pp.523-528.
- SALEH, H. M. 2012. Water hyacinth for phytoremediation of radioactive waste simulate contaminated with cesium and cobalt radionuclides. *Nuclear Engineering and Design*, **242**(0), pp.425-432.

- SANKARAN, S., S. PANIGRAHI and S. MALLIK. 2011. Olfactory receptor based piezoelectric biosensors for detection of alcohols related to food safety applications. *Sensors and Actuators B: Chemical*, **155**(1), pp.8-18.
- SASSOLAS, A., L. J. BLUM and B. D. LECA-BOUVIER. 2012. Immobilization strategies to develop enzymatic biosensors. *Biotechnology Advances*, **30**(3), pp.489-511.
- SAYLOR, J. R. 1995. PHOTOBLEACHING OF DISODIUM FLUORESCEIN IN WATER. *Experiments in Fluids*, **18**(6), pp.445-447.
- SCHOENENBERGER, C., J. A. M. SONDAG-HUETHORST, J. JORRITSMA and L. G. J. FOKKINK. 1994. What Are the "Holes" in Self-Assembled Monolayers of Alkanethiols on Gold? *Langmuir*, **10**(3), pp.611-614.
- SCHOLLE, M., A. HAAS, N. AKSEL, M. C. T. WILSON, H. M. THOMPSON and P. H. GASKELL. 2008. Competing geometric and inertial effects on local flow structure in thick gravity-driven fluid films. *Physics of Fluids*, **20**(12), p10.
- SIGMA ALDRICH. 2014a. *Phosphate buffered saline product page* [online]. [Accessed 28/08/2014]. Available from: <http://www.sigmaaldrich.com/catalog/product/sigma/p4417?lang=en®ion=GB>.
- SIGMA ALDRICH. 2014b. *Technical Bulletin AL-266 Preparing Self-Assembled Monolayers (SAMs)*
- A Step-by-Step Guide for Solution-Based Self-Assembly* [online]. [Accessed 03/12/2014]. Available from: <https://www.sigmaaldrich.com/content/dam/sigmaaldrich/docs/Aldrich/Instructions/1/al-266.pdf>.
- SONG, L., E. J. HENNINK, I. T. YOUNG and H. J. TANKE. 1995. Photobleaching kinetics of fluorescein in quantitative fluorescence microscopy. *Biophysical Journal*, **68**(6), pp.2588-2600.
- STONE, H. A., A. D. STROOCK and A. AJDARI. 2004. Engineering Flows In Small Devices. *Annual Review of Fluid Mechanics*, **36**(1), pp.381-411.
- STRUERS LTD. 2014. *Pure Gold (DiaPro) Preparation Method Guidelines* [online]. [Accessed 19/08/2014]. Available from: [https://e-shop.struers.com/AU/EN/methods/Non-Ferrous_Metals/Gold_and_Au_Alloys/Pure_Gold_\(DiaPro\)\(57344-1202\).aspx?discSize=200](https://e-shop.struers.com/AU/EN/methods/Non-Ferrous_Metals/Gold_and_Au_Alloys/Pure_Gold_(DiaPro)(57344-1202).aspx?discSize=200).
- STUBENRAUCH, K., U. WESSELS, R. VOGEL and J. SCHLEYPEN. 2009. Evaluation of a biosensor immunoassay for simultaneous characterization of isotype and binding region of human anti-tocilizumab antibodies with control by surrogate standards. *Analytical Biochemistry*, **390**(2), pp.189-196.
- TABAK, H., P. LENS, E. HULLEBUSCH and W. DEJONGHE. 2005. Developments in Bioremediation of Soils and Sediments Polluted with Metals and Radionuclides – 1. Microbial Processes and Mechanisms Affecting Bioremediation of Metal Contamination and Influencing Metal Toxicity and Transport. *Reviews in Environmental Science and Bio/Technology*, **4**(3), pp.115-156.

- TENCALIEC, A. M., S. LASCHI, V. MAGEARU and M. MASCINI. 2006. A comparison study between a disposable electrochemical DNA biosensor and a *Vibrio fischeri*-based luminescent sensor for the detection of toxicants in water samples. *Talanta*, **69**(2), pp.365-369.
- THÉVENOT, D. R., K. TOTH, R. A. DURST and G. S. WILSON. 2001. Electrochemical biosensors: recommended definitions and classification. *Biosensors and Bioelectronics*, **16**(1–2), pp.121-131.
- THORLABS.COM. 2011a. *FB490-10 - Bandpass Filter Support Documentation (Spec Sheet)* [online]. [Accessed 06/07/2011]. Available from: <http://www.thorlabs.com/thorproduct.cfm?partnumber=FB490-10>.
- THORLABS.COM. 2011b. *FB520-10 - Bandpass Filter Support Documentation (Spec Sheet)* [online]. [Accessed 05/09/2011]. Available from: <http://www.thorlabs.de/Thorcat/7000/7028-S01.pdf>.
- THORSEN, T., S. J. MAERKL and S. R. QUAKE. 2002. Microfluidic Large-Scale Integration. *Science*, **298**(5593), pp.580-584.
- TKAC, J. and J. J. DAVIS. 2008. An optimised electrode pre-treatment for SAM formation on polycrystalline gold. *Journal of Electroanalytical Chemistry*, **621**(1), pp.117-120.
- TSCHMELAK, J., G. PROLL, J. RIEDT, J. KAISER, P. KRAEMMER, L. BÁRZAGA, J. S. WILKINSON, P. HUA, J. P. HOLE, R. NUDD, M. JACKSON, R. ABUKNESA, D. BARCELÓ, S. RODRIGUEZ-MOZAZ, M. J. L. D. ALDA, F. SACHER, J. STIEN, J. SLOBODNÍK, P. OSWALD, H. KOZMENKO, E. KORENKOVÁ, L. TÓTHOVÁ, Z. KRASCSENITS and G. GAUGLITZ. 2005. Automated Water Analyser Computer Supported System (AWACSS) Part I: Project objectives, basic technology, immunoassay development, software design and networking. *Biosensors and Bioelectronics*, **20**(8), pp.1499-1508.
- Uniscan Instruments, PG581 Potentiostat - Galvanostat*. 2013. [online]. [Accessed 04 June 2013]. Available from: <http://uniscan.veriovps.co.uk/electrochemistry-instruments/potentiostat/>.
- VAN DORST, B., J. MEHTA, K. BEKAERT, E. ROUAH-MARTIN, W. DE COEN, P. DUBRUEL, R. BLUST and J. ROBBENS. 2010. Recent advances in recognition elements of food and environmental biosensors: A review. *Biosensors and Bioelectronics*, **26**(4), pp.1178-1194.
- VANDENHOVE, H. 2002. European sites contaminated by residues from the ore-extracting and -processing industries. *International Congress Series*, **1225**(0), pp.307-315.
- VERSTEEG, H. K. and W. MALALASEKERA. 2007. *An introduction to computational fluid dynamics: the finite volume method*. Pearson Education.
- VRANA, B., I. J. ALLAN, R. GREENWOOD, G. A. MILLS, E. DOMINIAK, K. SVENSSON, J. KNUTSSON and G. MORRISON. 2005. Passive sampling techniques for monitoring pollutants in water. *TrAC Trends in Analytical Chemistry*, **24**(10), pp.845-868.
- WALKER, D. A. 1987. A fluorescence technique for measurement of concentration in mixing liquids. *Journal of Physics E-Scientific Instruments*, **20**(2), pp.217-224.

- WHITESIDES, G. M. 2006. The origins and the future of microfluidics. *Nature*, **442**(7101), pp.368-373.
- WHO. 2004. Uranium in drinking-water: background document for development of WHO guidelines for drinking-water quality.
- WU, J., J. TANG, Z. DAI, F. YAN, H. JU and N. E. MURR. 2006. A disposable electrochemical immunosensor for flow injection immunoassay of carcinoembryonic antigen. *Biosensors and Bioelectronics*, **22**(1), pp.102-108.
- YANG, C.-H. 1998. Statistical mechanical study on the Freundlich isotherm equation. *Journal of colloid and interface science*, **208**(2), pp.379-387.
- YOSHIDA, N. and Y. TAKAHASHI. 2012. Land-Surface Contamination by Radionuclides from the Fukushima Daiichi Nuclear Power Plant Accident. *Elements*, **8**(3), pp.201-206.
- YU, J., L. GE, J. HUANG, S. WANG and S. GE. 2011. Microfluidic paper-based chemiluminescence biosensor for simultaneous determination of glucose and uric acid. *Lab on a Chip*, **11**(7), pp.1286-1291.
- YUNUS, S., A. JONAS and B. LAKARD. 2013. Potentiometric Biosensors. In: G. K. ROBERTS, ed. *Encyclopedia of Biophysics*. Springer Berlin Heidelberg, pp.1941-1946.
- ZAMORA, M. L., B. TRACY, J. ZIELINSKI, D. MEYERHOF and M. MOSS. 1998. Chronic ingestion of uranium in drinking water: a study of kidney bioeffects in humans. *Toxicological Sciences*, **43**(1), pp.68-77.
- ZANELLO, P. 2003. *Inorganic electrochemistry: theory, practice and applications*. Royal Society of Chemistry.
- ZHOU, Y. and G. ZHU. 1997. Rapid automated in-situ monitoring of total dissolved iron and total dissolved manganese in underground water by reverse-flow injection with chemiluminescence detection during the process of water treatment. *Talanta*, **44**(11), pp.2041-2049.
- ZHU, H., R. C. DERKSEN, C. R. KRAUSE, R. D. FOX, R. D. BRAZEE and H. E. OZKAN. 2005. Fluorescent intensity of dye solutions under different pH conditions. *Journal of ASTM International*, **2**(6), pp.1-7.
- ZHU, Y. G. and G. SHAW. 2000. Soil contamination with radionuclides and potential remediation. *Chemosphere*, **41**(1-2), pp.121-128.
- ZIENKIEWICZ, O. C., R. L. TAYLOR and P. NITHIARASU. 2005. *Finite Element Method for Fluid Dynamics (6th Edition)*. Amsterdam ; London Elsevier Butterworth Heinemann.
- ZOSKI, C. G. 2007. *Handbook of electrochemistry*. Elsevier.

APPENDIX A Matlab code for experimental investigations

A1. Relationship between luminescence intensity and fluorescein concentration

```
%Identify and acquire flow video of interest
readerobj = VideoReader('100 micromolar.avi');

%Define and display first video image
firstimage =read(readerobj,1);
image(firstimage);
title('First Image');
I=firstimage;
hold on
pause()

%Define a vertical line horizontally across the flow channel, display
%line, and then plot intensity profiles for the line region
p1 = [500,400];
p2 = [500,600];
plot([p1(2),p2(2)], [p1(1),p2(1)], 'Color', 'r', 'LineWidth', 1)
title('Selected horizontal line across flow channel');
hold off
pause()
x = [400 600];
y = [500 500];
improfile(I,x,y);
title('Intensity Profile For Selected Line y = 500');
pause()

%From the resultant plot, identify a representative minimum luminescence
%intensity for for the flow channel

%Define a Region Of Interest (mask) based upon minimum image intensity
mask=(I)>=40;
mask2=uint8(mask);
image(mask);
pause()

%Calculate the mean intensity within the region of interest
flowdomain_mean = mean(firstimage(mask));
disp(flowdomain_mean)
```

Figure A-1 Matlab code for the investigation of the relationship between luminescence intensity and fluorescein concentration

A2. Analysis of flow-fluorescence images

```
%Identify and acquire flow video of interest
readerobj = VideoReader('flowvideo09.avi');

%Define image frame representing the background luminescence intensity
background = read(readerobj,1);

%Define the last video image, representing maximum fluorescein
%concentration
lastimage =read(readerobj,3990);

%Subtract last image from the background image and display the resulting
%image (i.e. an image representing the luminescence intensity 'range')
images_filtered=lastimage-background;
I=images_filtered;
image(I);
title('First Image minus Last Image');
hold on
pause()

%Define vertical line through the 'images_filtered' image, display
%line, and then plot intensity profile for the line
p1 = [1,500];
p2 = [1004,500];
plot([p1(2),p2(2)], [p1(1),p2(1)], 'Color', 'r', 'LineWidth',1)
title('First Image minus Last Image (with lines for intensity plots)');
hold off
pause()
x = [500 500];
y = [1 1004];
improfile(I,x,y);
title('Intensity Profile For Selected Vertical Line x = 550');
pause()

%From the plot identify a threshold intensity value, to be used to define
%a region of interest (ROI), representing the flow channel

%Define a ROI (mask) based upon the threshold intensity value and
%display mask image to check ROI quality (& adjust threshold if necessary)
mask=(I)>=20;
mask2=uint8(mask);
image(mask);

%Define a range of video frames that relate to the presence of flow
%activity within the flow domain (k = start of flow : frame period : end of
%video) Note: 25 frames duration = 1 second of video time
i=0;
for k= 220:25:3990
i=i+1;

%Apply k to flow video of interest, and specifically to the video frame
%range selection defined as 'k' above
images = read(readerobj,k);

%Calculate scaled intensity (a proxy for scaled fluorescein concentration)
%for the range of video frames defined in 'images' above,
images_filtered1=images-background;
images_filtered2=lastimage-background;
images_filtered3=(single(images_filtered1)./single(images_filtered2));
```

```
%Force any resultant 'not a number'(NaN) and 'infinity' (Inf) values to
%zero
nan_locations = isnan(images_filtered3);
images_filtered3(nan_locations) = 0;
inf_locations = isinf(images_filtered3);
images_filtered3(inf_locations) = 0;

%Calculate the mean scaled intensity (i.e. mean scaled concentration)
%within the region of interest (flow channel)
flowdomain_mean(i) = mean(images_filtered3(mask));

end

%Plot mean intensity within ROI against time
plot(1:i,flowdomain_mean);
axis([1 160 0 1.1]);
title('Mean scaled intensity for flow domain region')
xlabel('Measurement Points');
ylabel('Mean scaled intensity (Mean scaled concentration)');
```

Figure A-2 Matlab code for the analysis of flow-fluorescence images